INFLUENCE OF THE SUBSTRATE SURFACE PREPARATION ON OPTICAL PROPERTIES AND COLOR OF ANODIZED TITANIUM

Quentin Cridling

▶ **To cite this version:**

HAL Id: tel-02155071

https://theses.hal.science/tel-02155071

Submitted on 13 Jun 2019

THESE de DOCTORAT DE L'UNIVERSITE DE LYON
opérée au sein de
l'Ecole des Mines de Saint-Etienne

Ecole Doctorale N° 488
Sciences, Ingénierie, Santé

Spécialité de doctorat : Material sciences and Engineering

Soutenue publiquement le 19/07/2018, par :
Quentin CRIDLING

INFLUENCE OF THE SUBSTRATE SURFACE PREPARATION ON OPTICAL PROPERTIES AND COLOR OF ANODIZED TITANIUM

Devant le jury composé de :

Vignal, Vincent	DR CNRS Université de Bourgogne, Dijon	Président & Examinateur
Lafon, Dominique	Maître-Assistant, Mines d'Alès	Rapporteure
Flury, Manuel	Maître de conférences, INSA Strasbourg Laboratoire ICube UMR CNRS 7357	Rapporteur
Delafosse, David	Professeur, Mines Saint-Etienne	Directeur de thèse
Pedeferri, Maria Pia	Professor, Politecnico di Milano	Co-directrice de thèse
Charrière, Renée	Maître-Assistant, Mines Saint-Etienne	Co-encadrante

EMSE : Enseignants-chercheurs et chercheurs autorisés à diriger des thèses de doctorat (titulaires d'un doctorat d'État ou d'une HDR)

ABSI	Nabil	CR	Génie industriel	CMP
AUGUSTO	Vincent	CR	Image, Vision, Signal	CIS
AVRIL	Stéphane	PR2	Mécanique et ingénierie	CIS
BADEL	Pierre	MA(MDC)	Mécanique et ingénierie	CIS
BALBO	Flavien	PR2	Informatique	FAYOL
BASSEREAU	Jean-François	PR	Sciences et génie des matériaux	SMS
BATTON-HUBERT	Mireille	PR2	Sciences et génie de l'environnement	FAYOL
BEIGBEDER	Michel	MA(MDC)	Informatique	FAYOL
BLAYAC	Sylvain	MA(MDC)	Microélectronique	CMP
BOISSIER	Olivier	PR1	Informatique	FAYOL
BONNEFOY	Olivier	MA(MDC)	Génie des Procédés	SPIN
BORBELY	Andras	MR(DR2)	Sciences et génie des matériaux	SMS
BOUCHER	Xavier	PR2	Génie Industriel	FAYOL
BRODHAG	Christian	DR	Sciences et génie de l'environnement	FAYOL
BRUCHON	Julien	MA(MDC)	Mécanique et ingénierie	SMS
CAMEIRAO	Ana	MA(MDC)	Génie des Procédés	SPIN
CHRISTIEN	Frédéric	PR	Science et génie des matériaux	SMS
DAUZERE-PERES	Stéphane	PR1	Génie Industriel	CMP
DEBAYLE	Johan	MR	Sciences des Images et des Formes	SPIN
DEGEORGE	Jean-Michel	MA(MDC)	Génie industriel	Fayol
DELAFOSSE	David	PR0	Sciences et génie des matériaux	SMS
DELORME	Xavier	MA(MDC)	Génie industriel	FAYOL
DESRAYAUD	Christophe	PR1	Mécanique et ingénierie	SMS
DJENIZIAN	Thierry	PR	Science et génie des matériaux	CMP
DOUCE	Sandrine	PR2	Sciences de gestion	FAYOL
DRAPIER	Sylvain	PR1	Mécanique et ingénierie	SMS
FAUCHEU	Jenny	MA(MDC)	Sciences et génie des matériaux	SMS
FAVERGEON	Loïc	CR	Génie des Procédés	SPIN
FEILLET	Dominique	PR1	Génie Industriel	CMP
FOREST	Valérie	MA(MDC)	Génie des Procédés	CIS
FRACZKIEWICZ	Anna	DR	Sciences et génie des matériaux	SMS
GARCIA	Daniel	MR(DR2)	Sciences de la Terre	SPIN
GAVET	Yann	MA(MDC)	Sciences des Images et des Formes	SPIN
GERINGER	Jean	MA(MDC)	Sciences et génie des matériaux	CIS
GOEURIOT	Dominique	DR	Sciences et génie des matériaux	SMS
GONDRAN	Natacha	MA(MDC)	Sciences et génie de l'environnement	FAYOL
GONZALEZ FELIU	Jesus	MA(MDC)	Sciences économiques	FAYOL
GRAILLOT	Didier	DR	Sciences et génie de l'environnement	SPIN
GROSSEAU	Philippe	DR	Génie des Procédés	SPIN
GRUY	Frédéric	PR1	Génie des Procédés	SPIN
GUY	Bernard	DR	Sciences de la Terre	SPIN
HAN	Woo-Suck	MR	Mécanique et ingénierie	SMS
HERRI	Jean Michel	PR1	Génie des Procédés	SPIN
KERMOUCHE	Guillaume	PR2	Mécanique et Ingénierie	SMS
KLOCKER	Helmut	DR	Sciences et génie des matériaux	SMS
LAFOREST	Valérie	MR(DR2)	Sciences et génie de l'environnement	FAYOL
LERICHE	Rodolphe	CR	Mécanique et ingénierie	FAYOL
MALLIARAS	Georges	PR1	Microélectronique	CMP
MOLIMARD	Jérôme	PR2	Mécanique et ingénierie	CIS
MOUTTE	Jacques	CR	Génie des Procédés	SPIN
NEUBERT	Gilles			FAYOL
NIKOLOVSKI	Jean-Pierre	Ingénieur de recherche	Mécanique et ingénierie	CMP
NORTIER	Patrice	PR1	Génie des Procédés	SPIN
O CONNOR	Rodney Philip	MA(MDC)	Microélectronique	CMP
OWENS	Rosin	MA(MDC)	Microélectronique	CMP
PERES	Véronique	MR	Génie des Procédés	SPIN
PICARD	Gauthier	MA(MDC)	Informatique	FAYOL
PIJOLAT	Christophe	PR0	Génie des Procédés	SPIN
PINOLI	Jean Charles	PR0	Sciences des Images et des Formes	SPIN
POURCHEZ	Jérémy	MR	Génie des Procédés	CIS
ROUSSY	Agnès	MA(MDC)	Microélectronique	CMP
ROUSTANT	Olivier	MA(MDC)	Mathématiques appliquées	FAYOL
SANAUR	Sébastien	MA(MDC)	Microélectronique	CMP
STOLARZ	Jacques	CR	Sciences et génie des matériaux	SMS
TRIA	Assia	Ingénieur de recherche	Microélectronique	CMP
VALDIVIESO	François	PR2	Sciences et génie des matériaux	SMS
VIRICELLE	Jean Paul	DR	Génie des Procédés	SPIN
WOLSKI	Krzystof	DR	Sciences et génie des matériaux	SMS
XIE	Xiaolan	PR0	Génie industriel	CIS
YUGMA	Gallian	CR	Génie industriel	CMP

Mise à jour : 03/02/2017

Remerciements :

Malgré la croyance populaire, le travail de thèse est loin d'être un travail solitaire, c'est pourquoi j'aimerais remercier un grand nombre de personnes dont la présence, les conseils ainsi que le regard critique sur mes recherches m'ont permis de mener à bien ce travail de recherche.

En premier lieu, je tiens à remercier mon directeur de thèse, monsieur David Delafosse, de m'avoir donné la chance de réaliser ce travail et d'avoir accepté des délais très courts lors de la relecture de mon manuscrit.

Je voudrais aussi fortement remercier Maria Pia Pedeferri de m'avoir accueilli dans le laboratoire du Politecnico di Milano comme un membre à part entière de l'équipe. Je tenais aussi à la remercier de sa patience et pour m'avoir prodigué de nombreux conseils et idées très avisés. J'en profite pour remercier aussi tous les membres du Politecnico de l'équipe du CMIC avec qui j'ai passé d'excellents moments notamment Davide et Arash, compagnons doctorants.

Je souhaiterais exprimer ma gratitude à Renée Charrière, sans qui cette thèse aurait été totalement différente. Je tenais à louer ses qualités humaines et professionnelles ainsi que sa disponibilité sans faille, même dans des conditions vraiment difficiles. Je n'oublierais surement jamais ses moments passés à la conférence de San Francisco où j'ai pu redécouvrir une encadrante avenante mais aussi une personne passionnante et d'une grande bienveillance.

Je tiens aussi à remercier tous les techniciens de l'Ecole des Mines de Saint-Etienne notamment ceux de l'atelier qui ont souvent fait l'impossible pour me fournir des pièces dans des délais extrêmement serrés. Je tiens à remercier tout particulièrement Max et Yohan avec qui j'ai partagé de délicieux moments mais aussi avec qui de nombreuses idées ont vu le jour.

Cette thèse n'aurait jamais pu être réalisée sans l'aide précieuse de Gilles Blanc. Un grand merci pour tout ce que tu as fait pour moi dans ton laboratoire parfaitement tenu de métallographie. Ce fut un réel plaisir de travailler et échanger avec toi.

Un grand merci à David Piot pour toutes ces heures de discussions vraiment enrichissantes aussi bien professionnelles que personnelles.

Ma vie de doctorant n'aurait surement pas été aussi plaisante sans la présence des autres doctorants de l'école des Mines.

Tout d'abord les Mathieu/Matthieu avec qui j'ai pu forger plus qu'une relation de travail mais je l'espère une amitié sincère. Je tiens à remercier le doctorant le plus K4 de J pour tout ce qu'il a fait, que cela soit nos raids chez Ikea pour monter des « Billy », pour m'avoir accompagné les dimanches matin au cinéma et/ou à la piscine mais aussi pour nous avoir permis d'utiliser aussi souvent son appartement pour nos soirées jeux. Puis le second, pour toutes nos aventures dans Saint-Etienne, ses blagues de qualités, toutes les soirées cinémas qu'il a organisé et surtout pour toutes nos discussions professionnelles et personnelles. Merci de m'avoir aidé à tenir le coup dans les moments les plus durs de ma thèse. J'espère vraiment que nos chemins se croiseront de nouveau bientôt.

Puis Clément et Lisa, le premier que je tenais à te remercier pour avoir égaillé nos journées par sa bonne humeur et ses blagues de mauvaise qualité mais aussi pour son incroyable sérieux dans nos discussions professionnelles (notamment d'avoir répondu à toutes mes questions sur Word pendant nos rédactions respectives !). La seconde pour sa gentillesse et son soutien moral sans failles mais aussi pour ses gâteaux, tous aussi bons que généreux !

Une grosse pensée, sans mauvais jeux de mot, à Joris, notre ronchon préféré avec qui nous avons eu de nombreux fous rires mais aussi de longues discussions. J'espère te revoir rapidement mon grand.

Une pensée sincère pour ma co-bureau Jessica que je n'oublierais pas que cela soit pour les fous rires ou les journées difficiles respectives mais aussi pour nos aventures en conférence de présentation de profilomètres sous la neige au milieu de nulle part ou nos galères respectives avec le Labex ! Une pensée pour Esther, mon autre co-bureau, j'espère que tu te portes bien et que ton nouvel environnement professionnel te permet de t'épanouir.

Une petite pensée aux prochains docteurs tels qu'Elia, Julia et Anthonis mais aussi à tous les anciens tels que Guillaume, Robin, Jigé, David, Ernesto et Aladji.

Un grand merci à ma mère et mon frère pour tout ce qu'ils ont fait jusqu'à ce jour.

TABLE OF CONTENT

ILLUSTRATIONS LISTING

Figures listing

Table listing

General introduction

Innovation by design is one of the industrial levers to improve the perceived value of a product and thus its attractiveness. The color and the surface texture of a product play a key role in its perceived value. The use of materials with complex colored effects is growing in different domains such as security printing [1], [2], automotive industry [3], [4] and jewelry [5].

Metals and in particular oxidized metals catch manufacturers attention because of both their color effects and the properties of metals. It is in particular the case for titanium, well known for properties such as corrosion resistance [6], biocompatibility [7], and its mechanical properties to density ratio [8]–[10], which open large domains of applications [11] such as automobile [12], medicine and aerospace [13].

Titanium dioxide is also used in building materials because of its photocatalytic properties [14][15], for surface self-cleaning [16]–[18] and depollution [19]–[21]. For architecture and design [22][23], manufacturers' attention is directed towards colored titanium oxides. Titanium is naturally covered by a thin transparent passive film of a few nanometers when exposed to the ambient air. However, when the oxide layer grows, oxidized titanium samples exhibits colors and, under specifics conditions, gonioappearance.

The American Society for Testing and Materials (ASTM) definition of gonioppearance [24] is "*exhibits different colors depending on the angle of illumination or sensing*". The ASTM standard does not specify whether the color change implies a change of one or all the attributes of the color (lightness, hue and saturation). According to this definition, a majority of the surrounding objects are gonioapparent, for example a glossy object is gonioapparent. The goniochromism is later defined by McCamy (1996) [25] as a significant change of the color hue and saturation with the incidence and/or observation angle. The iridescent and pearly products are for example goniochromic materials. Under specific conditions oxidized titanium is goniochromic.

Goniochromic effects are usually obtained by adding specific pigments. Metallic effects are obtained with microscopic metallic particles (copper, aluminum…) and goniochromic interferential effects are obtained with pigments such as mineral lamellae (mica, glass, alumina and silica) coated with a metallic oxide layer (TiO_2, Cr_2O_3…). Goniochromism stems from the interactions between light and the material structure, which result into interference and/or diffraction phenomena.

The study and the development of goniochromic materials remains a challenge both for industry and for scientific research. In industry, color quality control is made difficult by the complex color effects of these materials. The development of standard goniochromic samples with referenced color effects could simplify this color quality control. By comparing the manufactured materials to the reference, for example by acquiring pictures of both materials in given illumination and observation geometries could be major improvement for color quality control. The challenge for scientific research consists in being able to control the color evolution with the illumination and observation conditions and define color characterization geometries in agreement with perceived color effects.

In this context, this PhD work has been initiated. Its objectives are to produce and characterize goniochromic samples that could be used later as reference goniochromic/gonioapparent standard materials. The chosen material is oxidized titanium.

The following questions will be addressed:

→ What is the best oxidation technique in order to obtain colored and gonioapparent samples?

→ What is the impact of the titanium substrate surface preparation on the sample color and gonioapparent behavior?

→ How are the reflectance and thus the color linked to the material properties such as the oxide thickness and refractive indexes of titanium and titanium dioxide?

→ Which optical model can be used to predict the material reflectance?

The first chapter of this manuscript is dedicated to the basic elements necessary to define the concept of color, color attributes and how color is represented in the various color spaces. The interferential phenomena which are responsible for the coloration of oxidized metals are presented. The Abeles matrices formalism used to simulate the reflectance spectra of oxidized metals is also introduced. This chapter also describes the different devices and their specific measurements geometries used to characterize the color of a sample.

The second chapter presents the different techniques to oxidize titanium samples, namely anodizing, heating oxidation, laser assisted oxidation and plasma electrolytic oxidation. For each technique, the oxide layer composition, the oxide thickness range, the range of colors and the origin of the color are discussed. The second part of this chapter is dedicated to the parameters influencing the color of anodized titanium samples. They can either be anodizing parameters such as the current density, the cell potential, the electrolyte concentration and composition, or related to the titanium substrate such as the crystalline orientation or the surface roughness.

The third chapter studies the influence of an HF/HNO_3 etching of the substrate etching on the anodized titanium samples color and aspect. First are presented the experimental setup, the sample preparation and the anodizing parameters used to realize the study. The characterization protocol of the sample roughness before and after anodizing is then presented. A brief bibliographic review and preliminary studies about the impact of hydrofluoric acid on the titanium substrate microstructure and composition are presented. The samples visual aspect and reflectance measurements made with the goniospectrophotometer Optimines are then discussed to obtain the impact of etching on the sample colors. Different oxide layer thickness estimation techniques, in particular an estimation technique based on the extrema of the reflectance spectra are then introduced. The Bidirectional Reflectance Distribution Function (BRDF) spectral and angular variations are used to highlight the appearance of a diffuse component of the etched samples before anodizing.

The last chapter introduces a new series of samples in which the substrate roughness has been controlled by different mechanical and chemical polishing protocols. The goal of this new substrate preparation protocol is to obtain a better control of the substrate roughness and to avoid potential substrate chemical composition changes due to the HF/HNO_3 etching process. The new samples preparation protocol is presented. The BRDF angular variations are then used to characterize the appearance of a diffuse component, depending on the roughness of the substrate and the cell potential used to anodize the samples. Different oxide thickness

measurements techniques, namely ellipsometry and X-ray reflectometry, were compared to the estimation techniques presented in the previous chapter to obtain a robust assessment of the oxide layer thickness of the new samples series. Experimental reflectance spectra obtained with Optimines and reflectance spectra computed with an Abeles matrices-based model using the ellipsometric data as parameters are then compared. Diffuse and specular reflectance comparisons of the samples are compared and a first simple model of the diffuse reflectance of the samples is also presented. The BRDF spectral variations are then used to characterize the goniochromism/gonioappearence of the samples as a function of the substrate preparation and the anodizing cell potential.

Chapter 1: State of the art: From light to colors and how to color metallic samples

I. Light spectrum and color
1) White light

This section is based on references [26][27][28][29] and Natalya Matasapey's PhD work [30]. Visible radiation is the only part of the electromagnetic radiation perceived by the human eye. The wavelengths of visible light are between 380 nm to 780 nm. Each wavelength is associated with a color. A light characterized by a single wavelength is called a monochromatic light. White light is a combination of lights of different wavelengths in the visible spectrum. It is a specific instance of polychromatic light. This light causes the retina of the human eye to generate a sensation of white, hence its name of "white light". The references for white and black lights are the light coming from the sun. Its spectrum is represented in Figure 1.
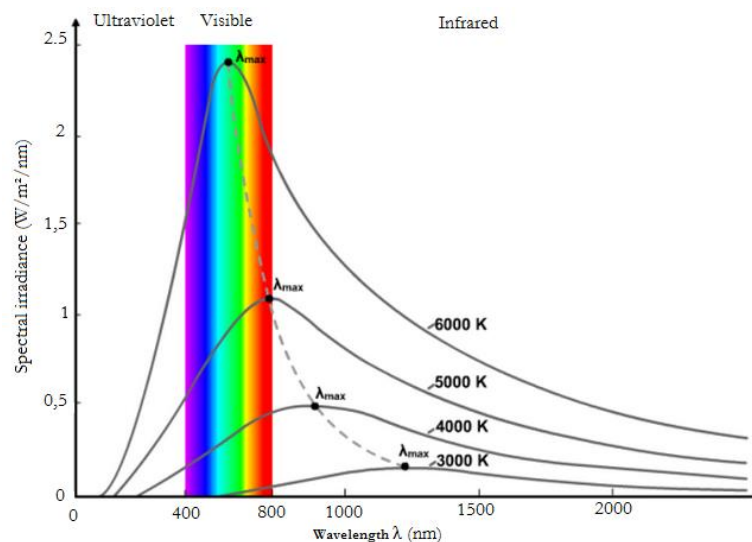
Figure 1: Spectral distribution of solar illumination for different temperatures.

The extraterrestrial solar radiation can be assimilated to the radiation of a Planck radiator at the temperature 6000K. The spectra measured by a human standing on earth's surface can be different because of the atmosphere, the variable distance between the earth and the sun and several other parameters (weather, altitude and geographic coordinates). The solar spectrum is strongly attenuated and modified by the components of the atmosphere: ozone, oxygen, water vapor, carbon dioxide, dust and aerosols. The perceived color of a surface comes from the modification of the spectrum of the incident light after reflection on this surface. The next section presents the possible origins of this modification.

2) The origins of color

When studying the spectrum of the light reflected from a surface, we observe that the shape of the spectrum varies, depending on the material properties. Indeed, the material can absorb some or all the wavelengths of the visible spectrum and therefore has a specific color. This color results from the chemical nature of the material and is often called "chemical color" or "color by absorption". Colors resulting from the presence of pigments in the material, which cause the

absorption of certain wavelengths, are good examples. The present study does not deal with such materials.

On the other hand, some colors result from physical phenomena occurring during the interaction of light with the structure of the material. These colors are called "physical colors" or "structural colors". The phenomena involved depend on the structure of the material and its characteristic dimension(s). These dimensions have to be compared to the visible light wavelengths:

- If the material structure size is greater than the visible wavelengths, color effects in a transparent material can result from the dispersion of light, as for example the dispersion observed at the output of a prism. Light dispersion is linked to the refractive index variation with the wavelength.

- If the material presents a structure at the same scale as the wavelength, the color is due to interference and diffraction phenomena [27]. It is such phenomena that govern the colors of anodized titanium. The principle of interferential color will be detailed later in this document. Other phenomena like scattering can also be observed.

In numerous contemporary color systems, color is characterized by three parameters. In the next section, some of these color systems, also referred to as "colorimetric spaces" are presented.

3) The three-color attributes

Color perception can be characterized by three independent attributes which are hue, purity and lightness. These three parameters are represented in
Figure **2**.

The Hue distinguishes colored sensations: blue, green, yellow, red, blue-green, etc. Pure colors (i.e.: monochromatic colors) are distributed over the circumference of a circle.

The Purity (or saturation) expresses how pure is a color. Gray is a fully desaturated color; as opposed to monochromatic colors, which are fully saturated colors.

The Lightness (tone) indicates whether a color is dark or bright.
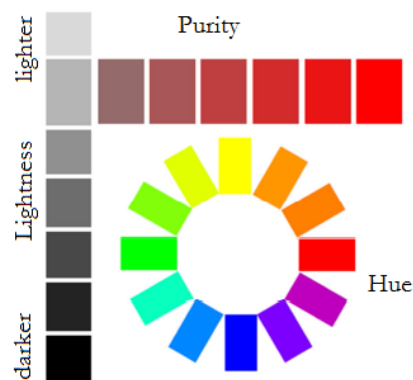
Figure 2: The three color attributes (from [26]).

4) Additional color properties:

Luminance describes the amount of light that is emitted, reflected or that passes through a particular area in a given solid angle. It is a measurement of the light intensity going in a given direction (i.e.: the intensity perceived by the human eye at a distance which is large compared to the light-emitting characteristic surface) per unit surface area of material. Its unit is the candela per square meter (cd/m²)

Brightness is the perception induced by the luminance of a visual target. It describes also the intensity of light sources. As a sensation, it depends on adaptation, i.e.: the same source may produce different perceptions depending on the environment.

Visual adaptation is a temporary change in perception when exposed to a new or intense stimulus and the lingering afterimage that may result after the disappearance of the said stimulus.

Chromaticity describes the quality of a color regardless of its luminance. It consists of two independent parameters which are the hue and the saturation.

5) Standard Observer and related color spaces

a) Standard observer

In order to universally define colors, the International Commission on Illumination (CIE) defined a fictional subject, called standard observer. Its "vision" of colors was defined from experimental results with human observers. The first standard colorimetric observer with a visual field angle of 2 ° was defined by the CIE in 1931. The 2° angle was chosen in accordance to the consideration that in the human eye, the color-sensitive cones lie in a 2° cone around the fovea, a region at the center of the human eye retina. The 1964 supplementary standard observer function is recommended when dealing with field of view wider than about 4°. It is conventionally defined with a field of view of 10°.

b) CIE XYZ Color space

The 2°, respectively 10°, standard observer is defined by the colorimetric functions, also called color-matching functions: $\bar{x}(\lambda)$, $\bar{y}(\lambda)$ and $\bar{z}(\lambda)$, respectively: $\bar{x}_{10}(\lambda)$, $\bar{y}_{10}(\lambda)$ and $\bar{z}_{10}(\lambda)$. These functions represent the color sensation response of the standard observer exposed to a given wavelength distribution. Using the colorimetric functions, the CIE has developed the color space CIE XYZ to represent colors from a spectrum taking into account the peculiarities of human vision.

The calculation of the tristimulus coefficients X, Y and Z (or trichromatic components) is carried out using the formulas in equation 1, where S(λ) is the spectral distribution of the illuminant, R(λ) the sample reflectance spectrum T(λ) in the case of a transmission measurement, K is a coefficient of normalization, and the integration domain used is the visible spectrum (380-780 nm). For the 2° standard observer:

$$X = K \int S(\lambda) \times \bar{x}(\lambda) \times R(\lambda)d\lambda$$

$$Y = K \int S(\lambda) \times \bar{y}(\lambda) \times R(\lambda)d\lambda$$

(1)

$$Z = K \int S\left(\lambda\right) \times \bar{z}(\lambda) \times R(\lambda)d\lambda$$

$$K = \frac{100}{\int S\left(\lambda\right) \times \bar{y}(\lambda)d\lambda}$$

This transposition method from a light spectrum to the tristimulus coefficients X, Y and Z is illustrated in Figure 3.
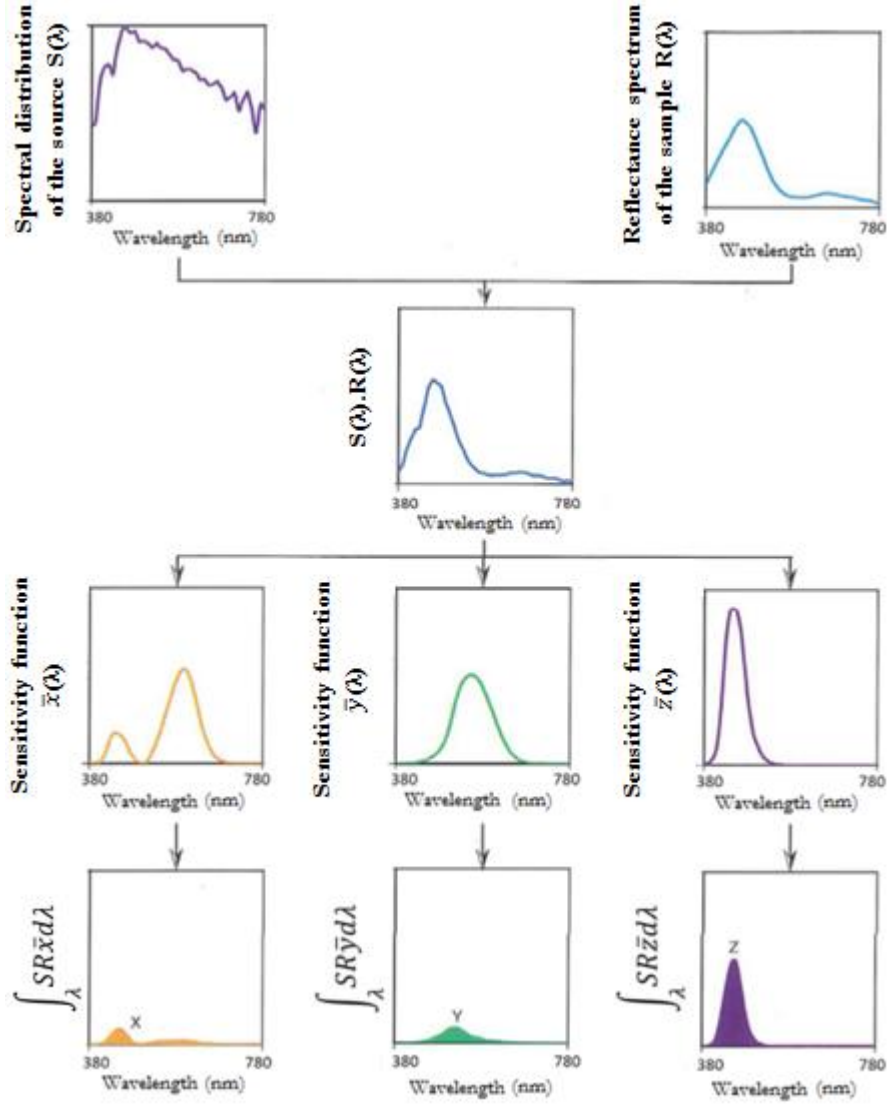
The chromaticity diagram is a commonly used method for color representation. It is presented in the following:

c) Chromaticity diagram CIE xy and CIE xyY color space

Since the human eye has three types of color sensors that respond to different ranges of wavelengths, a full plot of all visible colors is a three-dimensional figure. However, color can be defined using only 2 independent parameters: lightness and chromaticity. The CIE XYZ color space was designed with the Y parameter corresponding to the luminance of a color. The

chromaticity of a color was then specified by the two derived parameters x and y, two of the three normalized values which are functions of all three tristimulus values X, Y, and Z:

$$x = \frac{X}{X + Y + Z}$$

$$y = \frac{Y}{X + Y + Z}$$

$$z = \frac{Z}{X + Y + Z} = 1 - x - y$$

The derived color space specified by x, y, and Y is known as the CIE xyY color space.
The reverse operation is possible using the equation (3) to obtain the X and Z values and using the y value for Y:

$$X = \frac{Y}{y}x$$

$$Z = \frac{Y}{y}(1 - x - y)$$

$$(2)$$

The diagram (a) in Figure 4 shows the corresponding chromaticity diagram. The outer curved boundary is the *spectrum locus*, which corresponds to monochromatic lights. A straight line called the "line of purples" closes the surface. All colors perceived by the eye are within this limited area.

From this coordinate system, the Helmholtz coordinates (λ_d, ϱ_c) can be defined where λ_d is the dominant wavelength and ϱ_c is the purity. To determine the dominant wavelength of a color, one considers the radial segment starting from the point representing the color of the illuminant and passing through the point representing the color of the observed surface. If this half-line intercepts the spectrum locus, the wavelength corresponding to this intersection is λ_d (if it intercepts the line of purples, only the complementary dominant wavelength can be defined). ϱ_c on the chromaticity diagram is the ratio of the distance from the illuminant point to the color (a) to the distance between the illuminant and the dominant wavelength (a + b). This is represented in Figure 4 (b).
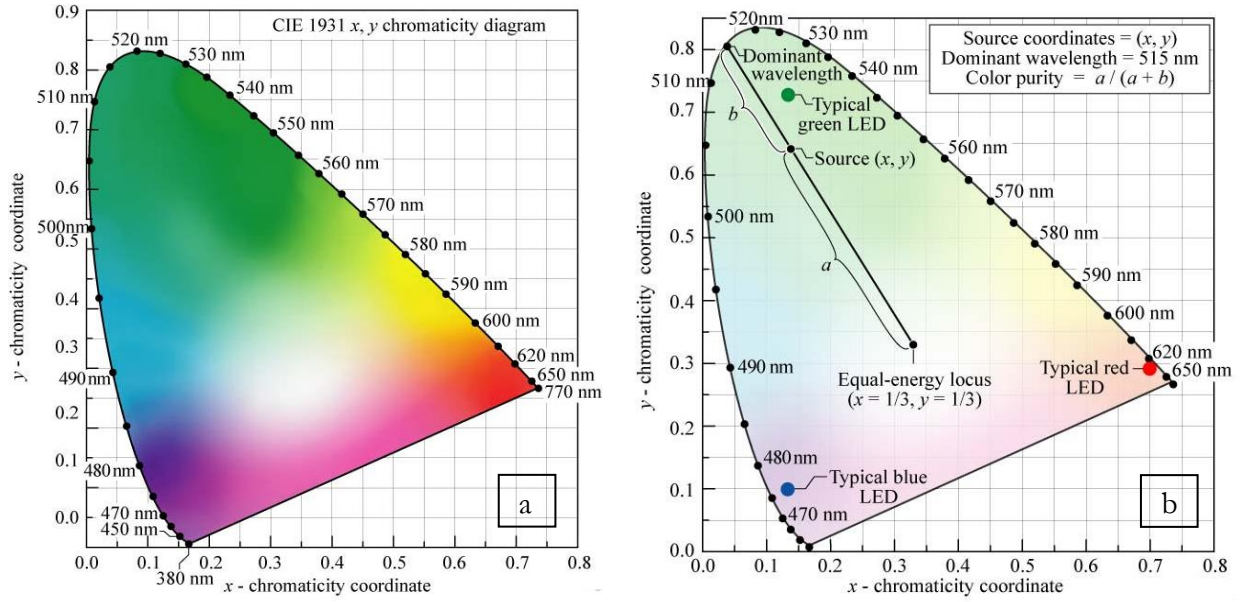
Figure 4: CIE xy chromaticity diagram (a) and chromaticity diagram showing the determination of the dominant wavelength and color purity using the equal-energy locus (x=1/3, y=1/3) as the white reference (b) (from [31]).

From the CIE XYZ color space, it is possible to determine other color spaces such as the CIELAB and the CIELCH color spaces.

6) CIELAB and CIELCH color spaces

CIE $L*a*b*$ (CIELAB) is a more perceptual uniform color space defined by the CIE in 1976. It describes all the visible colors and is obtained by a non-linear transformation of the CIE XYZ color space. The three coordinates of CIELAB represent the lightness of the color, its position between red and green and its position between blue and yellow. $L*$ is the lightness ($L* = 0$ yields black and $L* = 100$ indicates diffuse white; specular white may be higher). a* (negative values indicate green while positive values indicate red) and b* (negative values indicate blue and positive values indicate yellow) are the chromatic coordinates (see Figure 5). The CIELAB color space can only be represented properly in a three-dimensional space. Two-dimensional depictions are usually chromaticity diagrams which are sections of the color space with a fixed lightness. The nonlinear relations for $L*$, $a*$, and $b*$ are intended to mimic the nonlinear response of the eye. Furthermore, uniform changes of components, corresponding to a difference of distance in the CIELAB space, in the CIELAB color space aim to correspond to uniform changes in perceived colors.

9

It is possible to convert the XYZ coordinates into L*a*b* coordinates by using the following equations where X_n, Y_n and Z_n are the CIE XYZ tristimulus values of the reference white point:

$$L^* = 116\, f\left(\frac{Y}{Y_n}\right) - 16$$

$$a^* = 500\left(f\left(\frac{X}{X_n}\right) - f\left(\frac{Y}{Y_n}\right)\right)$$

$$b^* = 500\left(f\left(\frac{Y}{Y_n}\right) - f\left(\frac{Z}{Z_n}\right)\right) \tag{3}$$

With $f^{-1}(t) = \begin{cases} \sqrt[3]{t} & if\ t > \delta^3 \\ \frac{t}{3\delta^2} + \frac{4}{29} & otherwise \end{cases}$ and $\delta = \frac{6}{29}$

The CIELHC coordinates are defined as cylindrical coordinates in the CIELAB color space: a*, b* are changed into the coordinates C* (chroma, relative saturation) and H* (hue angle, angle of the hue in the CIELAB color space). The lightness L* remains unchanged. The conversion of a* and b* in C* and H* is done using the following formulas:

$$\begin{cases} H^* = atan\left(\frac{b^*}{a^*}\right) if\ a^* > 0\ and\ b^* \geq 0 \\ H^* = 2\pi + atan\left(\frac{b^*}{a^*}\right) if\ a^* > 0\ and\ b^* < 0 \\ H^* = \pi + atan\left(\frac{b^*}{a^*}\right) otherwise \end{cases} \quad and \quad C^* = \sqrt{a^{*2} + b^{*2}} \tag{4}$$

7) Estimation of the difference between two colors

In order to obtain the characterization of the difference between two colors, the CIE introduced color distance metrics (the distance between two colors within a color space).
In 1976, the CIE proposed the first color difference formula related to the CIELAB color space. Assuming two colors with given coordinates (L_1^*, a_1^*, b_1^*) and (L_2^*, a_2^*, b_2^*), the formula of ΔE_{AB}^*, also called ΔE_{76}^*, is given by the following equation:

$$\Delta E_{AB}^* = \sqrt{(L_2^* - L_1^*)^2 + (a_2^* - a_1^*)^2 + (b_2^* - b_1^*)^2} \tag{5}$$

The "Just Noticeable Difference", or JND, is defined as the smallest color difference that can be perceived by a human observer. In the case of ΔE_{AB}^*, the JND corresponds to $\Delta E_{AB}^* \cong 2.3$.
In order to address perceptual non-uniformities (the human eye is more sensitive to some colors than others), the CIE introduced in 1994 the ΔE_{94}^*. The ΔE_{94}^* is defined in the CIELCH color space with differences in lightness L^*, chroma C^* and hue H^* calculated from the $L^*a^*b^*$ coordinates. The ΔE_{94}^* is given by the following equation:

$$\Delta E_{AB}^* = \sqrt{\left(\frac{\Delta L^*}{k_L S_L}\right)^2 + \left(\frac{\Delta C_{ab}^*}{k_c S_C}\right)^2 + \left(\frac{\Delta H_{ab}^*}{k_H S_H}\right)^2} \tag{6}$$

With:
$\Delta L^* = L_2^* - L_1^*$
$\Delta C_{ab}^* = C_2^* - C_1^*$
$C_1^* = \sqrt{a_1^{*2} + b_1^{*2}}$
$C_2^* = \sqrt{a_2^{*2} + b_2^{*2}}$
$\Delta a^* = a_2^* - a_1^*$
$\Delta b^* = b_2^* - b_1^*$
$\Delta H_{ab}^* = \sqrt{\Delta E_{AB}^{*2} - \Delta L^{*2} - \Delta C_{ab}^{*2}} = \sqrt{\Delta a^{*2} + \Delta b^{*2} - \Delta C_{ab}^{*2}}$
$S_L = 1$
$S_C = 1 + K_1 C_1^*$
$S_H = 1 + K_2 C_1^*$

k_c and k_H are usually equal to one. The weight factors k_L, K_1 and K_2 are constants that depend on the application domain. Common values are given in the following Table 1:

	Graphic arts	Textiles
k_L	1	2
K_1	0.045	0.048
K_2	0.015	0.014

Table 1: k_L, K_1 and K_2 factors for the definition of the ΔE_{94}^* color distance.

In the next section, we present the interferential phenomena responsible for the coloration of the material studied in this work.

II. Interferential colors

1) Definition of the interference

Interferential colors occur in the presence of structural elements with length scales of the order of magnitude of the wavelengths of visible light. Interferences arise when two or multiple waves are superimposed. In the simple case of two waves:

- If the waves have their maxima simultaneously, the interference is called constructive and the generated wave is enhanced (the waves amplitudes are summed, Figure 6).
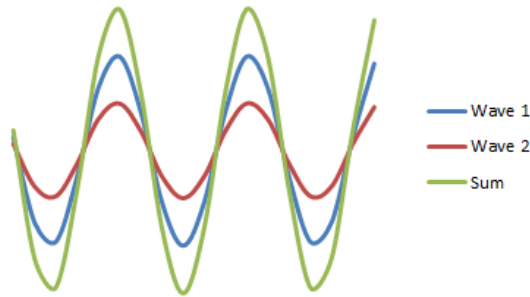
Figure 6: Waves with zero phase-shift: constructive interference of two waves.

- In the case where a wave passes through a maximum when the other passes through a minimum, the interference is called destructive and the resulting wave is null if the 2 waves have the same amplitude (Figure 7).
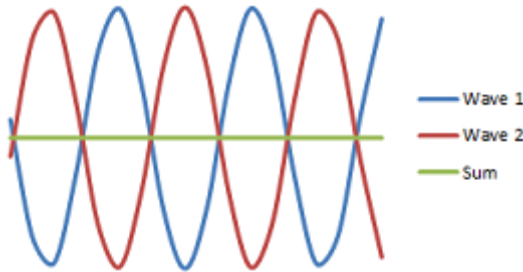
Figure 7: Waves with a π phase-shift: destructive interference, the generated wave amplitude is null.

The light vibration *s*, which oscillates sinusoidally at the pulsation ω at a given point is given by the following equation:

$$s = A \times \cos(\varphi + \omega t) \qquad (7)$$

where A is the amplitude of the vibration and φ the phase. The light intensity I is proportional to the average over time of the square of the amplitude of the scalar propagated vibration and is expressed as $I = \frac{A^2}{2}$.

2) Interference in a thin film

Let's consider a thin film with parallel faces having a thickness *e* and a refractive index *n*, an incident wave *i* is partially reflected on one face of the film according to the Snell-Descartes law (see Figure 8):
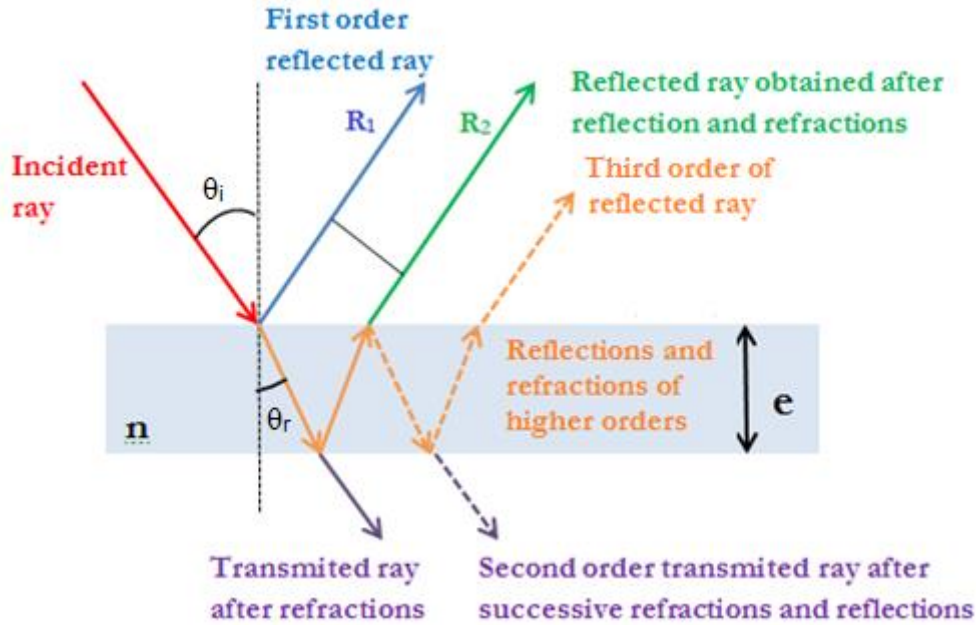
Figure 8: Optical paths of the first rays reflected and transmitted by a thin film.

The wave that enters the film undergoes refraction and becomes itself an incident wave at angle θ_r with regards to the second face at an angle [32]. The main part of the wave exits the material under the form of a transmitted wave of high amplitude, but a part is still reflected by the second face of the film with a smaller amplitude. This reflected wave is then also transmitted predominantly to the incident medium (from which the initial incident ray comes) but a portion of this reflected wave is again reflected. The coupling phenomenon between transmission and reflection continues to happen. The amplitude of the resulting waves is each time lower. Note that the amplitudes of the different waves are given by the Fresnel equations [32].

It is reasonable to consider the interferential phenomenon in reflection of an incident ray by a thin film as a two-waves interference, as the other rays reflected from higher orders have negligible intensities. These two reflected rays come from the same incident ray. They are coherent and interfere. The amplitude A of the resultant wave is expressed as a function of the amplitudes of the waves which interfere, A1 and A2. These waves have a φ1 and φ2 phase respectively:

$$A^2 = A_1^2 + A_2^2 + 2(A_1 \times A_2) \cos(\varphi_1 - \varphi_2) \qquad (8)$$

Demonstration:
Considering two coherent waves:

$u_1(t) = A_1 \cos(\omega t + \varphi_1)$ and $u_2(t) = A_2 \cos(\omega t + \varphi_2)$

The resulting amplitude is: $u(t) = u_1(t) + u_2(t) = A_1 \cos(\omega t + \varphi_1) + A_2 \cos(\omega t + \varphi_2)$.

13

The instantaneous wave intensity is proportional to the square of the amplitude:

$u^2(t) = A_1{}^2 \cos^2(\omega t + \varphi_1) + A_2{}^2 \cos^2(\omega t + \varphi_2) + 2A_1A_2\cos(\omega t + \varphi_1)\cos(\omega t + \varphi_2)$
$u^2(t) = A_1{}^2 \cos^2(\omega t + \varphi_1) + A_2{}^2 \cos^2(\omega t + \varphi_2) + A_1A_2\cos(2\omega t + \varphi_1\ \varphi_2) + A_1A_2\cos(\varphi_2-\varphi_1)$

If we take the average over time:

$$< u^2(t) > = \frac{A_1^2}{2} + \frac{A_2^2}{2} + A_1 A_2 \cos(\varphi_2 - \varphi_1)$$

The resulting intensity can be written as a function of the intensities of the waves 1 and 2 (respectively denoted as I_1 and I_2):

$$I = I_1 + I_2 + 2\sqrt{I_1}\sqrt{I_2} \cos(\varphi_2 - \varphi_1)$$

I reaches a maximum when $\cos(\varphi_1 - \varphi_2) = 2k\pi$. $I_{max} = \left(\sqrt{I_1} + \sqrt{I_2}\right)^2 = \frac{1}{2}(A_1 + A_2)^2$. It corresponds to constructive interferences.

I reaches a minimum when $\cos(\varphi_1 - \varphi_2) = 2\pi(k+1)$. $I_{min} = \left(\sqrt{I_1} - \sqrt{I_2}\right)^2 = \frac{1}{2}(A_1 - A_2)^2$. It corresponds to destructive interferences. This value is null if $A_1 = A_2$.

The phase shift $(\varphi_2 - \varphi_1)$ for a wavelength λ is equal to:

$$\varphi_2 - \varphi_1 = \frac{2\pi}{\lambda}\ \delta \ ; \ \delta = 2 \times n \times e \times \cos\theta_r + \frac{\lambda}{2} \tag{9}$$

where δ is the optical path difference between the first two reflected rays.

Demonstration: (See figure on the right)
If we consider an incident ray reflected by the thin film, the optical geometrical path difference δ_{geom} between the first reflected ray R_1 and the second reflected ray R_2 can be written:
$\delta_{geom} = n_2(OL + LM) - n_1OK = 2n_2OL - n_1OK$
with n_1 and n_2 respectively the refractive indexes of the media 1 and 2.
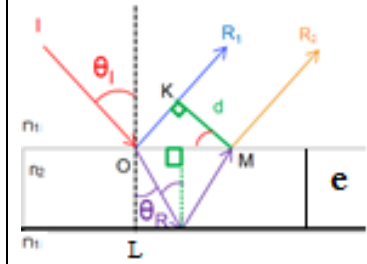
Taking into account some geometrical considerations:

$$\delta_{geom} = 2n_2 \frac{e}{\cos\theta_r} - 2n_1 OM \sin\theta_i \qquad \text{with OM} = 2e\tan\theta_r$$

By using the Snell-Descartes law: $n_1\sin\theta_i = n_2\sin\theta_r$ and triogonometric considerations $\tan(x) = \sin(x)/\cos(x)$ and $\cos^2(x) = 1 - \sin^2(x)$, we obtain:

$$\delta_{geom} = 2n_2 e \times \cos(\theta_r)$$

This optical path difference corresponds to a geometrical phase difference between the two rays and is equal to:

$$\Delta\varphi_{geom} = \frac{2\pi}{\lambda}\ \delta_{geom}$$

14

It is important to note that the reflected ray R_2 has undergone a phase-shift of π during the reflection from the medium 2 to the medium 1; which is not the case of R_1 (the refractive index n_2 is supposed to be higher than n_1).

The phase difference φ_2-φ_1 can then be written:

$$\Delta\varphi = \Delta\varphi_{geom} \pm \pi = \frac{4\pi n_2 e \times \cos(\theta_r)}{\lambda} \pm \pi$$

The condition for constructive interference corresponding to the maximum reflection for a given wavelength is:

$$\varphi_2 - \varphi_1 = 2k\pi \qquad \text{and} \qquad 2ne \times \cos\theta_r = \left(k \mp \tfrac{1}{2}\right)\lambda \qquad \text{with } k \text{ an integer} \qquad (10)$$

The wavelengths corresponding to constructive interferences are dependent on the direction of incidence; thus the reflected spectrum and the observed color depend on the direction of incidence. This phenomenon is called goniochromaticity, gonioappearence or iridescence.
The simple model developed above gives the position of the reflectance spectrum extrema. A more complete model is needed to compute the whole reflectance spectrum of the thin film.

3) Abeles Matrices formalism

All the simulated spectra presented in this document are based on the Abeles Matrix formalism presented in the following section. This formalism has been presented by Florin Abelès in 1950 in a series of articles [33], [34]. The Abeles matrix formalism is a transfer-matrix method. A transfer matrix is used to analyze the propagation of electromagnetic or acoustic waves through a stratified medium [35]. The Abeles matrix method is used to calculate the specular reflectance and transmittance from a layered interface and is based on Maxwell's equations. This method is adapted for flat multilayered and homogeneous materials.

Let us consider a stratified medium where each layer is homogeneous and isotropic as shown in Figure 9.

The electric field $\vec{E}$ and the magnetic field $\vec{H}$ can be written for a TE polarization with the following formulae (Eq. 12):

$$\begin{cases} E_x(y,z) = U(z)\exp(-i\omega t + i\gamma y) \\ H_y(y,z) = V(z)\exp(-i\omega t + i\gamma y) \\ H_z(y,z) = W(z)\exp(-i\omega t + i\gamma y) \end{cases}$$

where $\frac{\omega}{2\pi}$ is the light frequency and γ the projection on the y axis of the wave vector $\qquad (11)$

H (magnetic field strength expressed in A/m) can be related in vacuum to the magnetic field (magnetic flux density expressed in T) $\vec{B}$ by the relation $\vec{B} = \mu_0\vec{H}$ where μ_0 is the vacuum permeability.
In the case of non-absorbent media, one can write:

$$\gamma^2 = \frac{\omega^2}{c^2}n(z)^2\sin^2(\theta(z)) \quad \text{which is a constant according to the Snell-Descartes law.} \qquad (12)$$
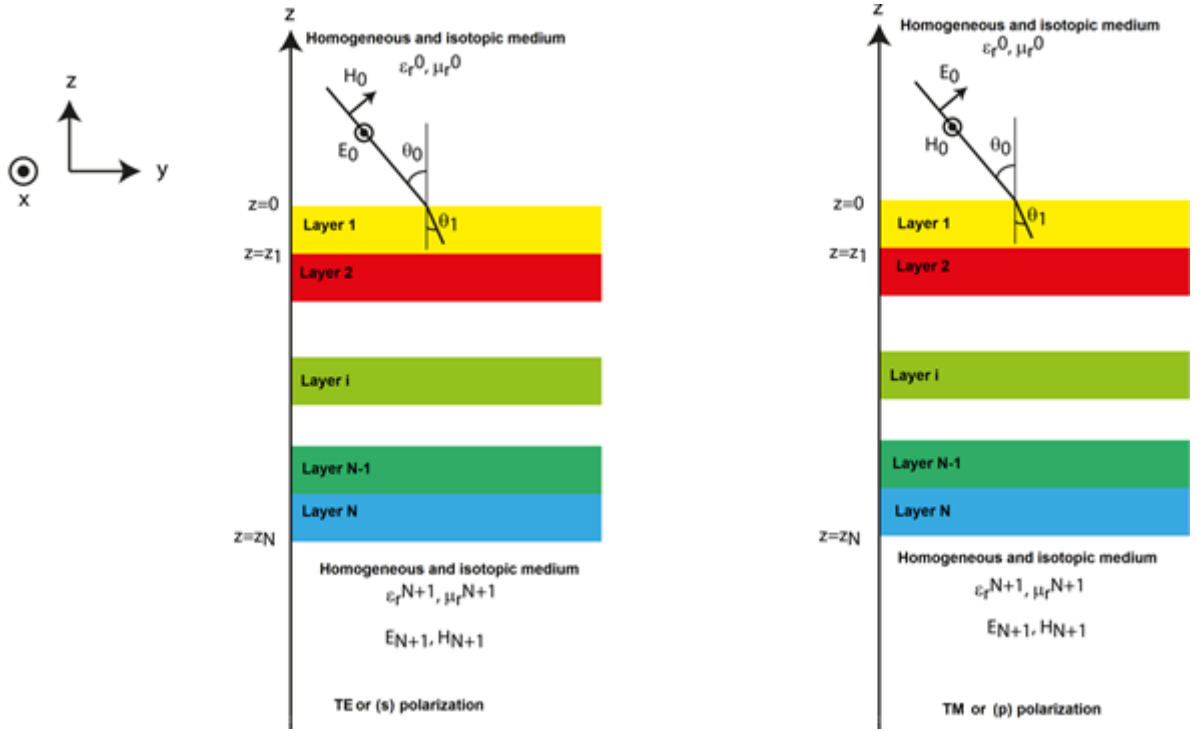
Figure 9: Interaction between a layered medium and an incident ray with either a TE polarization (polar (s) on the left) or TM polarization (polar (p) on the right).

a) Computation of the Abeles matrix

c is the light speed in vaccum and $n(z)$ the refactive index of the medium at the altitude z. The differential equation of $U(z)$ and $V(z)$ can then be written:

$$\begin{cases} \dfrac{dU}{dz} = i\omega\mu_0\mu_r(z)V(z) \\ \dfrac{dV}{dz} = i\omega\varepsilon_0 \left[\varepsilon_r(z) - \dfrac{S^2}{\mu_r(z)}\right]U(z) \end{cases} \qquad \text{where } S = \gamma\dfrac{c}{\omega} \qquad (13)$$

We also have: $W(z) = \dfrac{-\gamma}{\omega\mu_0\mu_r(z)}U(z)$

ε_r is the material's relative permittivity, μ_r is its relative permeability and ε_0 is the vacuum permittivity. The resolution of the differential equations system in U and V in each layer is used to calculate the Abeles matrices M_i as the following:

$$\begin{bmatrix} U(z_i) \\ V(z_i) \end{bmatrix} = M_i(z_i - z_{i-1}) \begin{bmatrix} U(z_{i-1}) \\ V(z_{i-1}) \end{bmatrix} \qquad (14)$$

From the differential equations system, one can deduce two uncoupled second order differential equations for U and V. In each homogeneous layer I, we have:

$$\begin{cases} \dfrac{d^2U}{dz^2} = \dfrac{-\omega^2}{c^2}(n_i^2 - S^2)U(z) \\ \dfrac{d^2V}{dz^2} = \dfrac{-\omega^2}{c^2}(n_i^2 - S^2)V(z) \end{cases} \qquad \text{where } n_i^2 = \varepsilon_r^i\mu_r^i \text{ is the} \atop \text{refractive index of the layer i} \qquad (15)$$

16

We then obtain:

$$M_i(z) = \begin{bmatrix} U_2^i(z) & U_1^i(z) \\ V_2^i(z) & V_1^i(z) \end{bmatrix} \text{ with } \begin{cases} U_1^i(z) = \frac{i}{P_i}\sin(k_z^i z) \\ U_2^i(z) = \cos(k_z^i z) = V_1^i(z) \\ V_2^i(z) = iP_i \sin(k_z^i z) \end{cases} \quad (16)$$

where $P_i = \dfrac{\sqrt{n_i^2 - S^2}}{c\mu_0 \mu_r^i}$ and $k_z^i = \dfrac{\omega}{c}\sqrt{n_i^2 - S^2}$

U_1 and U_2 are particular solutions of the second order differential equation verified by U and thus form a basis of the solutions for the electric field. It is also the case for V_1 and V_2 as solutions of the second order differential equation verified by V. The $\vec{E}$ and $\vec{H}$ fields are not independent. This implies a coupling between solutions U_1 and V_1, as well as between U_2 and V_2.

b) <u>Computation of the electric field reflection and transmission coefficients</u>

Let us first compute the electric field reflection coefficient. The electric field E_x^0 in the incident medium can be written as:

$$E_x^0(y, z) = E_x^{inc}(y, z) + E_x^{ref}(y, z) \quad (17)$$

where E_x^{inc} is the incident electric field propagating towards the negative value of z and with an expression proportional to $\exp(-i\omega t - ik_z^0 z)$ and E_x^{ref} is the reflected electric field propagating towards the positive value of z and with an expression proportional to $\exp(-i\omega t + ik_z^0 z)$. U_1^0 and U_2^0 are a solutions base to obtain the electric field in the incident medium, and we can note its expression as:

$$E_x^0(y, z) = U^0(z)\exp(-i\omega t + i\gamma y) = [AU_1^0(z) + BU_2^0(z)]\exp(-i\omega t + i\gamma y)$$

$$= \left[A\frac{i}{P_0}\sin(k_z^0 z) + B\cos(k_z^0 z)\right]\exp(-i\omega t + i\gamma y) \quad (18)$$

It can also be written as:
$$E_x^0(y, z) = \frac{1}{2}\left[\exp(ik_z^0 z)\left(\frac{A}{P_0} + B\right) + \exp(-ik_z^0 z)\left(B - \frac{A}{P_0}\right)\right]\exp(-i\omega t + i\gamma y) \quad (19)$$

We thus have:
$$\begin{cases} E_x^{inc}(y, z) = \frac{1}{2}\left(B - \frac{A}{P_o}\right)\exp(-ik_z^0 z)\exp(-i\omega t + i\gamma y) \\ E_x^{ref}(y, z) = \frac{1}{2}\left(B + \frac{A}{P_o}\right)\exp(+ik_z^0 z)\exp(-i\omega t + i\gamma y) \end{cases}$$

The electric field reflection coefficient in amplitude can be written as:

$$r_E^{TE} = \frac{E_x^{ref}(y, 0)}{E_x^{inc}(y, 0)} = \frac{B + \dfrac{A}{P_o}}{B - \dfrac{A}{P_o}} \quad (20)$$

Let us express A and B as a function of $U^0(0)$ and $V^0(0)$.

$$V^0(z) = \frac{1}{i\omega\mu_0\mu_r^0}\frac{dU^0}{dz} = \frac{1}{i\omega\mu_0\mu_r^0}\left[A\frac{dU_1^0}{dz} + B\frac{dU_2^0}{dz}\right] = AV_1^0(z) + BV_2^0(z) \tag{21}$$

So we have: $\begin{cases} U^0(0) = B \\ V^0(0) = A \end{cases}$

And finally:

$$r_E^{TE} = \frac{E_x^{ref}(y,0)}{E_x^{inc}(y,0)} = \frac{U^0(0) + \dfrac{V^0(0)}{P_o}}{U^0(0) - \dfrac{V^0(0)}{P_o}}$$

With Abeles formalism, we can write:

$$\begin{bmatrix} U^{N+1}(0) \\ V^{N+1}(0) \end{bmatrix} = M_N(0) \dots M_i(z_i - z_{i-1}) \dots M_1(z_1)\begin{bmatrix} U^0(0) \\ V^0(0) \end{bmatrix} = M\begin{bmatrix} U^0(0) \\ V^0(0) \end{bmatrix},$$

Thus we have $U^{N+1}(0)\begin{bmatrix} 1 \\ -P_{N+1} \end{bmatrix} = M\begin{bmatrix} U^0(0) \\ V^0(0) \end{bmatrix}$ or $\begin{bmatrix} U^0(0) \\ V^0(0) \end{bmatrix} = U^{N+1}(0)M^{-1}\begin{bmatrix} 1 \\ -P_{N+1} \end{bmatrix}$.

By noting $M^{-1} = \begin{bmatrix} M_{11}' & M_{12}' \\ M_{21}' & M_{22}' \end{bmatrix}$ it is possible to write:

$$r_E^{TE} = \frac{M_{11}'P_0 - M_{12}'P_0P_{N+1} + M_{21}' - P_{N+1}M_{22}'}{M_{11}'P_0 - M_{12}'P_0P_{N+1} - M_{21}' + P_{N+1}M_{22}'} \tag{22}$$

Let us now compute the electric field transmission coefficient. The electric field below the multilayers can be written as:

$$E_x^{N+1}(y,z) = \frac{1}{2}\left[\exp(ik_z^{N+1}z)\left(\frac{A'}{P_{N+1}} + B'\right) + \exp(-ik_z^{N+1}z)\left(B' - \frac{A'}{P_{N+1}}\right)\right]\exp(-i\omega t + i\gamma y) \tag{23}$$

As there is no incident electric field coming from under the multilayer, the electric field from under the multilayer has a propagation direction only towards the negative values of the z axis. We thus have $B' = -\dfrac{A'}{P_{N+1}}$, that is $U^{N+1}(0) = -\dfrac{V^{N+1}(0)}{P_{N+1}}$.

The electric field under the multilayer is then written as:

$$E_x^{N+1}(y, z - z_n) = U^{N+1}(0)\exp(-i\omega t + i\gamma y)\exp\left(-ik_z^{N+1}(z - z_N)\right) \tag{24}$$

The electric field transmission coefficient in amplitude is then written as:

$$t_E^{TE} = \frac{E_x^{N+1}(y,0)}{E_x^{inc}(y,0)} = \frac{2U^{N+1}(0)}{U^0(0) - \dfrac{V^0(0)}{P_o}} \tag{25}$$

Introducing the Abeles matrices, we obtain:

$$t_E^{TE} = \frac{2P_0}{M_{11}'P_0 - M_{12}'P_0P_{N+1} - M_{21}' + P_{N+1}M_{22}'} \tag{26}$$

18

The computation of the Abeles matrices as well as the transmission and reflection coefficients in TM polarization are detailed in Appendix C. Note that r_E^{TE} and t_E^{TE} depend on the light frequency ω (and thus on its wavelengths λ) through the parameters P_0 and P_{N+1} and the matrix elements $M'_{11}, M'_{12}, M'_{21}$ and M'_{22}. Computing r_E^{TE} or t_E^{TE} versus the light wavelengths gives then the reflectance or transmittance spectrum of the multilayers.

After having briefly introduced some color spaces, the phenomenon responsible for interferential colors and how to model a reflectance spectrum, we will then explain how to measure colors.

III. Color measurements

1) Standard illuminants

a) CIE standard illuminant A

This illuminant represents typical, domestic, tungsten-filament lighting. CIE standard illuminant A should be used in all applications of colorimetry involving the use of incandescent lighting. Planck's law gives the spectral exitance of a black body (in W/m³):

$$M_{e,\lambda}(\lambda, T) = \frac{c_1 \lambda^{-5}}{e^{\frac{c_2}{\lambda T}} - 1} \qquad (27)$$

With $c_1 = 2\pi h c^2$ and $c_2 = h\,c/k_b$, where k_b is the Boltzman constant ($1.38064852 \times 10^{-23}$ J/K), and c is the speed of light in vacuum (299 792 458 m/s). The relative spectral power distribution (SPD) of the illuminant A is that of a Planckian radiator at a temperature of 2856K. The CIE defines the spectral distribution $S_A(\lambda)$ of the illuminant A as:

$$S_A(\lambda) = 100 \times \left(\frac{560}{\lambda}\right)^5 \times \frac{e^{\frac{1435*10^7}{2848*560}} - 1}{e^{\frac{1435*10^7}{2848*\lambda}} - 1} \qquad (28)$$

where λ is the wavelength in nanometers and the numerical values in the two exponential terms are definitive constants originating from the first definition of Illuminant A in 1931. This spectral power distribution is normalized to the value 100 at the wavelength 560 nm. CIE standard illuminant A is defined over the spectral region 300 nm to 830 nm. This wavelength range is used for evaluating luminescent samples because the UV spectral range is relevant. For most colorimetric investigations the restricted wavelength range, 380 nm - 780 nm, can be used.
CIE standard illuminant A has to be realized by a gas-filled tungsten filament lamp operating at a correlated color temperature of 2856 K.

b) CIE standard illuminant D65 and other D illuminants

CIE standard illuminant D65 represents a midday sun in Western/Eastern Europe. Its relative spectral power distribution corresponds to a correlated color temperature of approximately 6500 K (called also nominal correlated color temperature of the daylight illuminant) and is noted $S_{D65}(\lambda)$. It should be used in all colorimetric calculations requiring this kind of daylight. When D65 cannot be used, the CIE recommends using one of the following daylight illuminants: D50, D55, or D75. At present, no artificial source is recommended to realize the CIE standard illuminant D65 or any other illuminant D with a different correlated color temperature.

The relative spectral power distributions of these illuminants can be found in Appendix A.

c) CIE standard illuminant E

The equal-energy illuminant E is an interesting fictitious standard source with constant spectral distribution throughout the visible spectrum. It is useful as a theoretical reference.

2) Definitions of the CIE geometry standards for color measurement

The following definitions are taken from references [28], [29], [31]. Before introducing how the device is used to characterize the color of an object, we will introduce some important terms (some others are defined in Appendix B).

Specular reflection: When a light beam strikes a perfect mirror surface, all the incident light is reflected by the surface and the angles from the normal to the surface of the reflected light and the incident light are equal (see Figure 10(a)). This is related to high gloss surfaces where the diffused reflection of light is very weak.

Diffuse reflection: When a light beam strikes a non-perfect mirror surface, the incident light is reflected back at different angles; these angles depend on the texture of the surface (see Figure 10(b)). This usually happens with rough surfaces.

Figure 10: Specular (a) and diffuse (b) reflections

Specular Component Included (SCI): This type of measurement includes both specular and diffused lights. It measures the "true color" of the object and is affected by its gloss. In the following section SCI mode will correspond to di (diffuse with specular component included).

Specular Component Excluded (SCE): This type of measurement excludes the specular component. It measures the "apparent" color of the object and is unaffected by its gloss. In the following section SCE mode will correspond to de (diffuse with specular component excluded).

The CIE advises the use of the following geometries to measure the color of an object. Most of the geometries are represented in Figure 11, Figure 12 and Figure 13.

a) Diffuse: eight-degrees geometry, specular component included (di:8°)

For the di:8° geometry, the sample is irradiated by an integrating sphere to diffusely illuminate the sample and uses a viewing angle of 8° from the normal to the sample surface. If a specular port (or gloss trap) is used (this is an opening in the sphere wall placed at a given angle, symmetrical to the detector from the normal to the surface), this port is closed. Baffles prevent the source from directly illuminating the sample surface.

b) Diffuse: eight-degrees geometry, specular component excluded (de:8°)

For the de:8° geometry, the conditions of illumination and observation are the same as for the di:8° geometry. The only difference is that the specular port is opened.

c) Eight degrees: diffuse geometry, specular component excluded (8°:de)

For the 8°:de geometry, the conditions of illumination and observation are the same as for the de:8° geometry but with the light path reversed. The sample is irradiated under 8° and the reflected flux at the sampling aperture is collected at all angles, thanks to an integrating sphere (see Appendix B for the definition of the sampling aperture). The specular port is opened.

d) Eight degrees: diffuse geometry, specular component included (8°:di)

For the 8°:di geometry, the conditions of illumination and observation are the same as for the 8°:de geometry. The specular port is closed.

e) Diffuse : diffuse geometry (d:d)

In this geometry, the illumination and the detection are diffuse. This geometry is rarely used.

f) Alternative diffuse geometry (d:0°)

The d:0° geometry is similar to the di:8° or de:8° geometries with the detection angle fixed at 0°.

g) Forty-five degrees annular: normal geometry (45°a:0°) or (45°c:0°)

For the 45°a:0° geometry, the sample is illuminated at an angle of 45° and the observation direction is normal to the sampling aperture. The sampling aperture is irradiated uniformly from all directions between two circular cones with their axes normal to the sampling aperture; the smaller cone has a half angle of 40° and the larger of 50°. This illuminating geometry can be approximated by the use of numerous light sources put on circle or numerous fiber bundles illuminated by a single source and terminating at a circle. This geometry is called 45°c:0° for "circumferential/normal geometry".

h) Normal: forty-five degrees annular geometry (0°:45°a)

For the 0°:45°a geometry, the angular conditions are similar to the conditions for the 45°a:0° geometry, but with a reversed light path. The sampling aperture is irradiated at normal incidence and the reflected radiation is collected within an annulus centered at an angle of 45° with respect to the normal to the sample.

i) Forty-five degrees directional: normal geometry (45°x:0°)

For the 45°x:0°, the angular conditions are similar to the conditions for the 45°a:0° geometry, except for the lighting conditions. The illumination is only at one azimuth angle. The "x" symbol indicates that the azimuthal direction of the incident beam is the x direction of the sample plane. The zenith angle of the incident beam relative to the normal of the surface is 45°.

j) Normal: forty-five degrees directional geometry (0°:45°x)

For the 0°:45°x geometry, the angular conditions are similar to the conditions for the 45°x:0° geometry, but with a reversed light path. The sampling aperture is irradiated at normal incidence and the reflected radiation is collected at one azimuthal angle with a zenithal angle of 45° with respect to the normal of the sample.

The 45°x:0° and 0°:45°x geometries exclude the specular component but emphasize texture and directionality. These geometries are influenced by a potential sample anisotropy.
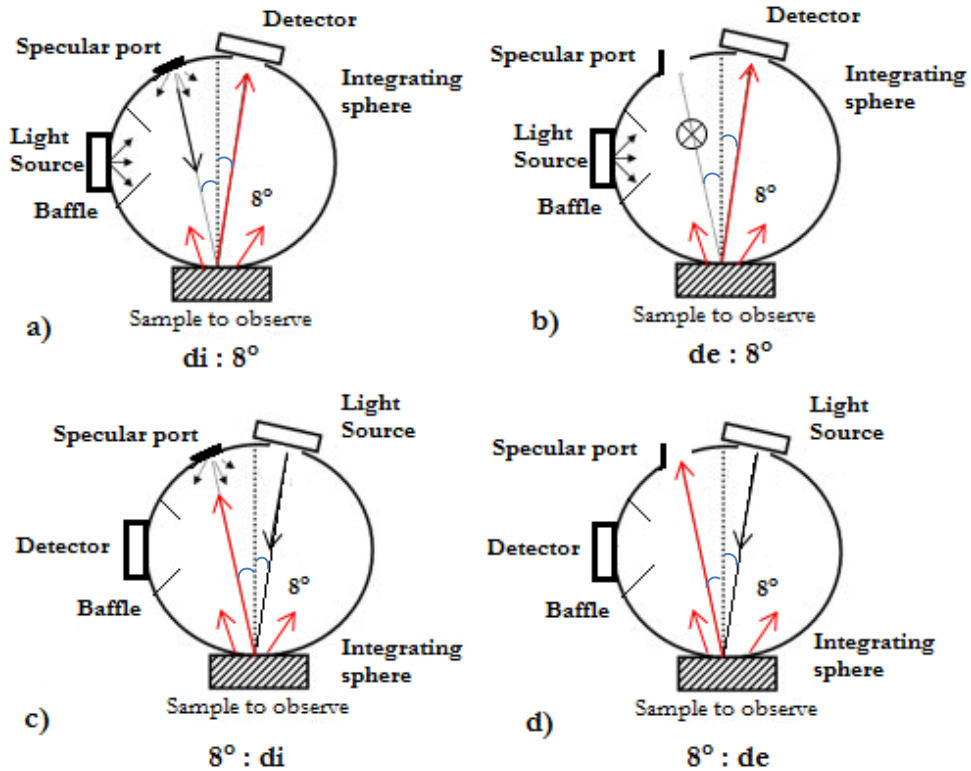
Figure 11: CIE diffuse geometries including (di) or excluding (de) the specular component by the use of a closed or opened specular port. The geometries d:0° corresponds to the d:8° geometries with the detector observing at normal incidence.
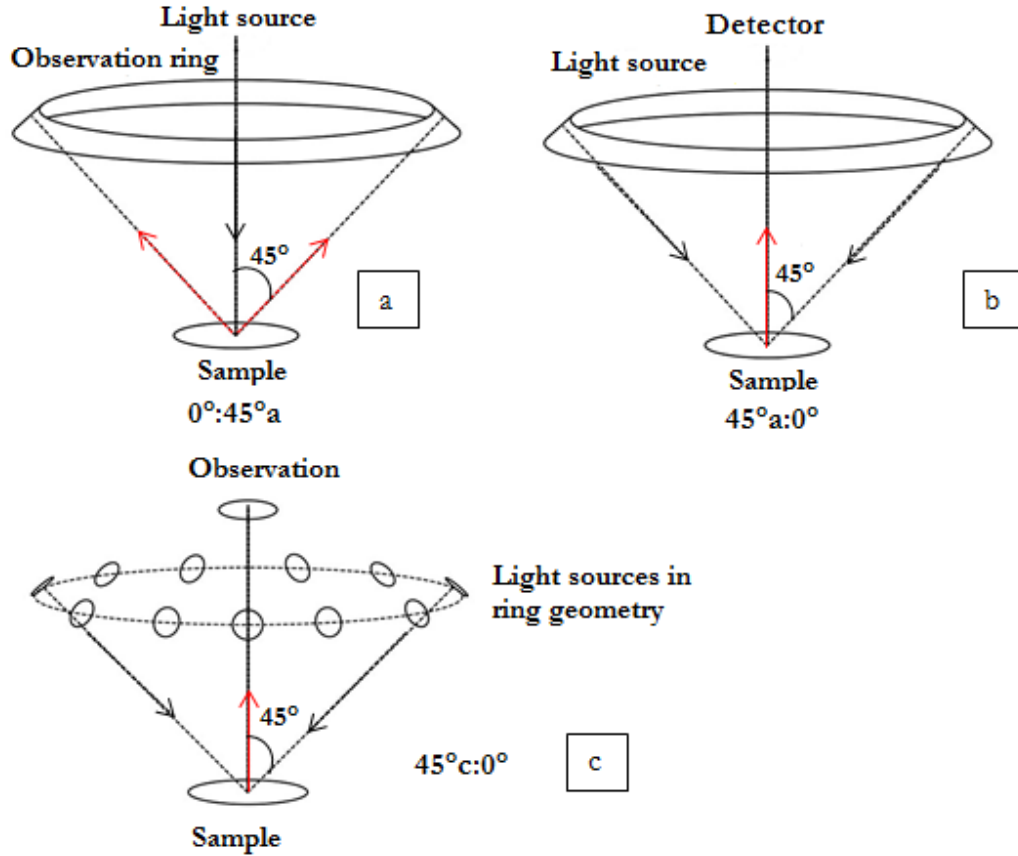
Figure 12: CIE geometries using an observation ring (0°:45°a on the subfigure a) or an annular light source (45°a :0° on the subfigure b). On the subfigure c, the annular illumination is approximated by multiple light sources disposed on a ring (45°c: 0°).
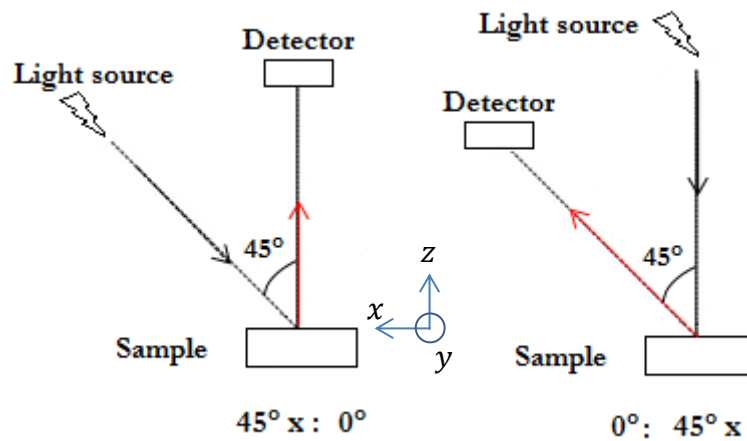
Figure 13: CIE geometries using a directional detector (45°x: 0° on the left) or a directional light source (0°: 45°x on the right). x symbol indicates that the azimuthal direction of the incident beam is the x direction on the sample plane.

3) Color measurement devices

The most common experimental setups to measure color are colorimeters and spectrophotometers. These devices are presented in this section and are based on the previously presented geometries.

a) Colorimeters

Colorimeters can be found with the either diffuse or 45°:0° geometries. The light reflected by the sample is collected through a series of three and sometimes four colored filters, which represent the relative amounts of red, green, and blue light reflected from the sample. The reason for the use of an optional fourth filter is the shape of the CIE spectral color-matching functions. In fact, the colorimetric functions $\bar{y}(\lambda)$ and $\bar{z}(\lambda)$ are single-lobe functions and $\bar{x}(\lambda)$ is a double-lobe one. Two filters are used to collect the $\overline{x_1}(\lambda)$ and $\overline{x_2}(\lambda)$ components as shown on Figure 14. Wenzel [36] showed that the fourth filter is not mandatory because the tristimulus component X_2 can be computed from the value of the tristimulus component Z with a nearly perfect accuracy.
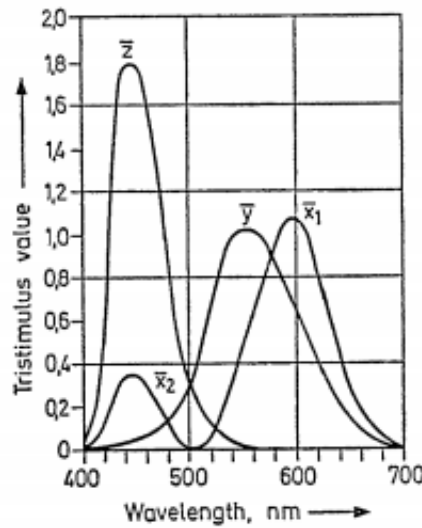
Figure 14: CIE spectral color-matching functions (from [36]).

These filters are designed to ideally simulate the three colorimetric functions $\bar{x}(\lambda)$, $\bar{y}(\lambda)$ and $\bar{z}(\lambda)$ of the CIE standard observer so that the instrument directly measures the three tristimulus values X,Y,Z for the specific illuminant used, as shown in Figure 15.
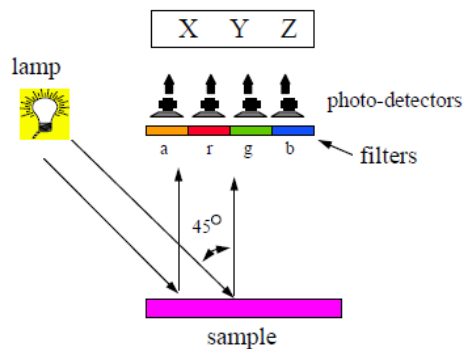
Figure 15: Diagram of a tristimulus colorimeter with 4 filters (from [37]).

Colorimeters are simple to use and affordable. They are used mostly as fast quality control instruments. These devices cannot detect and quantify metamerism, that is: two colors with the same components but having different spectra.

b) Spectrophotometers

Spectrophotometers are composed of a light source, a way to separate the light into spectral components, a detector and, for most of them, a micro-processor for data processing and computations. These components are represented in Figure 16. The positioning of these elements and their mode of operation determines the optical geometry of the instrument. Spectrophotometers measure reflectance, transmittance, or absorbance for various wavelengths.
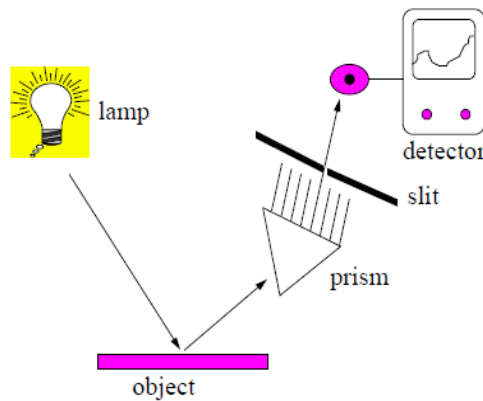
Figure 16: Diagram of a spectrophotometer (from [37]).

Instruments using 45°:0° or 0°:45° type geometries (i.e.: directional geometries) are used for color quality. During a sample evaluation, a human observer avoids the specular gloss component and evaluates the diffuse reflectance which is sensitive to changes in colorant but not to the surface characteristics. Such instruments best match human visual evaluation of matte samples.
The spectrophotometers with 0°:45° or 45°:0° geometries cannot measure variations in gloss. The main drawback of this geometry is the inability to examine transparent or translucent samples.

A device with a specular included diffuse geometry does not differentiate whether the surface is structured or not because it measures all the light reflected by the object (i.e.: it ignores the surface influence of the object). A textured and a glossy sample, both with the same pigmentation, result into approximatively the same spectral curve.

c) Spectrocolorimeters

A spectrocolorimeter is capable of providing colorimetric data such as X,Y,Z or CIEL*a*b* values for various standard illuminants. The spectrocolorimeter is a spectrophotometer that does not process spectral data at the various wavelengths.

d) Multiangle spectrophotometers

Multiangle spectrophotometers are spectrophotometers that can measure several detection angles, from three to five. The common angles relative to the normal to the surface are usually 45°, 30°, 20°, 0°, -30°, and -65°, keeping the incident light at -45°. When measured relative to the specular position the angles are 0°, 15°, 25°, 45°, 75°, and 110° as shown in Figure 17.
.
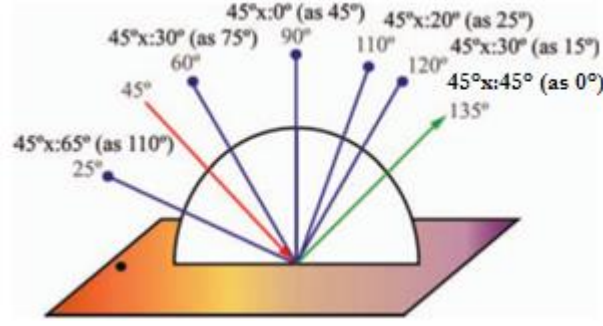
Figure 17: Illumination and observation angles for a multi-angle spectrometer following the CIE nomenclature. From [38].

Such instruments are mainly used to characterize printed samples, for which the gloss has a significant impact not only on appearance but also on the perception of the color. Metallic, pearlescent or other complex finishes also need measurements at multiple angles to fully characterize their complex colors.

The use of materials with specific visual rendering showed significant growth in the industry specifically in the form of gonioapparent surfaces [39]. However, multi-angle spectrophotometers do not give satisfying results for certain complex materials [40]. Alternative measurement systems are developed which allow for more complete measurements. They are called goniospectrophotometers.

e)   Goniospectrophotometer and BRDF

The Bidirectional Reflectance Distribution Function (BRDF) provides a full description of the reflected light within a whole hemisphere containing both incident and observation directions. A BRDF measurement consists in illuminating a sample in a particular geometrical configuration and then detecting the light reflected by this sample in another particular geometrical configuration.

The BRDF function (in [41], the spectral BRDF is considered) is defined as the ratio of the spectral radiance Lr $(\theta_r, \varphi_r, \lambda)$ reflected from a surface in a given viewing direction (θ_r, φ_r) to the spectral irradiance Ei $(\theta_i, \varphi_i, \lambda)$ on the surface arising from an illuminant source in the incident direction (θ_i, φ_i) (see Figure 18), where λ is the wavelength:

$$\text{BRDF } (\theta_i, \varphi_i, \theta_r, \varphi_r, \lambda) = \frac{Lr\ (\theta r, \varphi r, \lambda)}{Ei\ (\theta i, \varphi i, \lambda)} \qquad (\ 29\ )$$
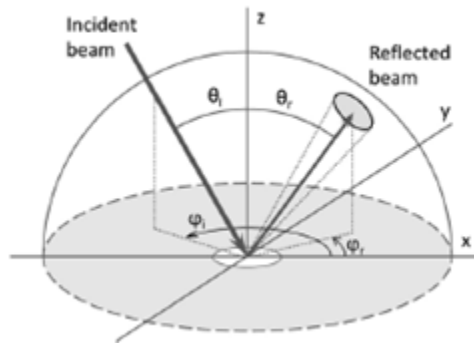
Figure 18: Geometry for the definition of the BRDF (from [42])

The spectral irradiance Ei (θ_i, φ_i, λ) is the spectral flux per unit area that is incident on a specified surface. It is expressed in W.m^{-3}. If we consider dF (θi, φ_i, λ) an elementary spectral flux coming from a given direction (θi, φ_i) on an elementary area dS, the spectral irradiance is:

$$Ei\ (\theta_i, \varphi_i, \lambda) = \frac{dF\ (\theta i, \varphi i, \lambda)}{dS}$$

(30)

The spectral radiance Lr (θ_r, φ_r, λ) is the flux per unit projected area and per solid angle that is emerging from a specified point of a specified surface in a specified direction (θ_r, φ_r). It is expressed in Wsr^{-1}m^{-2} (See Figure 19). The projected area dS_p is the projected area of the elemental by area dS onto a plane perpendicular to the direction (θ_r, φ_r) and dΩ is the solid angle. By definition: $dS_p = dS \times \cos(\theta_r)$.
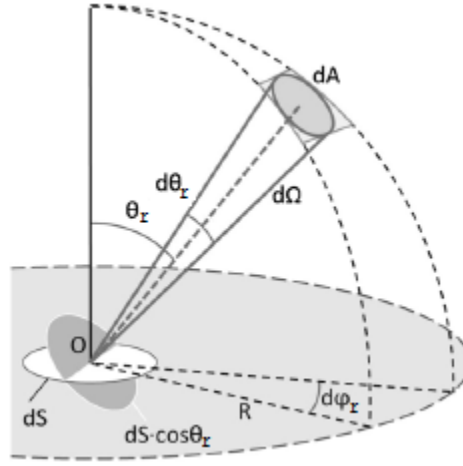
Figure 19: Geometry for the definition of radiance and solid angle (from [42])

The radiance is defined by the following equation (32):

$$Lr\ (\theta_r, \varphi_r, \lambda) = \frac{d^2F\ (\theta_r, \varphi_r, \lambda)}{dS_p.d\Omega}$$

(31)

where d²F(θ_r,φ_r,λ)is the elementary spectral flux coming from the surface dS in the direction (θ_r, φ_r) and in the solide angle dΩ.

There are several setups to measure the BRDF but only a few can measure the spectral variations with a high angular accuracy that allow obtaining the colorimetric characterization of gonio-apparent surfaces (it is important to keep in mind that the angular resolution of the human eye is about 0.02°or 0.0003 radians [43]). LNE-CNAM, the national metrological institute for France, has developed a goniometer with an angular resolution better than 0.03° [44]. The National Institute of Standards and Technology (NIST USA) developed an innovative robotic arm-based goniometer in order to obtain in-plane and out-of-plane BRDF measurements at nearly any combination of incident and observations angles. The experimental setup, the exploratory measurements and the measurements uncertainties are presented in the following reference [45]. The Optimines goniospectrophotometer [42] is presented in the following. It is used for the measurements presented in this document.

Goniospectrophotometers are divided in two categories: sequential-scanning devices [46][47] and simultaneous-scanning devices [48][49]. Sequential-scanning devices acquire each angular position one after the other. Optimines belongs to this category. Simultaneous-scanning devices are able to measure the BRDF in almost the whole hemisphere in one measurement.

Optimes was developed at Mines de Saint-Etienne to characterize highly specular materials such as metals, alloys and metallized surfaces. It comprises three main sub-systems. It is presented schematically in Figure 20:

- A rotating illumination arm collimated by an optical system containing a 50-W fibered halogen lamp or a fibered broadband laser-driven light source (Energetiq EQ 99 FC) to illuminate the sample
- A rotating, tilting and movable sample holder
- A rotating detection arm coupled to an optical system which focuses the reflected beam from the sample onto a fibered Maya2000 Pro spectrometer with a spectral sampling interval of 0.5nm and a spectral resolution of 3nm.
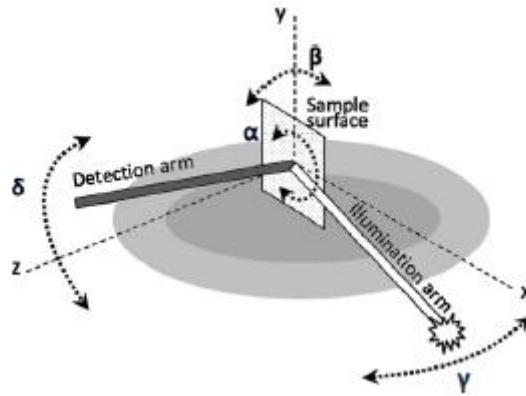
Figure 20: Schematic representation of OptiMines and the four motorized movements (from [42]).

The Laser-Driven Light Source (LDLS) uses a continuous laser to a heat a Xenon-filled cell in order to produce a high brightness plasma with a broad spectral range (170 nm - 2100 nm). The light source and the detector arms are mounted in the xy-plane and can rotate around the z-axis (γ and δ angles) from -90 to $90°$ with a resolution of about $0.01°$. The sample can rotate around its normal axis (α angle) and around the x-axis (β angle). The angles α and β can vary from 0 to $360°$ and from -90 to $90°$ respectively with resolution of $0.02°$ and $0.01°$ respectively. It is possible to scan the whole reflection hemisphere with these four degrees of freedom, as well as to characterize the sample anisotropy. By rotating the sample around the x-axis (β angle), the out-of-plane components of the BRDF can be obtained. A coordinate system related to the sample is used for the definition of illumination and detection angles ($\theta i, \phi i, \theta r, \phi r$). Performing a coordinate transformation between the system related to the sample and the one related to the apparatus is mandatory in order to find the motor positions ($\alpha, \beta, \gamma, \delta$) for particular illumination and detection directions ($\theta i, \phi i, \theta r, \phi r$). The relationships between the illumination and detection angles $\phi i, \theta i, \phi r, \theta r$ and the motor angles α, β, γ and δ can be found in the appendix of [42].

This goniospectrometer offers a high-angular positioning accuracy of about 0.02°, a good spectral resolution (3 nm) and low incident light divergence (+0.1°), low detection angular acceptance (+ 0.1°) and large signal dynamics.

The BRDF measurements are performed in two steps:

- a direct measurement of the spectral flux F_{source} of the source to get a reference spectrum
- a measurement of the spectral flux F_{sample} reflected by the observed sample.

The following equation gives the experimental expression of the BRDF given the illumination solid angle Ω_S:

$$BRDF\ (\theta_i,\ \varphi_i,\ \theta_r,\ \varphi_r,\ \lambda) = \frac{Fsample\ (\lambda, \theta r, \varphi r\ )}{Fsource\ (\lambda) \times \Omega S \times \cos(\theta i)} \qquad (\ 32\ )$$

f) Measurement repeatability uncertainty of the goniospectrophotometer

The measurement repeatability uncertainty of Optimines has been investigated in reference [39] during five BRDF measurements of an aluminum mirror. The measurements were made around the specular direction in the incidence plane for an incidence angle of 45°. From these measurements, it is possible to evaluate the measurement repeatability uncertainty both for the spectral variations of the BRDF as well as for its angular variations. For the spectral variations uncertainty evaluation, the BRDF is considered in the specular direction. For the angular variations uncertainty evaluation, the BRDF is averaged over the visible spectrum [380 nm-780 nm]. The uncertainty is evaluated here as the ratio of the standard deviation of the five measurements over the average value. Note that the goniometer arms positioning uncertainty is not taken into account here as all the data are compared relatively to the specular direction (i.e. the maximum of the BRDF angular variations is always taken equal to 45°).

Figure 21 shows the BRDF spectral variations in the specular direction for the five measurements, as well as the measurement repeatability uncertainty. The measurement repeatability uncertainty is lower than 2% over the visible wavelength range [380 nm-780 nm]. The uncertainty is higher in the blue region (380-400 nm) due to the low signal to noise ratio in this wavelength range caused by the poor sensitivity of the spectrometer.
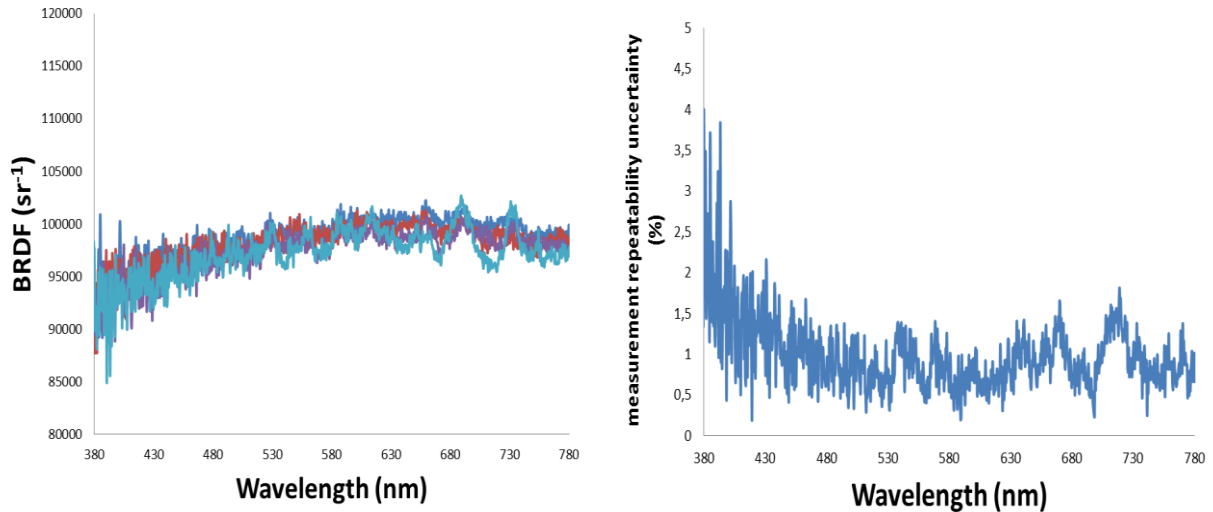
Figure 21: Five measurements of the BRDF spectral variations of an aluminum mirror in the specular direction with an incidence angle of 45° (a) as well as the measurement repeatability uncertainty (b).

Figure 22 shows the BRDF angular variations (averaged over the visible spectrum [380 nm-780 nm]) for the five measurements, as well as the measurement repeatability uncertainty. The measurement repeatability uncertainty is lower than 10% ±0.1° around the specular direction and gets very high (between 10% and 50%) further from the specular direction, due to the very low signal to noise ratio far from the specular direction for a mirror polished sample.

29
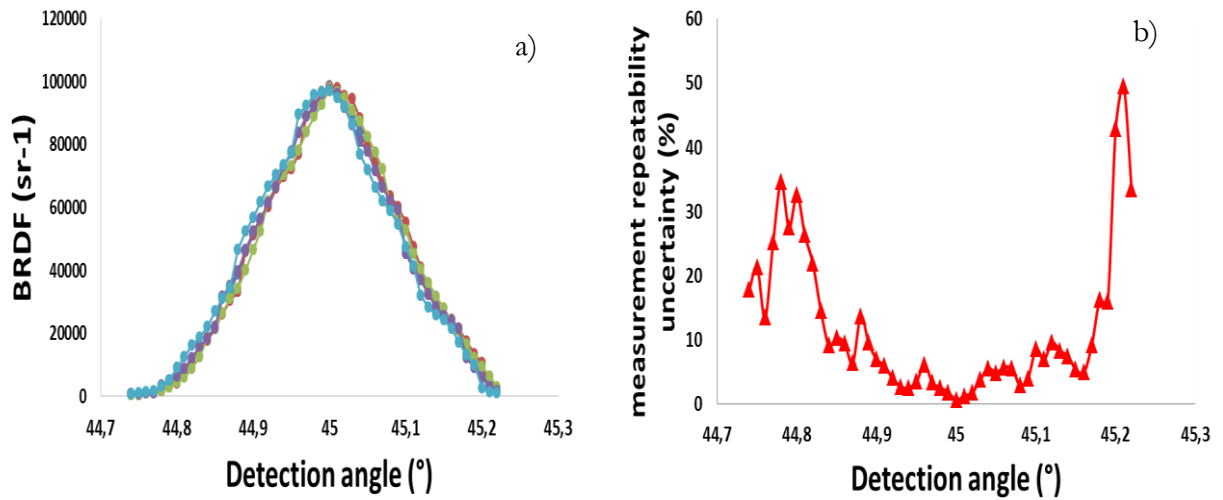
Figure 22 : Five measurements of the BRDF angular variations (averaged over the visible spectrum [380 nm-780 nm]) of an aluminum mirror in the specular direction with an incidence angle of 45° (a) as well as the measurement repeatability uncertainty (b).

Conclusions

In the current section, we presented the vocabulary needed to describe the color and the color representation of an object and the different types of devices used to measure the color of a material such as spectrophotometers and goniosprectophotometers. The later are used in order to characterize gonioapparent materials which need a complete angular analysis, difficult to obtain with fixed angular measurement geometries given by common spectrophotomer. Abeles matrices formalism is used to simulate the reflectance spectrum of the samples in order to obtain a comparison with experimental data measured with the goniospectrophotometer.

Chapter 2 presents a review of the oxidation technics which allow to obtain a colored oxidized metal. With a focus on oxidation by anodizing, we will present the parameters influencing the color and properties of the oxidized sample.

Chapter 2: State of the art: how to color titanium?

Different phenomena can be used to color metals such as painting or by forming a thin layer. These thin layers are responsible of interferential colors if the layer thickness is of the same order of magnitude as the wavelengths of the incoming light, as presented in Chapter 1. Numerous metals exhibit interferential colors when oxidized such as niobium [50][51], zirconium[52], stainless steel [53][54] and titanium. The present work focuses on titanium oxidation.

I. Oxidation techniques:

Titanium can be colored by using Laser Assisted Oxidation (LAO), heat treatments, Plasma Electrolytic Oxidation (POE) or electrolytic anodizing. In the following sections, we explain the basic principles of each of these techniques, the nature of the oxide layer (crystallinity and type of oxide) and the color properties of the oxide layer. All the encountered crystalline phases obtained during titanium oxidation when using the different techniques are given in Table 2.

Phase name	Formula	Crystal system	Lattice parameters [Å]
Anatase	TiO_2	Tetragonal	a = 3.78, c = 9.52
Rutile	TiO_2	Tetragonal	a = 4.59, c = 2.96
Titanium monoxide	TiO	Face-centered cubic	a = 4.18
Titanium(III)oxide / Tistarite	Ti_2O_3	Corundum	a = 5.15
Dititanium monoxide	Ti_2O	Hexagonal	a = 2.96, c =4.85

Table 2: Crystal system and lattice parameters of the principal oxide crystalline phase encountered during titanium oxidation while using LAO, POE, heat treatment and electrolytic anodizing. From [55].

1) Laser-assisted oxidation
   a) Technical description and general information

In this section an overview of [56]–[58] is presented, focusing on laser assisted oxidation. In these articles, the substrate is made of pure titanium (grade 1 and 2) or titanium alloy (Ti-6Al-4V or TA6V). It can be coated with several powders to change the lased (the region that has been in contact with the laser) layer composition (titanium, graphite…). The laser treatment can be made under an argon flux or performed in air. In a simple way, laser oxidation can be defined as a process of using a laser as a source of high energy to perform oxidation of the surface. There are various types of laser oxidization methods with different laser sources, such as Neodymium Yttrium Lithium Fluoride (Nd:YLF), Neodymium Yttrium Aluminium Garnet (Nd:YAG), Titanium Sapphire (Ti:Sapphire), CO_2 laser, etc… The experimental protocol is presented in Figure 23. This process involves heating of the specimen through continuous or pulse wave laser irradiation, rapid melting of the surface, intermixing or diffusion of oxygen, and rapid solidification of the surface to form an oxide layer. This protocol is characterized by the output power of the laser (and its optional optical system), the laser scanning velocity and its type (pulsed or continuous).

This oxidation technique is primarily used in biomedical devices, especially in the preparation of dental prosthesis in which the titanium oxide shows interesting surface properties (biocompatibility, excellent mechanical behavior...).
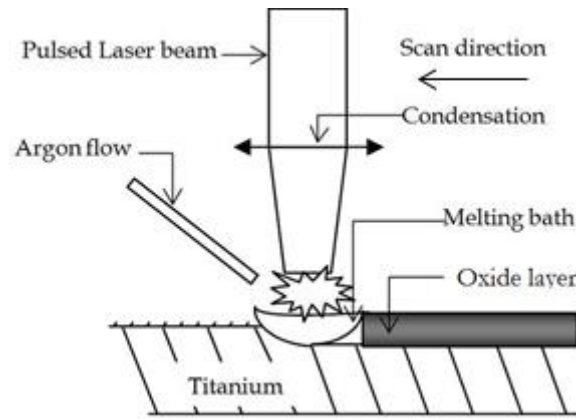
Figure 23: Principle of the laser-assisted oxidation (adjusted from [59])

b) Obtained colors

Laser oxidations were performed with a Baasel Lasertech Nd:YAG laser system (λ= 1.064 µm) with a galvanometric mirror system that allows the beam to be deflected [56]. The beam was focused by an optical system leading to a laser intensity of 55kW/cm² (corresponding to a 56W mean power) and operated in pulsed mode at 30 kHz repetition rate. A wide range of colors can be obtained by laser assisted oxidation, as shown in Table 3 (from [57]).

v (mm/s)	350	260	240	140	100	80
Color	Golden	Purple	Blue	Yellow–green	Pink–golden	Green–pink
x	0.44	0.21	0.23	0.35	0.38	0.30
y	0.41	0.20	0.25	0.37	0.33	0.32
Y	235	138	188	465	312	269
n	2.4	2.4	2.4	2.4	2.4	2.4
d (nm)	25	44	49	91	119	166

Table 3: Colors obtained through Laser assisted oxidation with a pulsed Nd:YAG laser system on ASTM grade 2 titanium samples. v is the laser scanning velocity, (x,y,Y) are the chromaticity coordinates, n the refractive index and d the oxide layer thickness. From [57].

In order to characterize the optical properties of the samples, reflectance spectra in the 300 –800 nm range were recorded with a Shimadzu UV-2101PC double-beam spectrophotometer using a BaSO4 reference. The authors could determine the refractive index and thickness of the transparent oxide surface layers by using a simulation with a simple model, i.e.: a reflectance thin film model described in [56], where the reflectance was the result of light interferences within a perfectly transparent layer on a metallic titanium substrate. The authors tried different couples of values for the refractive index and thickness of the transparent layer. The optimal values of both parameters were chosen when the simulated spectra matched with the recorded ones. The oxide thickness range was about 25 to 200 nm.

O'Hana conducted a similar study on titanium alloy (Ti-6Al-4V) samples obtained through LAO in [58] using a 60 W pulsed Universal versal X-660 Laser Platform (an mean power close to the one used in the previous study). By changing the mean power of the laser or the scanning speed, the color was changed, as described in Table 4.

Sample	Mean power, W	Speed, mm s^{-1}	Colour	R	G	B
A	6	20	Golden	137	102	64
B	12	20	Deep blue	28	45	71
C	18	20	Green blue	81	109	110
D	24	20	Pale green	124	130	118
E	30	20	Pink brown	132	119	111
F	36	20	Brown	84	81	72
G	60	6·67	Grey	70	89	96
H	60	20	Brown grey	62	61	56
I	60	33·33	Dull green red	110	95	88
J	60	53·33	Pink brown	114	116	94
K	60	66·67	Mid green	82	89	81
L	60	100	Blue green	34	52	62

Table 4: Colors obtained through Laser assisted oxidation with a Universal versal X-660 Laser Platform on a Ti-6AL-4V titanium alloy samples. This figure is extracted from [58].

c) <u>Nature of the oxide layer</u>

In order to obtain the oxide layer composition, analysis were performed by Grazing Incidence X-Ray Diffractometry (GIXRD) with a Siemens D500 diffractometer (Cu Kα λ = 1.54 A°) using an incidence angle of 1° relative to the plane tangent to the sample surface. These results were confirmed by Raman spectroscopy and Secondary Ion Mass Spectrometry (SIMS).

In [58], a comparative study between samples obtained through LAO and samples obtained through anodizing, a commonly used oxidation technique presented later in this document, is presented. The anodizing conditions, such as the current density or the concentration of the solution are not specified. The authors used different analysis techniques to compare the oxide layer composition of the samples obtained with both oxidation methods. The GIXRD spectra showed the presence of several phases on the laser colored sample: α-Ti, amorphous TiO_2, anatase and rutile TiO_2, β-Ti_2O_3 and γ-TiO (Figure 24). On the other hand, GIXRD measurements of the anodized samples only showed the characteristic peak pattern of a polycrystalline α-Ti structure in all the cases.
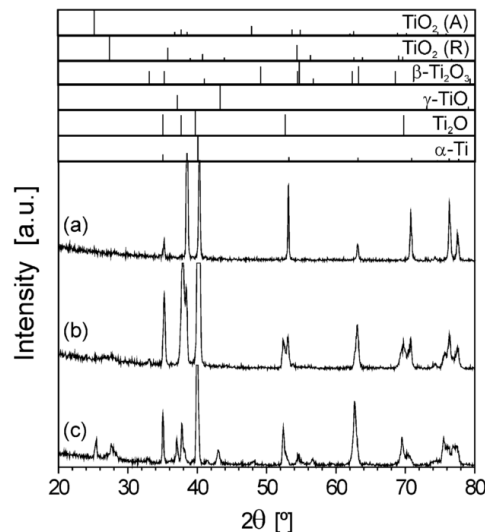
Figure 24: GIXRD spectra (with an incidence angle of 1° in all cases) of (a) the anodized sample obtained at 97 V, and the laser treated samples obtained at laser scanning velocities of (b) 240, and (c) 80 mm/s. In addition, the powder diffraction patterns corresponding to α-Ti, Ti_2O, γ-TiO, β-Ti_2O_3, and TiO_2 rutile (R) and anatase (A) are presented. From [56].

The SIMS depth profile showed a gradual decrease of the oxygen content (Figure 25). The SIMS profile revealed that the oxygen concentration was higher at the extreme surface of the anodized sample where the oxide layer (mainly TiO2) was present, and droped abruptly after a specific thickness was reached (boundary between the oxide layer and the titanium sample bulk). In the case of the lased sample, the oxygen concentration decreased rather linearly with the sputter time (i.e.: the deeper the oxide layer thickness was analyzed).
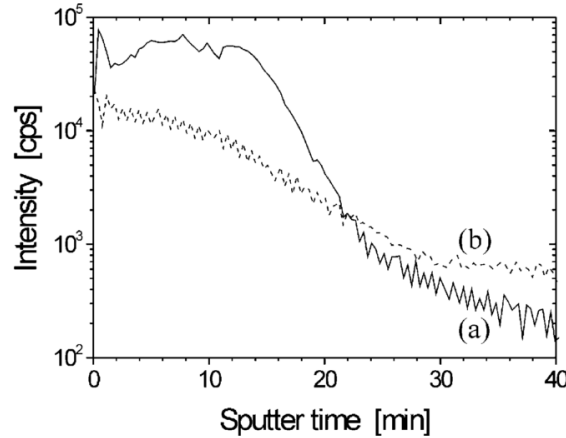
Figure 25: SIMS oxygen profiles of an anodized sample at 73 V (a) and of a sample treated by laser at a scanning velocity of 80 mm/s (b). From [56].

When combining GIXRD and SIMS results, one can represent the oxide layer of the laser treated sample as in Figure 26.
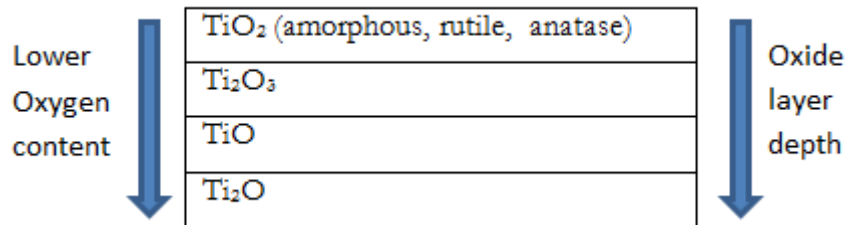
Figure 26: Oxide layer composition of a sample obtained through LAO

A TiO_2 amorphous phase with the presence of crystalline phases of rutile and anatase was identified at the outermost surface of the sample (transparent). In depth, the oxide layer contained Ti_2O_3, TiO and Ti_2O. Finally, there was a solid solution of trapped oxygen in the Ti matrix below the oxide layer.

X-Ray Diffraction (XRD) measurements from [56] (with a laser scanning velocity of 100 mm/s) evidenced in the oxide layer composition:

- a hexagonal TiO_2 phase corresponding to amorphous TiO_2 (which can be explained by the fact that this layer is partly mixed with the underlying α-Ti lattice structure),
- a tetragonal TiO_2 phase (rutile),
- and a cubic TiO phase

No anatase or Ti_2O_3 phases were found in this study.

One cannot draw conclusions about the origins of the oxide layer composition change because of the lack of data with comparable laser scanning velocities. It can be due to the nature of the substrate or to a change of the scanning speed.

O'Hana and coworkers showed in their study that the surface may exhibit surface cracking if the power of the laser is too high. This may prohibit the use of this technique for applications like jewelery for example.

d) Origin of the colors

The understanding of the mechanisms explaining the color of oxidized titanium has evolved with the progress of surface analysis techniques.

The first explanation was given by Langlade [60], who treated a commercially pure titanium T40 with a pulsed Nd:YAG laser. Langlade concluded that the layer thickness may have an effect but that the different colors they observed corresponded mainly to a different nature of the oxide layer. The layer included more than one type of titanium oxide. The first study performed by Perez Del Pino [57] tends to confirm these results. Additionally, different oxides layer types were found to form at higher specific energies. This energy is defined as the ratio between the laser power and the product between the scanning speed and the beam diameter. However, in a later study [56], Perez Del Pino concluded that a light interference phenomenon within an upper TiO_2 surface layer was the mechanism driving the color of the oxidized titanium sample. This result was obtained by comparing the colors obtained with anodizing and LAO. Other oxides, with a degree of oxidation and crystallinity increasing when the laser scanning velocity decreased, were found in a deeper layer. Those oxide layers were not playing a significant role in the titanium coloration. The samples exhibited a uniform color formed by a strong dominating tone coming from the TiO_2 layer, and a weaker one, coming from the other layer(s) with a higher degree of oxidation.

2) Oxidation by heat treatment

a) Technical description

It is important to note that oxidation by heat treatment is rarely used to obtain colored titanium. It is most of the time a "side effect" of a heat treatment of titanium used to change its mechanical properties, to relieve residual stresses, or to homogenize its chemical composition. Oxidation by heat treatment can be performed using a furnace (stationary vertical structure with a circular or rectangular section), a kiln (horizontal, cylindrical, rotating vessel), by using a flame (blowpipe), or by heating with an electrical resistance.

Bartlett presented [61] a color description of titanium sample oxidized using a heat treatment. The heat treatment was performed in a kiln at 700°C. Two types of titanium were used, a "scrap" material of an unknown origin and commercially pure titanium (unknown grade) called RMS. Some were mechanically polished (1000 grade paper).

b) Obtained colors

Colors were simply characterized visually and no further information was investigated (such as, e.g.: the oxide layer thickness or the refractive index of the material). These results are shown in Table 5.

Metal source[a]/type	Mechanical finish	temp.°C	Colour
Scrap	Unpolished	3 min/700 °C	Royal blue
Scrap	Polished	3 min/700 °C	Royal blue
RMS	Unpolished	2 min/700 °C	Royal blue
RMS	Polished	2 min/700 °C	Royal blue
Scrap	Unpolished	4 min/700 °C	Gold
Scrap	Polished	4 min/700 °C	Gold
RMS	Unpolished	7 min/700 °C	Pink
RMS	Polished	7 min/700 °C	Gold
Scrap	Unpolished	10 min/700 °C	Pink/green
Scrap	Polished	10 min/700 °C	Pinkish
RMS	Polished	12 min/700 °C	Turquoise
RMS	Unpolished	12 min/700 °C	Yellow/green
Scrap	Unpolished	15 min/700 °C	Brownish/green
Scrap	Polished	15 min/700 °C	Brownish/green
RMS	Unpolished	16 min/700 °C	Gold
RMS	Polished	16 min/700 °C	Greenish

Table 5: Sample color after heating treatment depending of the type of the material (RMS for commercially pure titanium and Scrap for unknown origin). This table is adapted from [61].

The initial state of the material surface can influence the observed color of the oxidized sample. This study does not offer a direct comparison between the two different materials (the oxidation parameters are different) and does not give any measurement or estimate of the oxide layer thickness.

c) Nature of the oxide layer

Lu *et al.* [15] studied the structure of a titanium oxide layer with XRD measurements and gave an estimation of the oxide layer thickness. It is important to note that the material and the protocol used were different: a titanium coating on a special Al_2O_3 substrate made of Al_2O_3 beads was used. They performed the oxidation on a titanium film (with an average thickness of 50 to 150 µm). This film was obtained by the compression of pure titanium powder (99.1 %: same purity level as CP grade 2 Ti). The Ti-coated substrates were heated in air in a range of temperature of 973 to 1273K (700 to 1000°C) and with heating time ranging from 0.5h to 50h. Depending on the temperature, different TiO_2 phases were detected by XRD (Figure 27). At 700°C, anatase and rutile crystalline phase were detected. At 800°C, the anatase peaks disappeared, which indicates that as a metastable phase, anatase phase could not be formed at this temperature or had been transformed into rutile. Nano-sized TiO_2 needles and micro-sized columnar TiO_2 crystals were formed in the coating during the oxidation process (the growth occurs along a specific direction, the surface normal, explaining their needle shape).
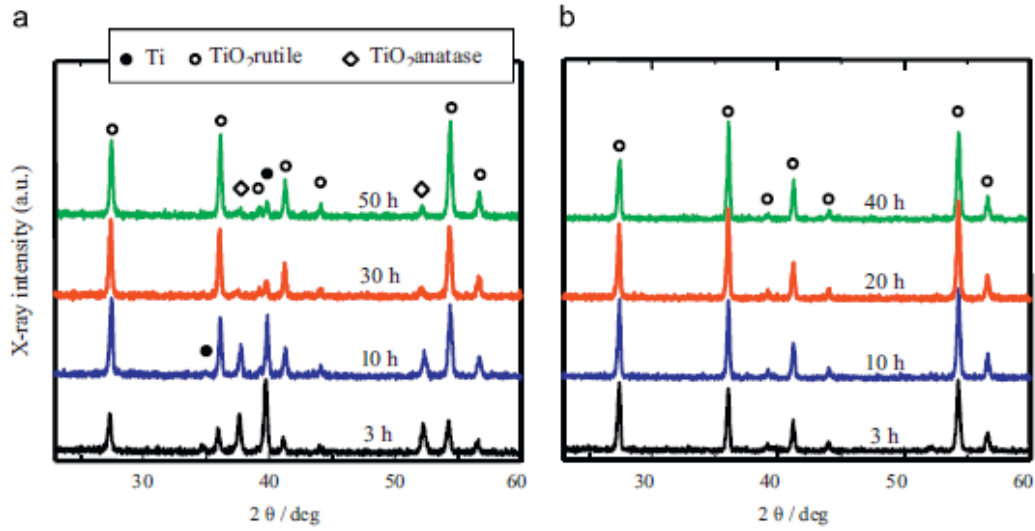
Figure 27: XRD patterns of oxidized Ti coating at 700°C (a) and 800°C (b) (from [15])

Lu *et al.* [15] also measured the oxide layer thickness by two methods (Figure 28):
- Estimated by using cross section Scanning Electron Microscope (SEM) images
- Calculated using the mass gain measured by a thermal balance and equation (34):

$$\text{T(TiO}_2) = \Delta W \frac{A(TiO_2)}{2A(0)} \times \frac{1}{\Delta\rho(\text{TiO2})} \times \frac{1}{\pi D^2} \qquad (33)$$

Where ΔW is the mass gain of one Al_2O_3 ball, $A(O)$ and $A(TiO_2)$ are respectively the oxygen atomic weight (16.00) and molecule weight of TiO_2 (79.88), $\varrho(TiO_2)$ is the density of TiO_2 (4.26 g.cm^{-3}) and D is the average diameter of an Al_2O_3 bead (1.093 mm).
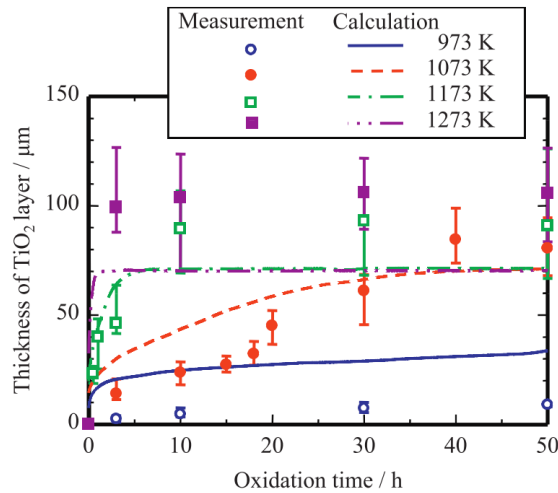
Figure 28: TiO$_2$ layer thickness as a function of oxidation time for different heating temperature, calculated from equation (12) or estimated by SEM imaging (measurement) (extracted from [15]).

Measurement dispersions are high for the highest temperatures and times but give us the order of magnitude of the oxide layer thickness: it is ranging from a few microns to more than 100 microns. This type of oxide layer thickness does not exhibit any structural color because it is far thicker than the order of magnitude of the visible wavelengths.

Several groups highlighted the potential of heat-induced oxidation in the jewelery industry, but in her study Bartlett [61] showed the unpredictability of the evenness of color obtained by titanium heating, attributing it to 'flower oxides', a specific structuration of the oxide layer with the shape of a flower.

3) Plasma electrolytic oxidation (PEO)

a) Technical description

Plasma electrolytic oxidation, also known as MicroArc Oxidation (MAO), is an electrochemical surface treatment process for generating oxide coatings on metals. It is similar to anodizing (see section 4a), but it uses higher potentials, so that discharges occur (see definition in Appendix B). The resulting plasma modifies the structure of the oxide layer.
The next paragraphs are mainly based on a study by Galvis *et al.* [62]. They presented a nearly complete characterization of the oxide layer composition. They also observed the color of the samples which presented an oxide layer thickness that allowed the occurrence of a colored interference phenomenon in the visible domain. They used mechanically polished grade 2 titanium (600 grit paper). Samples were processed at current densities of 10, 30 and 50 mA.cm^{-2} in two different electrolytic solutions 0.1 M H_3PO_4/1.5 M H_2SO_4 and 0.9 M H_3PO_4/1.5 M H_2SO_4. These solutions were not stirred during anodization. During the treatments, the temperature of the electrolytes rose above room temperature, respectively 35°C, 75°C and 90 °C for 10, 30 and 50 mA cm^{-2} current densities. To account for the possible influence of the electrolyte temperature, they also prepared samples in a cooled bath (20°C) with a current density of 50 mA/cm².

b) Obtained colors

It is important to note that the titanium samples are colored only at the beginning of the PEO treatment. The samples exhibit different colors during the cell charging when the cell potential is in the range of the potential used in a galvanostatic anodization regime (i.e.: 10 V to 120 V). It is thus reasonable to consider PEO merely as an anodization method at this stage of the experimental process because of the cell potentials involved. At this stage, the driving reaction is the evolution of the oxygen, which accounts for the low oxide layer growth efficiency. During the first few seconds, the color follows the sequence of interference colors due to the formation of an oxide with increasing thickness (see Figure 29).
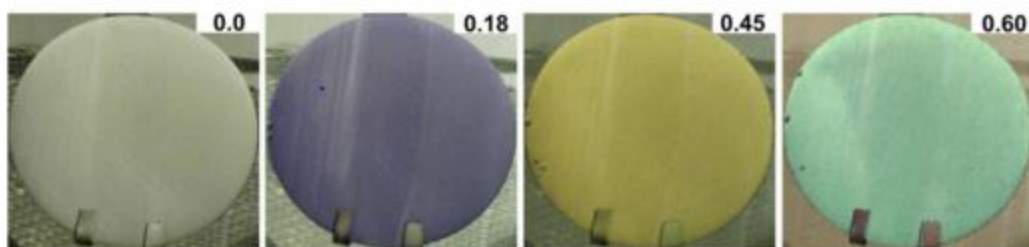
Figure 29: Titanium showing interferential color at the early stage of the PEO process at 30 mA/cm² in 0.9M HPO$_4$/1.5 H$_2$SO$_4$ electrolytes, the number in the right corner is the cell charge in C/cm² (from [62]).

After roughly 30 seconds and at a potential of 125V, blue sparks were observed. The coated surface is gradually covered by these sparks and the surface color changes to pink. After more than one minute, the sparks density decreases while their size increases and their color turn to white. At the same time the sample color turns from pink to black (see Figure 30).
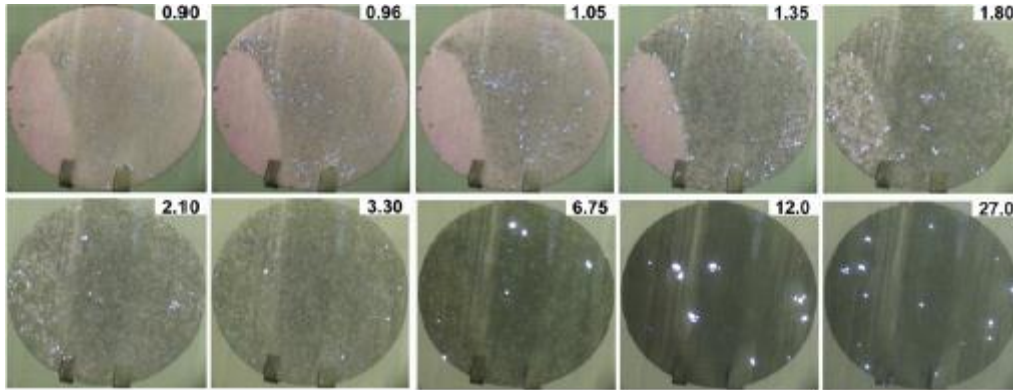
Figure 30: Sample discharge appearance during PEO of titanium at 30 mA/cm² in 0.9 M HPO4/1.5 H2SO4 electrolyte. The number in the right corner is the cell charge in C/cm² (from [62]).

c) Nature of the oxide layer

The oxide layer thickness has been measured with SEM cross section images (see Figure 31). Depending on the current density and the electrolyte composition, the oxide layer thickness is in the range of 3 μm to 11 μm. In this thickness range, the oxide layers do not exhibit any interferential color, as they are far larger than the order of magnitude of visible wavelengths.
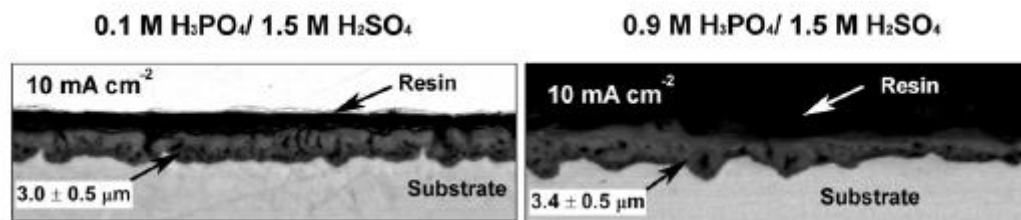
Figure 31: SEM (backscattered electrons) showing cross-sections of oxidized titanium formed after the whole PEO treatment at 10 mA/cm² in 0.1M H_3PO_4/1.5 M H_2SO_4 and 0.9 M H_3PO_4/1.5 M H2SO4 electrolytes showing the grooved surface morphology appearing with the first sparks (from [62]**Erreur ! Source du renvoi introuvable.**).

The titanium oxide layer formed in a galvanostatic regime, at current densities from 10 to 50 mA.cm^{-2} in 0.1 M H_3PO_4/1.5 M H_2SO_4 and 0.9 M H_3PO_4/1.5 M H_2SO_4 electrolytes, shows initially a grooved surface morphology, which precedes the formation of a more usual porous morphology. This morphological transition undergone by the oxide layer appears in a range of cell charges that depend strongly on the composition of the electrolyte, but weakly on the current density. This transition coincides with the changes of the spark population density, color and sparks intensity. These two morphologies have been investigated by XRD analysis. In the porous structure that occurs at the end of the PEO process, anatase and rutile crystalline phases are present, for both electrolyte solutions. In the grooved structure, which corresponds to the first sparks, only the anatase phase is present. It is consistent with the fact that anatase is stable at low temperature, but may be converted into rutile when heated above 900 °C. In the literature [63], it has been shown that the temperature and pressure in the discharge zones may reach 3700–37,000 °C and 102–103 MPa respectively, thus allowing the occurrence of the anatase to rutile phase transformation.

The PEO process does not seem to be suited to produce oxidized titanium surfaces that show interferential colors because the produced oxide layer is too thick compared to the visible wavelengths. The corrosion and tribocorrosion behavior of titanium after PEO treatment have been investigated [64]. Commercially pure titanium and Ti6AL4V alloy anodized by PEO showed

a better resistance to corrosion in a NaCl medium than non-treated samples. The alloy samples also showed a better tribocorrosion resistance with a wear beginning later and a change in the wear mechanism from a delamination of the coating to an abrasive wear, thus decreasing the risk of component failure. PEO in electrolytic solutions containing Ca [65] was proven to provide an enhanced biocompatibility, enabling the osteoblast adhesion and differentiation necessary for good implant osseointegration.

4) Oxidation by anodizing

   a) Technical description

Anodizing is an electrolytic passivation process used to increase the thickness of the natural oxide layer on the surface of metal parts. The process is called anodizing because the part to be treated forms the anode of an electro-chemical circuit.
A metallic sample is immersed in an electrolytic bath where either AC or DC current is passing. The bath is generally based on sulphuric or phosphoric acid but others electrolytes [66]–[68] can also be found such as acetic acid or calcium hydroxide. The cathode used to close the electrical circuit is usually made of aluminium or titanium. The final layer thickness and structure depend on the anodizing parameters, such as the electrolyte characteristics, the type of current (direct or alternating), the process duration, the operating temperatures and voltages, the current density, and also the composition of the material to be treated. The influence of such parameters will be presented later in this chapter.

   b) Obtained colors

This section presents the results of [69]–[71], as they measured the colors resulting from anodizing.
In 2003, Van Gils *et al.* [69] observed and measured the anodized aluminum and titanium colors, the oxide layer thicknesses and evaluated their refractive index. We will focus our review on the titanium analysis. For their experiments, Van Gils and coworkers used CP titanium (presumably ASTM Grade 2 because of the 99.5% purity). The samples were polished and anodized in a galvanostatic regime in a 0.5M H_2SO_4 solution. The current density was kept at 10 mA/cm² for cell potential up to 30 V and 20 mA/cm² for cell potentials up to 80 V. To measure the color, they used an Ultrascan XE spectrophotometer from Hunterlab. It is based on an integrating sphere geometry (di:8°) and a Xenon lamp light source. The colors are summarized in Table 6 in the CIE Lab color space:

Anodising voltage (V)	Colour	L^*	a^*	b^*	Chromaticity
10	Gold	57.86	4.34	31.67	31.97
15	Copper	37.89	21.05	13.46	24.99
20	Blue–purple	30.56	19.97	− 41.23	45.81
30	Blue	67.2	− 9.1	− 12.23	15.24
40	Light blue	65.91	− 8	− 4.78	9.32
50	Green	68.95	− 7.35	15.97	17.58
60	Yellow	66.58	0.33	29.88	29.88
80	Rose	55.97	30.99	− 4.11	31.26

Table 6: Anodized Titanium color properties: Observed colors and measured colors expressed in the CIELAB color space (extracted from [69]). The chromaticity ($\sqrt{a^{*2} + b^{*2}}$) describes a color regardless of its luminance.

Diamanti and Pedeferri [71] showed the high quality of the oxide layer obtained after anodizing in terms of color homogeneity and color repeatability. For these reasons, anodizing is well fit to be used for jewel production (see Figure 32). Twenty specimens were anodized by applying a 70 V potential with a 40 mA/cm² current density in H_2SO_4 without any surface pretreatment. Color

was measured by using a Konica Minolta CM-2500C portable spectrophotometer that with a 45°a:0° geometry. An integrating hemisphere, an illumination slit and a ring-shaped light source give a perfect annular illumination. This system, supported by a collimator lens, grants a very good uniformity. The wavelength range of the measurement is from 360 nm to 740 nm with a resolution of 10 nm. The anodizing process produces a determined color, with an average relative error of the a^* and b^* coordinates of 1.8% (calculated from 20 measurements).
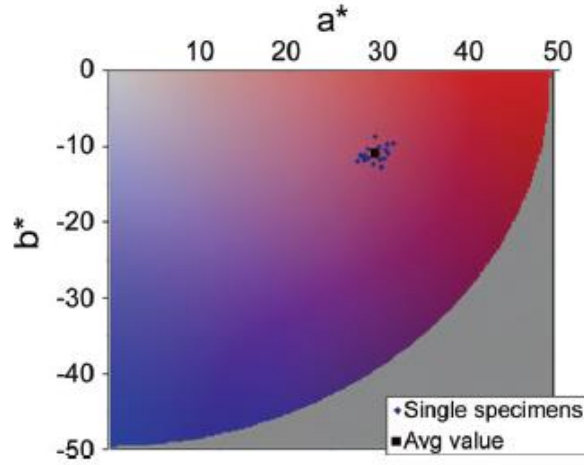
Figure 32: Section of the CIELAB a*-b* plane containing color points produced by 20 titanium samples anodized in a 0.5M H_2SO_4 solution with a potential of 70 V [71].

c) Nature of the oxide layer

Van Gils *et al.* [69] used the interference phenomenon to calculate the thickness of the oxide layer using the reference value of the refractive index n of different TiO_2 phases. This measurement method of the oxide layer thickness is called "spectrometric measurement". The index values are $n = 2.2$ for a wavelength of 632 nm for an amorphous layer and $n = 2.5$ for an anatase crystalline phase layer for the same wavelength. They used the extrema of the measured reflectance spectra of the samples curves and equation (35) to obtain the thickness (n is the refractive index, d the thickness of the oxide layer, λ the wavelength of the incident light, θ the angle of the incident light relative to the normal of the sample surface and p the order of the interference):

$$2n \times dcos\theta = p\lambda \tag{34}$$

Destructive interferences correspond to minima of the reflectance spectra and arise when the optical path difference is equal to $p\lambda/4$, where p is a half-integer. In this case, we still can use the paraxial approximation ($\cos\theta = 1$) because the measurement angle is small (8°). The minima of the reflectance spectra denoted as $\lambda_{1/2}$, $\lambda_{3/2}$ and $\lambda_{5/2}$ follow the conditions:

$$nd = \lambda_{\frac{1}{2}}/4 \; ; \; 3\lambda_{\frac{3}{2}}/4 \; ; \; 5\lambda_{\frac{5}{2}}/4 \ldots \tag{35}$$

Constructive interferences correspond to maxima of the reflectance spectra and the constructive interference condition is obtained when p is an integer. The maxima of the reflectance spectra denoted as λ_1, λ_2 and λ_3 follow the conditions:

$$nd = \lambda/2 \; ; \; \lambda \; ; \; 6\lambda/4 \ldots \tag{36}$$

Van Gils *et al.* also measured the thickness of the oxide layer by spectroscopic ellipsometry using a rotating compensator ellipsometer, a J.A.Woollam Co. VASE system (at incidence angles of 65°, 75° and 85°). Ellipsometric and spectrometric measurements of the oxide layer thickness were in quite good agreement as shown in Figure 33:
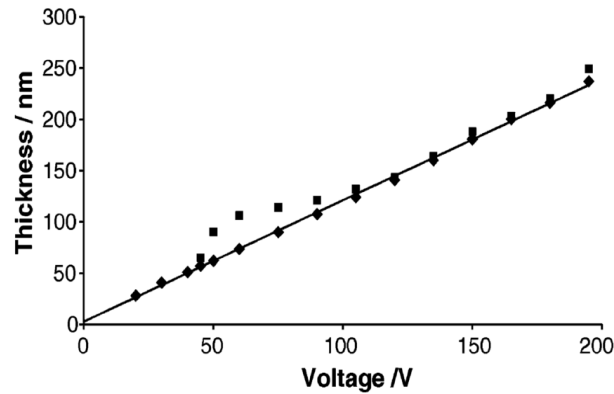
Figure 33: Ellipsometry (square) and spectrometric (diamond) measurements of anodized titanium samples at different potentials in a 0.5M H_2SO_4 solution (from [69]).

The oxide layer thickness resulting from titanium anodization is in the range 20 to 150 nm.

Diamanti *et al.* also [71] calculated the oxide layer thickness by using the reflectance spectra extrema, as Van Gils *et al.* did. ASTM Grade 2 pure titanium and ASTM Grade 5 titanium alloy (Ti6Al4V) were used and anodized in H_2SO_4 electrolytic solutions with concentrations ranging from 0.25M to 2M or in 0.5M H_3PO_4. The oxide layer thickness measurements corresponding to the same condition (0.5 M H_2SO_4) are in a good agreement in both studies (See Figure 34).
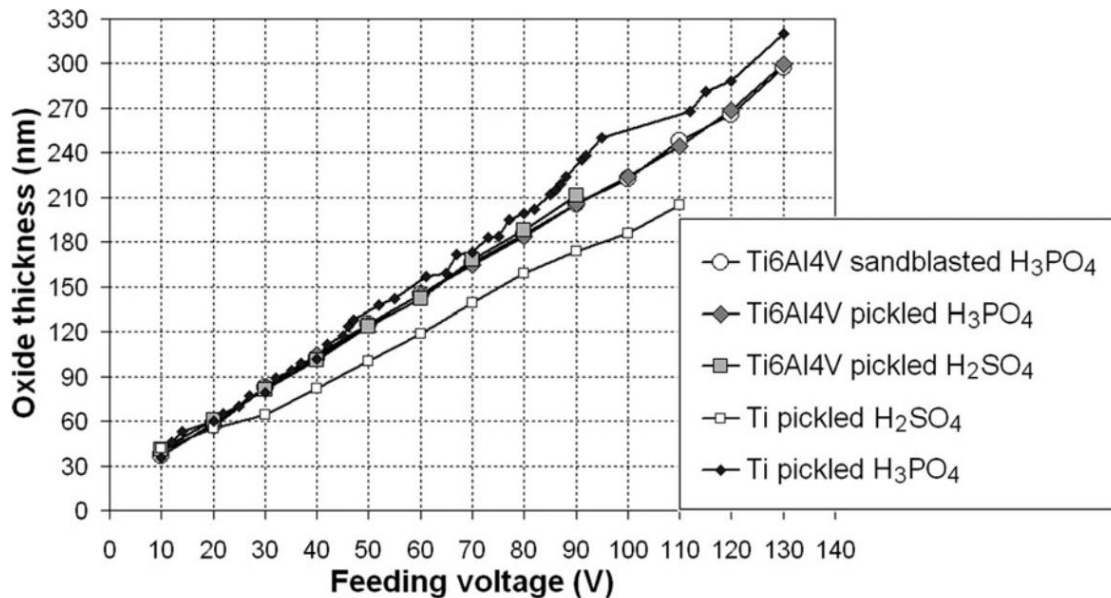
Figure 34: Oxide layer thickness as a function of the anodizing potential for different substrates (CP titanium or Ti6Al4V) in different solution (0.5M H_3PO_4 or 0.5M H_2SO_4) with different surface finishes (pickled or sandblasted, see Appendix B). From [71].

Van Gils *et al.* also measured the oxide layer refractive index by ellipsometry [69] and compared it with the TiO_2 refractive index found in [72] (see Figure 35).
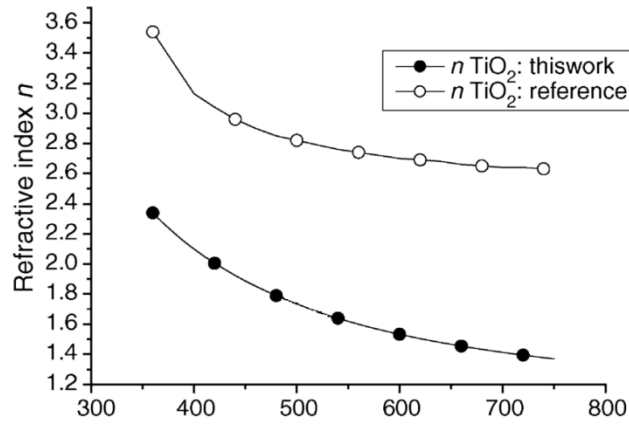
Figure 35: Comparison between TIO₂ refractive index from reference [72] (white circles) and obtained from ellipsometric measurements (black circles) at a 10 V anodizing potential [69] (from [69]).

The values measured by ellipsometry are lower than the ones found in the literature. This may indicate the presence of an amorphous phase, as opposed to the crystalline phase assumed in [72].

In a subsequent study [19], Diamanti and Pedeferri used two ASTM grade 2 titanium samples. These samples were anodized in a 0.5M H_2SO_4 electrolyte solution at 200 mA/cm² at 60 V and 90 V. Ellipsometry was used to determine the TiO₂ refractive index changes for visible wavelengths for the two samples. One has a totally amorphous oxide layer obtained at a cell potential of 60 V and the other is partially crystallized, obtained at a cell potential of 90 V with an anatase phase (see Figure 36).
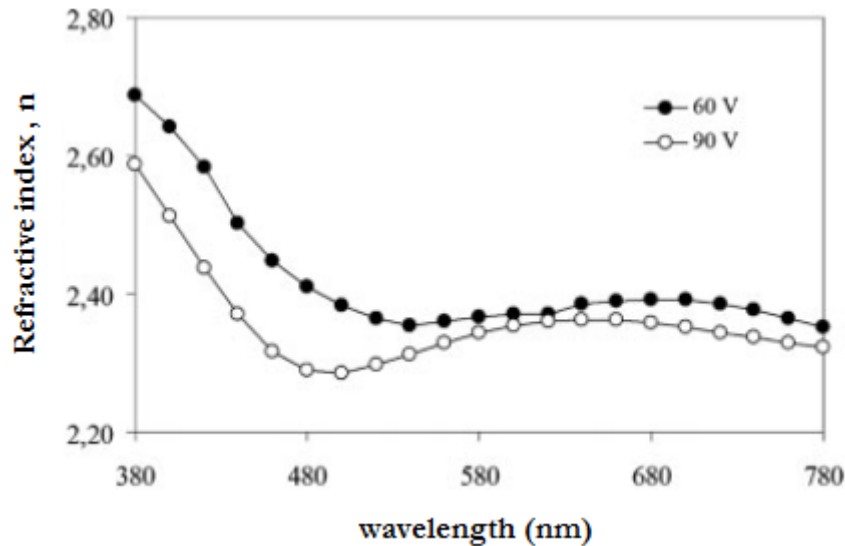
Figure 36: Variation of the refractive index for two different oxide layer thicknesses and crystallinity. The samples are two ASTM grade 2 titanium samples anodized in a 0.5M H_2SO_4 electrolytic solution at 200 mA/cm². The 60 V sample oxide is amorphous whereas the 90 V sample oxide is partially crystalline (anatase phase). From [73].

In [70], Diamanti *et al.* proposed a characterization of the oxide layer composition using XRD for different anodizing potentials (see Figure 37).
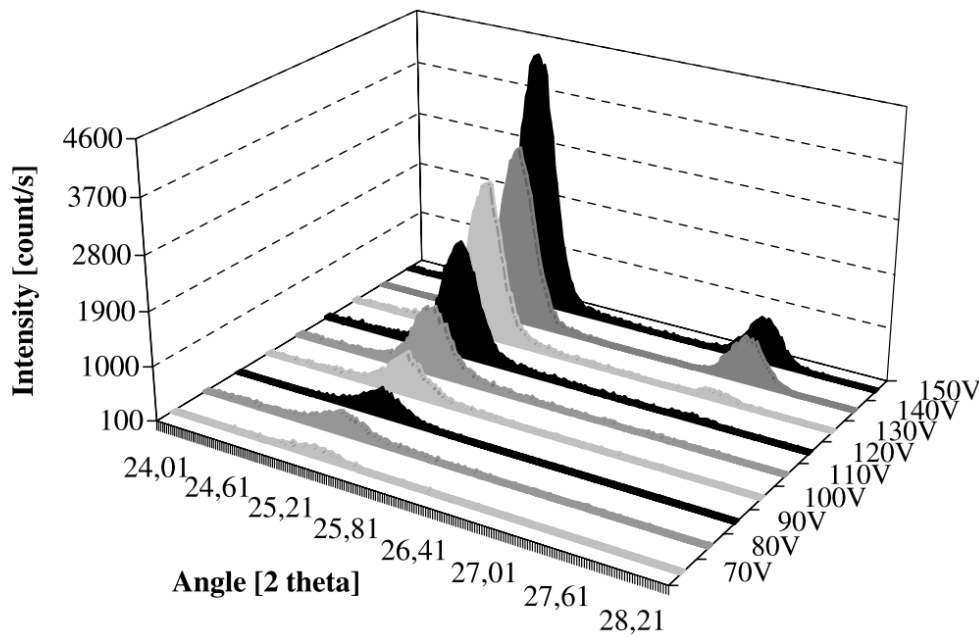
Figure 37: XRD analysis of samples anodized in 0.5M H₂SO₄ and at a current density of 108 mA/cm² for potentials ranged from 70 V to 150 V (extracted from [70]).

On the XRD diffractograms, a peak observed for an angle value of $2\theta = 24.6°$ indicates the presence of a TiO₂ anatase phase and a peak at an angle value of $2\theta = 27.4°$ corresponds to the TiO₂ rutile crystalline phase. When the electrolytic solution is H₃PO₄, the oxide layer is always amorphous, regardless the potential [73].

d) Tribocorrosion behavior of anodized samples

Diamanti *et al.* [68] presented evaluations of the wear resistance in synthetic sweat (chemical wear) of titanium samples anodized at different potentials in two different electrolytic solutions, H₂SO₄ and NH₄BF₄. The choice of the electrolyte was based on its availability, its absence of toxicity and its reasonable price range (30€ to 75€ per kilogram) to envisage an industrialization of the process. The choice of the electrolyte was also based on the color obtained after the anodizing process. The samples series should exhibit a wide range of colors with high saturation and high anodization kinetics. Anodizing was performed at a current density of 10 mA/cm² with a cell potential equal to 25V, 60 V and 90 V. The wear tests (pin-on-disk tests) were performed in a synthetic sweat solution containing NaCl (0.5%), Urea (0.1%), Lactic acid (0.1%) and KOH (potassium hydroxide) to obtain a solution with a pH of 5.6, corresponding to the pH of the skin. These tests were used to simulate the contact of the skin with colored samples, corresponding to 8 months of wear, in synthetic sweat solution. Depending on the sample, the wear test may result in a color change (thinning of the oxide layer) or in a color disappearance (destruction of the oxide layer). In order to quantify the color change before and after the wear test, the ΔE_{76}^* was calculated between the two colors. The results are presented in Table 7:

	Voltage (V)	Thickness (nm)	Colour	$a*$ CIELab Before	$a*$ CIELab After	$b*$ CIELab Before	$b*$ CIELab After	ΔE
NH$_4$BF$_4$	25	75	Blue	5	3	-29	-28	1.6
	60	150	Gold	5	6	22	21	1.3
	90	220	Green	-11	-9	3	8	6.1
H$_2$SO$_4$	25	70	Blue	6	4	-18	-16	3.1
	60	120	Light yellow	-4	-4	9	10	0.6
	90	185	Pink	15	13	-12	-14	3.0

Table 7: Thickness and associated sample colors before wear test and CIELAB coordinates before and after the wear test. The thickness is evaluated by spectrophotometry (from [33]).

It is important to note that the measurement spot was larger than the wear trace, implying a smaller influence of the wear region on the calculated ΔE^*_{76}. The color difference seems more noticeable after the wear test in the case of the sample anodized in H$_2$SO$_4$, as shown by values of ΔE^*_{76} over 2.3, i.e.: over the JND value. Visual results indicated a higher wear resistance of samples anodized in NH$_4$BF$_4$, represented by a more uniform remaining color, while a clearer mark of the polymeric pin could be observed on the surface of the samples anodized in H$_2$SO$_4$, as shown in Figure 38.

Diamanti *et al.* also presented a process enabling a recoloration of the worn area by anodizing the sample again at a smaller potential. The new potential is chosen by taking into account the periodicity of the color with the potential, i.e. a color obtained at a high potential has a close counterpart with a lower potential (even if the color saturation could be changed in some cases). This process could allow the restoration of the scratched/worn area without replicating the surface preparation of the whole object, as for example repairing a scratch on a ring without repolishing the whole ring.
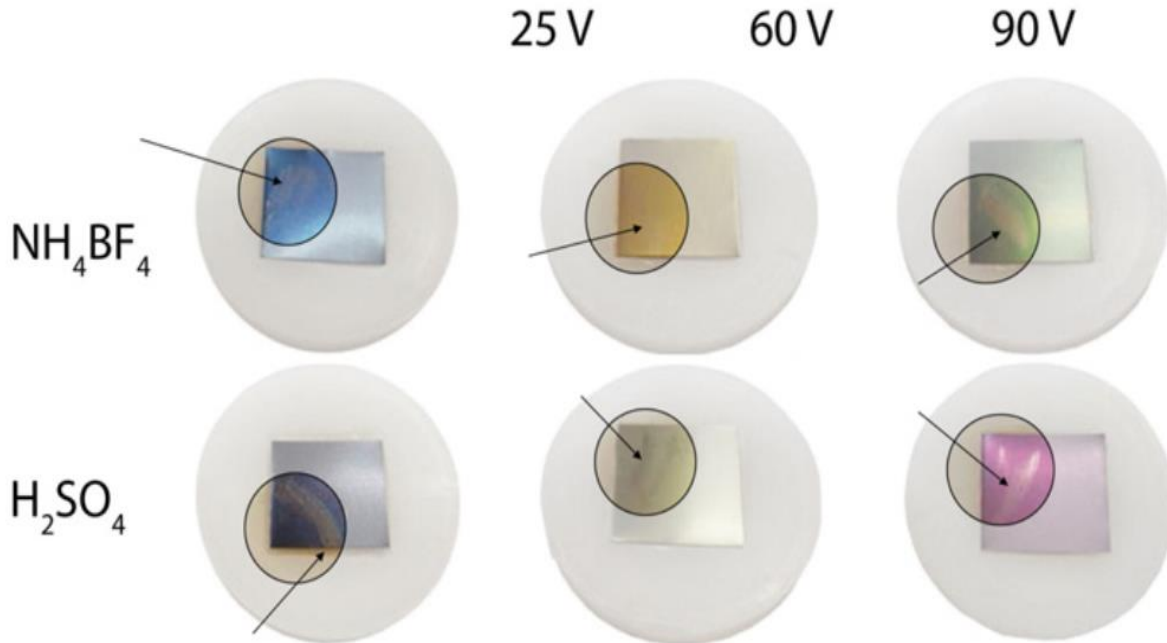
Figure 38: Pictures of the anodized samples after the pin-on-disk test. Color changing or color disappearance resulting from the wear tests are highlighted (from [68]).

The wear behavior of titanium oxide layers in air and in vacuum was studied by Yetim [74], with a different anodizing process. The samples were produced by potentiostatic anodizing on ASTM Grade 2 titanium. The anodizing was performed in H$_2$SO$_4$ (1.5 M)–H$_3$PO$_4$ (0.3 M) with a constant

voltage of 200 V and an anodizing time of 1200s. The wear tests were also realized by a pin-on-disk method. The resulting oxide layer is porous and is mainly composed of anatase, with a small amount of rutile. This oxide layer improved the wear resistance of the sample due to the self-lubricating property of the wear debris. This study could be useful for the understanding of the wear behavior of titanium tools in manufacturing or aerospace industries.

Alves et al. [75] studied the tribocorrosion behavior of calcium- and phosphor-doped anodized titanium. They used ASTM Grade 2 titanium and the samples were anodized in a potentiostatic regime at a potential of 300 V in an electrolytic solution containing calcium acetate in order to incorporate these bioactive species in the oxide film. The wear tests (pin-on-disk) were performed in a NaCl solution. The amount of calcium acetate in the solution plays an important role in the chemical composition and structure of the oxide layer. The presence of rutile in the oxide layer decreases significantly the mechanical damage after sliding, showing the importance of the crystallinity of the oxide layer in the tribocorrosion behavior of the sample. When the oxide layer is worn out, the wear rate becomes more important than the one measured on CP titanium samples in the same conditions, implying the participation of oxide wear debris located in the contact area. This study aims at a better understanding of the tribocorrosion behavior of implants subjected to micro-movements in aggressive biologicals fluids such as saliva or synovia.

e) Anodizing and titanium nanotubes

In 2012, Moon *et al.* [76] grew titanium dioxide nanotube arrays through anodizing. The authors used ASTM Grade 2 titanium and the samples were anodized in a potentiostatic regime and an electrolyte containing 0.5 wt% (weight percentage) of HF (hydrofluoric acid) at different cell potentials ranging from 7 to 20 V.

XRD measurements did not show any crystalline phase. The morphology of the nanotubes changes by changing the cell potential (length, thickness and pore diameter). The morphology of the prepared samples was observed with a scanning electron microscope (See Table 8).

Voltage, V	Pore diameter, nm	Wall thickness, nm	Tube length, nm	
7	17	16	134	
10	32	10	231	
15	45	14	271	
20	90	29	340	
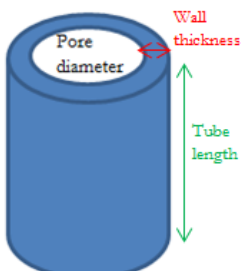
Table 8: Morphology parameters of the nanotubes at different cell potentials for an anodizing time of 30 min. (from [76]**Erreur ! Source du renvoi introuvable.**). A nanotube is represented on the right with the definition of the different parameters.

Moon *et al.* also prepared samples anodized at a cell potential of 20 V, but with different anodizing times and reported the color of the sample as a function of the nanotube length (see Figure 39).
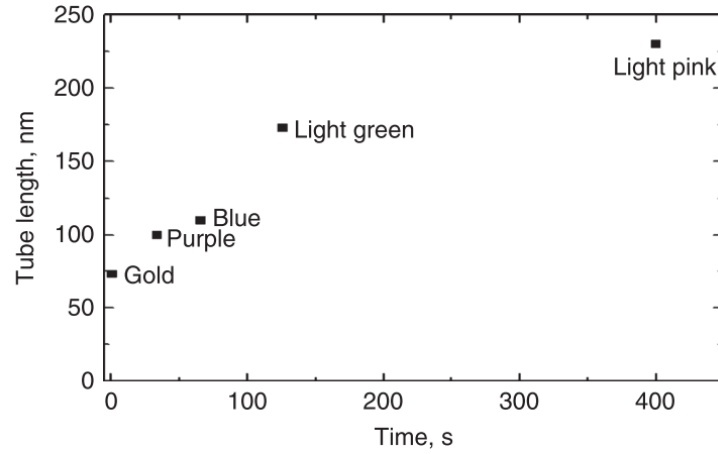
Figure 39: Relationship between anodizing duration, nanotube length (mainly corresponding to the oxide thickness) and color of titanium samples anodized at 20 V (from [76]).

They also compared the tube growth and the interferential colors displayed by titanium during anodizing: gold, purple, blue, light green and light pink. The sequence of the colors displayed by the sample during the growth of the nanotube is in agreement with the results obtained during anodizing of grade 2 titanium samples [69][71]. The growth mechanisms are described step by step in Figure 40.

Figure 40: Different steps of the nanotudes growth (from [76]).

At the beginning of the anodizing, a 70 nm thick oxide layer formed after 2-5 seconds displays a gold color (step 1). The TiO₂ layer does not exhibit nanotubes yet. The oxide continues to grow and exhibits a purple color (90 nm thickness - step 1). After around thirty seconds, small pores start to appear at the surface of the oxide layer and the color changes to blue (step 2). As the anodizing process continues, after about one minute, the pores spread out over the entire surface and have thin walls (step 3). After two minutes, the interferential color changes to light green, the length of the nanotubes reaches 170 nm and the pores form a particular structure (step 4) where they start to form tubes. The anodizing terminates after over 5 minutes. The TiO₂ nanotubes reach a depth of 240 nm, the color displayed by the layer is pink with a greenish shade and nanotubes are all over the surface (step 5). The colors, of the nanotubes samples have been measured in the CIELab color space using a CM-700d, Konica Minolta Sensing spectrophotometer. They are compiled in Table 9. The color differences between a colored sample and a reference titanium sample are given in terms of ΔE_{ab}^* values, (the higher the value, the higher the color difference between the titanium reference and the colored anodized sample).

Sample	Time, s	Voltage, V	Thickness, nm	L	a*	b*	ΔE*ab (D65)
Ti				60.66	1.47	5.24	
a	1800	7	134	61.29	−5.41	−2.51	10.54
b	1800	10	231	61.80	0.02	22.39	17.27
c	1800	15	271	54.46	−4.00	4.53	8.46
d	1800	20	340	57.27	1.89	8.43	4.66
e	1	20	73	39.28	9.62	25.98	30.82
f	34	20	91	29.32	14.82	−21.64	43.32
g	66	20	113	51.42	−6.82	−14.92	23.76
h	126	20	173	58.57	−6.51	8.19	8.99
i	400	20	240	52.05	2.70	2.35	9.14

Table 9: Interference colors of anodic nanostructured TiO₂ films prepared at different voltages (from [76]).

The colors of the samples are represented on the chromaticity diagrams Figure 41. The reflectance spectra of samples with nanotubes (porous or with a tubular structure) showed a relatively low reflectance value (5 to 30%) and the color measurements showed that these samples exhibit high color differences depending on the used parameters such as voltage and anodizing time.
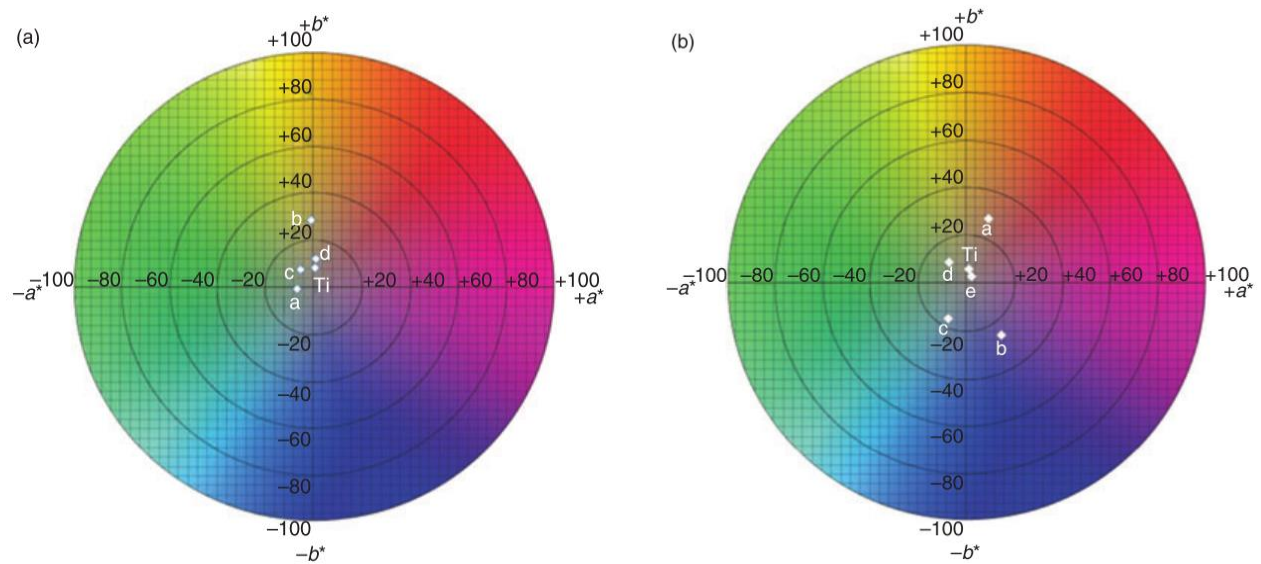
Figure 41: Chromaticity diagram of TiO₂ nanotube samples: a) as a function of the potential (a: 7V; b: 10 V; c: 15V; d: 20 V) and b) as a function of anodizing time (a: 1–2s; b: 34s; c: 66 s; d: 126 s; e: 400 s) (from [76]).

5) Discussion and conclusions: towards a standard calibration color chart for metallic gonioapparent materials

Some challenges must be overcome to produce a standard calibration color chart for metallic gonioapparent surfaces. A requirement list for such a tool may be put-together as follows:

- A wide range of colors is needed in order to span as best as possible the whole color space.
- The metallic gonioapparent references would also have to follow various color paths and to exhibit different roughness levels in order to be able to characterize samples with different levels of glossiness.
- The colors of the reference samples have to be homogeneous. The colors must also be stable over time.

48

- The final product has to be able to resist manipulations which could include scratching, wear and contacts with some body fluids such as sweat or saliva.

We showed that different techniques can be used to color metals, with a focus on titanium.

Laser assisted oxidation can be used to prepare a wide range of colors but the samples may lack the necessary color homogeneity. The color is indeed formed by a strong dominating tone coming from the TiO_2 layer, and a weaker one coming from other layers with a higher degree of oxidation. The color is also often generated by a surface scanning of the laser beam, which might degrade the color homogeneity. It is also important to remind the risk of cracks formation of on the surface of the sample.

Oxidation by heating can also produce a large array of colored samples but the process is difficult to control. The unpredictability of the evenness of the color obtained has been observed and was attributed to the 'flower' structure of the oxide layer.

Plasma electrolytic oxidation does not seem to be suited to produce oxidized titanium surfaces that show interferential colors because the produced oxide layer is too thick compared to the visible wavelengths. The samples exhibit colors only during the first step of the process, i.e. the cell charging, when the PEO is roughly equivalent to electrolytic anodizing.

Titanium anodizing has been proved to be able to produce samples with good color homogeneity, with a wide range of colors. The TiO_2 oxide layer is also known for its good chemical stability. An oxide layer restoration process was also proposed in the literature to address the issue of wear during usage. Anodizing is also a cheap and easy to use process. For all these reasons, anodizing was selected to be the oxidation technique used during this work.

In the next section, we will present the parameters having an impact on the color of the anodized samples. These can be anodizing parameters such as current density, cell potential and electrolytic solution, or samples properties, such as sample roughness or material composition and microstructure.

II. Parameters influencing the color of anodized titanium samples

Many parameters affect the color of anodized titanium samples. They might be experimental parameters such as the current density, the cell potential, the electrolyte concentration and composition, or related to the titanium substrate such as the crystalline orientation or the surface roughness.

1) Influence of the current density
   a) Influence of the current density on the oxide growth rate

Diamanti *et al.* [70] tested the influence of the current density on titanium anodizing. They anodized ASTM grade 2 titanium samples in a solution of H_2SO_4 with a concentration of 0.5M. The different current densities were 10, 20, 40, 80 and 108 mA/cm². The samples were observed by X-Ray Diffraction (XRD) in order to characterize the crystallinity of the oxide layer. By neglecting any parasitic reaction, as for example the anodic oxygen evolution reaction, the oxide growth rate can be considered proportional to the growth rate of the anodizing potential versus time. This potential growth rate can be used to obtain information about the oxidation kinetics. The potential growth rate has been measured for all the sample series in the first ten seconds of anodizing. The value of the anodizing time necessary to reach a potential of 70 V was also measured, as show in Table 10.

	100 A/m^2	200 A/m^2	400 A/m^2	800 A/m^2	1080 A/m^2
dV/dt [V/s] (first 10″)	1.64	3.54	5.36	13.79	18.97
T$_{70V}$ [s]	418	45	24	5.5	3.6

Table 10: Potential growth rate in the first 10 seconds of anodizing (dV/dt) and anodizing time required to reach 70 V (T$_{70}$ v) as a function of current density (from [70]).

The higher the current density, the higher the potential growth rate, and therefore the faster the oxidation reaction. An increase of the current density also corresponds to an increase of the maximum cell potential attained, as shown in Table 11. The maximum potential is defined as the potential at which oxide growth slowed down significantly.

	Maximum potential attained (V)
100 A/m^2	70
200 A/m^2	110
400 A/m^2	120
800 A/m^2	140
1080 A/m^2	150

Table 11: Maximum value of potential reached during anodizing as a function of current density for anodizing in H$_2$SO$_4$ 0.5M (from [70]).

b)   Influence of the current density on the crystallinity of the oxide layer

The current density also plays a role on the crystallinity of the oxide layer. Diamanti *et al.* [70] compared samples anodized at 20 mA/cm² and 108 mA/cm² for different obtained cell potentials. Anodizing is stopped when the potential reaches a chosen value. This chosen value is called "cell potential" by the authors. By comparing the two graphs shown in Figure 42, we can observe that for the same cell potential, the anatase peak (2θ=24.6°) is lower for the lowest current density, implying a lower crystallinity for a lower current density. It also interesting to note that the anatase peak appears at a higher cell potential for the lowest current density.
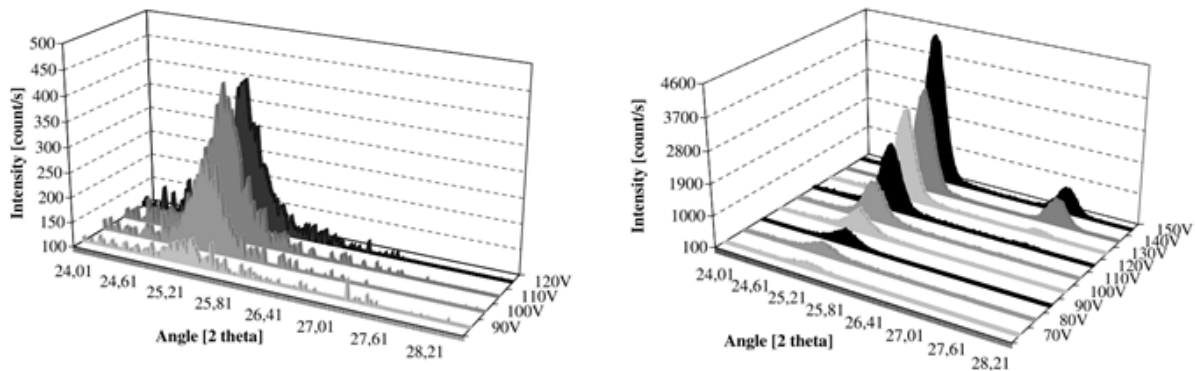
Figure 42: XRD analysis of samples anodized in 0.5M H$_2$SO$_4$ at 20 mA/cm² (on the left) and 108 mA/cm² (on the right). The peak at 2θ = 24.6° corresponds to the anatase phase and the peak at 2θ = 27° to the rutile phase (from [70]).

The crystallinity of the oxide layer might also affect the color of the titanium sample as the average refractive index of the whole oxide layer might change: the value of the refractive index of the TiO$_2$ anatase phase is larger than that of the TiO$_2$ amorphous phase.
Diamanti *et al.* [73] showed that the lightness (L^* component in the CIELAB colorspace) of a sample is also linked to the applied current density, i.e.: the higher the current density the higher the lightness, as shown in Figure 43.
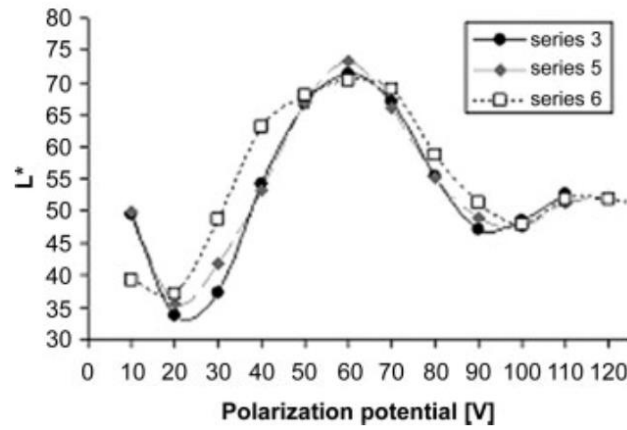
Figure 43: Lightness as a function of the cell potential (denoted as polarization potential in this graph) for grade 2 titanium samples anodized in a solution of H_2SO_4 0.5M at different current densities: 20 mA/cm² for the series 3, 40 mA/cm² for the series 5 and 80 mA/cm² for the series 6 (from [73]).

2) Influence of the electrolytic solution
    a) Influence of the electrolytic solution on the crystallinity of the oxide layer

Diamanti *et al.* [73] studied the influence of the electrolytic solution used and its concentration. ASTM Grade 2 titanium samples were anodized at a 20 mA/cm² current density in H_3PO_4 (concentration not reported) or H_2SO_4 with concentrations ranging from 0.25M to 1M. The samples were analyzed with XRD. On the one hand, the samples anodized in H_3PO_4 do not exhibit any crystalline phase even at a potential over 90 V, as shown in Figure 44(a). On the other hand, partially crystallized anatase phase is observed for all the samples anodized in H_2SO_4 when a certain cell potential is reached. This potential is dependent on the concentration of the solution: the higher the concentration, the smaller the potential at which the anatase phase appears, as shown in Figure 44 (b), 42(c) and 42(d).
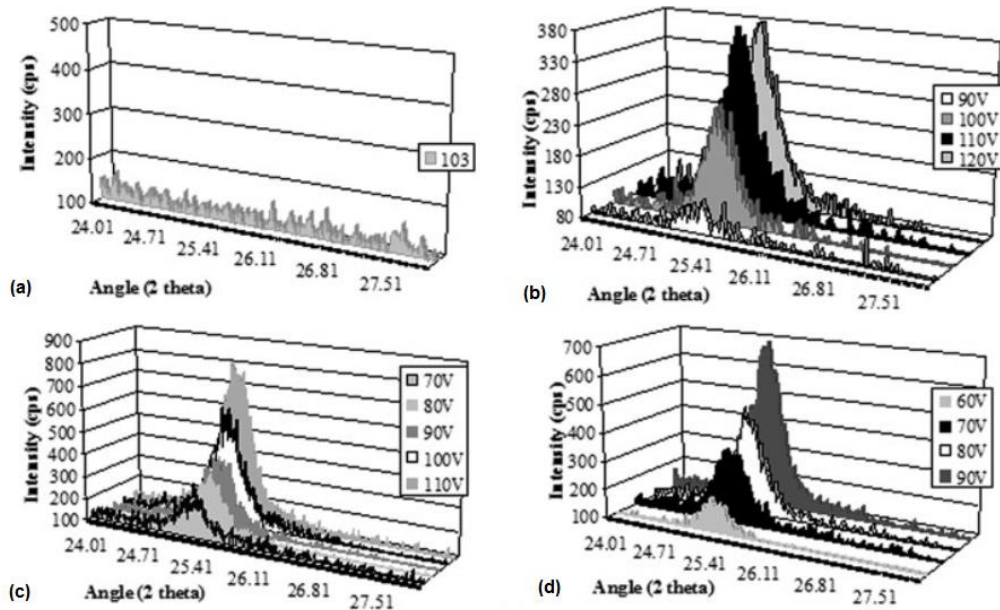
Figure 44: X-Ray diffractograms of sample series anodized at a current density of 20 mA/cm² in H_3PO_4 solution at a cell potential of 103 V (a) or in H_2SO_4 with a concentration of 0.25M (b), 0.5M (c) or 1M (d) for different cell potentials (from [73]).

b) Influence of the electrolytic solution on the oxide growth rate

Diamanti *et al.* [70] proved that the concentration of the electrolytic solution has an effect on the kinetics of the oxidation reaction: increasing the concentration from 0.25M to 0.5M leads to a higher oxide growth rate and an anatase phase formation at a lower cell potential. A further increase of the concentration leads again to an earlier formation of the anatase phase, but with a decrease of the oxide growth rate, as shown in Table 12. The effect of crystallinity on the color of the sample is not studied in this paper.

	H_2SO_4 0.25 M	H_2SO_4 0.5 M	H_2SO_4 0.7 M	H_2SO_4 1 M	H_2SO_4 2 M
dV/dt [V/s] (first 10″)	3.37	3.54	2.97	2.90	1.58
$T_{70\,V}$ [s]	58	45	44	60	510

Table 12: Potential growth rate in the first 10 seconds of anodizing (dV/dt) and anodizing time required to reach 70 V ($T_{70\,V}$) as a function of the concentration of the solution (from [70]).

Diamanti *et al.* also showed [77] that the concentration of the solution has no effect on the final oxide layer thickness for anodizing with cell potentials under 50 V, as shown in Figure 45. The oxide layer thickness is evaluated through spectrophotometric measurements, using a spectrophotometer with a 45°a:0° geometry. The extrema of the reflectance spectrum correspond to constructive (maxima) or destructive (minima) interferences. By assuming amorphous TiO_2 for the refractive index value (2.4) of the oxide layer (obtained by ellipsometry in [73]), its thickness can be deduced from equation (11). This effect was not studied in the case of higher potentials, for which the anatase crystalline phase is present and thereby might change the refractive index and/or the oxide layer thickness.
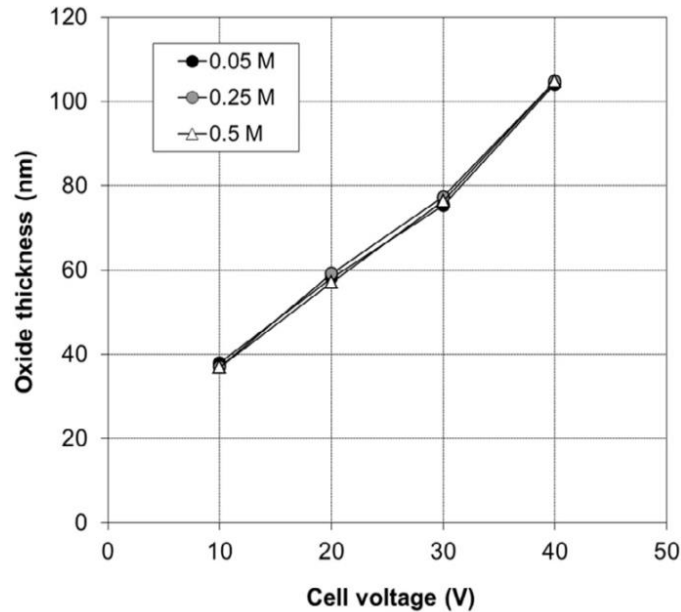
Figure 45: Oxide layer thickness calculated from spectrophotometric measurements of ASTM grade 2 titanium samples anodized at a current density of 20mA/cm² in different solution of H_2SO_4 with concentrations ranging from 0.05 M to 0.5M for different cell potentials (from [77]).

According to the previous studies [70], sulphuric acid seems to be the optimal electrolyte when the aim of anodization is to obtain an anatase phase. The optimal concentration in terms of oxide growth rate is 0.5M.

Diamanti *et al.* [68] also studied numerous different electrolytic solutions at different cell potentials. The tested electrolytes were H_3PO_4, NA_3PO_4, $NH_4H_2PO_4$, H_2SO_4, NA_2SO_4, $(NH_4)_2SO_4$, HBF_4, $NABF_4$ and NH_4BF_4. Anodizing was performed at a current density of 10 mA/cm^2 with cell potentials ranging from 10 V to 100 V. HBF_4 was discarded because no anodizing could be achieved in this solution.
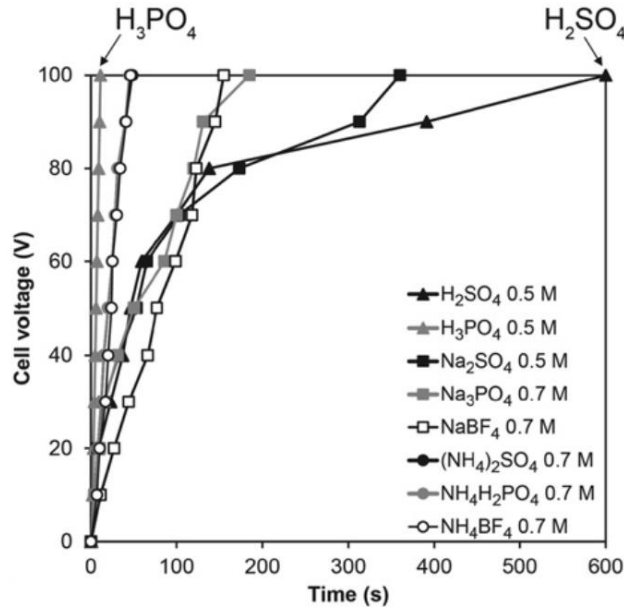
Figure 46: Anodizing kinetics of ASTM Grade 2 titanium samples anodized at a current density of 20mA/cm² in different electrolytic solutions (from [68]).

Anodization resulted in the destruction of the surface of the sample, even with diluted solutions. A study of the kinetics of the oxidation reaction was performed for all the solutions. The growth rate results from three main contributions: the oxide solubility in the electrolytic solution, the anodic oxygen evolution reaction and the presence of Anodic Spark Deposition (ASD), which changes locally the temperature and slows down the reaction. In earlier studies, Diamanti *et al.* [73][77] showed that H_3PO_4 and H_2SO_4 correspond to the two extreme behaviors. Anodizing is the fastest in phosphoric acid, while the reaction is the slowest in sulphuric acid. Phosphate and fluoroborate-based solutions give the fastest growth rates followed by ammonium-based electrolytes. The presence of sodium largely slows down the process as shown in Figure 46.

c) <u>Influence of the electrolytic solution on the final oxide layer thickness</u>

The kinetics of the reaction is an important parameter but is not the parameter which drives the color of the sample. The sample color is indeed linked to the oxide thickness, so the range of oxide thicknesses obtained during anodizing is more representative of the performance of the electrolyte. If the oxide layer can reach a wide range of thickness values, it may exhibit a wider range of colors. The oxide layer final thicknesses are different even for the same cell potential (100 V) and were evaluated through spectrophotometric measurements (considering an amorphous TiO_2 layer for the refractive index [73]), as shown on Figure 47. Na_2SO_4, $H2SO_4$, NH_4BF_4 and $NaBF_4$ offer the widest range of oxide layer thickness values and might be the most effective electrolytes.
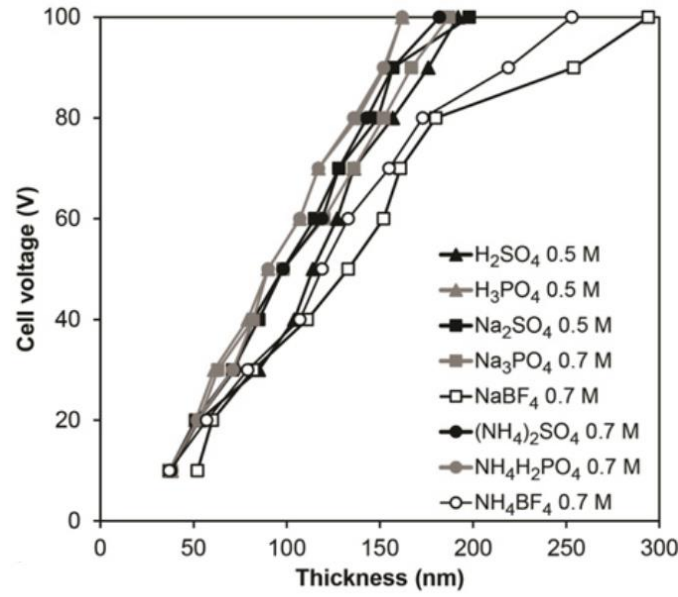
Figure 47 : Oxide layer thickness of ASTM Grade 2 titanium samples anodized at a current density of 20mA/cm² in different electrolytic solutions as a function of the cell potential for different electrolytes (from [68]).

d) <u>Influence of electrolytic solution on the color of the anodized titanium samples</u>

i. <u>Color saturation</u>

The quality of a sample color is evaluated in this study as its chroma (C^* in the CIELCH color space, see Chapter 1 section 1 f)). The chroma of the anodized samples in all the electrolytes is presented in Figure 48. The solutions containing phosphate, H_3PO_4 and $NH_4H_2PO_4$, produce colored samples with a low saturation. The solutions with neutral or slightly alkaline pH offer samples with a higher saturation.
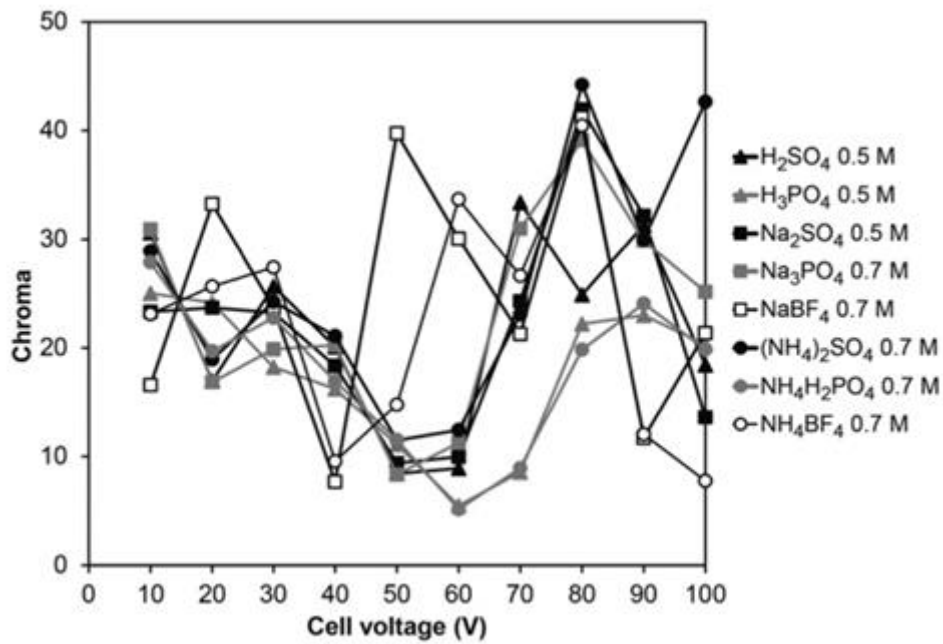
Figure 48: Chroma C* of the anodized samples as a function of the cell potential in different electrolytes (from [68]).

ii. Color reproducibility

Reproducibility tests were done for the solutions which gave the highest color saturations. Fifteen samples were anodized consecutively at a cell potential of 100 V in each solution. Note that the the electrolytic solution was not replaced between each sample, so aging of the solution (i.e. the contamination of the solution by metal dissolution and consumption of the reagent) and possible temperature changes may occur between each sample anodizing. Colors are represented in the CIELAB color space, in the $a^* - b^*$ plane, and the color reproducibility is represented in terms of maximum hue angle difference between the replicates (See Figure 49). The anodizing time was also recorded and its variations are shown of the Figure 49. Despite exhibiting high color saturations, the solutions containing fluoroborate offer a poor reproducibility. It is especially the case for $NaBF_4$ where the hues can differ by 66°, which is a not acceptable in an industrial context. The best reproducibility is obtained with samples anodized in sulphate based solutions, in particular H_2SO_4, which is consistent with the results presented in Chapter 2 part I section 4.b. Unfortunately, this is the highest time consuming process, particularly for cell potentials over 80 V where anodizing reaction is slowed down by the onset of dielectric breakdown (ASD) [70], [78] (see Figure 49). Despite having an anodizing time similar to NH_4BF_4, $(NH_4)_2SO_4$ offers a more limited range of oxide layer thicknesses (and potentially a more limited range of hues) but with decent reproducibility results. NH_4BF_4 presents a good compromise between color hues (high range of oxide layer thicknesses) and saturation with high anodizing kinetics. However, the reproducibility of the sample with the NH_4BF_4 solution still needs to be improved.

Note that in a context where the cost of the solution is not an issue, as for example for producing parts with a high unit value, repeatability tests where the solution is renewed after each experience might lead to a smaller hue difference between the repeated samples.
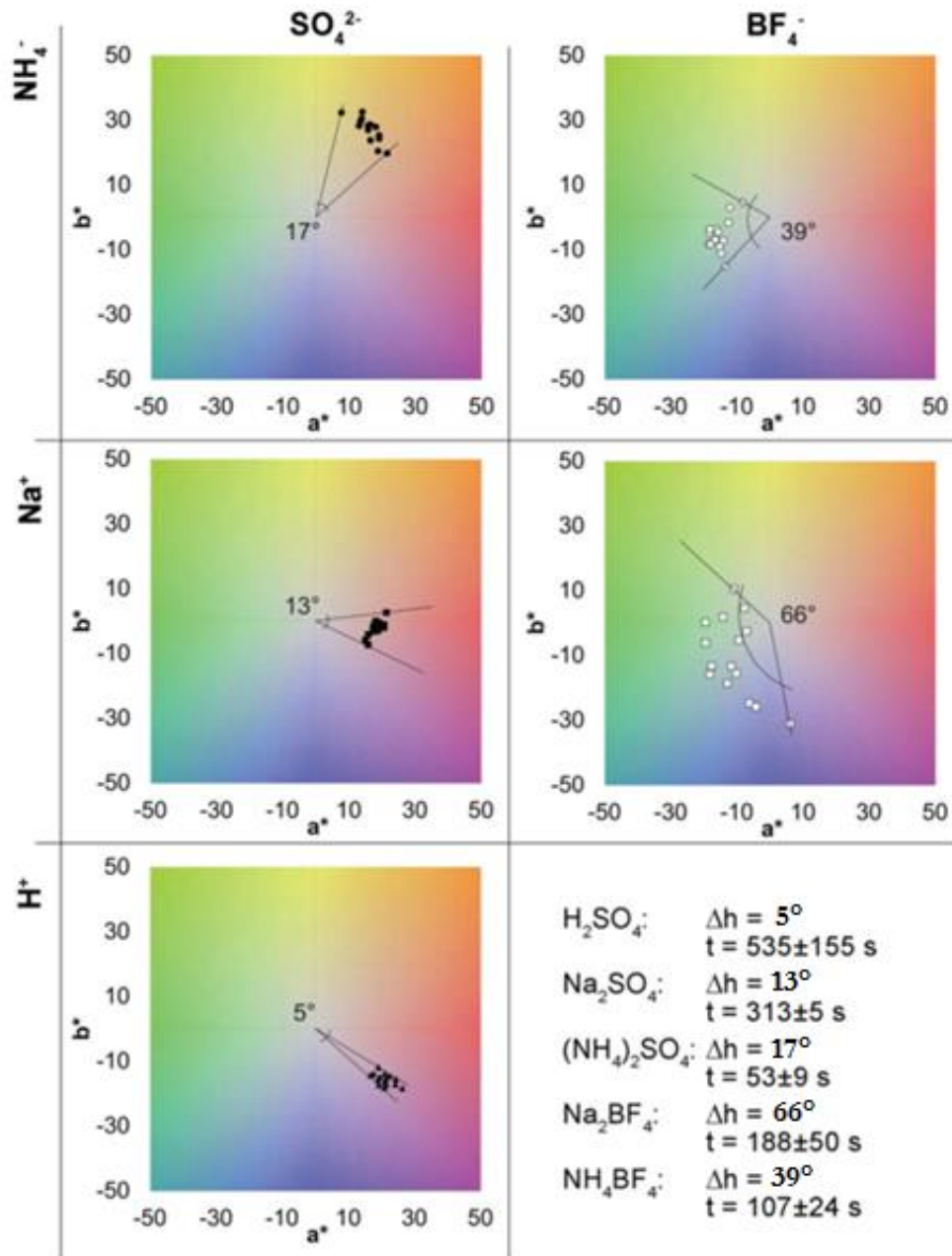
Figure 49: Color coordinates in an a*–b* plane of 15 replicates of ASTM grade 2 titanium samples anodized at 100 V at a current density of 20 mA/cm² in different electrolytes. The angular value reported in the graphs corresponds for each solution to the maximum hue variations between all the samples series. Anodizing times and their standard deviation are also reported on the right of the figure (from [68]).

Further investigations on NH_4BF_4 and $(NH_4)_2SO_4$ solutions were proposed to develop a process that could combine all necessary features: low anodizing time, high repeatability of color hue, high saturation and wide range of achievable hues. Hues and thicknesses of titanium anodized in $(NH_4)SO_4$ are compared with the ones obtained in NH_4BF_4 (see Figure 50). To reach the same final oxide thickness in both electrolytes, the cell potential in $(NH_4)SO_4$ must reached 140 V against 100 V in NH_4BF_4.
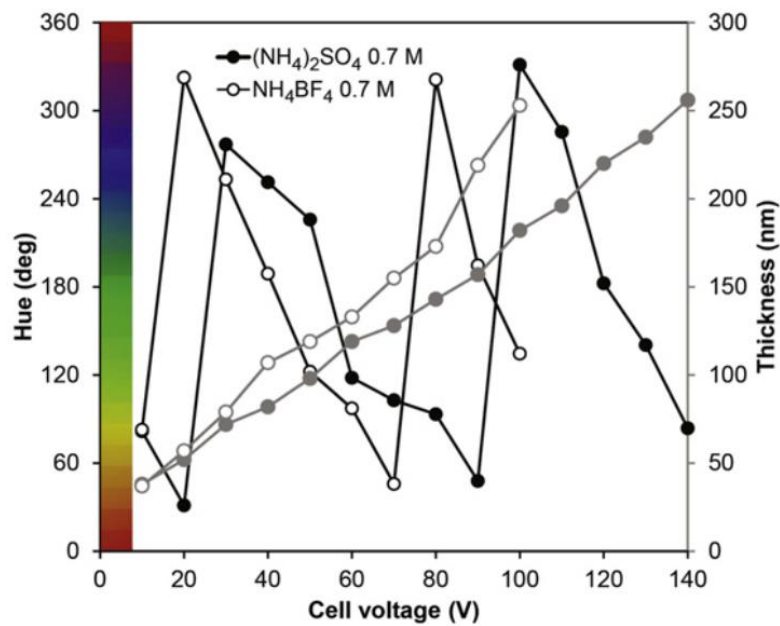
Figure 50: Comparison of the hues and oxide layer thicknesses obtained for anodized ASTM Grade 2 titanium samples for a cell potential up to 140 V and for a current density of 20 mA/cm² in $(NH_4)SO_4$ and NH_4BF_4 solutions. The oxide thicknesses are represented on the grey curves and the sample hues on the black curves. Full circles represent $(NH_4)SO_4$ results and empty circles NH_4BF_4 ones.

On one hand, $(NH_4)_2SO_4$ is suggested when a better reproducibility is required but higher voltages are needed to obtain a wide range of oxide layer thicknesses, which might increase the equipment cost. On the other hand, NH_4BF_4 allows to obtain the same range of oxide layer thicknesses by using lower voltages but with a decrease of color reproducibility.

Both of them might be used for different applications. The first might be used for architectural panels and the second for semi-luxury jewelry.

3) <u>Influence of the substrate crystallographic orientation on the color of anodized titanium samples</u>

Diamanti *et al.* [79] showed the influence of the crystallographic orientation of the titanium substrate on the oxide layer growth during anodizing. ASTM grade 2 titanium samples were mechanically polished first with silicon carbide (SiC) grinding paper and then with a grinding cloth with diamond and alumina slurries. The samples are then etched twice, first in an ammonium peroxide/hydrogen peroxide solution and then in a hydrofluoric acid/nitric acid solution (unknown concentrations). These etching steps were mainly used to dissolve the TiO_2 amorphous layer left on the surface by mechanical polishing. The crystallographic characterization of the titanium substrate was performed by Electron Back Scatter Diffraction (EBSD). Anodizing has been performed in an H_2SO_4 0.5M solution at room temperature at a constant current density of 20mA/cm². Figure 51(a) shows the map of the crystallographic orientation of the titanium substrate with the inverse pole figure color code shown on the Figure 51(b).
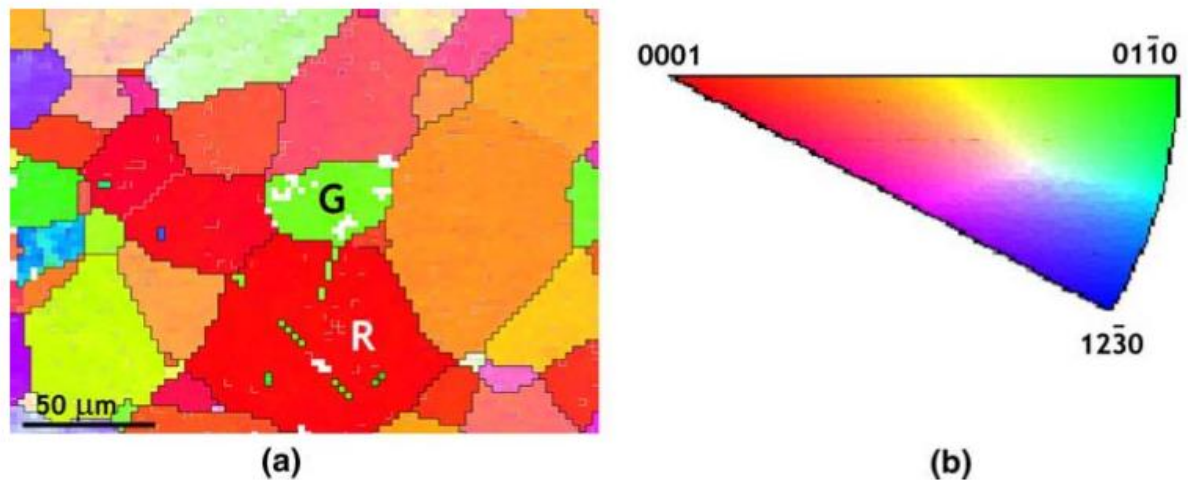
Figure 51: (a) Crystallographic orientation map of ASTM Grade 2 titanium substrate. (b) Inverse pole figure color code (extracted from [79]).

The color of each grain after anodizing was observed under a white light optical microscope (see Figure 52) at normal incidence as the same area as on Figure 51(a). We can observe different colors corresponding to the different crystallographic orientations of the substrate. In order to characterize the oxide thicknesses related to each grain, a calibration relationship associating an oxide color to an oxide layer thickness has been proposed. Diamanti *et al.* prepared samples coming from the same ASTM grade 2 titanium sheet following the European Patent EP 1199385A2 [80]. This procedure allows an oxide growth independent of the substrate crystallographic orientation. The samples were anodized at cell potentials of 11, 14, 16, 18 and 21V (see Figure 53). The oxide thicknesses of these reference samples were measured by spectrophotometry following the method described in [73].
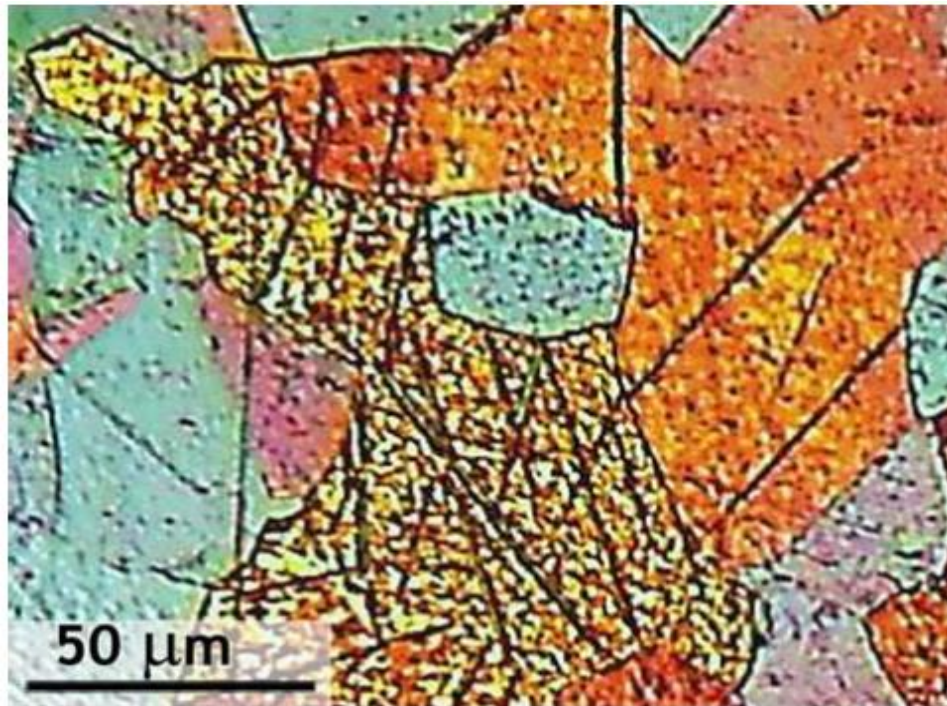
Figure 52: White light optical microscope image of a titanium sample anodized at a cell potential of 21V in 0.5M H_2SO_4 at a current density of 20mA/cm² on the same area as on Figure 51 (a) (from [79]).
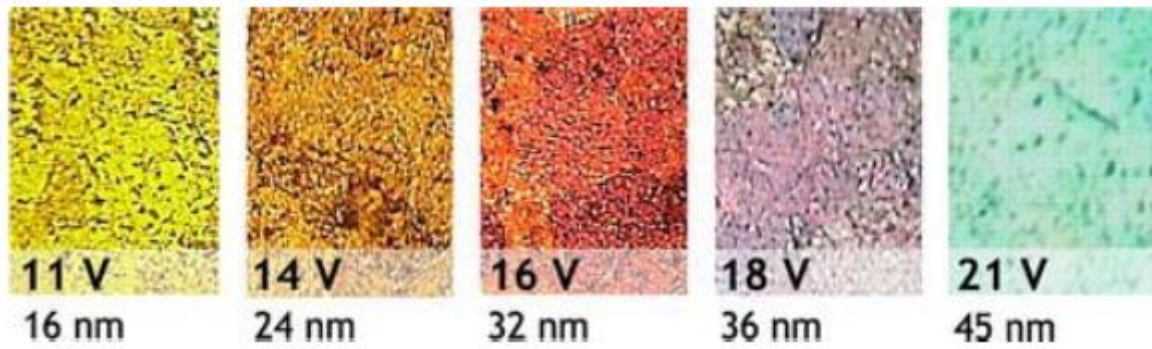
Figure 53: ASTM Grade 2 titanium samples anodized following the procedure described in reference [80] at cell potentials varying from 11V to 21V. The values at the bottom are the oxide layer thicknesses obtained through spectrophotometry and are given with an uncertainty of $\pm$ 2nm (from [79]). Note that no scale are indicated in the reference.

By comparing the colors of the reference samples to the colors reported in the white light optical microscope image, a mapping of the oxide layer thickness of each grain has been performed as shown in Figure 54. The oxide thickness is indeed depending on the crystalline orientation of the grains of the substrate. The grains oriented in the direction $(01\bar{1}0)$ exhibit a thickness value of 45nm (corresponding to the color of an oxide layer obtained with a cell potential of 21V) against a value of 22nm for grains oriented in the (0001) direction. By producing reference colored samples with a strong color homogeneity, Diamanti *et al.* also showed that this influence of the substrate crystallographic orientation on the color of anodized titanium samples can be overcome by a careful surface preparation.
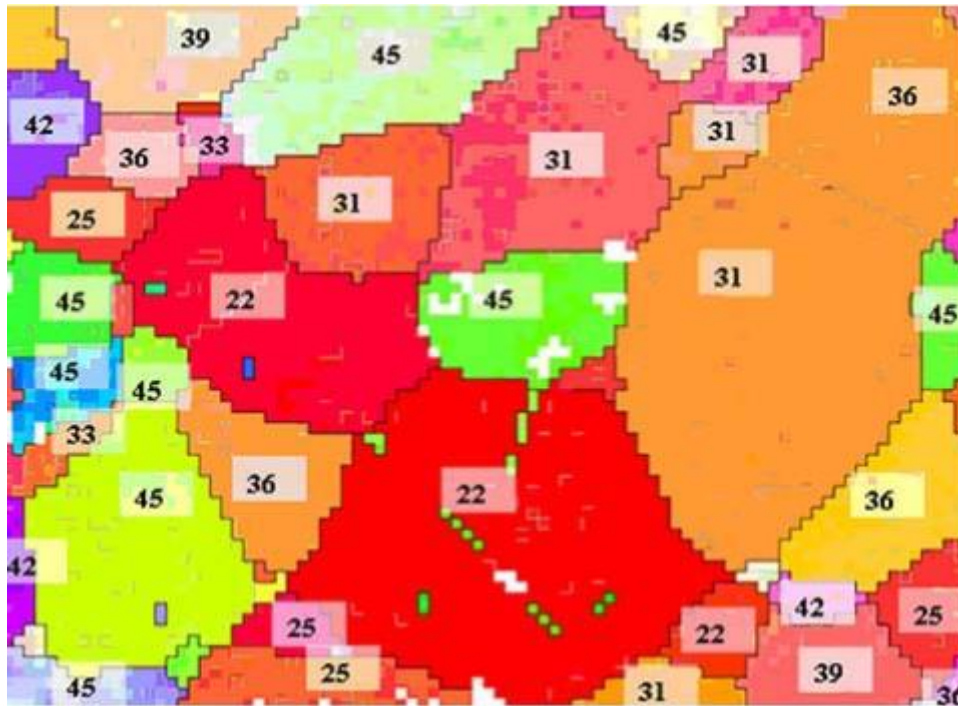
Figure 54: Estimated oxide layer thickness values (in nm) for each grain based on a color comparison to reference anodized samples which oxide layer thicknesses were obtained through spectrophotometry. Those values were superimposed on the crystallographic orientation map (from [79]). The scale is the same as the one presented on Figure 50.

4) <u>Influence of the substrate surface finishing on the color of anodized titanium samples</u>

In a previous study made at Mines Saint-Etienne, Charrière *et al.* [39] observed the influence of the substrate preparation on the color of anodized titanium samples. Series of samples with different surface finishing and different composition were prepared and anodized in a 0.5M H_2SO_4 electrolytic solution with a galvanostatic regime at three different cell potentials: 10 V, 20 V and 90 V. The current density was set to 50 mA/cm². The different series are presented in Table 13. Grade 1 samples will not be discussed in the present document.

Denomination	Material	Sample thickness (mm)	Initial surface finishing	Surface preparation	R_a (µm)
Series 1	Grade 1	2	Smooth	Mirror polishing	0.15
Series 2	Grade 2	1.3	Rough	No preparation	1.9
Series 3	Grade 2	2	Smooth	No preparation	0.33
Series 4	Grade 2	2	Smooth	Mirror polishing	0.15

Table 13: Samples characterization: initial surface finishing and surface preparation, grade of the substrate, sample thickness and roughness (from [39]).

The mirror polished substrate is obtained through a complete mechanical polishing with the use of a 0.25 mm colloidal silica suspension for final polishing. The roughness R_a parameters indicated in [39] were measured with an optical profilometer. The roughness measurement protocol is unknown and the measure is only made after sample anodizing.
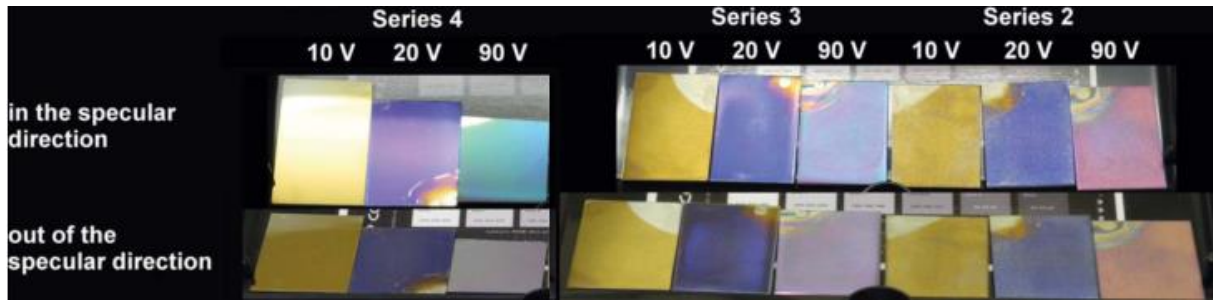
Figure 55: Digital color pictures of the series 2, 3 and 4 (anodized Grade 2 titanium samples). The incidence angle of the illuminant source is 45°. The observation angle is 70° in case of the "out of the specular direction" pictures (from [39]).

Figure 55 presents digital color pictures of different anodized samples series with an incident angle for the illuminant of 45°. The observation angle is either equal to the incidence angle, thus corresponding to the specular case, or different from the incident angle, for the "out of specular direction" geometry. The color of the samples obtained at the same cell potential may vary with the surface finishing. It is indeed the case for the samples anodized at 90 V and observed in the specular direction, the sample with a Ra=1.9 µm exhibits a pink color against a blue color for the sample with a lower Ra (0.33 µm) and a green color when the Ra is further decreased as shown on the Figure 56. The surface finishing, and thus the roughness Ra, seems to play and significant role on the color of the sample.
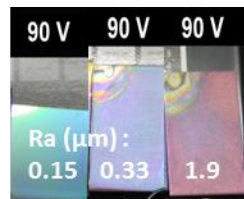
Figure 56: Picture of three ASTM Grade 2 anodized samples with different R_a. These samples were anodized in a 0.5M H_2SO_4 solution with a 50 mA/cm² current density. The three samples exhibit a different color (from [39]).

Diamanti *et al.* [71] also noticed an influence of the surface preparation on the color of anodized Ti6Al4V titanium alloy samples. Three series were prepared with different surface finishing: an "as received" smooth series, a sandblasted series and a pickled series, with respective R_a of 460 nm, 490 nm and 1740 nm. The R_a was estimated from an average of measurements made by optical profilometry on three specimens from each series randomly measured at three different points. The pickled series has been obtained by using an HF/HNO_3 solution (unknown concentration). Note that the sandblasted series has received an additional slight pickling step in HF/HNO_3 in order to clean the surface from the alumina powder used during the sandblasting process. One sample of each series has been anodized in H_3PO_4 0.5M at a cell potential of 60 V for a current density of 40 mA/cm². These samples were measured by spectrophotometry (45°a:0° geometry) and the reflectance spectra are reported on the Figure 57.
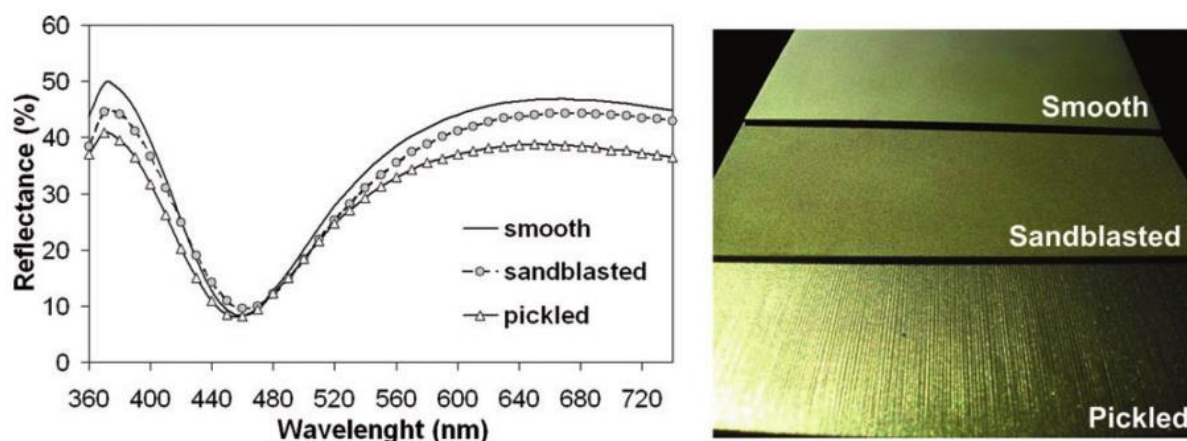
Figure 57: Reflectance spectra and pictures of anodized Ti6Al4V titanium alloy samples in H_3PO_4 0.5M at a cell potential of 60 V for a current density of 40 mA/cm² for a smooth, sandblasted and pickled surface finishing (from [71]).

The reflectance curves exhibited extrema located at the same wavelength regardless of the surface finishing. The saturation of the resulting color, characterized by the peak height (extrema), is the only difference among the three series. The saturation of the resulting color is lower for a rough surface.

5) <u>Influence of the substrate finishing on the gonioappearance of anodized titanium samples</u>

The surface finishing seems also to play a role in the gonioappearance of the anodized samples as shown in [39]. For example, the color of the sample anodized at 90 V from the series 4 changes from cyan in the specular condition to grayish in the out of specular condition. This color change is not as marked for the samples from series 2 and 3 (see Figure 55).

Figure 58 shows the color variations around the specular direction in the CIE xy-chromaticity diagram of the 10 V (series 2 and 3) samples and 90 V (series 2 and 4) samples. The saturation of the color for the mirror-polished surface, evaluated here as the color purity with a D65 white point reference (see Chapter 1, part I, section 1e iii), exhibits higher variations around the specular direction than for non-polished samples. The most saturated color corresponds to the specular direction, which is consistent with the interferential origin of the colors.
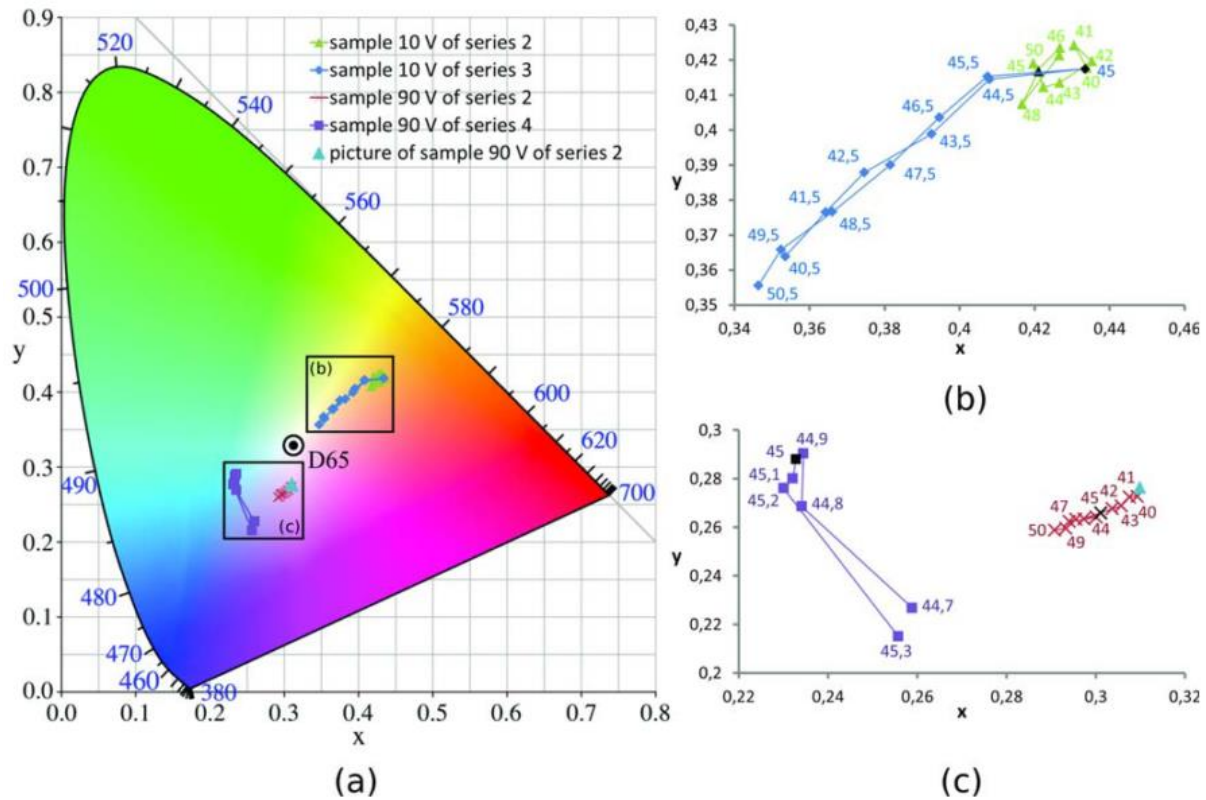
Figure 58: (a) Evolution around the specular direction in the CIE xy-chromaticity diagram of the colors of the samples anodized at 10 V of series 2 and 3 and the samples anodized at 90 V of series 2 and 4. The incidence angle is equal to 45° and the illuminant is D65, represented as a circled black dot. The figures (b) and (c) correspond to a magnification of the chromatic paths of the samples anodized at 10 V (b) and 90 V (c). The observation direction (in degrees) is indicated in the graphs. The blue triangle on the subfigures (a) and (c) corresponds to the (x, y) chromaticity coordinates of the 90 V sample of series 2 deduced from a calibrated digital picture of the sample in the specular direction and for an incidence angle of 45°. The black points on subfigures (b) and (c) indicate the specular direction (from [39]).

For the two samples anodized at 10 V, their variations in the chromaticity diagram are almost along a straight line passing through the D65 point. The hue is thus invariant for all the observation angles, meaning that these samples aren't gonioapparent. However, this variation of hue with the angle of observation is significant in the case of the sample anodized at 90 V from the series 4. The 90 V anodized sample from series 2 exhibits a smaller hue variation. This result is consistent with the qualitative observations of the gonioappearance of these samples presented in Figure 55.

III. Discussion and conclusion

As we showed previously in this chapter, anodic oxidation is the best suited technique to obtain a calibration color chart for metallic gonioapparent samples. We presented the anodizing parameters, such as current density, electrolytic solution type and concentration, influencing the characteristics of the oxide layer of anodized titanium samples. We also showed that the substrate roughness has an influence on the color of the oxide layer and on its gonioappearance.

For our purposes, anodizing time is not a key parameter but the color reproducibility is important to obtain standard samples that could be used as a metallic color chart. H_2SO_4 has been selected because it exhibits the highest color reproducibility and a wide range of colors (even if it is not the solution which produces the widest range of oxide layer thicknesses). To optimize the oxide growth rate, the concentration has been fixed to 0.5M. Depending on the cell potential, the oxide

layer of samples anodized in H_2SO_4 is either amorphous or partially crystalline (an anatase phase is observed for cell potentials over 70 V and a rutile one is observed for cell potentials over 130 V).

To be able to calibrate samples with different levels of gloss, a calibration color chart should exhibit samples with different roughness levels. The previous literature review revealed that the substrate roughness influences the color of the samples after anodizing and could also affect their gonioappearance. However, this influence has not been much studied yet.

In order to confirm these observations, further studies are needed. We thus prepared anodized titanium samples with different controlled levels of roughness: first by performing an HF/HNO_3 etching (a commonly used surface finishing process) and secondly by using different levels of mechanical polishing. The mechanical polishing process allowed us to obtain a very good control of the substrate roughness.

Chapter 3: Anodizing of HF/HNO₃ etched titanium: characterization of the diffuse aspect, colors of the samples and optical models to determine the oxide thickness sample.

I. General description of the anodizing experimental setup

Samples were anodized both in the Chimica, Materiali e Ingegneria Chimica "Giulio Natta" Laboratory (CMIC, Milan, Italy) and in the Georges Friedel laboratory (GFL, Saint-Etienne, France) with two similar protocols. The samples were anodized in a galvanostatic regime, i.e.: the provided current is constant, at different cell potentials. Figure 59 shows the typical potential variation observed during our anodizing process. The maximum potential reached while anodizing is called "cell potential". The experimental setup used at GFL is shown in Figure 60. A "Micronics systems Microlab type MX200-100" generator supplies a constant current that can reach a potential up to 200 V. A cathode made of titanium coated with a small layer of iridium is used to avoid the dissolution of the counter electrode during the anodizing process. The iridium oxide layer is indeed perfectly stable in the electrolyte and decreases drastically the dissolution rate of the electrode.
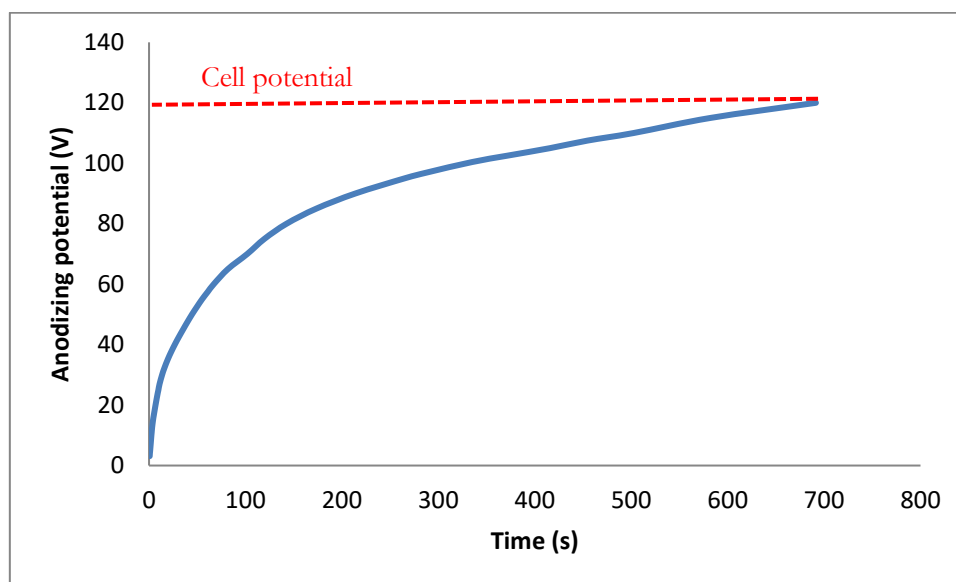
Figure 59: Anodizing potential vs time curve of a rough titanium sample anodized in an 0.5M H_2SO_4 solution at a cell potential of 120 V.

The experimental setup used at GFL is the following. The counter electrode is circular and made of activated titanium, as shown in Figure 61. On the picture, we can see a beaker containing the electrolytic solution, the counter electrode (in black) and the sample to anodize (in the center). On the right, the generator (Aim TTi PLH120 DC) provides the current needed to perform the anodizing and a recorder monitors the values of the cell potential during the anodizing process.
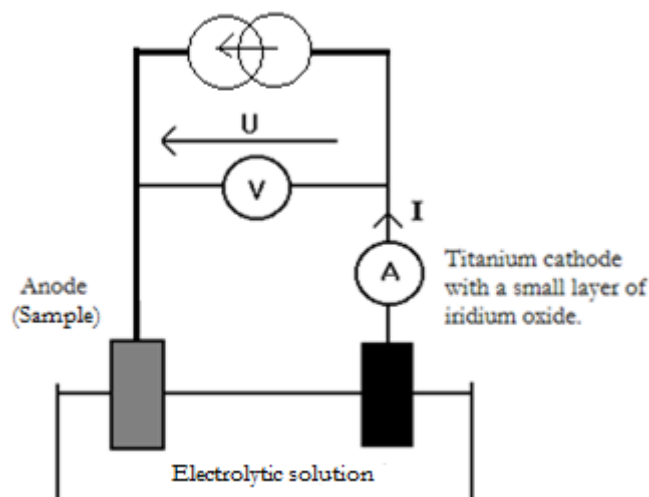
Figure 60: Anodizing setup with a current generator, an iridium coated titanium cathode, an electrolytic solution and the sample at the anode.

When the cell potential is higher than 120 V, electric sparks tend to develop and damage the oxide layer by making craters. In these craters, the conditions of pressure and temperature lead to a more complex oxide layer composed of multiple crystalline phases, anatase and rutile. These craters also prevent the oxide surface, and thus the sample color, to be homogeneous. The cell potential will be thus maintained in the range of 5 V-120 V. The current density will be set at 20 mA/cm² unless stated otherwise. The samples have been anodized in a 0.5M H_2SO_4 electrolytic solution, which corresponds to the highest oxide growth rate in a sulphuric acid solution [70] (see chapter 2 section II).
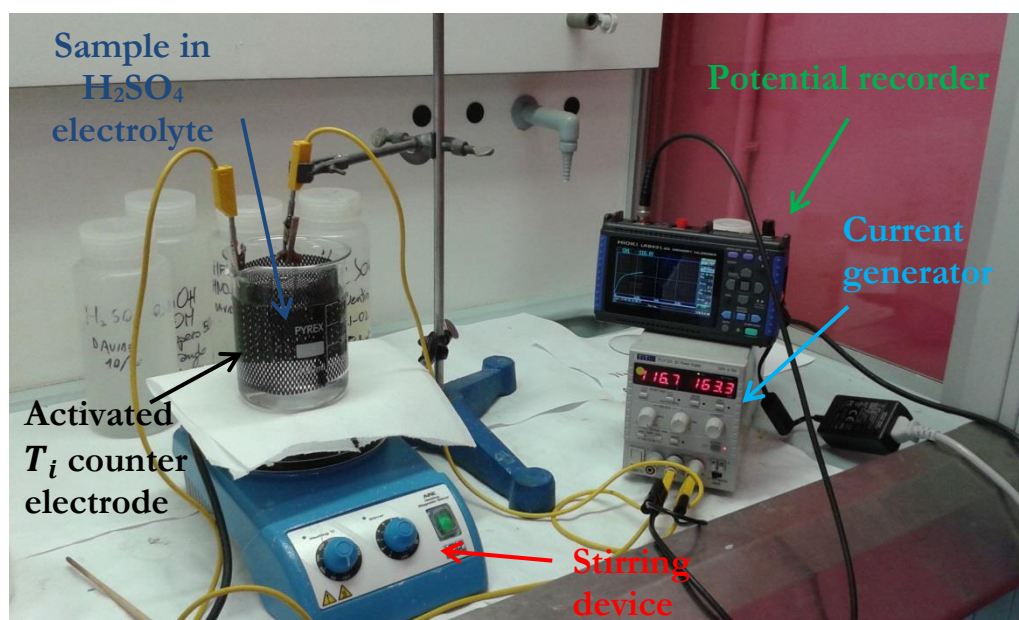
Figure 61 : Picture of the experimental setup used at the CMIC Laboratory composed of: a beaker containing a magnetic stirrer, the electrolytic solution, the activated titanium counter-electrode and the sample, a current generator and a potential recorder.

When the potential reaches the desired value, the current is shut down and the sample is removed from the bath, cleaned in an acetone solution in an ultrasound bath for two minutes, then cleaned

two more minutes in distilled water in the ultrasonic bath, and is finally dried out with dry air.

The base material is ASTM Grade 2 titanium which was cut into small pieces (4 to 9 cm²). The composition of the base material is given in Table 14.

Component	Wt. %
C	Max 0.1
Fe	Max 0.3
H	Max 0.015
N	Max 0,03
O	Max 0.25
Ti	Balance

Table 14 : ASTM Grade 2 titanium composition in weight %

Samples with different roughnesses were prepared. In this chapter, the substrate roughness and thus the anodized samples roughness, is changed by HF/HNO_3 etching. In the next chapter, samples with roughnesses obtained through different mechanical and chemical polishing levels will be studied. We will now describe how the HF/HNO_3 etched samples are prepared and discuss the influence of the etching on the roughness, oxide thickness and color of the anodized samples is discussed as well as its influence on the microstructure and the surface composition.

II. Samples preparation and description
1) Sample preparation

Two series of samples were prepared in GFL. All the samples were mechanically polished, first with silicon carbide grinding papers from P300 to P2400, and then using a vibratory polisher and 0.25 μm colloidal silica suspensions. One series has been etched in an HF/HNO_3 solution (4% and 26% respectively in volume %) for 30 seconds in order to perform a roughness modification. The samples are first cleaned in acetone and then in water in an ultrasonic bath for 2 min each. Note that HF/HNO_3 etching is a commonly used process to clean the surface from any natural oxide layer [77], from any pollutants[81], and also to change its roughness [82].
Some samples were anodized in a 0.5M H_2SO_4 electrolytic solution in a galvanostatic regime at two different cell potentials: 10 V and 90 V. The current density was set at 40 mA/cm². The other samples were not anodized. The non-etched samples are designated with the name "Ref" and the etched ones with the name "Etc".

2) Roughness measurements protocol

Roughness measurements have been carried out by a non-contact white light interferometric optical profilometer, Bruker Nanoscope Wyko ® NT9100. The size of the measured area is 0.86mm x 1.15mm (representing 480x640 points) with a spacing resolution of 1.8 μm in both in-plane directions and a vertical resolution of 3 nm. For each sample, three measurements have been made at random positions on the surface of the sample and the given roughness parameters R_a are an average of these 3 measurements. It is important to note that the R_a values are taken after anodizing for the anodized samples.
The R_a parameter is the arithmetic average on the observed area of the absolute values of the difference between the height of a point and the average height of the surface. The material is considered isotropic so the R_a (1-dimension parameter) and the S_a (2-dimensions parameter) can be considered equal in this case. Other roughness parameters were also collected but not discussed in the present document. The R_a parameter is given by the following equation (38):

$$R_a = \frac{1}{S} \int_S |Z(x,y)| dxdy \qquad (37)$$

where S is the measured surface area and $Z(x,y)$ is the difference between the elevation of the surface at the position (x,y) and the average surface elevation. The optical profilometer roughness measurements were confirmed by Atomic Force Microscopy (AFM). Figure 62 shows the surface profile of a sample anodized at a cell potential of 10 V and measured by both techniques.
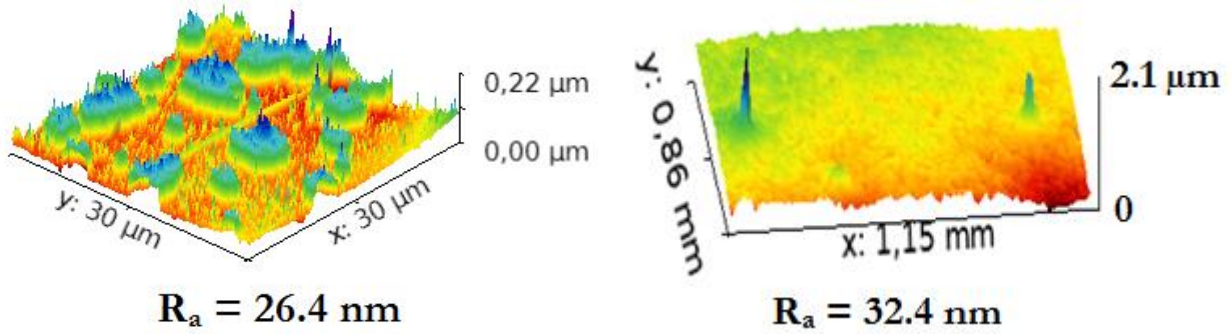
Figure 62: Roughness R_a measurements made by AFM (on the left) and optical profilometry (on the right). The value of the R_a measured by AFM is 26.4 nm and 32.4 nm by optical profilometry.

We observe comparable values for the R_a parameters given by AFM and optical profilometry. Note that the AFM and the profilometer measurements were not made on the exact same position on the sample. The AFM measured surface is also smaller than the surface measured by optical profilometry (30μm × 30μm for the AFM instead of 0.86 mm × 1.15 mm for the profilometer).

3) Visual observations of the samples

Figure 63 shows a picture of the two series of samples as well as the R_a parameter values; the picture has been taken in a light booth with a D65 illuminant. The pictures were taken with a Nikon Coolpix P7000 and the white balance was set to automatic mode. As expected, the etching process results in a modification of the surface roughness. In fact, the roughness R_a of the reference non-anodized samples is increased from 20 nm to 80 nm, corresponding to an increase of 300%. The etched sample is also less bright (matte gray color). On one hand, for the sample anodized at 10 V, the color of the etched sample is less bright and the color hue is a bit changed, from faded goldish yellow to gold with a higher saturation. In addition, the effect of the anodizing reaction on the R_a value is different for the two surface finishing, an increase of 50% in the case of the non-treated sample against more than 100% in the case of the etched sample. On the other hand, for the sample anodized at 90 V, the color of the etched sample is different from the color of the non-etched sample. The color is changed from faded purple to yellow-green. In addition, the effect of the anodizing reaction on the sample roughness R_a value is different for the two surface finishing, an increase of more than 400% in the case of the non-etched sample instead of 125% in the case of the etched sample. Note that the non-colored areas on the anodized samples (upper right or left corners) are due to the clamp used to hold the sample in the electrolytic solution. The samples are not anodized in this area.
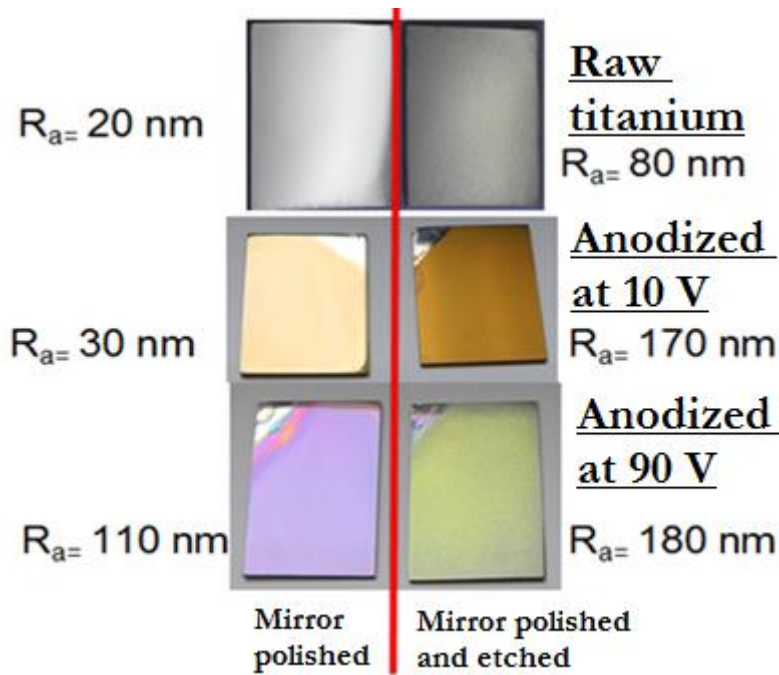
Figure 63: Picture of raw and anodized ASTM Grade 2 titanium samples under a diffuse D65 illuminant. All the samples were mirror polished before any treatment. The samples on the right side were etched in HF/HNO₃ solution (4%-26% in volume) prior anodizing. All the anodized samples were anodized in an 0.5 M H₂SO₄ electrolytic solution at a current density of 40 mA/cm² for two different cell potentials (10 V and 90 V). The pictures were taken with a Nikon Coolpix P7000 and the white balance was set to automatic mode.

In the following section, the influence of the etching on titanium samples is presented through a literature review and the analysis of the etched samples presented in section II 1).

III. Influence of HF/HNO3 etching on titanium samples.

1) State of the art

Several studies showed different effects of the etching on the microstructure of the samples but also on the chemical composition of the sample.

Diamanti *et al.* [77] showed that the HF/HNO₃ etching (diluted solution with an unknown concentration) helps to obtain larger oxide thicknesses during anodizing of ASTM Grade 2 titanium samples in an 0.5M H₂SO₄ solution as shown in Figure 64. This is in accordance with our observations (see section III 2). They also reported that etching promotes higher oxide color homogeneity when observed visually.
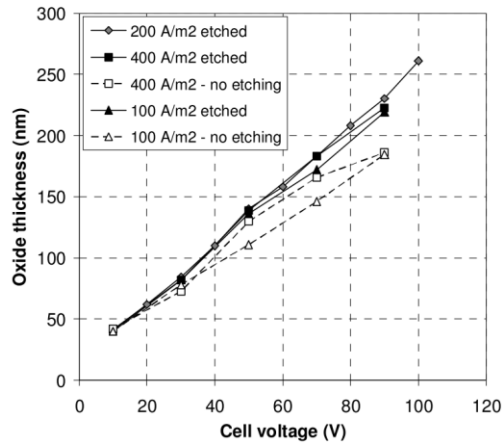
Figure 64: Influence of the HF/HNO₃ etching on the oxide thickness of ASTM Grade 2 titanium anodized in 0.5M H_2SO_4 with different current densities (from [77]).

Guo *et al.* [83] showed a composition change of the surface of samples prepared by TiO_2 grit blasting using 75 μm TiO_2 particles and etched afterwards in hydrofluoric acid (unknown solution composition and unknown etching time). The composition of the etched and non-etched series was analyzed by X-ray Photoelectron Spectroscopy (XPS) and is presented in Table 15. 0.8% of fluoride atoms were found on the samples that were etched.

Surface	C	N	O	F	Ti
TiO_2	23.92±4.0	0.27±0.3	52.75±2.14	–	22.73±1.59
TiO_2/HF	21.7±0.26	0.4±0.07	53.7±0.45	0.8±0.17	23.6±0.24

Table 15: XPS analysis in atomic percent of TiO_2 grit blasted samples prepared with or without HF etching (from [83]).

They also reported a change of the microstructure of the etched samples through Scanning Electron Microscopy (SEM) as shown in Figure 65. The microstructure evolved from a micro-structuration to a nano-structuration after etching.
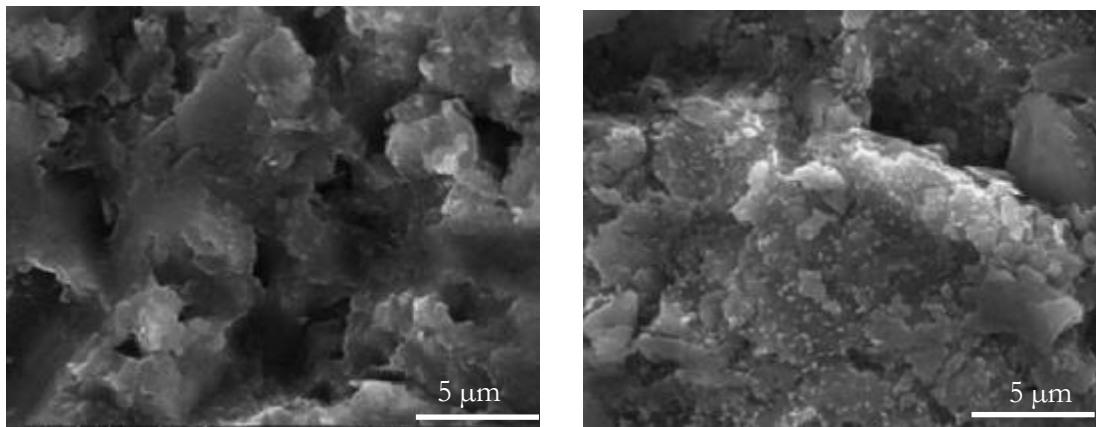
Figure 65: SEM images (JEOL SEM JEM 6300) with a x5000 magnification of the reference implant sample (on the left) and of the etched sample (on the right) (from [83]).

Lamolle *et al.* [84] also confirmed the presence of fluorine after etching (0.2% HF in volume) of CP titanium (unknown grade) disks for different etching times. The chemical composition has been investigated through XPS (with a Quantum 2000 scanning XPS Microprobe from Physical Electronics). The fluorine concentration was found the highest for an etching time of 90 sec (see Table 16).

Elements	Control	40 s	90 s	120 s	150 s
Ti	23.2	25.1	25.7	25.5	25.9
O	53.2	54.1	54.4	54.9	57.2
C	21.4	19.3	17.2	17.6	15.6
F	–	0.5	1.9	1.1	0.9

Table 16: XPS measured elemental composition in atomic percent of the surface of CP titanium disks for different HF etching times. Control corresponds to the reference sample that isn't etched (from [84]).

Lamolle *et al.* also investigated possible bonding states of each element for the first 5 nm of the surface layer, by the same technique, showing that the fluorine was mainly found in the form of fluorine (not forming any bonds with titanium, oxygen or carbon). The surface topography of all the sample series was investigated by three techniques, with blue light interferometry (Sensofar Plm 2300 from Terrassa) with a scanned surface of 255×191 μm², by SEM (Philips XL 30 ESEM, FEI Electron Optics) with a maximum magnification of x100000 and by AFM (MFP-3D Asylum research) with a scan size of 1×1 μm². These results are presented in Figure 66. Etching time was proven to have a great influence on the structure of titanium disks for etching times above 90 seconds. A longer exposure time corresponds to a higher modification of the surface nanostructure as shown by the AFM images. The SEM images also show the restructuration of the surface by the dissolution of the metallic layer and the formation of bigger structures.

Lamolle *et al.* also measured, by Secondary Ion Mass Spectroscopy (SIMS), the penetration of the O, F and H elements in the metallic layer as a function of etching time. The longer the etching time, the deeper goes the fluorine, as shown in Figure 67. The hydride (H+) was able to penetrate deeper in the surface structure than the fluoride (F-) and the oxide (O^{2-}).
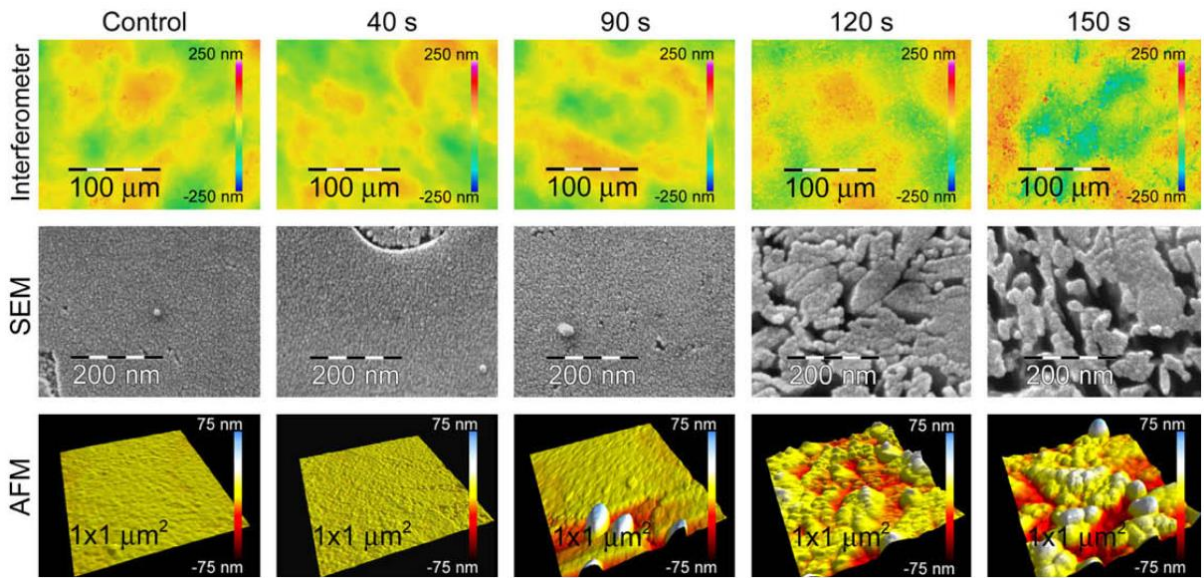
Figure 66: Blue light interferometry, SEM and AFM imaging of etched CP titanium samples in 0.2% vol HF solution for etching times varying from 0 to 150 seconds (from [84]).
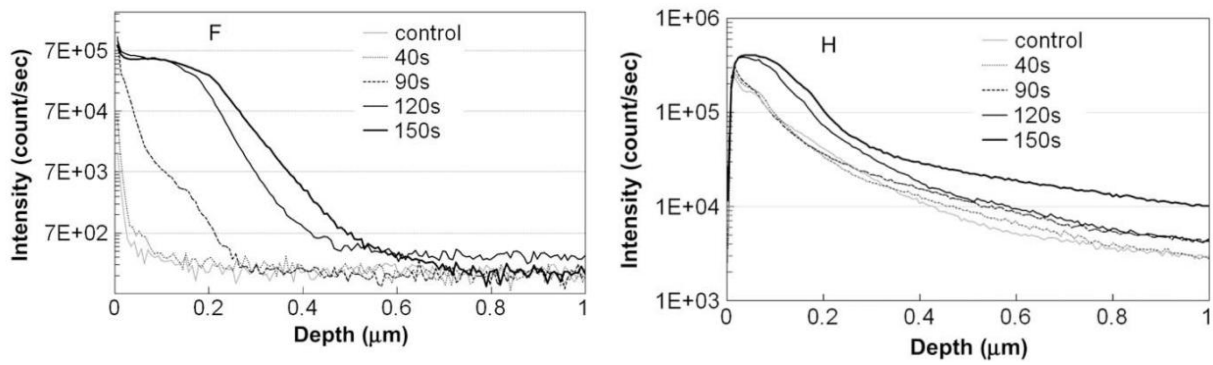
Figure 67: SIMS depth profile of fluoride (on the left) and hydride (on the right) in the titanium disk surface for different etching times (extracted from [84]).

Takashi *et al.* studied the influence of an HF/HNO₃ etching step on the gloss of JIS Grade 1 titanium samples. The different initial surface conditions are reported in Table 17.

	Glossiness Gs45 (%)	Surface roughness R_a (µm)	Grain Size Number (GSN)
(a) Low glossiness and coarse grain size	44	2.51	6
(b) High glossiness and coarse grain size	70	1.96	6
(c) Low glossiness and fine grain size	50	2.45	9.5
(d) High glossiness and fine grain size	87	1.58	9.5

Table 17: Glossiness Gs45, surface roughness R_a and Grain Size Number of four types of titanium sheets: (a) Low glossiness and coarse grain size, (b) High glossiness and coarse grain size, (c) Low glossiness and fine grain size and (d) High glossiness and fine.

The sample grain size is controlled by an annealing process with different time and temperature and the surface glossiness and roughness are adjusted by light cold rolling with dull rolls. Note that the higher the grain size, the lower the Grain Size Number. The glossiness Gs45 was measured with a Nippon Denshoku Model VG-1D digital variable angle glossmeter. The glossiness Gs45 corresponds to the reflectivity with incidence and observation angles both equal to 45°. The etching solution is composed of 20 g/L of HF and 20 to 100 g/L of HNO₃.

First, Takashi *et al.* showed [85] that the initial grain size influences the gloss after etching (see Figure 68). On the one hand, when the initial grain size is coarse, the gloss after etching is almost the same as before etching; it can be explained by the fact that the irregularities formed on the grains during etching have the same size as the initial surface irregularities (due to the initial roughness). On the other hand, when the initial grain size is fine, the irregularities formed during etching are finer than the initial surface irregularities and thus govern the gloss of etched titanium by scattering the visible light rays. The etching process thus modified in this case the glossiness of the samples.

Figure 68 shows also that the glossiness Gs45 after etching is higher when the HNO₃ concentration is high (100g/L) and lower when the HNO₃ concentration is lower (20g/L). Takashi *et al.* also showed [86] that the etching time is an important parameter; the grains appear more uneven when the etching time is longer.

71
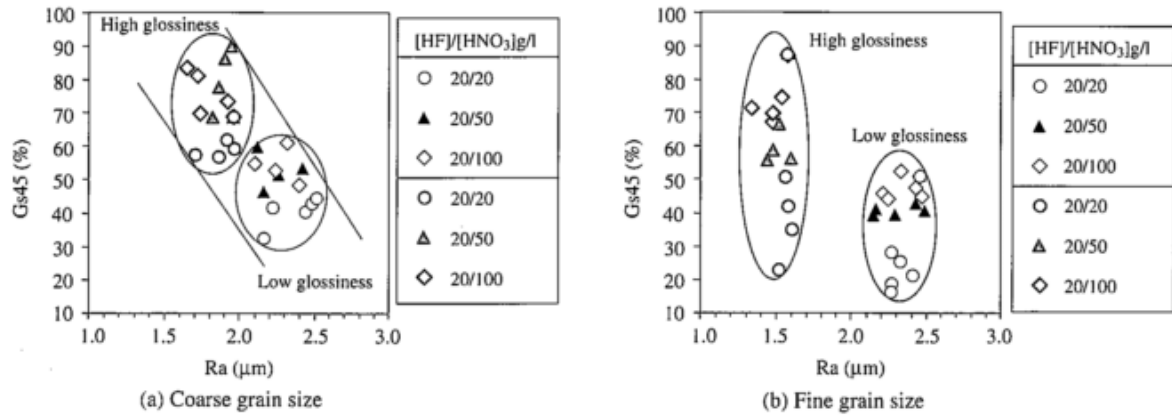
Figure 68 : Relationship between surface roughness R_a and glossiness Gs45 of titanium sheets after etching in nitric-hydrofluoric acid solutions of different compositions.

2) Study of the influence of HF/HNO₃ etching on the microstructure and the chemical composition of the titanium substrate

The non-anodized etched sample presented in Chapter 3 section II 1) has been investigated through different technics in order to confirm the information obtained in the state of the art section.

a) Microstructure analysis

The two non-anodized samples were observed through a Scanning Electron Microscope (Zeiss Supra 55VP equipped with a FEG Gemini column) in order to investigate the surface after etching. The results are presented in Figure 69.
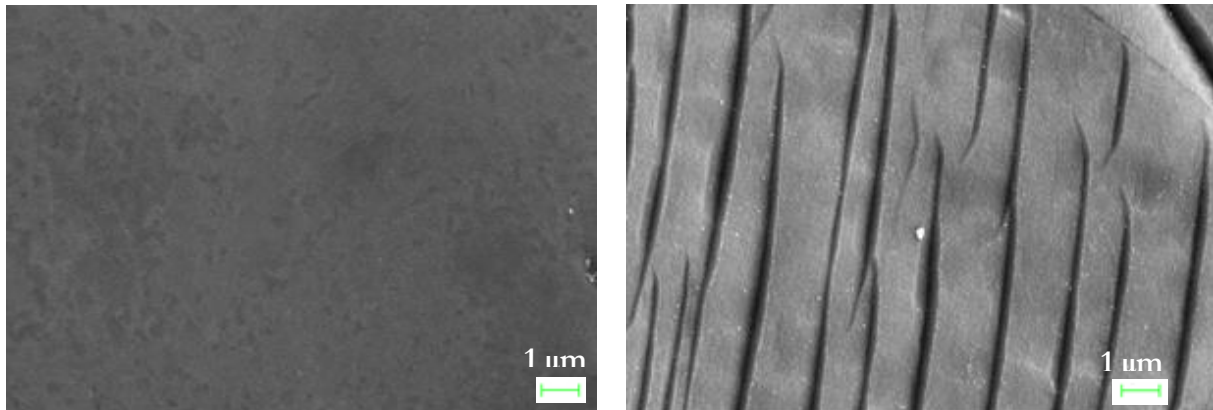
Figure 69: SEM images obtained with a 20K magnification. On the left is presented the mirror polished Grade 2 titanium sample. On the right is presented the surface of the etched sample for 30s in HF/HNO₃ (4%-26% in volume) solution.

The microstructure is visible on the image of the etched sample and some particles (white dots) are visible on the surface. The titanium has been dissolved during etching revealing the lamellar α phase as shown on the SEM image in Figure 70. This is consistent with the [85][86], where irregularities were reported to appear on an individual grain basis. Other SEM images are presented for different magnifications in Appendix D.
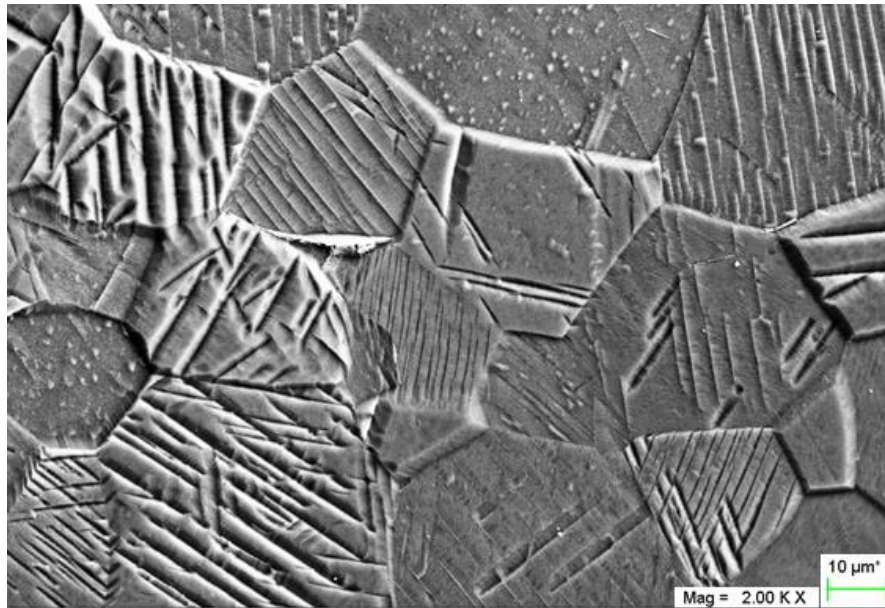
Figure 70: : SEM images obtained with a 2K magnification of the surface of the etched sample for 30s in HF/HNO₃ (4%-26% in volume) solution. The lamellar α phase is revealed after etching.

In Figure 71 is presented a picture of a sample dried in air after etching. The particle density is higher than for the etched sample presented in Figure 69. This sample is only used to illustrate the presence of particles in more severe conditions. We remind that the etched samples presented in section II 1) were cleaned in acetone and water after etching.
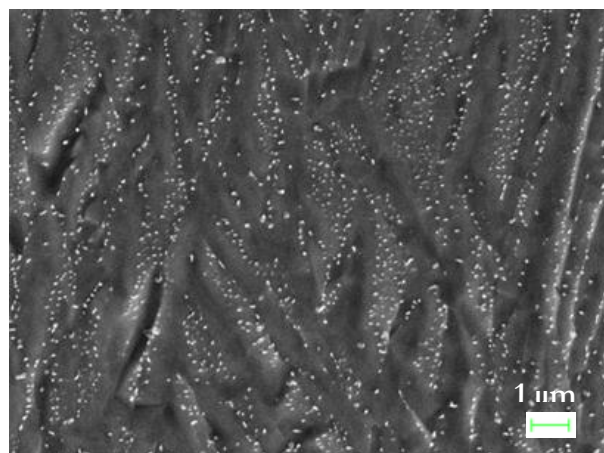
Figure 71: SEM image obtained with a 20K magnification of the surface of a mirror polished sample after a 30 sec etching in HF/HNO₃ solution (4wt%-26wt%) and dried in air directly after etching.

b) Chemical composition analysis

The surface composition has been studied by Energy-Dispersive X-ray spectroscopy (EDX) with an EDX Oxford XMAX^N 80 nm² detector on the non-anodized etched sample. The results are presented in Table 18. On the EDX spectrum the fluorine peak is very close and partially covered by the titanium peak. Also the fluorine peak height is in the order of magnitude of the measurement noise. So the measured concentration of fluorine is not well defined. The low value in atomic % of fluorine could also be explained by the use of a solution with a lower concentration of HF and by a smaller etching time when compared to the literature. Moreover,

the EDX technique is more adapted to measure the chemical composition of layers thicker than 50 nm than for extreme surface measurements.

Element	Element concentration	at.%	wt.%
O	3.38	1.09%	3.19
F	0.90	0.15%	0.37
Ti	513.85	98.76%	96.44

Table 18: EDX elemental composition of the surface of the non-anodized titanium sample etched for 30 sec in HF/HNO₃ (4%-26% in volume) solution.

In order to confirm EDX observations, the non-anodized etched sample was measured by using XPS. XPS is much more adapted to measure the extreme surface because its measurement depth is about 5nm to 10 nm. The results are given in Table 19 without prior ionic abrasion, which explains the presence of carbon on the surface. Because of this measurement depth of a few nanometers, we are mainly measuring the passive oxide layer naturally formed on the titanium substrate. It explains the observation of an atomic composition of nearly $\frac{1}{3}$ of titanium atoms for $\frac{2}{3}$ of oxygens atoms. Fluorine is also detected on the sample surface with 2at.%.

Element	%Atomic
C1s	9,79
F1s	2,1
O1s	61,85
Ti2p	26,27

Table 19: XPS elemental composition of the surface of the non-anodized titanium sample etched for 30 sec in an HF/HNO₃ (4%-26% in volume) solution.

We obtain a larger fluorine atomic percentage with XPS than EDX, attesting for the presence of fluorine mainly on the surface rather than in the sample bulk.

After presenting the samples series and the effect of the HF/HNO₃ etching on the titanium surface of our samples, the characterizations of the optical properties of these samples will be presented in the following section.

IV. Bidirectional Reflectance Distribution Function (BRDF) measurements of the different samples with the goniospectrophotometer Optimines: analysis of the spectral variations

To obtain an optical characterization of the samples, their BRDF were measured by using the goniospectrophotometer Optimines (presented in the Chapter I section 3). Note that all the BRDF measurements are made in the incidence plane. We will first analyze the spectral variations of the BRDF. The angular variations of the BRDF will be presented later.

1) General observations of the spectral BRDF and first oxide layer thickness estimations

Figure 72 shows the spectra representing the BRDF as a function of the wavelength (visible range) in the specular direction for a fixed incidence angle $\theta_i = 45°$ relative to the normal of the sample surface. The measurements were made more than once but only one spectrum for each case is presented on the Figure 72 because the repeatability error is on the same scale of the line width. The spectra exhibit different shapes due to the different colors of the samples. We also observe that the BRDF values of the etched samples are reduced when compared to the non-etched samples. The BRDF is divided by more than four in the case of the non-anodized titanium reference samples. It is more pronounced when the samples are anodized, the BRDF is reduced by more than two orders of magnitude for the etched samples. It is in accordance with the matte appearance of the etched samples and the glossy appearance of the non-etched ones. The graphs (c), (e) and (f) of Figure 72 exhibit local extrema from which can be deduced an oxide layer thickness. According to equation (11) with a $+\pi$ phase shift we have for a maximum:

$$2n_{TiO_2}(\lambda)e \times cos\,\theta_r(\lambda) = \left(k - \frac{1}{2}\right) \lambda \text{ with } k \in \text{ N} \tag{38}$$

where $n_{TiO_2}(\lambda)$ denotes the refractive index of the TiO$_2$ oxide layer at the wavelength λ and e the oxide layer thickness. The refractive index is taken from [72]. From the Snell-Descartes law, we can deduce:

$$\theta_r(\lambda) = \arcsin\left(\frac{\sin(\theta_i)}{n_{TiO_2}(\lambda)}\right)$$

The formula for a minimum is:

$$2n_{TiO_2}(\lambda)e \times cos\,\theta_r(\lambda) = k\lambda \text{ with } k \in \mathbb{N} \tag{39}$$

Note that these formulas have been used in the literature to evaluate the oxide thickness of anodized titanium samples [73] [87] and other anodized materials [69]. In this section, θ_i corresponds to the incidence angle and θ_r to the refracted angle.

It is also interesting to note that a "reading error" is also made when determining the wavelength position of an extremum. This reading error is mostly inferior to 2 nm and has a negligible impact on the final thickness value, indeed lower than 1 nm.
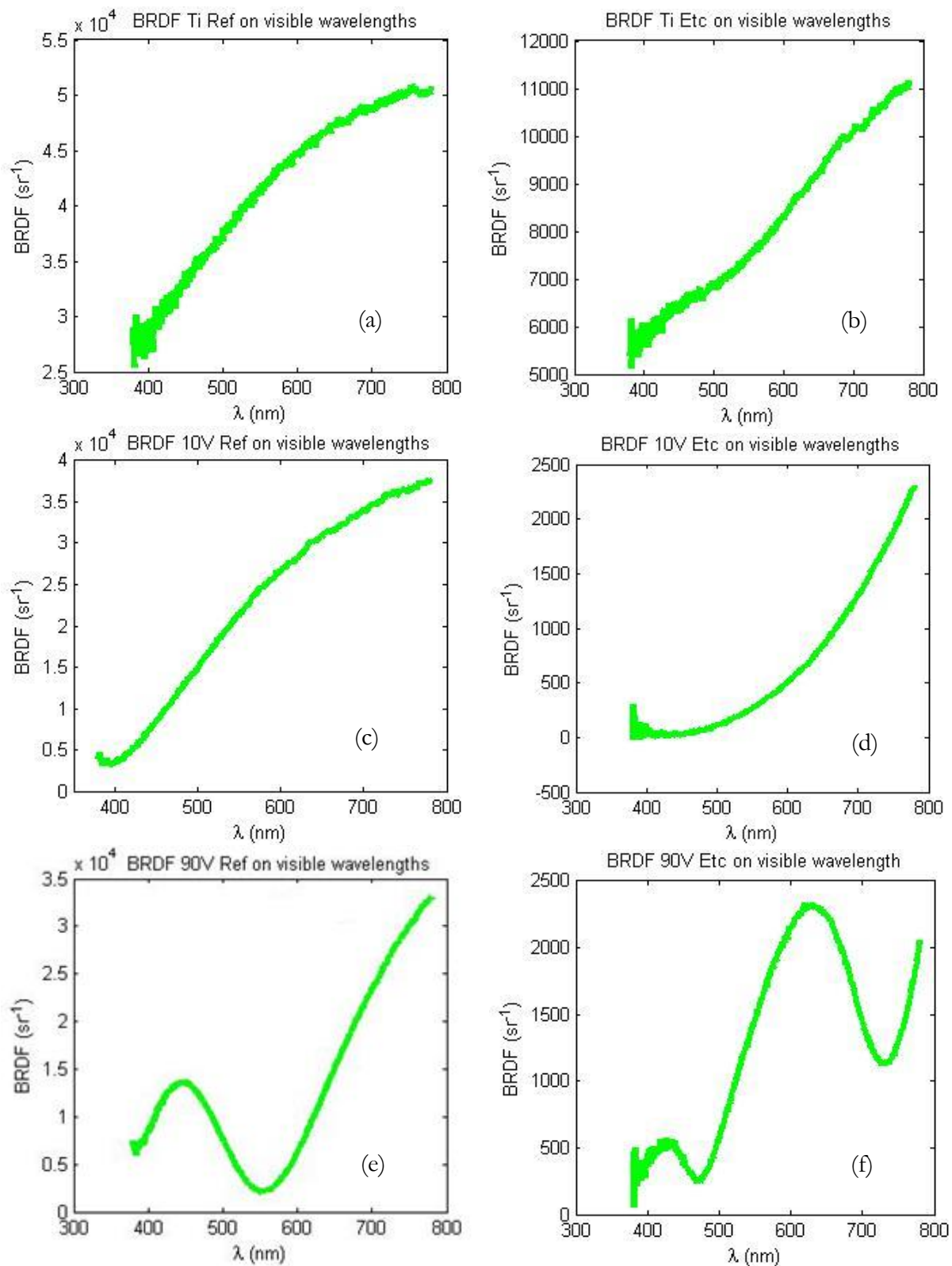
Figure 72: BRDF versus the visible wavelengths (380 nm to 780 nm) of the mirror polished samples (Ref) and of the etched (in HF/HNO$_3$ for 30 seconds after mirror polishing) samples (Etc). BRDF of the non-anodized samples Ref (a) and Etc (b). BRDF of the 10 V anodized Ref (c) and Etc (d) samples and of the 90 V anodized Ref (e) and Etc (f) samples. Anodizing parameters are a 0.5 M H$_2$SO$_4$ solution and a current density of 40 mA/cm². Note that the Y axis scale can be different between the graphs.

76

The values of the oxide layer thickness are reported in Table 20. Estimated values are larger for etched samples than for non-etched samples anodized with the same cell potential. Moreover, the samples obtained at higher cell potentials have a higher oxide layer thickness. One can notice that the estimated thickness values show discrepancies up to 40 nm for estimated values from a maximum or a minimum for the same sample.

	Extremum wavelength in nm (type)	Interference order k	Refractive index $n_{TiO_2}(\lambda)$	$\theta_r(\lambda)$ (°)	Thickness (nm)
10 V Ref	390 (min)	1	3.39	12.04	58.8
10 V Etc	435 (min)	1	3.16	12.93	70.6
90 V Ref	445 (max)	2	3.15	12.97	108.7
	550 (min)	1	2.96	13.82	95.7
90 V Etc	430 (max)	3	3.17	12.89	174.5
	470 (min)	2	3.11	13.14	155.7
	630 (max)	2	2.88	14.21	169.9
	730 (min)	1	2.82	14.52	134.2

Table 20: Oxide thickness values estimated from the extrema of reflectance spectra obtained with goniospectrophotometric measurements. The refractive index of the TiO$_2$ layer used to obtained the oxide layer thickness is taken from [72].

In order to confirm these oxide thickness estimates, a more complex model has been developed, based on the Abeles matrices formalism (see Chapter 1 section II 3)). This formalism allows to model the reflectance spectrum of a material composed of different layers. A MATLAB® code was developed at GFL by Renee Charrière based on this formalism. This code allows to estimate the oxide layer thickness by fitting an experimental spectrum, but the metal and the oxide refractive indexes need to be known.

2) Reflectance spectrum fit with an Abeles matrices-based model to obtain the oxide layer thickness

    a) Simple fit of the experimental reflectance spectra considering a homogeneous oxide thickness

Once again, the refractive indexes of titanium and titanium dioxide will be taken from [72]. The incident light is assumed to be non-polarized. The order of magnitude of the oxide layer thickness is needed to start the fit. The model is used to generate a reflectance spectrum (on the visible wavelengths range) which is compared to the experimental reflectance spectrum. Reflectance spectra are generated with refined values of the oxide layer thickness until a convergence is found. This model is based on a least-squares method. The solution minimizes the sum of the squares of the difference between the rescaled modeled values and the experimental values over the visible wavelengths range:

$$\min_{e_{TiO_2}}\left(\sum_{\lambda_i}\left(\Omega^{simulated}_{e_{TiO_2}}(\lambda_i)\times\frac{mean_{\lambda_i}\left(\Omega^{measured}(\lambda_i)\right)}{mean_{\lambda_i}\left(\Omega^{simulated}_{e_{TiO_2}}(\lambda_i)\right)}-\Omega^{measured}(\lambda_i)\right)^2\right) \quad (40)$$

Important note: the wavelengths λ_i are taken in the interval [380 nm-780 nm].

$\Omega^{simulated}_{e_{TiO_2}}(\lambda_i)$ corresponds to the modeled reflectance at a given wavelength λ_i for an oxide layer thickness of e_{TiO_2} and $\Omega^{measured}(\lambda_i)$ corresponds to the experimental reflectance at the same wavelength λ_i. Note that Figure 72 shows spectral BRDF and not spectral reflectance. The BRDF measurements are converted into reflectance measurements according to the formula:

$$\rho(\theta_i, \lambda) = BRDF\,(\theta_i, \theta_r = \theta_i, \lambda) \times \Omega_s \times \cos(\theta_i) \qquad (41)$$

where Ω_s is the source solid angle (12.10^{-6}sr) and θ_i the value of the incidence angle.

This formula gives indeed the ratio of the flux reflected by the sample over the incident flux according to the experimental expression of the BRDF (equation (33)). The validity of this formula will be discussed later. This fitting procedure has been applied to the measured reflectance spectra of the anodized samples (etched or not) presented earlier in this chapter. The fit of the reflectance spectrum of the reference non-anodized sample anodized at a cell potential of 10 V is presented on Figure 73. Two modeled curves are shown: one which is called "rescaled model" and one which is called "raw model". Both models are obtained with the minimization of the quantity presented in the equation (41).

The rescaled model corresponds to $\Omega^{simulated}_{e^0_{TiO_2}}(\lambda) \times \dfrac{mean_{\lambda_i}\left(\Omega^{measured}(\lambda_i)\right)}{mean_{\lambda_i}\left(\Omega^{simulated}_{e_{TiO_2}}(\lambda_i)\right)}$, where $e^0_{TiO_2}$ is the

oxide layer thickness minimizing equation (41). The raw model corresponds to $\Omega^{simulated}_{e^0_{TiO_2}}(\lambda)$.

We observe on Figure 73 that, whereas the rescaled model fits properly the experimental curve, the raw model gives higher reflectance values. This could be due to a misalignment of the goniospectrophotometer implying an underestimation of the flux reflected by the sample. This could also be due to a bad estimation of the reflectance of the sample from its BRDF measurement, but we will see later in this chapter that equation (41) gives a good estimate of the sample reflectance for non-etched samples. The value of the oxide thickness given by the fit is 12 nm.
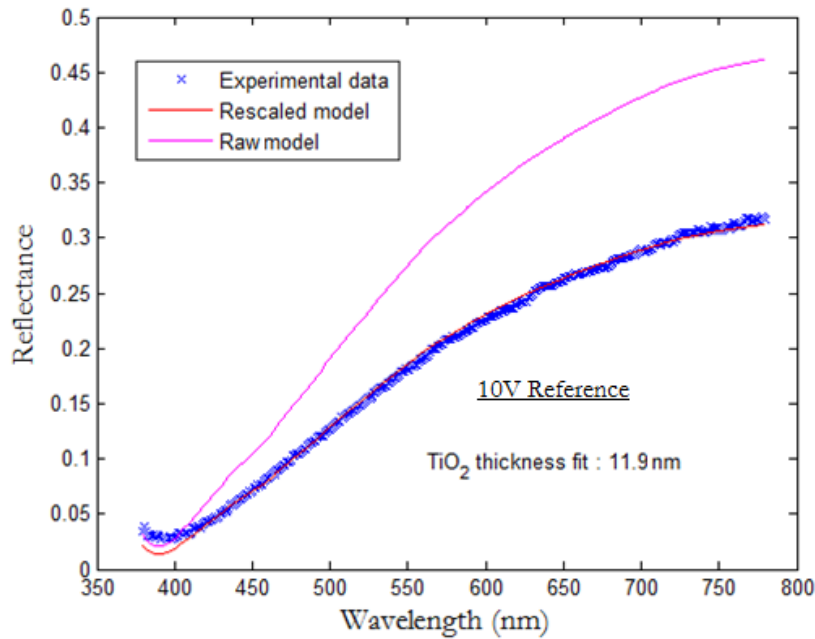
Figure 73 : Oxide layer thickness estimation fit with two Abeles matrices-based models on the reference non-etched sample anodized at a 10 V cell potential. The fit gives a thickness value of 12 nm.

In the case of the etched sample anodized at a cell potential of 10 V, the raw model gives reflectance values almost 40 times higher than the experimental data, as shown in Figure 74 a). We will see later in this chapter that in the case of the etched samples, equation (41) does not give a good estimation of the sample reflectance. Thus, for etched samples, comparing the raw model and the experimental data is not practical. As the measured reflectance spectrum variations cannot be observed on Figure 74 a) the experimental data and the rescaled model are presented on Figure 74 b). The fit gives a value of the oxide layer thickness of 18 nm. The fit is not as good as for the 10 V non-etched sample, i.e. the shape is different between the model and experimental data.
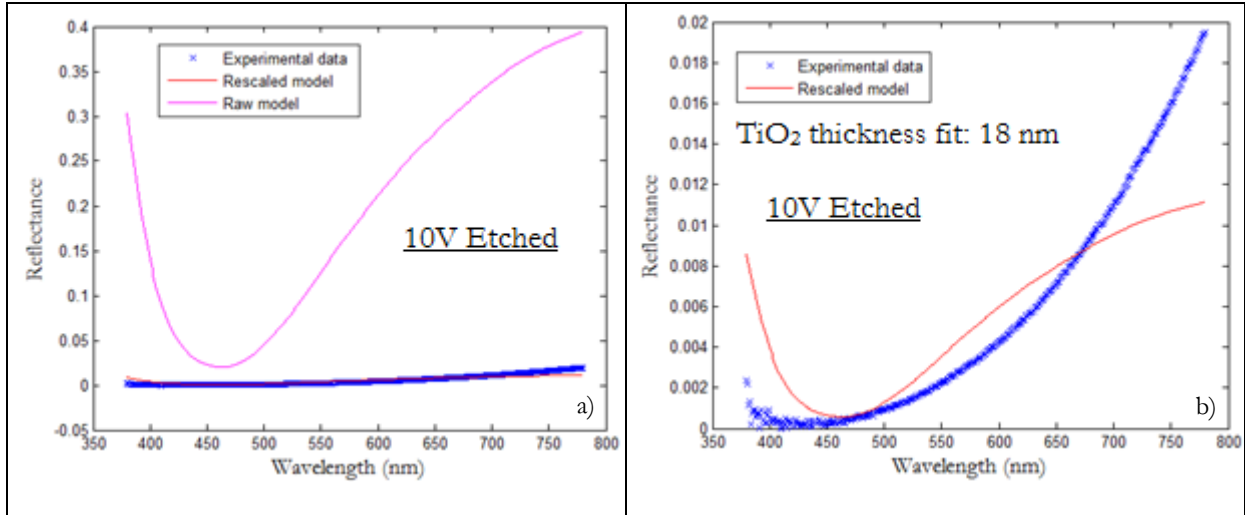
Figure 74: Oxide layer thickness estimation fit with two Abeles matrices-based models on the etched sample anodized at a 10 V cell potential; a) raw, rescaled model and experimental reflectance; b) rescaled model and experimental reflectance. The fit gives a thickness value of 18 nm.

The same fit procedure has been also applied to the samples anodized at a cell potential of 90 V. The results are presented in Figure 75 for the reference non-etched sample and in Figure 76 for the etched sample. As for the 10 V non-etched sample, we observe that for the 90 V non-etched sample the raw model gives reflectance values higher than the experimental data. However, the fit with the rescaled model does not match the experimental data as well as for the 10 V non-etched sample. Nevertheless, the extrema of the modeled spectrum are in good agreement with the extrema of the experimental curve, which means that the oxide layer estimation remains correct. The fit gives a value of 123 nm for the oxide layer thickness.
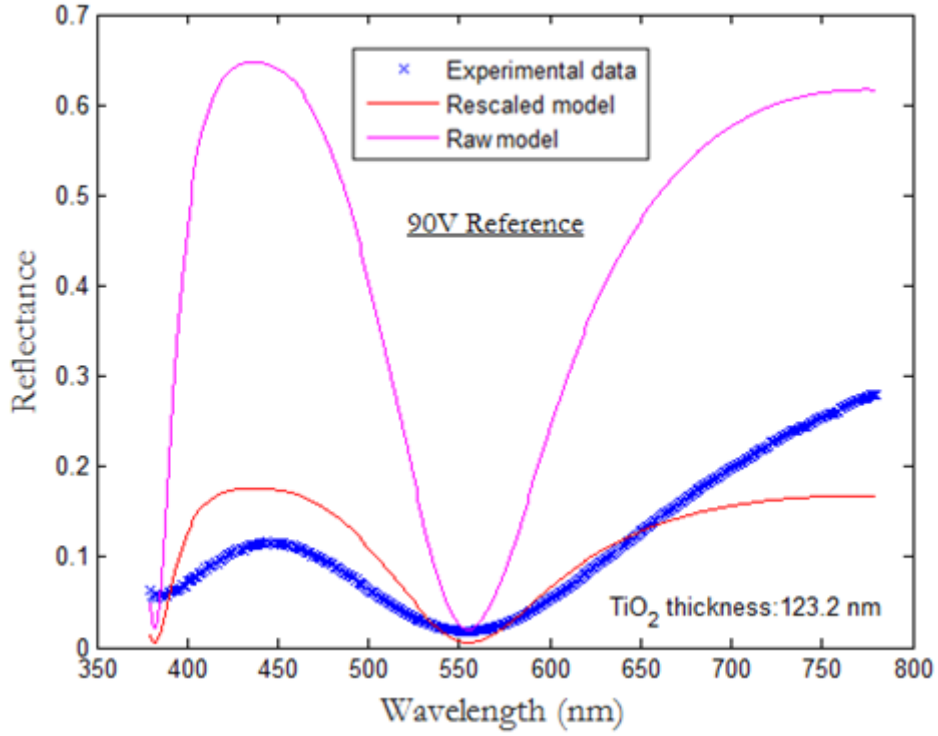
Figure 75: Oxide layer thickness estimation fit with two Abeles matrices-based models on the reference non-etched sample anodized at a 90 V cell potential. The fit gives a thickness value of 123 nm.

In the case of the 90 V etched sample, the fit is no longer accurate. The position of the extrema and the shape of the reflectance spectrum are not in agreement between the model and the experimental spectrum. It could be explained by a problem of convergence of the fitting procedure. The thickness value given by the model in this case is thus inaccurate.

We tried to optimize empirically by trial and error the oxide layer thickness in order to obtain the same position for the last minimum for both the model and the experimental data (see Figure 77). We observe that even in this case, the positions of the other extrema are not in good agreement between the model and the experimental data. We obtain in this case an oxide layer thickness of 180 nm, against 189 nm for the value given by the automatic fit.

We decided to investigate the impact of a non-homogeneity of the oxide layer thickness on the reflectance spectrum; it could indeed explain the difference between the fitted reflectance spectra and the experimental ones.
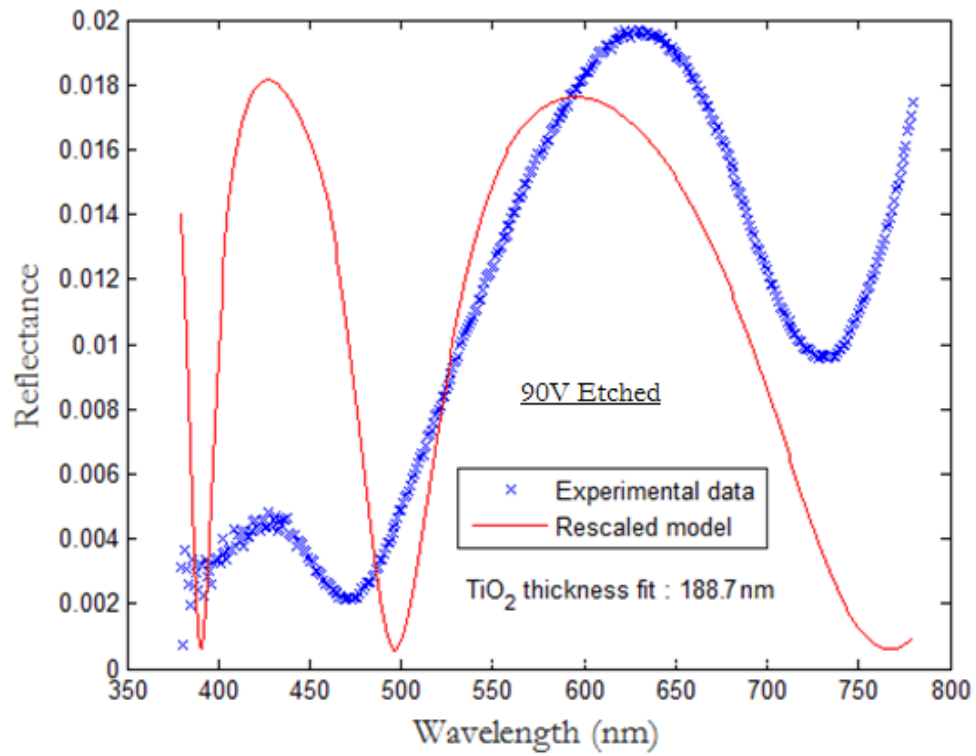
Figure 76: Oxide layer thickness estimation fit with an Abeles matrices-based model on the etched in HF/HNO₃ sample anodized at a 90 V cell potential. The fit gives a thickness value of 189 nm.
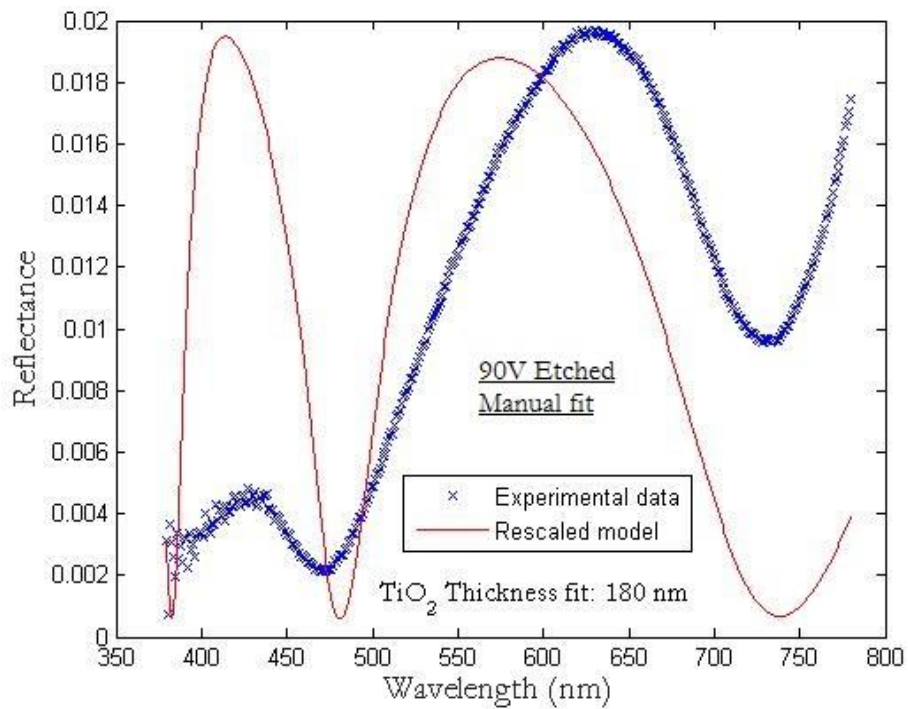
Figure 77: Oxide layer thickness estimation manual fit on the etched in HF/HNO₃ sample anodized at a 90 V cell potential. The fit gives a thickness value of 180 nm.

b) <u>Fit of the experimental reflectance spectra including oxide thickness variations</u>

The oxide layer thickness can be inhomogeneous across the BRDF measurement area. In the measurements presented before, the measurement area is elliptical with a minor axis of 25 mm and a major axis of $\frac{25}{\cos(45°)}$ mm (~35mm), as the incidence angle was 45°. As a first approximation, a uniform thickness probability density function with an average thickness e_0 value and a total thickness variation Δe is defined (see Figure 78). A Gaussian thickness probability density function could be used in another study. The total reflectance spectrum of the sample is modeled by taking into account the contribution of each oxide thickness. As we assumed a uniform thickness probability density function, this total spectrum is here just an average of the reflectance spectra obtained for each thickness taken in the interval $\left[e_0 - \frac{\Delta e}{2}, e_0 + \frac{\Delta e}{2}\right]$.
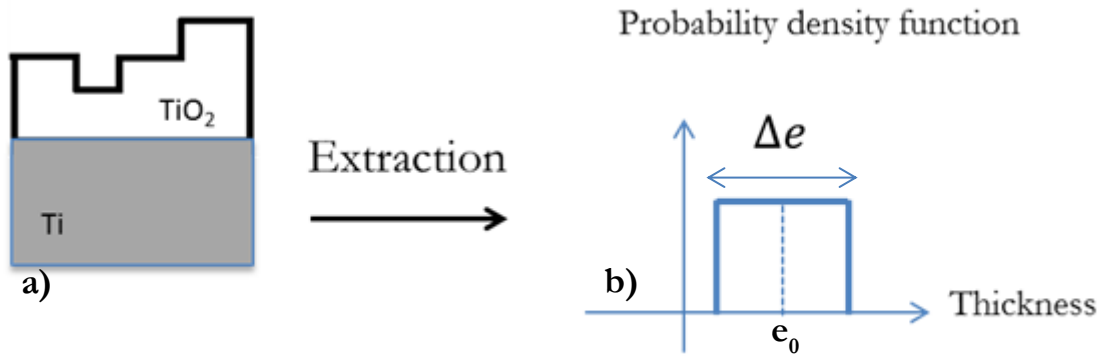
Figure 78: Representation of a sample with an inhomogeneous oxide layer thickness (a). These inhomogeneities are defined with an average oxide layer thickness e_0 and a total thickness variation Δe, assuming a uniform thickness probability density function.

Figure 79 shows different Abeles modeled reflectance spectra with different oxide layer thicknesses varying from 133 nm to 143 nm ($\Delta e = 10$ nm and $e_0 = 138$ nm) with a 1 nm step. The incident light is assumed to be non-polarized, the incidence angle is equal to 45° and the refractive indexes are extracted from the reference [2]. Figure 80 shows the average of these reflectance spectra, modeling a sample with an average oxide layer thickness $e_0 = 138$ nm and a total thickness variation of $\Delta e = 10$ nm.

To take into account oxide layer thickness inhomogeneities in our model, the experimental data are now fitted with an average reflectance spectrum and the parameters of the fit are both the average oxide layer thickness of e_0 and the total thickness variation Δe. The solution now minimizes the following equation:

$$\min_{e_0, \Delta e} \left(\sum_{\lambda_i} \left(mean_{e \in \left[e_0 - \frac{\Delta e}{2}, e_0 + \frac{\Delta e}{2}\right]} (\Omega_e^{simulated}(\lambda_i)) \right. \right.$$

$$\left. \left. \times \frac{mean_{\lambda_i}\left(\Omega^{measured}(\lambda_i)\right)}{mean_{\lambda_i}\left(mean_{e \in \left[e_0 - \frac{\Delta e}{2}, e_0 + \frac{\Delta e}{2}\right]}(\Omega_e^{simulated}(\lambda_i))\right)} - \Omega^{measured}(\lambda_i) \right)^2 \right) \right) \qquad (42)$$
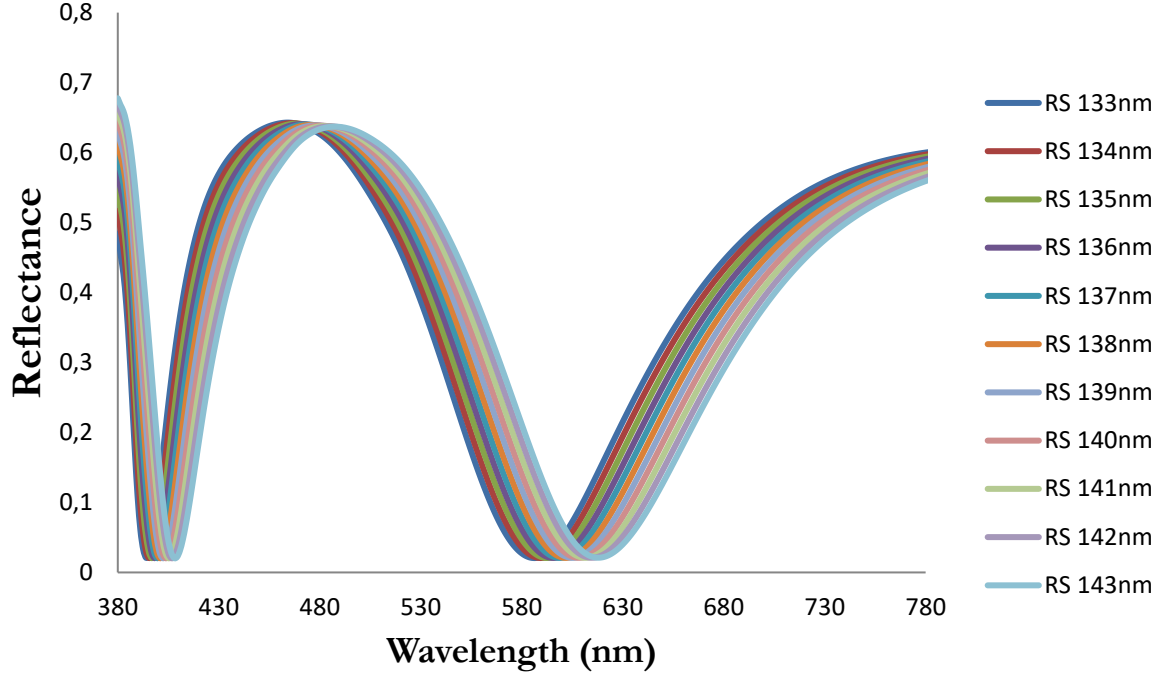
Figure 79: Modeled reflectance spectra for a total thickness variations interval $\Delta e = 10$ nm and an average thickness value $e_0 = 138$ nm with a 1 nm step.
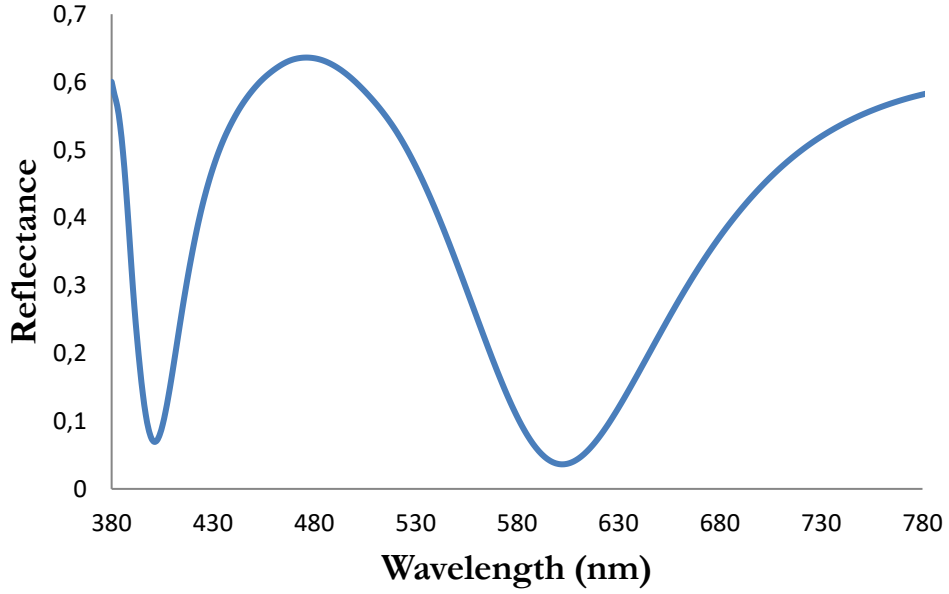
Figure 80: Average of the modeled reflectance spectra for a total thickness variations interval $\Delta e = 10$ nm and an average thickness value $e_0 = 138$ nm with a 1 nm step.

The number of thicknesses taken in the interval $\left[e_0 - \frac{\Delta e}{2}, e_0 + \frac{\Delta e}{2}\right]$ is chosen to correspond to a step about 1nm between two successive thicknesses:

$$N_e = round\left(\frac{\Delta e}{s}\right)$$

where round designates the closest integer and s= 1 nm.

In the case of the reference non-etched samples, the new model taking into account a potential inhomogeneity of the oxide layer thickness gives better results. The shape of the reflectance spectrum is indeed better for the reference sample anodized at a cell potential of 10 V than the one obtained with the first model, with a perfect agreement between the model and the experimental data (see Figure 81). The first model gave values lower than the experimental data around 400 nm (see Figure 73). The average thickness given by this new model is equal to $e_0 = 12$nm with a total thickness variation $\Delta e = 5$nm. The average thickness is the same as the thickness obtained previously with the first model.
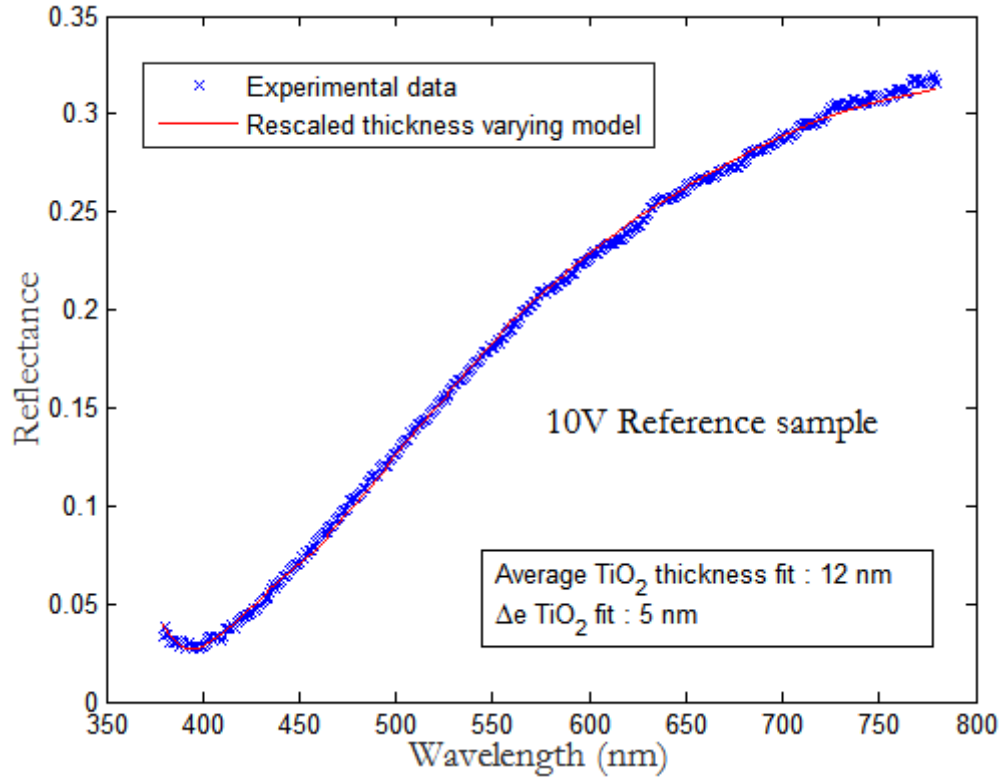
Figure 81: Oxide layer thickness parameters estimation fit with a thickness varying model on the reference non-etched sample anodized at a 10 V cell potential. The fit gives an average thickness of $e_0 = 12$ nm with a total thickness variation of $\Delta e = 5$ nm.

The fitted reflectance is also improved for the reference non-etched sample anodized at 90 V. By comparing Figure 75 and Figure 82, one can observe that the shape of the varying thickness modeled curve is closer to the first local maximum and around the second local minimum. The average thickness given by this model is equal to $e_0 = 121$ nm with a total thickness variation $\Delta e = 30$ nm. The average thickness is almost the same as the thickness obtained previously with the first model (123 nm with the first model).

In the case of the etched samples, the benefit of using the model taking into account a potential thickness variation is not as visible as for reference non-etched samples. By comparing Figure 74b) and Figure 83, no improvement of the fit when taking into account the thickness variations is observed. The estimated average thickness value with the varying thickness model remains really close to the one previously found (17 nm against 18 nm) and the computed total thickness variation is only $\Delta e = 1.5$ nm. Thickness inhomogeneities do not seem to explain the disagreement between the model and the experimental data.
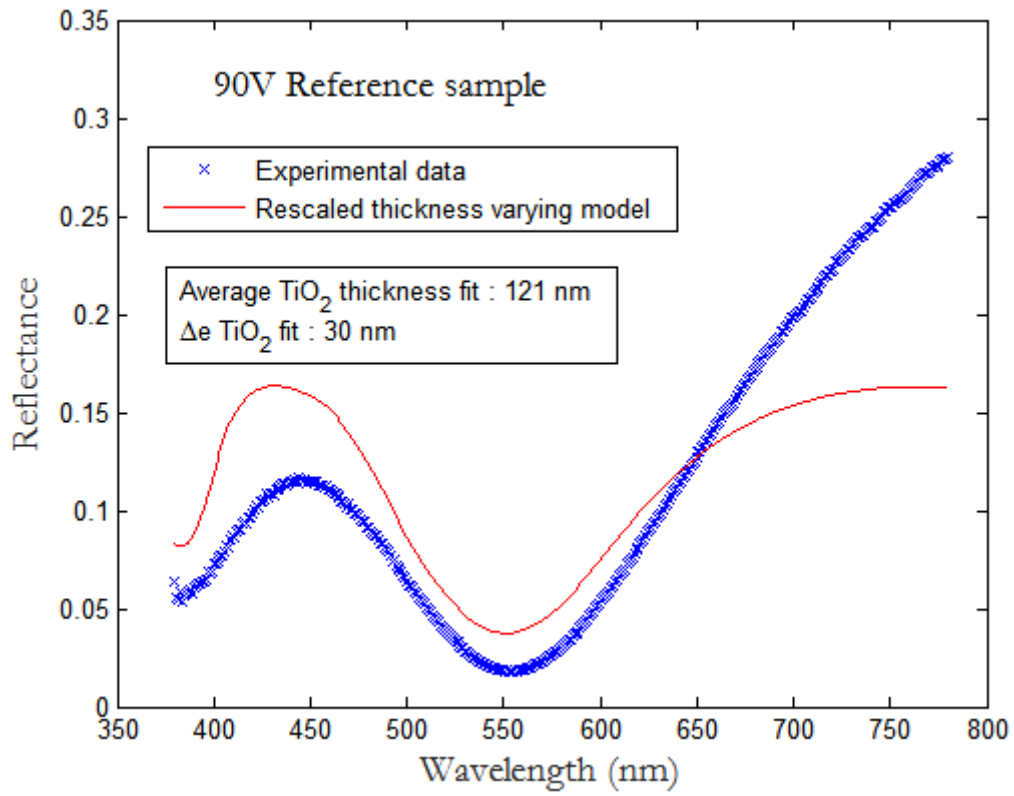
Figure 82: Oxide layer thickness parameters estimation fit with a thickness varying model on the reference non-etched sample anodized at a 90 V cell potential. The fit gives an average thickness of $e_0 = 121$ nm with a total thickness variation of $\Delta e = 30$ nm.
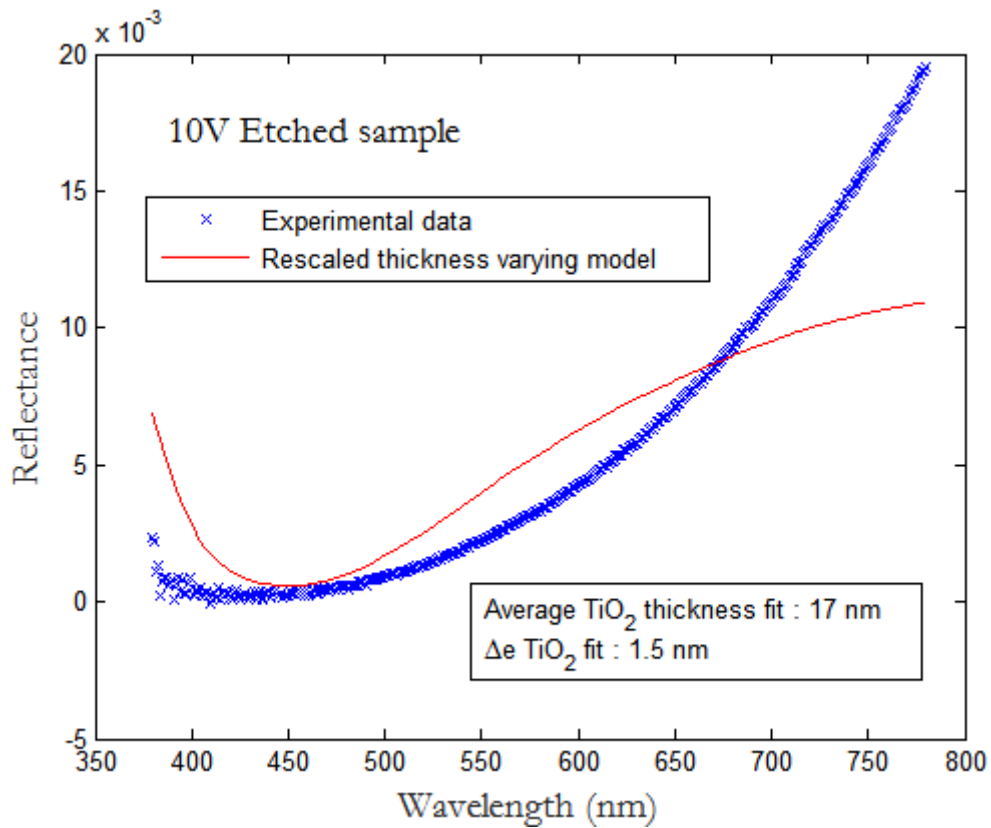
Figure 83: Oxide layer thickness parameters estimation fit with a thickness varying model on the etched in HF/HNO₃ sample anodized at a 10 V cell potential. The fit gives an average thickness of $e_0 = 17$ nm with a total thickness variation of $\Delta e = 1.5$ nm.

Figure 84, one can observe that the new model is not working properly for the etched sample anodized at a cell potential of 90 V. The modelled positions of the extrema are worse than for the first model and the modeled spectrum is far from the experimental one. The model did not properly converge in this case.
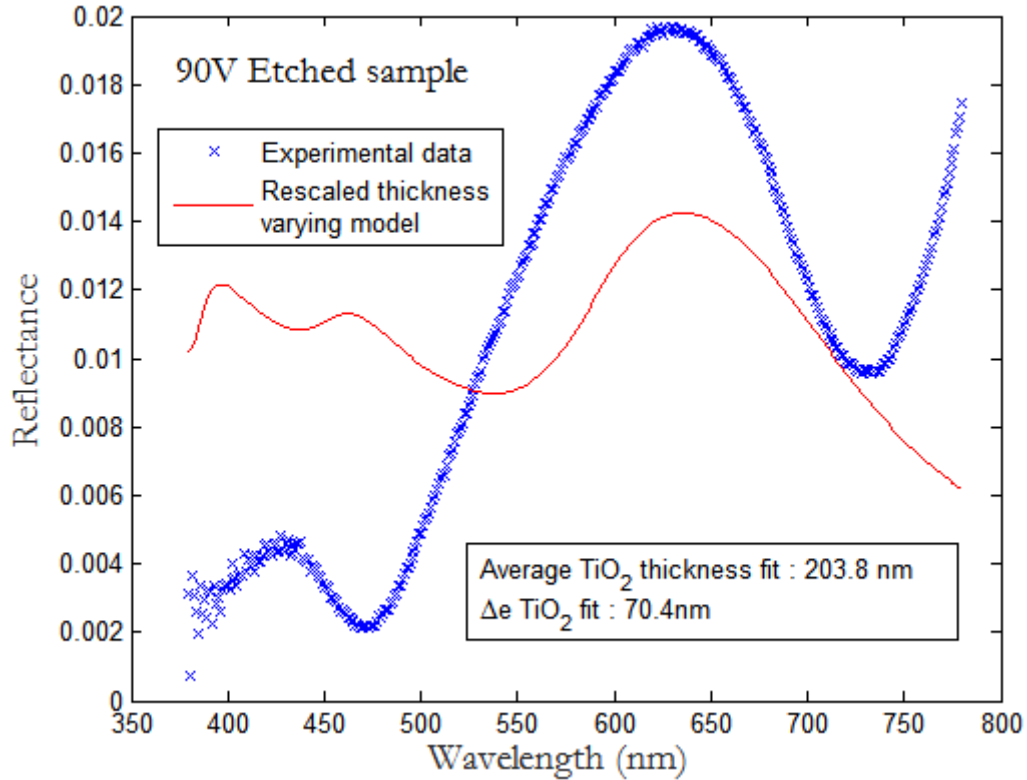
Figure 84: Oxide layer thickness parameters estimation fit with a thickness varying model on the etched in HF/HNO₃ sample anodized at a 90 V cell potential. The fit seems not to have properly converged in this case.

c)   Conclusions about the Abeles matrices-based models

Two different models have been implemented in this section to fit the oxide layer thickness parameters. The first model assumes a homogeneous oxide layer thickness whereas the second one takes into account thickness variations.

Both models fit well the experimental data for the 10 V non-etched sample. Despite an improvement of the fit with the second model for the 90 V non-etched reference sample, the fit is not as good as for the 10 V non-etched reference sample. Titanium anodized in the same conditions exhibit usually an amorphous oxide layer for a 10 V cell potential whereas it exhibits a partially crystallized anatase oxide layer for a 90 V cell potential [70]. This could lead to refractive index inhomogeneities not taken into account in our model. Also, the assumption of a uniform thickness probability density function might not be adequate. Both models do not work well for the 10 V and 90 V etched samples, where the shapes of the experimental spectra are not in agreement with the modeled spectra. Further investigations are needed to explain these discrepancies.

We also observe large discrepancies between the oxide layer thicknesses obtained through the Abeles matrices-based fits and the oxide layer thicknesses obtained by looking at the experimental spectra extrema (see section 3 a) of this chapter), as shown in Table 21. The discrepancies can reach 500% for the 10 V non-etched samples.

	Extremum wavelength in nm (type)	Thickness obtained with equations (39) and (40) (nm)	Simple thickness fit (nm)	Thickness fit with varying thickness model (Δe) (nm)
10 V Ref	390 (min)	58.8	11.9	12 (5)
10 V Etc	435 (min)	70.6	18	17 (1.5)
90 V Ref	445 (max) 550 (min)	108.7 95.7	123.2	121 (30)
90 V Etc	430 (max) 470 (min) 630 (max) 730 (min)	174.5 155.7 169.9 134.2	188.7	203.8 (70.4)

Table 21: Comparison between oxide layer thicknesses estimated by Abeles matrices-based model fit with and without varying the oxide thickness and thicknesses estimated from the positions of the extrema of the experimental spectra.

In the next section, the origin of theses thicknesses estimation discrepancies will be explained in detail.

3) Analysis of the reflectance spectrum extrema of a sample composed of a layer and a substrate
   a) Case of a TiO₂ / Ti sample

In order to understand the discrepancies between the Abeles model fitted oxide layer thicknesses and the ones evaluated through the extrema of the experimental data, we decided to model through the Abeles matrices the reflectance of a TiO₂ oxide layer located on top a Ti substrate. The oxide layer was set to 150 nm and the refractive indexes n_{Ti} and n_{TiO_2} were taken from [72] (see Figure 85). The modeled non-polarized reflectance spectrum is presented in Figure 86. Note that Re and Im correspond respectively to the real and the imaginary parts of the refractive indexes.
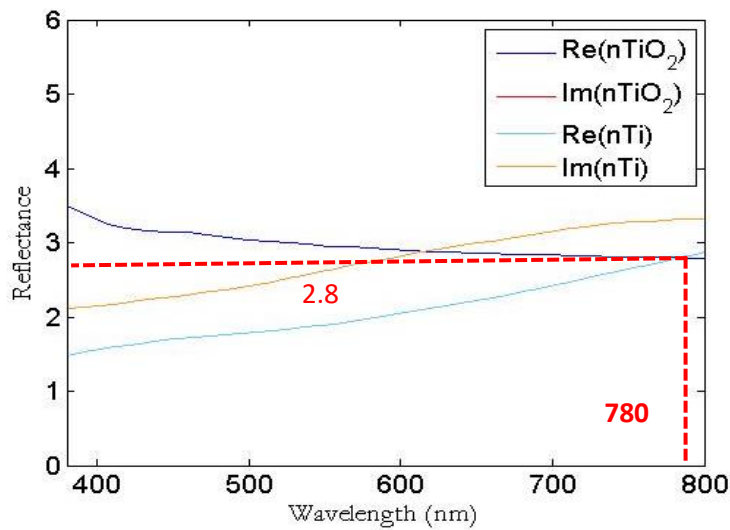
Figure 85: Refractive indexes (from [72]) of titanium and titanium dioxide on the visible wavelengths range (380 nm-780 nm). The red curve is not visible because the imaginary part of the refractive index of titanium dioxide is null in this wavelengths range.
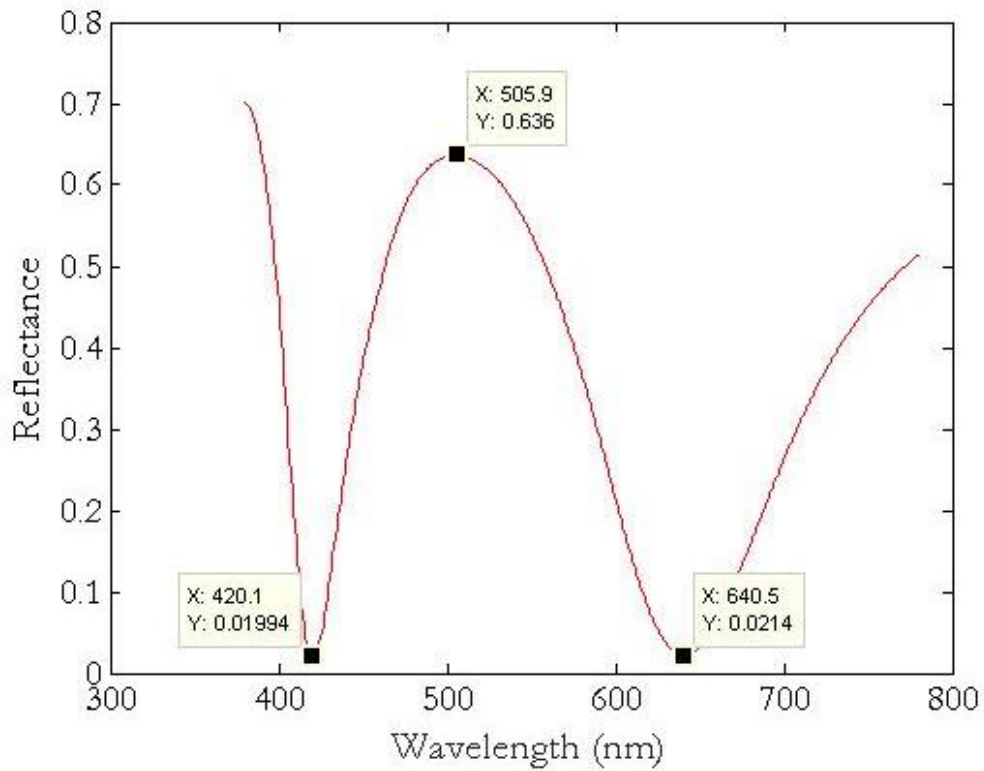
Figure 86: Modeled reflectance spectrum for non-polarized light of a 150 nm thick TiO₂ layer on top on a titanium substrate. The refractive indexes are from [72]. The values presented on the graph correspond to the positions of the extrema.

The extrema (one maximum and two minima) have been collected and the equations (38)-(39) have been used to recalculate the thickness of this simulated reflectance spectrum (see Table 22).

	Extremum wavelength in nm (type)	Interference order k	$n_{TiO_2}(\lambda)$	$\theta_r(\lambda)$ in degree	Thickness (nm)
Extremum 1	420.1 (min)	2	3.19	12.15	135
Extremum 2	503.4 (max)	2	3.03	13.5	128.1
Extremum 3	639.7 (min)	1	2.87	14.26	115

Table 22: Calculated thicknesses from the extrema of a modeled reflectance spectrum of a sample composed of a TiO₂ layer on top of a titanium substrate using equations (38)-(39). (refractive indexes from [72])

The values calculated from the extrema positions through equations (38)-(39) are not equal to the 150 nm value that we used as parameter for the model. The error can reach more than 20% (extremum 3).

In order to understand and correct these errors, we will need to introduce the Fresnel coefficients which are used to characterize the reflection or the transmission of light at an interface between linear, isotropic, homogeneous and potentially absorbent materials.

b) Fresnel coefficients

α) Amplitude Fresnel coefficients

In order to characterize the reflection or the transmission of light at an interface between linear, isotropic homogeneous and potentially absorbent materials, we need to compute the Fresnel coefficients. The optical properties of such materials are described by complex refractive indexes. The Fresnel coefficients provide the information about the portion of the amplitude of the incident wave which is reflected or transmitted. These coefficients are defined for the transverse electric (TE) and transverse magnetic (TM) linear polarizations (see Figure 87).

TE Polarization   TM Polarization
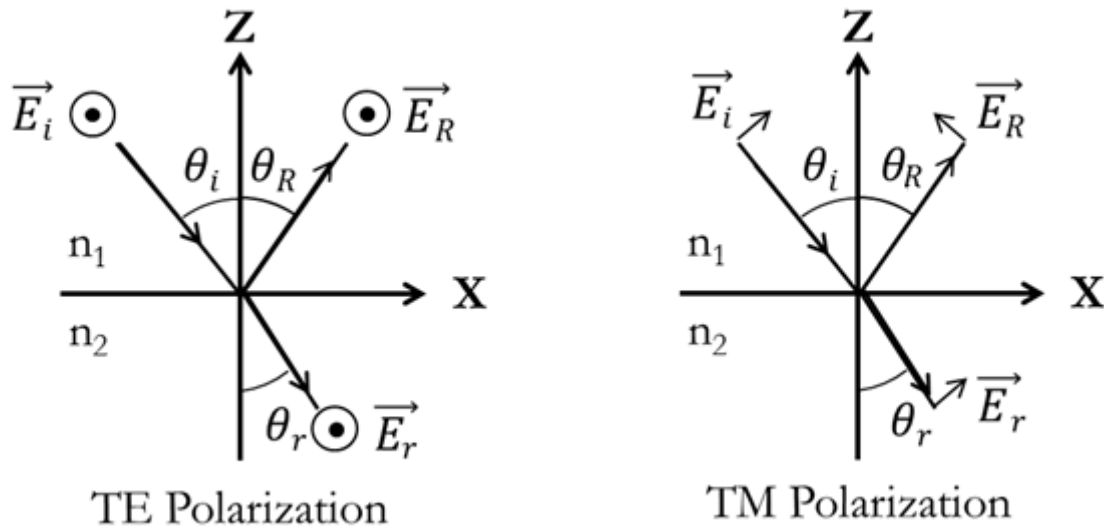
Figure 87 : Geometries used to define the reflection and transmission Fresnel coefficients at an interface between a material with a refractive index n_1 and a material with a refractive index n_2. $\vec{E_i}, \vec{E_R}$ and $\vec{E_r}$ are respectively the incident, reflected and refracted (or transmitted) electric fields. θ_i, θ_R and θ_r are respectively the incidence, reflection and refraction (transmission) angles.

The Fresnel coefficients are determined by using the continuity of the electric and magnetic field components tangent to the interface.

Fresnel coefficients in TE polarization

If we neglect the temporal dependence $exp(-i\omega t)$ and if we use the Snell-Descartes laws, the incident, reflected and transmitted electric fields can be written as:

$$\vec{E_i} = E_0\vec{e_y}\exp[i(\alpha x - \gamma_1 z)]$$
$$\vec{E_r} = r_s E_0\vec{e_y}\exp[i(\alpha x + \gamma_1 z)]$$
$$\vec{E_r} = t_s E_0\vec{e_y}\exp[i(\alpha x - \gamma_2 z)]$$

(43)

If the incident medium is transparent (n_1 is a real number), the x component of the wave vector is written:

$$\alpha = n_1 \frac{\omega}{c} \sin(\theta_i)$$

with θ_i the incidence angle c the light speed in vacuum and ω the wave pulsation

(44)

Each wave has to verify the Helmholtz equation which leads to (for j=1,2):

89

$$\Delta\vec{E} + \|\vec{k}\|^2\vec{E} = \vec{0} \qquad \text{where } \vec{k} \text{ the wave vector and } \vec{E} \text{ the electric field.} \qquad (45)$$

We can then write: $\alpha^2 + \gamma_j^2 = n_j^2 \frac{\omega^2}{c^2}$ \hfill (46)

The wave vector components on the z axis in the two media are thus given by:

$$\gamma_j = \left(n_j^2 \frac{\omega^2}{c^2} - \alpha^2\right)^{\frac{1}{2}} \qquad (47)$$

When the components are complex, the square root sign is chosen so that $Re(\gamma_j) > 0$ and $Im(\gamma_j) > 0$, where Re stands for the real part and Im for the imaginary part.
By using the electric field tangential components continuity relation at the interface z=0 we obtain:

$$1 + r_s = t_s \qquad (48)$$

With the Faraday's law of induction and the relationship $\overrightarrow{rot}\,\vec{E} = -\frac{\partial\vec{B}}{\partial t}$ and $\vec{B} = \mu_0(\vec{H} + \vec{M})$, we get:

$$rot\,\vec{E} = i\omega\mu_0\vec{H} \qquad (49)$$

where $\vec{M}$ is the magnetization of the sample (considered null in this case), $\vec{B}$ is the magnetic field flux, $\vec{H}$ is the magnetic field intensity and μ_0 is the vacuum permittivity. By using equation (49) and the magnetic field tangential components continuity we obtain:

$$\gamma_1(1 - r_s) = \gamma_2 t_s \qquad (50)$$

From the equations (48)-(50), we can deduce the expressions of the amplitude Fresnel coefficients for the TE polarization:

$$r_s = \frac{\gamma_1 - \gamma_2}{\gamma_1 + \gamma_2} \qquad\qquad t_s = \frac{2\gamma_1}{\gamma_1 + \gamma_2} \qquad (51)$$

Fresnel coefficients in TM polarization

The Fresnel coefficients r_p and t_p for the TM polarization can be computed the same way. Note that these coefficients correspond to the amplitude reflection and transmission coefficients of the magnetic field $\vec{H}$. We have:

$$r_p = \frac{n_2^2\gamma_1 - n_1^2\gamma_2}{n_2^2\gamma_1 + n_1^2\gamma_2} \qquad\qquad t_p = \frac{2n_2^2\gamma_1}{n_2^2\gamma_1 + n_1^2\gamma_2} \qquad (52)$$

The reflection and transmission Fresnel coefficients r'_p and t'_p for the amplitude of the electric field $\vec{E}$ in TM polarization are:

$$r'_p = r_p \qquad\qquad t'_p = \frac{2n_1 n_2 \gamma_1}{n_2^2 \gamma_1 + n_1^2 \gamma_2} \tag{53}$$

<u>β) Energetic Fresnel coefficients:</u>

In order to determine the reflection and transmission Fresnel coefficients in energy, we need to calculate the transmitted and reflected powers. To define these powers, it is necessary to calculate the Poynting vector. As a reminder, the Poynting vector represents the directional energy flux, which is the energy transfer per unit area per unit time, of an electromagnetic field. Its unit is the watt per square meter (W/m²). The Poynting vector is defined as:

$$\vec{\Pi} = \vec{E} \wedge \vec{B} \tag{54}$$

Using the relationship (49), it is possible to define the temporal average value of the Poynting vector of a monochromatic linearly polarized (along the unit vector $\vec{e}$) electromagnetic plane wave with a wave vector $\vec{k}$, written as $\vec{E}(\vec{r}) = E_0 \vec{e} \exp(i\vec{k}.\vec{r})$, as:

$$\langle \vec{\Pi} \rangle = \frac{1}{2\omega\mu_0} |E_0|^2 Re(\vec{k}) \tag{55}$$

Only the component along the z axis is needed to calculate the energy flux associated to the incident, reflected and transmitted fields through the z=0 interface:

$$\langle \vec{\Pi_z} \rangle = \frac{1}{2\omega\mu_0} |E_0|^2 Re(\gamma)\vec{e_z} \tag{56}$$

where γ is the wave vector component along the z axis.

The reflection and transmission Fresnel coefficients in energy (often called reflectivity and transmitivity) are defined as the flux ratio at the interface:

$$R = \frac{\langle \Pi_z^R \rangle}{\langle \Pi_z^i \rangle} \quad T = \frac{\langle \Pi_z^r \rangle}{\langle \Pi_z^i \rangle} \tag{57}$$

where $\langle \Pi_z^i \rangle$, $\langle \Pi_z^R \rangle$ and $\langle \Pi_z^r \rangle$ are the average Poynting vector components along the z axis of the incident, reflected and refracted (transmitted) fields. If we use the definition of the Fresnel coefficients in amplitude and the expression of the average Poynting vector of a plane wave, we obtain for both the TE and TM polarizations:

$$R = |r|^2 \qquad\qquad T = |t|^2 \frac{Re(\gamma_2)}{Re(\gamma_1)} \tag{58}$$

where r and t are the electric field Fresnel coefficients in amplitude (r_s, t_s, r'_p and t'_p).

c) <u>Origin of the non-validity of expressions (38) and (39)</u>

In section III 1) of the present chapter, we calculated the oxide thickness with equations (38) and (39). This model implied the use of a non-geometrical phase shift equal to π. As a reminder, we had for the total phase shift Δφ between the ray transmitted into the layer and reflected by the substrate and the ray reflected at the top of the layer:

$$\Delta\varphi = \Delta\varphi_{geom} \pm \pi = \frac{4\pi e \times n_{TiO_2}(\lambda) \times \cos(\theta_r(\lambda))}{\lambda} + \pi \qquad (59)$$

The formulas used to obtain the oxide thickness from the reflectance spectrum extrema were:

for a maximum ($\Delta\varphi = 2k\pi$):
$$e_{max} = \frac{(k-\frac{1}{2})\lambda_{max}}{2n_{TiO_2}(\lambda_{max})\cos(\theta_r(\lambda_{max}))} \qquad (60)$$

for a minimum ($\Delta\varphi = 2(k+1)\pi$):
$$e_{min} = \frac{k\lambda_{min}}{2n_{TiO_2}(\lambda_{min})\cos(\theta_r(\lambda_{min}))}$$

But the formulas are not valid if the substrate is metallic, i.e.: has a complex refractive index. The Fresnel coefficients corresponding to the TiO₂/Ti interface will thus have an argument different from π (see Figure 88). The expression of the phase shift is thus in our case:

$$\Delta\varphi = \frac{4\pi e n_{TiO_2}(\lambda)\cos\theta_r(\lambda)}{\lambda} + \arg(r_{2-3}(\lambda)) - \arg(r_{1-2}(\lambda)) \qquad (61)$$

where r_{1-2} and r_{2-3} are the Fresnel coefficients in amplitude respectively at the interface between medium 1 (Air) and medium 2 (TiO₂), and between medium 2 (TiO₂) and medium 3 (Ti). These factors depend on the polarization of the incident light according to equations (51) and (53).
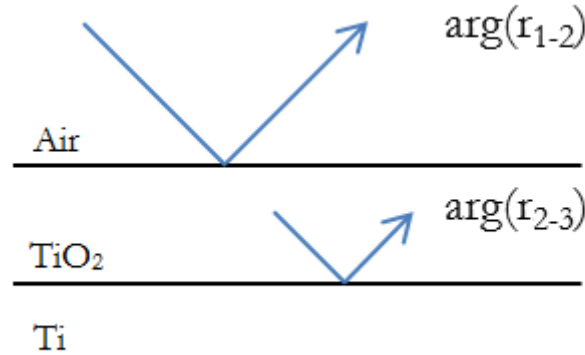
Figure 88: Reflection phase shift of the electric field at the interfaces for a TiO₂ layer of with a refractive index n_{TiO_2} located between air (n_Air=1) and a titanium substrate with a refractive index n_{Ti}.

As air and TiO₂ have real refractive indexes, $\arg(r_{1-2}(\lambda)$ is either equal to π for TE polarization or to 0 for TM polarization. The non-π phase-shift at the TiO₂/Ti interface requires a correction term when calculating the oxide layer thickness from the reflectance spectrum extrema. For the TE polarization we have:

for a maximum:	$e_{max} = \dfrac{(k-\frac{1}{2})\lambda_{max}}{2n_{TiO_2}(\lambda_{max})\cos(\theta_r(\lambda_{max}))} - \dfrac{\lambda_{max}\times \arg(r_{2-3}(\lambda_{max}))}{4\pi \cos(\theta_r(\lambda_{max}))\times n_{TiO_2}(\lambda_{max})}$	(62)
for a minimum:	$e_{min} = \dfrac{k\lambda_{min}}{2n_{TiO_2}(\lambda_{min})\cos(\theta_r(\lambda_{min}))} - \dfrac{\lambda_{min}\times\arg(r_{2-3}(\lambda_{min}))}{4\pi\cos(\theta_r(\lambda_{min}))\times n_{TiO_2}(\lambda_{min}}$	

For the TM polarization the formula are the following:

for a maximum:	$e_{max} = \dfrac{k\lambda_{max}}{2n_{TiO_2}(\lambda_{max})cos(\theta_r(\lambda_{max}))} - \dfrac{\lambda_{max}\times \arg(r_{2-3}(\lambda_{max}))}{4\pi\,cos(\theta_r(\lambda_{max}))\times n_{TiO_2}(\lambda_{max})}$	(63)
for a minimum:	$e_{min} = \dfrac{\left(k+\frac{1}{2}\right)\lambda_{min}}{2n_{TiO_2}(\lambda_{min})cos(\theta_r(\lambda_{min}))} - \dfrac{\lambda_{min}\times \arg(r_{2-3}(\lambda_{min}))}{4\pi\,cos(\theta_r(\lambda_{min}))\times n_{TiO_2}(\lambda_{min}}$	

d) Analysis of reflectance spectrum extrema in various cases

In order to understand the effects produced when changing the refractive index of the layer and/or of the substrate, we used the Abeles matrices model to simulate virtual materials.
In all cases, we modeled the reflectance spectrum of layer/substrate samples with a layer thickness equal to 150 nm in TE and TM polarizations, as well as for non-polarized light. The refractive indexes will be first fixed to a constant value, then varied linearly with the wavelength, then an imaginary part is added to the substrate refractive index. Finally, values corresponding to a (TiO₂/Ti) material with refractive indexes taken from [72] are considered.
We collected the position of the extrema (in nm) of the reflectance spectra and these extrema values were used to estimate the layer thickness with two different approaches:

- the first approach using the equations (60)
- the second using the Fresnel coefficients phase shift to correct the estimated thickness value (equations (62) for TE polarization and (63) for TM polarization).

The Fresnel coefficients are dependent on the polarization of the incident light. This is the reason why we decided to represent the reflectance spectra in three different polarizations: TE, TM and non-polarized. Only the TE polarization will be treated in the following section, but the same operation could be done by using the extrema values for the TM reflectance spectra. By analogy with our TiO₂/Ti samples, the refractive index of the layer will be noted n_{TiO_2} and the refractive index of the substrate n_{Ti}.

i. Case for $n_{TiO_2} = 2.4$ and $n_{Ti} = 2$

In this simple case, we do not consider dispersion and the refractive index of the layer is always larger than the refractive index of the substrate for any wavelength. The substrate is not absorbent. The reflectance spectra for TE, TM and non-polarized light are presented in Figure 89. The calculated values of oxide thickness and the thickness corrections are given in Table 23. The correcting factor $\arg(r_{2-3})$ in this case is null. It corresponds to the hypothesis of the first model based on the equation (60). The thickness value given by this equation is thus correct in this case.
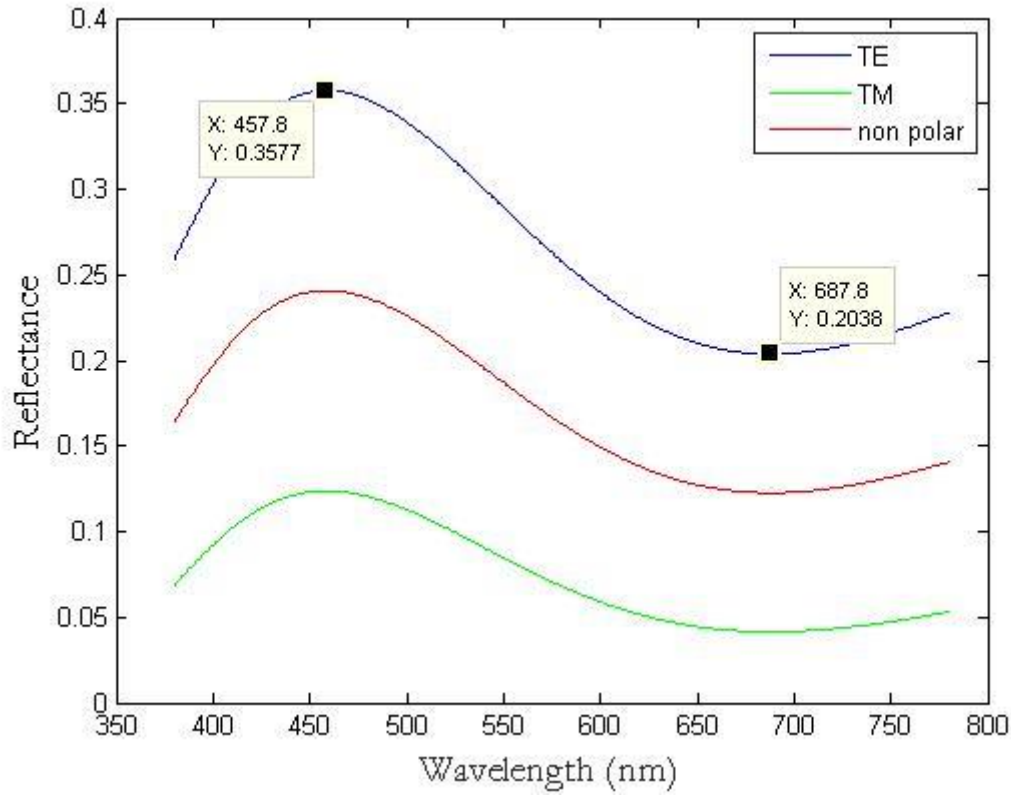
Figure 89: Modeled reflectance spectra (TE, TM and non-polarized light) of a 150 nm thick oxide layer on top of a non-absorbent substrate. The refractive indexes are $n_{TiO_2} = 2.4$ for the layer and $n_{Ti} = 2$ for the substrate. The values presented on the graph correspond to the positions of the extrema of the TE polarization reflectance.

	Extremum wavelength in nm (type)	Interference order k	$n_{TiO_2}(\lambda)$	$\theta_r(\lambda)$ (°)	$\arg(r_{2-3})$ (°)	Thickness equation (60) (nm)	Corrected thickness (62) (nm) (correction)
Extremum 1	457.8 (max)	2	2.4	17.14	0	149.7	149.7 (0)
Extremum 2	687.8 (min)	1	2.4	17.14	0	150	150 (0)

Table 23: Calculated thickness of a 150 nm thick layer on top of a non-absorbent substrate by using (60) and (62) equations. The refractive indexes are $n_{TiO_2} = 2.4$ for the layer and $n_{Ti} = 2$ for the substrate.

ii. <u>Case $n_{TiO_2} = 2.4$ and $n_{Ti} = 3$</u>

In this simple case, the refractive index of the layer is always smaller than the refractive index of the substrate for any wavelengths. The substrate is not absorbent. The reflectance spectra for TE, TM and non-polarized light are presented in Figure 90. The correcting factor $\arg(r_{2-3})$ in this case is equal to -π. The thickness value given by the equation (60) is not correct in this case, with an error reaching 33% as shown in Table 24, but the corrected value given by the equation (62) corresponds to the thickness value put into the model.

<u>Remark:</u> In this case the term $\arg(r_{2-3}) - \arg(r_{1-2})$ is null (instead of being equal to π) in the equation (60) and this corresponds to an inversion of the calculation formulas for a maximum and a minimum, i.e. the formula for a maximum is used for a minimum and reciprocally.
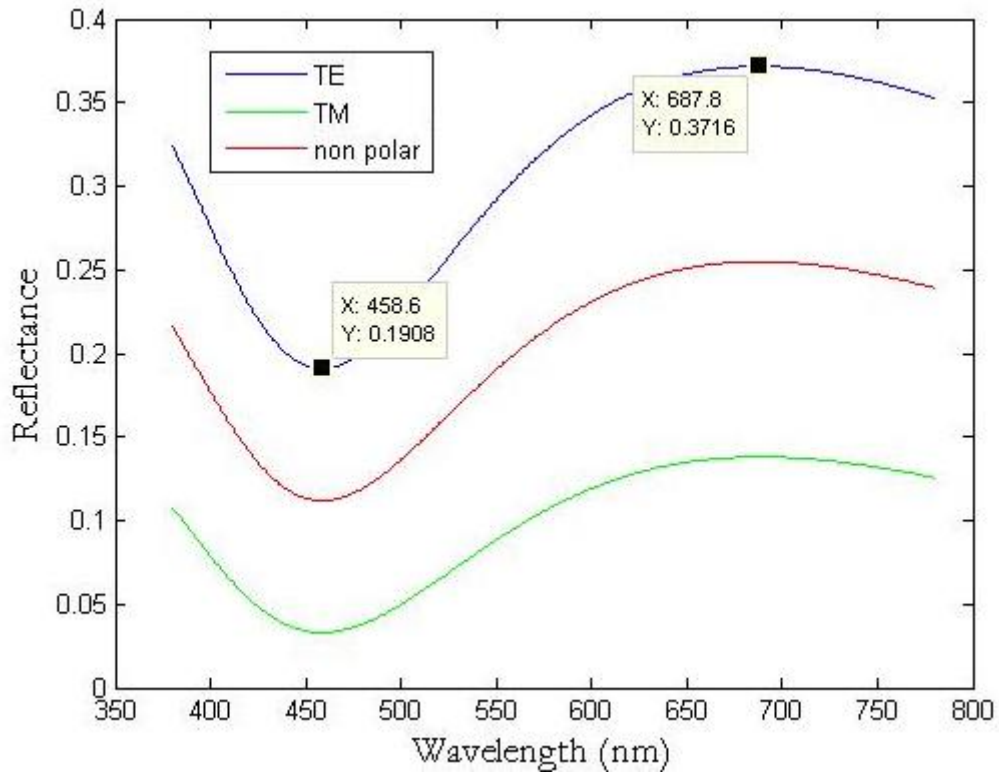
Figure 90: Modeled reflectance spectra (TE, TM and non-polarized light) of a 150 nm thick oxide layer on top of a non-absorbent substrate. The refractive indexes are $n_{TiO_2} = 2.4$ for the layer and $n_{Ti} = 3$ for the substrate. The values presented on the graph correspond to the positions of the extrema of the TE polarization reflectance.

	Extremum wavelength in nm (type)	Interference order k	$n_{TiO_2}(\lambda)$	$\theta_r(\lambda)$ (°)	$\arg(r_{2-3})$ (°)	Thickness equation (60) (nm)	Corrected thickness (62) (nm) (correction)
Extremum 1	458.6 (min)	1	2.4	17.14	-180	100	150 (50)
Extremum 2	687.8 (max)	1	2.4	17.14	-180	75	150 (75)

Table 24: Calculated thickness of a 150 nm thick layer on top of a non-absorbent substrate by using equations (60) and (62). The refractive indexes are $n_{TiO_2} = 2.4$ for the layer and $n_{Ti} = 3$ for the substrate.

iii.   Case $n_{TiO_2} = 2.4$ and and $n_{Ti} = 3 + 3i$

In this case, the real part of the refractive index of the substrate is always larger than the refractive index of the layer for any wavelengths and the substrate is absorbent. The reflectance spectra for TE, TM and non-polarized light are presented on Figure 91. The correcting factor $\arg(r_{2-3})$ in this case is equal to -132.4°. The thickness value given by equation (60) is not correct in this case, with an error reaching 27% as shown in Table 25. When the phase-shift correction coming from the Fresnel coefficients is applied, the calculated value from equation (62) corresponds to the set value.
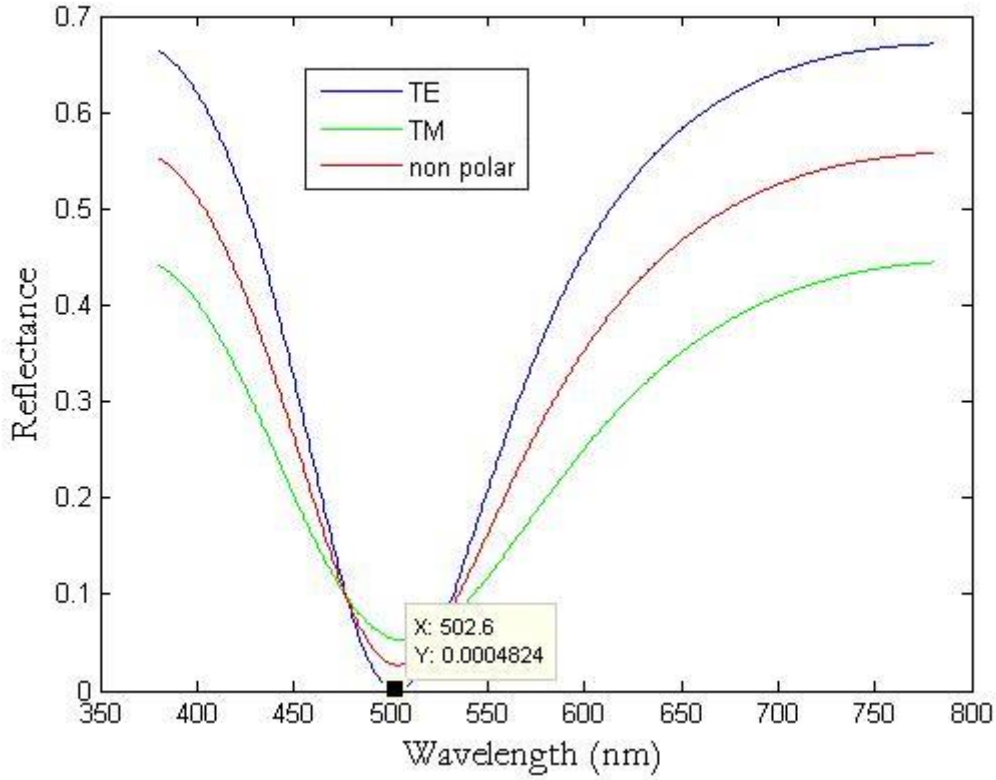
Figure 91: Modeled reflectance spectra (TE, TM and non-polarized light) of a 150 nm thick oxide layer on top of an absorbent substrate. The refractive indexes are $n_{TiO_2} = 2.4$ for the layer and $n_{Ti} = 3 + 3i$ for the substrate. The values presented on the graph correspond to the positions of the extrema of the TE polarization reflectance.

	Extremum wavelength in nm (type)	Interference order k	$n_{TiO_2}(\lambda)$	$\theta_r(\lambda)$ (°)	$\arg(r_{2-3})$ (°)	Thickness equation (60) (nm)	Corrected thickness (62) (nm) (correction)
Extremum 1	502.6 (min)	1	2.4	17.14	-132,4	109.6	149.9 (40.3)

Table 25:: Calculated thickness of a 150 nm thick layer on top of an absorbent substrate by using (61) and (63) equations. The refractive indexes are $n_{TiO_2} = 2.4$ for the layer and $n_{Ti} = 3 + 3i$ for the substrate.

iv. Case $n_{TiO_2} = 2.4$ and n_{Ti} varying linearly versus the wavelength from 2 at 380 nm to 3.3 at 780 nm.

In this case, the refractive index of the substrate is varying linearly with the wavelength starting from a value smaller than the refractive index of the layer and ending with a larger value. We also removed the imaginary part of the substrate refractive index in order to study only the effect of a crossing between the two refractive indexes. The variation of the substrate refractive index versus the wavelength is presented on Figure 92. We chose the substrate refractive index in a way that the crossing takes place (both values are equal to 2.4) in the "middle" of the visible wavelengths range (at a wavelength equal to 500 nm). The reflectance spectra for TE, TM and non-polarized light are presented in Figure 93. The estimated thickness values with equations (60) and (62) are shown in Table 26.
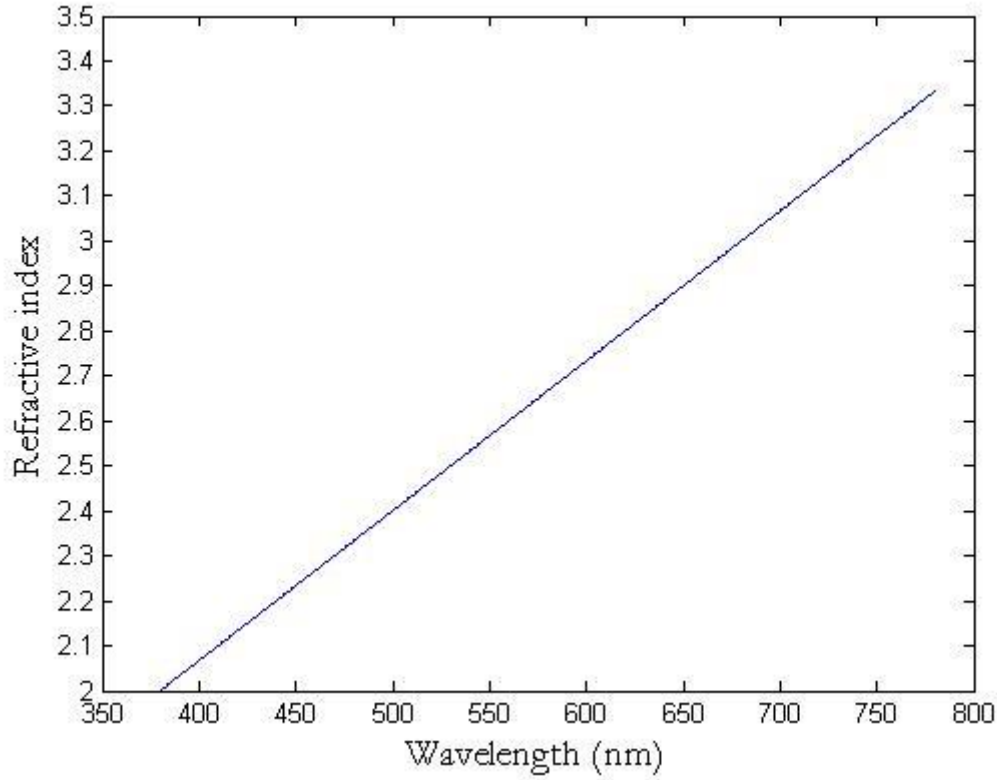
Figure 92: Linear variation of the modeled substrate refractive index from 2 at a wavelength equal to 380 nm to 3.3 at a wavelength equal to 780 nm. The refractive index is equal to 2.4 at a wavelength equal to 500 nm.

In this case, the estimation of the layer thickness is not as good as for the previous cases even with the corrected formula (62). An error up to 14% can be found, reduced to 7% when the average over all the extrema is taken. The closer the extremum wavelength is to the crossing wavelength, the higher is the error on the estimated thickness. This is due to the sudden change of the $\arg(r_{2-3})$ value at the crossing, from 0° before the crossing to -180° after. Nevertheless the error is reduced when using the corrected equation (62) compared to the non-corrected equation (60) with which the error can reach 45%.
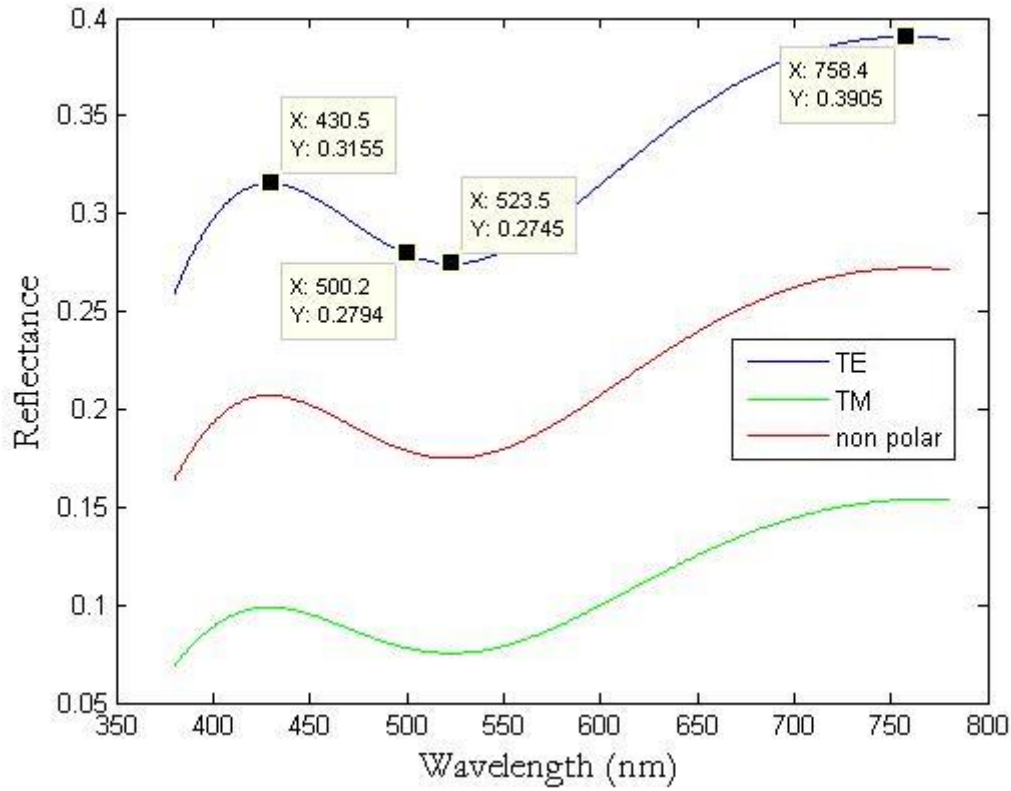
Figure 93: Modeled reflectance spectra for TE, TM and non-polarized light of a 150 nm thick oxide layer on top of a non-absorbent substrate. The refractive indexes are $n_{TiO_2} = 2.4$ for the layer and n_{Ti} varying linearly versus the wavelength from 2 at 380 nm to 3.3 at 780 nm for the substrate. The values presented on the graph correspond to the positions of the extrema of the TE polarization reflectance or to the position where the two refractive indexes cross.

	Extremum wavelength in nm (type)	Interference order k	$n_{TiO_2}(\lambda)$	$\theta_r(\lambda)$ (°)	$arg(r_{2-3})$ (°)	Thickness equation (60) (nm)	Corrected thickness (62) (nm) (correction)
Extremum 1	430.5 (max)	2	2.4 (2.17)	17.14	0	140.8	140.8 (0)
Extremum 2	523.5 (min)	1	2.4 (2.48)	17.14	-180	114.1	171.2 (+57.1)
Extremum 3	758.4 (max)	1	2.4 (3.26)	17.14	-180	82.7	165.4 (+82.7)

Table 26: Calculated thickness of a 150 nm thick layer on top of a non-absorbent substrate by using (61) and (63) equations. The refractive indexes are $n_{TiO_2} = 2.4$ for the layer and n_{Ti} varying linearly versus the wavelength from 2 at 380 nm to 3.3 at 780 nm for the substrate.

v. <u>Case $n_{TiO_2} = 2.4$ and $Re(n_{Ti})$ varying linearly versus the wavelength from 2 at 380 nm to 3.3 at 780 nm with $Im(n_{Ti}) = 3$</u>

This case corresponds to the previous case where the two refractive indexes cross each other in the "middle" of the visible wavelengths range (at 500 nm) but an imaginary part equal to 3 has been added to the substrate refractive index. The reflectance spectra for TE, TM and non-polarized light are presented on Figure 94.

The estimated thickness value is given in Table 27. The extremum is obtained at a value of 510.7 nm which is very close to the wavelength where the refractive indexes cross (500 nm). The correcting factor $\arg(r_{2-3})$ case is equal to -125.02°. Despite the fact that this crossing had a large impact on the estimated value of the layer thickness when the substrate is non-absorbent (previous case), we note that adding an imaginary part to the substrate refractive index highly improves the thickness estimation. Having a non-null imaginary part for the substrate refractive index removes the discontinuity of $\arg(r_{2-3})$ when the refractive indexes cross. The value given by equation (62) is correct whereas the value given by the equation (60) gives an error of 26%.
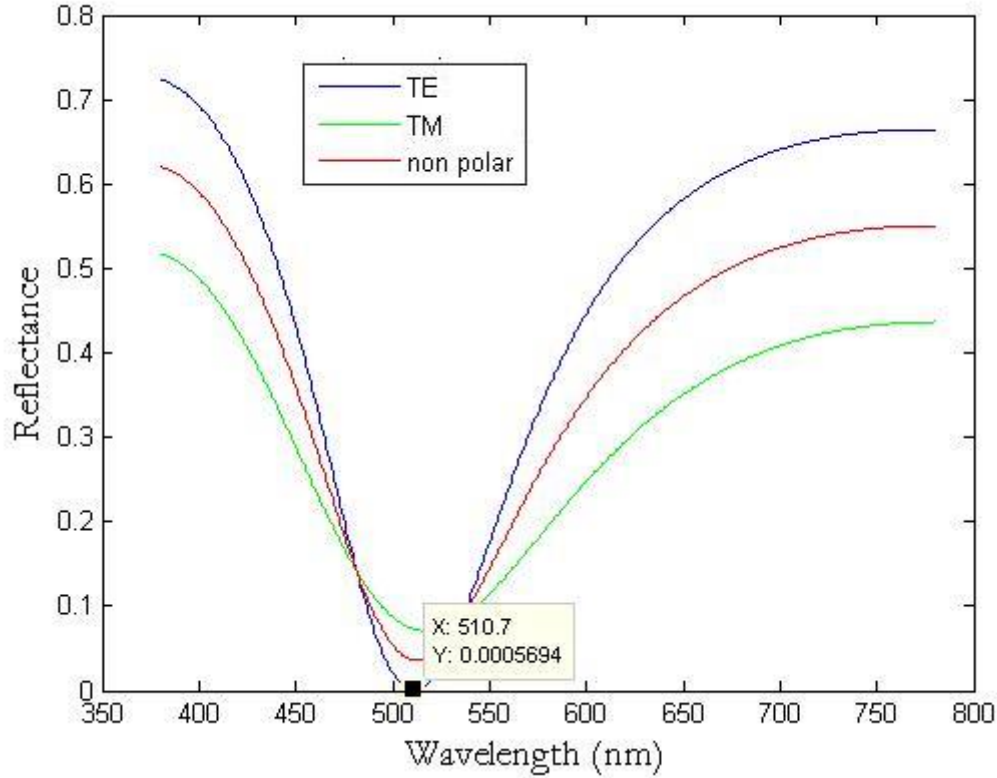
Figure 94: Modeled reflectance spectra for TE, TM and non-polarized light of a 150 nm thick oxide layer on top of a metallic substrate. The refractive indexes are $n_{TiO_2} = 2.4$ and $Re(n_{Ti})$ varying linearly versus the wavelength from 2 at 380 nm to 3.3 at 780 nm and $Im(n_{Ti})= 3$. The values presented on the graph correspond to the positions of the extrema of the TE polarization reflectance.

	Extremum wavelength in nm (type)	Interference order k	$n_{TiO_2}(\lambda)$	$\theta_r(\lambda)$ (°)	$\arg(r_{2-3})$ (°)	Thickness equation (60) (nm)	Corrected thickness (62) (nm) (correction)
Extrema 1	510.7 (min)	1	2.4 (2.44)	17.14	-125.02	111.3	150 (38.7)

Table 27 : Calculated thickness of a 150 nm thick layer on top of an absorbent substrate by using (61) and (63) equations. The refractive indexes are $n_{TiO_2} = 2.4$ varying linearly versus the wavelength from 2 at 380 nm to 3.3 at 780 nm and $Im(n_{Ti})= 3$

vi.   Case n_{TiO_2} and n_{Ti} taken from [72]
      Thickness estimation from the TE reflectance extrema

Our thickness estimation methods are then applied to the case presented in section 3)a) in which the refractive indexes were taken from [72]. This corresponds to a sample made of a layer of

titanium dioxide on the top of titanium substrate. The TiO$_2$ refractive index crosses the Ti refractive index at the border of the visible wavelengths range (784 nm see Figure 85). The reflectance spectra for TE, TM and non-polarized light are presented on Figure 95. The TiO2 refractive index and both the real and imaginary part of the titanium substrate are dependent of the wavelength. The estimated thickness values with equations (60) and (62) are shown in Table 28.
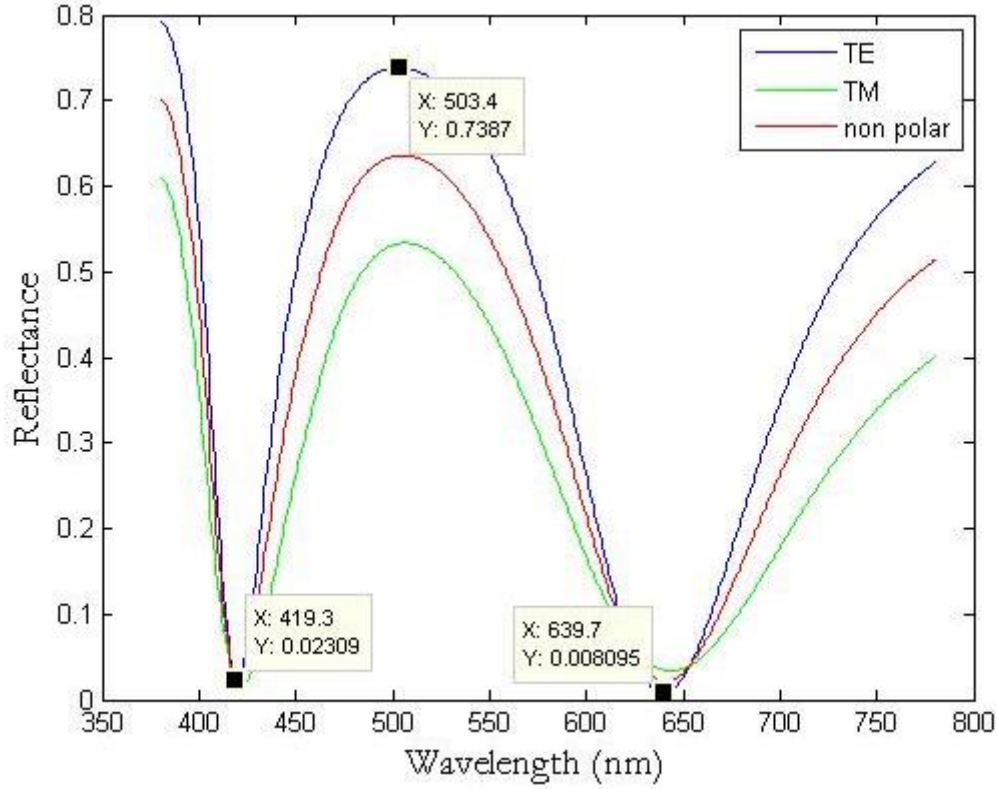
Figure 95: Modeled reflectance spectra for TE, TM and non-polarized light of a 150 nm thick TiO$_2$ layer on top of a titanium substrate. The refractive index are extracted from the reference [72]. The values presented on the graph correspond to the positions of the extrema of the TE polarization reflectance.

	Extremum wavelength in nm (type)	Interference order k	$n_{TiO_2}(\lambda)$	$\theta_r(\lambda)$ (°)	$\arg(r_{2-3})$ (°)	Thickness equation (60) (nm)	Corrected thickness (62) (nm) (correction)
Extrema 1	420.1 (min)	2	3.19 (1.62+2.2i)	12.81	-81.76	135.1	150.4 (15.3)
Extrema 2	503.4 (max)	2	3.03 (1.8+2.44i)	13.5	-92.61	128.1	150.1 (22)
Extrema 3	639.7 (min)	1	2.87 (2.19+2.96i)	14.26	-109.61	115	150.1 (35.1)

Table 28: Calculated thickness of a 150 nm thick TiO$_2$ layer on top of a titanium substrate by using (61) and (63) equations. The TiO$_2$ and Ti refractive indexes are extracted from the reference [72].

The estimated thickness values with the corrected equation (62) are really close (less than 1 nm) to the oxide layer thickness value set as parameter for the model. The error with the non-corrected equation (60) can reach 23%.

<u>Comparison between TE, TM and non-polarized reflectance extrema</u>

On Figure 96, it is possible to see that the reflectance spectrum reaches an extremum at slightly different wavelengths for TE, TM and non-polarized light. As the anodized titanium samples reflectance is usually measured with a non-polarized light, it is interesting to study the influence of the extrema shift for non-polarized light on the estimation of the oxide layer thickness.
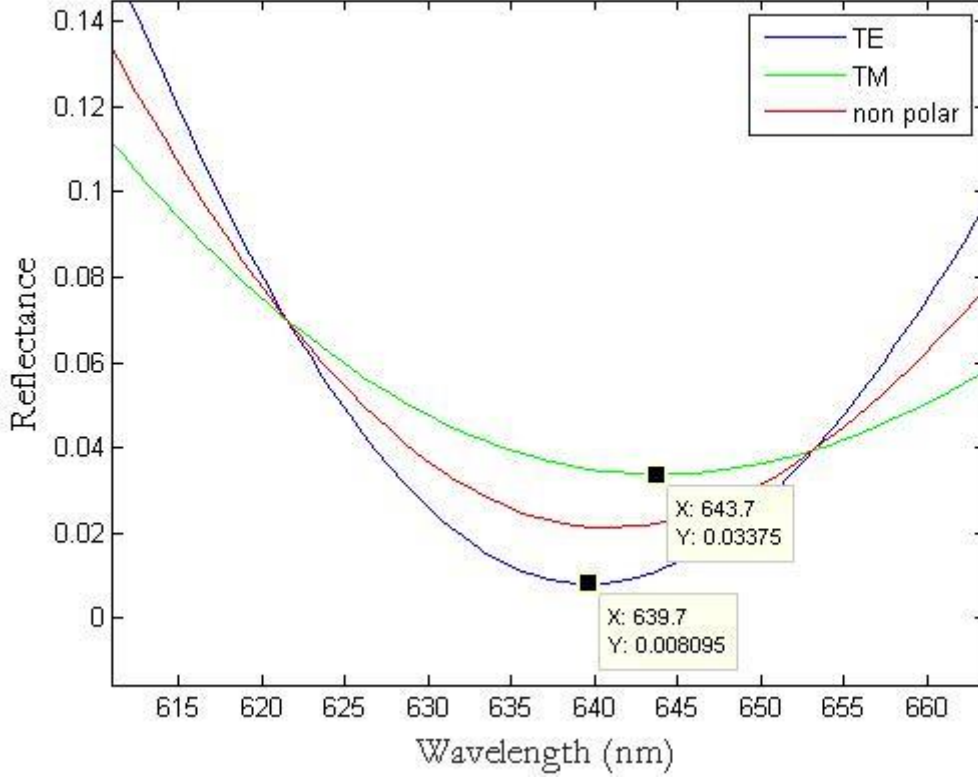
Figure 96: Zoom on the last extremum of Figure 95. The values presented on the graph correspond to the positions of the extremum in the TE and TM polarizations.

At a minimum we can write for TE polarization by using equation (61) with $\arg_{TE}(r_{1-2}) = -\pi$:

$$(2k + 1)\pi = \frac{2\pi}{\lambda} 2n_{TiO_2}(\lambda)ecos\theta_r(\lambda) + \arg(r_{2-3}^{TE}) + \pi \tag{64}$$

where r_{2-3}^{TE} is the Fresnel coefficient for TE polarization at the TiO$_2$/Ti interface.
Thus we have:

$$\lambda_{min}^{TE} = \frac{4\pi n_{TiO_2}(\lambda_{min}^{TE}) \times e \times \cos(\theta_r(\lambda_{min}^{TE}))}{2k\pi - \arg(r_{2-3}^{TE}(\lambda_{min}^{TE}))} \tag{65}$$

where λ_{min}^{TE} is the position of the kth extremum of the TE polarization reflectance.
Similarly, for TM polarization we have:

$$\lambda_{min}^{TM} = \frac{4\pi n_{TiO_2}(\lambda_{min}^{TM}) \times e \times cos\theta_r(\lambda_{min}^{TM})}{(2k + 1)\pi - \arg(r_{2-3}^{TM}(\lambda_{min}^{TM}))} \tag{66}$$

101

The difference of position between the kth extremum is defined TE and TM polarization by $\Delta\lambda(k)$:

$$\Delta\lambda(k) = \lambda_{min}^{TM} - \lambda_{min}^{TE} = 4\pi e \left[\frac{n_{TiO_2}(\lambda_{min}^{TM}) \times cos(\theta_r(\lambda_{min}^{TM}))}{(2k+1)\pi - \arg(r_{2-3}^{TM}(\lambda_{min}^{TM}))} - \frac{n_{TiO_2}(\lambda_{min}^{TE}) \times cos\theta_r((\lambda_{min}^{TE}))}{2k\pi - \arg(r_{2-3}^{TE}(\lambda_{min}^{TE}))} \right] \qquad (67)$$

In our case the numerical application gives $\Delta\lambda = 5.2$ nm (see Table 29 for the parameters values).

	Extremum position (nm)	$n_{Ti}(\lambda)$	$n_{TiO_2}(\lambda)$	θ_r (°)	$\arg(r_{2-3})$ (°)	k
TM polarization	643.7	2.2+2.971i	2.867	14.279	74.569	1
TE polarization	639.7	2.186+2.958i	2.869	14.268	-109.558	1

Table 29: Parameters used to calculate the extremum position difference $\Delta\lambda$ between TE and TM polarization.

If we take into account an estimation error of about 1 nm on the extrema values read on Figure 96 due to the sampling interval, the estimated value of $\Delta\lambda$ is in agreement with the 4 nm read on Figure 96. This difference of position between the minimum in TE and TM polarizations is induced by the difference between the arguments of the Fresnel coefficients in TE and TM polarization. It corresponds to the difference between the two terms $\pi - \arg(r_{2-3}^{TM})$ and $-\arg(r_{2-3}^{TE})$ in equation (67). Figure 97 represents the difference in the current studied case (parameters indicated in Table 29).
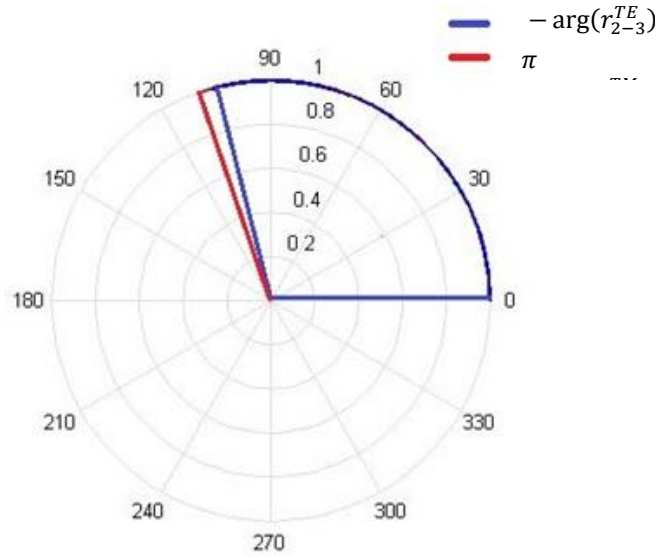
Figure 97: Angular representation of the terms $\pi - \arg(r_{2-3}^{TM})$ and $-\arg(r_{2-3}^{TE})$ in the case presented on **Erreur ! Source du renvoi introuvable.** explaining the difference of position between TE and TM extrema.

We already showed that the corrected equations (62) are able to give a very good estimation of the oxide layer thickness with an incident TE polarized light. As the goniospectrophotometer measurements are made with a non-polarized incident light, we will now estimate the error on the oxide layer estimation for a non-polarized reflectance spectrum.

We consider the non-polarized spectrum of Figure 86, from which we extract the extrema positions. The corrected equations (62) are then applied to compute the thickness value. First the phase-shift taken into account for the correction is $\arg(r_{2-3}^{TE}(\lambda))$, which is the phase-shift for

TE polarized light. Then, to obtain a more accurate correction the phase-shift taken into account is:

$$\partial \varphi_{corr}(\lambda) = \frac{1}{2} [\arg(r_{2-3}^{TE}) + \arg(r_{2-3}^{TM}) - \pi)]$$

(68)

We first applied the corrected equations with the two different phase-shits to the modeled reflectance spectrum obtained with the refractive indexes extracted from the reference [72]. The results are presented in Table 29.

	Extremum position in nm (type)	Interference order k	$n_{TiO_2}(\lambda)$ $n_{Ti}(\lambda)$	$\arg(r_{2-3}^{TE}(\lambda))$ $[\arg\left(r_{2-3}^{TM}(\lambda)\right)$ $-\pi]$ (°)	$\delta\varphi_{corr}(\lambda)$ (°)	Thickness corrected with $\arg(r_{2-3}^{TE}(\lambda))$	Thickness corrected with $\delta\varphi_{corr}(\lambda)$ (nm)
Extremum 1	420.1 (min)	2	3.19 1.62+2.2i	-81.76 [-76.27]	-79.02	150.4	149.9
Extremum 2	505.1 (max)	2	3.03 1.8+2.44i	-92.61 [-87.39]	-90	150.9	150
Extremum 3	640.5 (min)	1	2.87 2.19+2.96i	-109.61 [-105.08]	-107.35	150.2	149.5

Table 29: Calculated thickness of a 150 nm thick TiO₂ layer on top of a titanium substrate by using the two correction methods for a non-polarized incident light. The first method takes into account the correction phase-shift for TE polarized light $arg(r_{2-3}^{TE}(\lambda))$ and the second one the correction phase-shift $\partial\varphi_{corr}(\lambda)$. The refractive indexes are taken from [72].

The thickness values estimated through both correction methods are correct, even when only considering the TE polarization correction $arg(r_{2-3}^{TE}(\lambda))$. We have to bear in mind that we compare here the evaluated thickness with the thickness value put in our model, in which we know exactly the refractive index values of the materials. This will not be the case with "real" materials, so an error of ± 1 nm is totally acceptable.

vii. Oxide layer estimation from the extrema of the spectral BRDF of our titanium anodized samples.

We will now apply our corrected estimation methods to the spectral BRDF measurements of the samples presented in the section III 1). The results are presented in Table 30. Once again, the refractive indexes are taken from [72].

As for the modeled TiO₂/Ti sample, we observe that the thickness values obtained with TE phase-shift correction $arg(r_{2-3}^{TE}(\lambda))$ and the ones obtained with $\delta\varphi_{corr}$ phase-shift correction are the same. Nevertheless, particularly for the 90 V etched sample, the oxide layer thickness values obtained through different extrema are different. For this sample, the oxide layer averaged over all the extrema is 185.7 nm for the $\delta\varphi_{corr}$ correction with a standard deviation of 7%. Discrepancies between the oxide thicknesses obtained from different extrema could be due to the fact the refractive indexes of our material are different from those taken from the litterature [72].

	Extremum position in nm (type)	Interference order k	$n_{TiO_2}(\lambda)$ $n_{Ti}(\lambda)$	$\arg(r^{TE}_{2-3}(\lambda))$ [$\arg(r^{TM}_{2-3}(\lambda))$ $-\pi$] (°)	$\delta\varphi_{corr}(\lambda)$ (°)	Thickness corrected with $\arg(r^{TE}_{2-3}(\lambda))$	Thickness corrected with $\delta\varphi_{corr}(\lambda)$ (nm)
10 V Ref	390 (min)	0	3.39 (1.52+2.13i)	-74.84 [-69.41]	-72.13	12.2	11.8
10 V Etc	435 (min)	0	3.16 (1.65+2.24i)	-83.66 [-78.21]	-80.94	16.4	15.9
90 V Ref	445 (max)	2	3.15 (1.68+2.26i)	-84.68 [-79.29]	-81.98	125.8	125.2
	550 (min)	1	2.96 (1.89+2.62i)	-98.88 [-93.59]	-96.12	122.0	121.2
90 V Etc	430 (max)	3	3.17 (1.65+2.23i)	-83.22 [-77.78]	-80.50	190.0	189.5
	470 (min)	2	3.11 (1.74+2.33i)	-87.79 [-82.52]	-85.16	174.1	173.6
	630 (max)	2	2.88 (2.15+2.97i)	-108.99 [-104.43]	-106.71	203.4	202.7
	730 (min)	1	2.82 (2.56+3.24i)	-118.44 [-114.42]	-116.43	177.7	177

Table 30: Calculated TiO₂ layer thickness from the extrema of the spectral BRDF of anodized titanium samples presented in section II 3) a) with the two correction methods with correction phase shifts equal to $\boldsymbol{arg(r^{TE}_{2-3}(\lambda))}$ and $\boldsymbol{\partial\varphi_{corr}(\lambda)}$. The refractive indexes are extracted from the reference [72].

Oxide layer thicknesses estimated from the extrema of the spectral BRDF with the corrected equation (62) with a correction phase-shift $\delta\varphi_{corr}$ for non-polarized incident light are close to the oxide layer thickness estimated through the Abeles model fit presented in the section 2) as shown in Table 31.

	Extremum wavelength in nm (type)	Thickness corrected with $\arg(r^{TE}_{2-3}(\lambda))$ (nm)		Thickness corrected with $\delta\varphi_{corr}(\lambda)$ (nm)		Thickness obtained through simple Abeles fit / fit with thickness variations (nm)
10 V Ref	390 (min)	12.2		11.8		11.9 / 12.1±5
10 V Etc	435 (min)	16.4		15.9		18 / 17.1±1.5
90 V Ref	445 (max) 550 (min)	125.8 122.0	Avg=123.9 Std=2.7	125.2 121.2	Avg=123.2 Std=2.8	123.2 / 121±30
90 V Etc	430 (max) 470 (min) 630 (max) 730 (min)	190.0 174.1 203.4 177.7	Avg=186.3 Std=13.3	189.5 173.6 202.7 177	Avg=185.7 Std=13.2	188.7 / 203.8±70.4

Table 31 : Comparison between the thickness values estimated with the correction phase-shifts equal to $\boldsymbol{arg(r^{TE}_{2-3}(\lambda))}$ and $\boldsymbol{\partial\varphi_{corr}(\lambda)}$ and with the two Abeles matrices based fits, with and without taking into account possible thickness variations, on the samples presented in the section III 1). The average and standard deviation of the oxide thickness over the different extrema are also indicated.

Note that the refractive indexes for TiO₂ and Ti are taken from [72] and might not correspond to our samples. These refractive index values are used in both models possibly inducing an error on the thickness value estimations of our samples.

Remark: The estimated value of the thickness of the sample anodized at 10 V and etched in HF/HNO₃ is equal to 15.9 nm and is consistent with a value reported in [79] (16 nm for an etched sample anodized in similar conditions at a cell potential of 11 V).

4) Discussion about the choice of the Ti and TiO_2 refractive indexes

The reflectance spectra of the non-anodized titanium non-etched and etched samples are presented on the Figure 98, as well as an Abeles modeled spectrum for bulk Ti with refractive indexes given in [72]. The shapes of the modeled spectrum and the experimental spectra are different, implying that the refractive indexes of our material might be different than the ones in [72]. Note that the discrepancies between the spectra shapes observed on Figure 98 might also be simply due to the goniometer chromatic aberration (see hereafter).
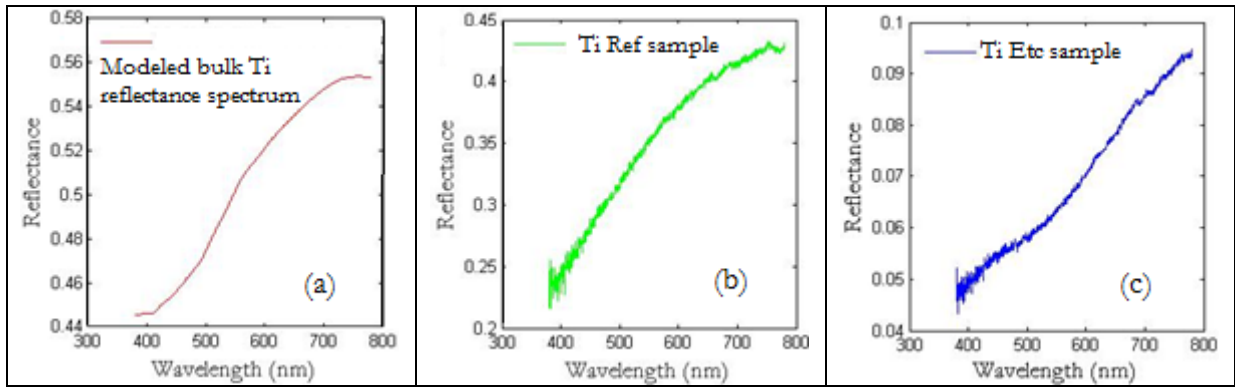
Figure 98: Reflectance spectra of non-anodized titanium samples: (a) modeled with Abeles matrices with Ti refractive index from [72]; (b) computed from the spectral BRDF measurements of the non-anodized non-etched titanium sample (Ref); (c) of the non-anodized etched titanium sample (Etc).

Also, the spectrum shape of the etched titanium sample (Ti Etc) is different from the spectrum shape of the non-etched titanium sample (Ti Ref), implying that HF/HNO₃ etching might have an influence on the titanium refractive index. Nevertheless, these preliminary observations have to be confirmed by additional experiments. We characterized the reflectance spectra of the titanium etched sample out of the specular condition by varying the observation angle ±1° around the specular direction (see Figure 99). To compare the shape of the spectra, each spectrum was rescaled by dividing each spectrum by its average over the visible wavelength range [380 nm -780 nm]. The spectra obtained for angles far from the specular direction are more impacted by the noise, in particular in the wavelengths corresponding for the blue color. In fact, the light intensity is low in this spectrum region and the signal-to-noise ratio is less good.
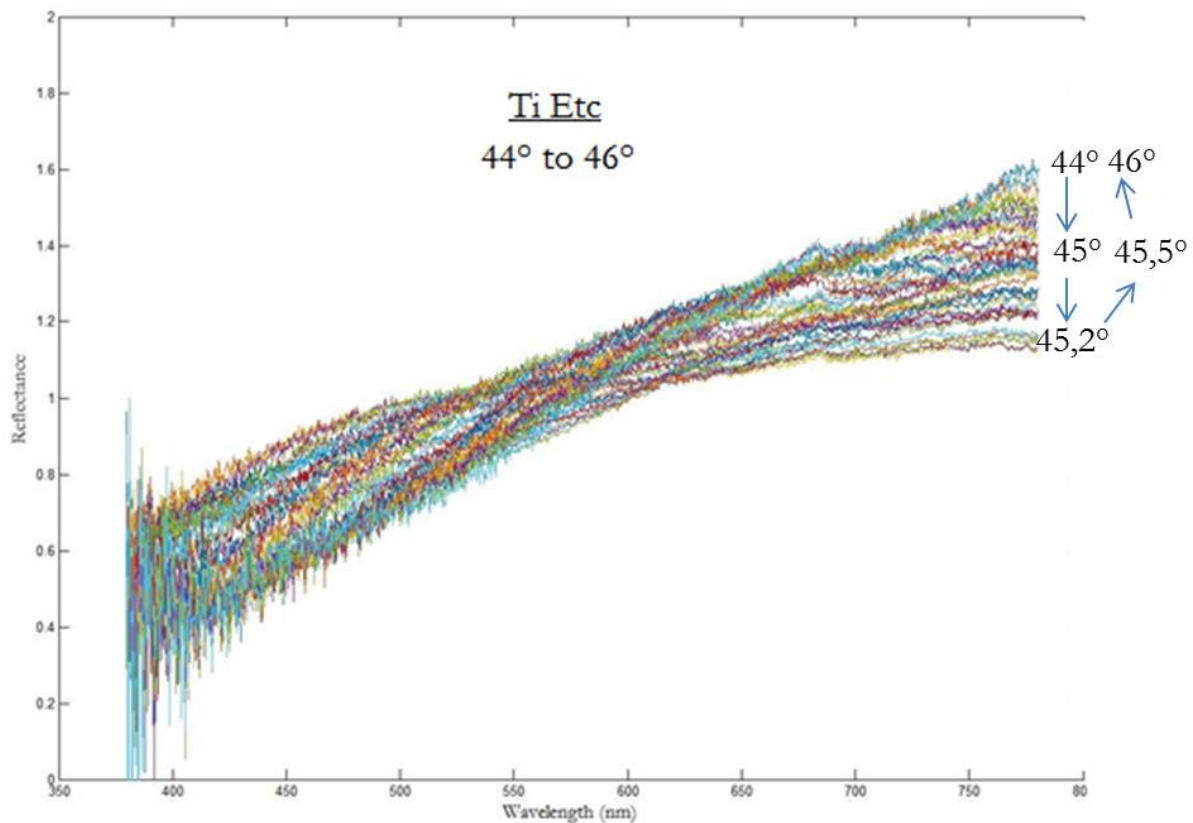
Figure 99: Normalized reflectance spectra of the titanium etched sample for an incidence angle of 45° with observation angles ranging from 44° to 46°. To compare the shape of the spectra, each spectrum was rescaled by dividing each spectrum by its average over the visible wavelength range [380 nm -780 nm].

We observe on Figure 99 that for observations angles far from the specular direction the reflectance spectra have lower values on the "blue" wavelengths (around 450 nm) and higher values on the "red" wavelengths (around 700 nm) than the reflectance spectra close to the specular direction. This could be explained by the chromatic aberration of the goniometer optical system. The chromatic aberration is the fact that a lens fails to focus all colors to the same convergence point (see Figure 100) because of the dispersion of the refractive index of the lens glass. Considering a position of the goniometer detector at the "blue focus", we observe that close to the lens optical axis the detector will get more signal from the "blue" wavelengths, as for the "close to the specular" spectra, whereas further from the optical axis, the detector will get more signal for the "red" wavelengths as for the "far from specular" spectra.
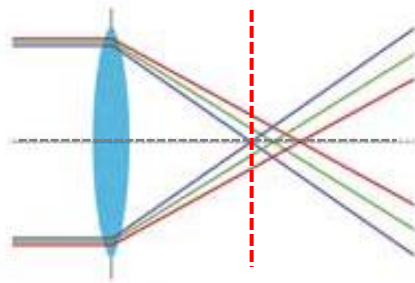
Figure 100: Chromatic aberration: due to the dispersion of the lens glass refractive index, the lens is unable to focus all the wavelengths at the same point. The dashed line represents the goniometer detector position.

In this section, we studied the spectral variations of the samples BRDF and explored different ways to deduce the oxide layer thickness from these variations. We will now analyze their angular variations.

V. BRDF measurements of the different samples with the goniospectrophotometer Optimines: analysis of the angular variations

Important note: in this section θ_r denotes the observation angle and not the refracted angle as in the previous sections.

1) General observations

Figure 101 shows the average BRDF on the visible wavelengths range as a function of the angle of observation θ_r for our six samples. As the BRDF variations with the wavelength have various shapes for the different samples, we decided to represent the average BRDF (instead of taking a single wavelength) over the entire visible wavelength range (380 nm to 780 nm) to be able compare the different samples. The incidence angle is fixed at 45°. The results are presented in the angular range of 44° to 46°. In all cases, the BRDF exhibits a peak centered at 45° attesting for a specular behavior of the sample. We also observe that the maximum values of the BRDF are lower for the etched samples than for the non-etched ones. Also the etched samples BRDF exhibits "wings" around the peak which are not visible for the non-etched ones.

Figure 102 illustrates a comparison between the BRDF values of the 90 V etched sample (Etc) and the 90 V non-etched sample (Ref) close to and far from the specular direction. On Figure 102 (a) we can observe that the values of the BRDF are lower in the case of the non-etched sample than for the etched sample when the angle of observation is more than 0.4° away from the specular direction. The etched sample BRDF has thus a more important diffuse part that the non-etched one. On Figure 102 (b) we can observe that the values of the BRDF are higher in the case of the non-etched sample than for the etched sample when the angle of observation is closer to the specular direction, confirming the more specular behavior of the non-etched sample.
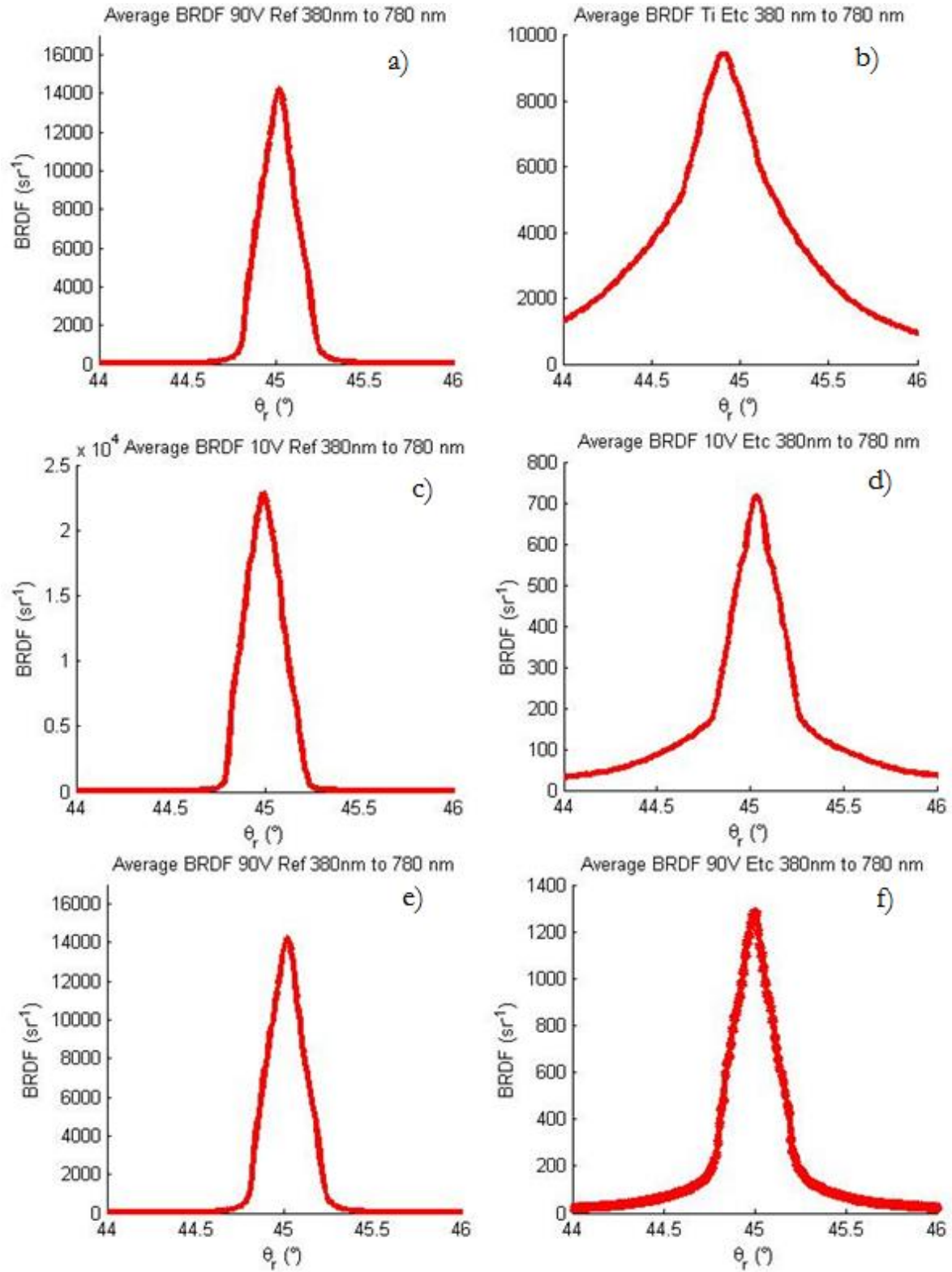
Figure 101: Average BRDF on the visible wavelengths (380 nm to 780 nm) versus the observation angle θ_r of the mirror polished samples (Ref) and of the etched (in HF/HNO$_3$ for 30 seconds after mirror polishing) samples (Etc). BRDF of the non-anodized samples Ref (a) and Etc (b). BRDF of the 10 V anodized Ref (c) and Etc (d) samples and of the 90 V anodized Ref (e) and Etc (f) samples. Anodizing parameters are a 0.5M H$_2$SO$_4$ solution and a current density of 40 mA/cm². Note that the y axis scale can be different between the graphs.
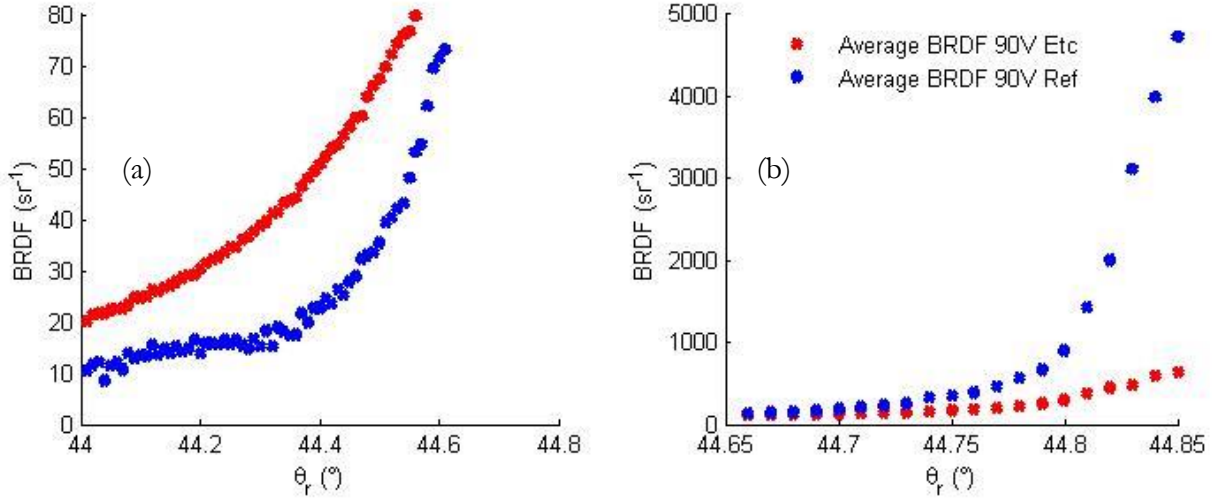
Figure 102: Comparison of the BRDF measurements of the etched sample and reference non-etched samples anodized at 90 V in 0.5M H₂SO₄ solution with a 40 mA/cm² current density. Subfigure (a) is used compare the BRDF values in the "out of specular" angular range and subfigure (b) is used to observe the "close to the specular" values.

2) Analysis of the non-etched sample BRDF

In order to quantify the amount of diffuse and specular contributions to the BRDF peaks as well as to characterize the Full Width at Half Maximum (FWHM) of the peak we fitted the BRDF of the different samples with a Gaussian function:

$$ y = y_0 + \frac{A exp\left(-2 \times \left(\frac{x - x_c}{w}\right)^2\right)}{\left(w \times \sqrt{\frac{\pi}{2}}\right)} \tag{69} $$

where x_c is the position of the center of the peak, $w\sqrt{2ln2}$ is the FWHM and A is the integral under the curve. This fit is obtained through a Levenberg-Marquardt algorithm.

Figure 103 shows the BRDF of the non-etched and non-anodized reference sample (black curve) as well as its Gaussian fit (red curve). The parameters of the Gaussian function are represented in a table on the figure.

y0	8
xc	44,98
w	0,21
A	10793
FWHM	0,24
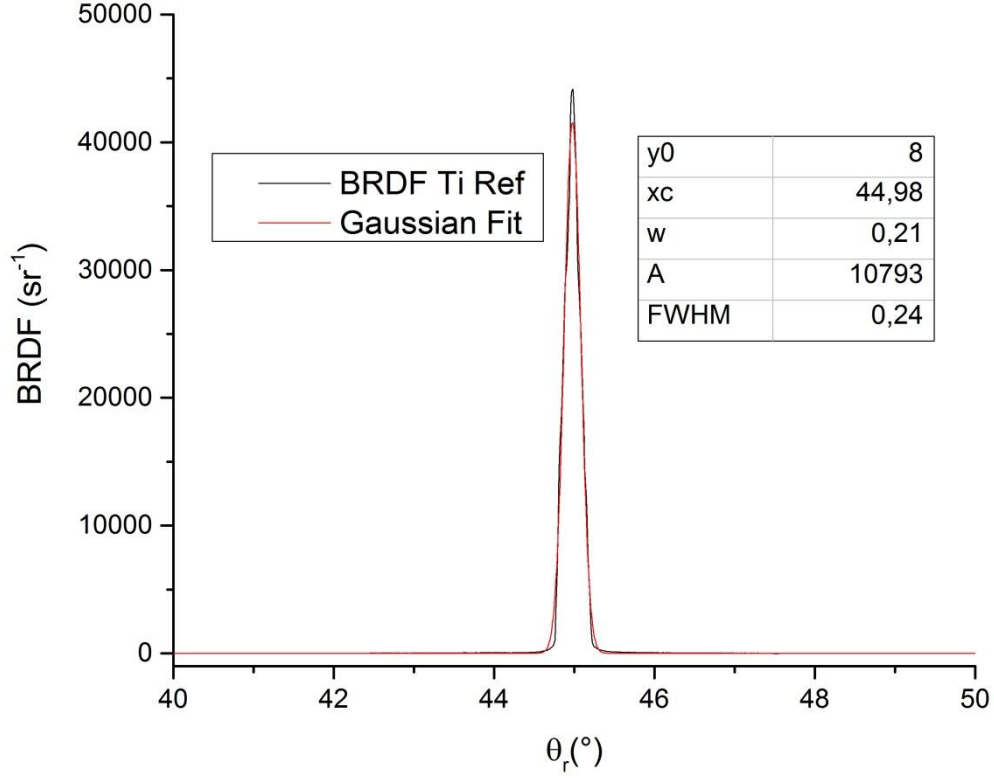
Figure 103: Gaussian fit (red curve) of the BRDF of the non-anodized non-etched sample (black curve). The parameters of the Gaussian function obtained through the fit algorithm are shown in a table in the right corner of the figure.

The same operation was conducted for all the non-etched samples (See appendix E) and the FWHM values are reported in Table 32. In any cases the value of the FWHM is roughly equal to 0.24°, which corresponds to the angular resolution of our goniospectrophotometer.

	FWHM of the Gaussian fit
Ti Ref sample	0.24°
10 V Ref sample	0.24°
90 V Ref sample	0.25°

Table 32: Full Width at Half Maximum (FWHM) values of the Gaussian fit of all the non-etched samples.

This means that for the non-etched samples the angular shape of the BRDF is not a characteristic feature of the sample. The BRDF maximum value thus corresponds to the total flux reflected by the sample divided by the source solid angle, the cosine of the incidence angle and the total incident flux (see Chapter I II 3) e)). Thus, the total reflectance of the sample $\rho(\theta_i, \lambda)$ can be computed with the following equation:

$$\rho(\theta_i, \lambda) \ = \ BRDF\ (\theta_i, \theta_r = \theta_i, \lambda) \times \Omega_s \times cos\ (\theta_i) \qquad (70)$$

where Ω_s is the source solid angle (12.10^{-6}sr) and θ_i the value of the incidence angle.

3) Analysis of the etched sample BRDF

In the case of the etched samples, a simple Gaussian function does not fit properly the BRDF. A more complex fitting procedure is proposed to characterize these peaks. To first extract the diffuse part of the BRDF, a baseline is extracted by interpolating 14 points on the BRDF excluding an angular range around the specular direction. By looking at Figure 101, it is possible to see a curve slope change on the BRDF of the etched samples: the excluded angular range around the specular direction excluded corresponds to this curve slope change. The baseline is obtained by interpolating the curve on both sides. Then the baseline is subtracted from the BRDF data and the resulting data are fit with the previous Gaussian function (equation (61)). The FWHM of the Gaussian fit is extracted to measure the width of the peak. Its parameter A is also extracted and will be noted "A specular" in the following.

Figure 104 shows the fit of the BRDF of the etched non-anodized sample: we can observe in black the BRDF measured with the goniospectrophotometer, the baseline is in blue and the sum of the fitted baseline and the Gaussian fit of the baseline-subtracted experimental data is in red. On the right of the figure, the values of the Gaussian function parameters are also given.
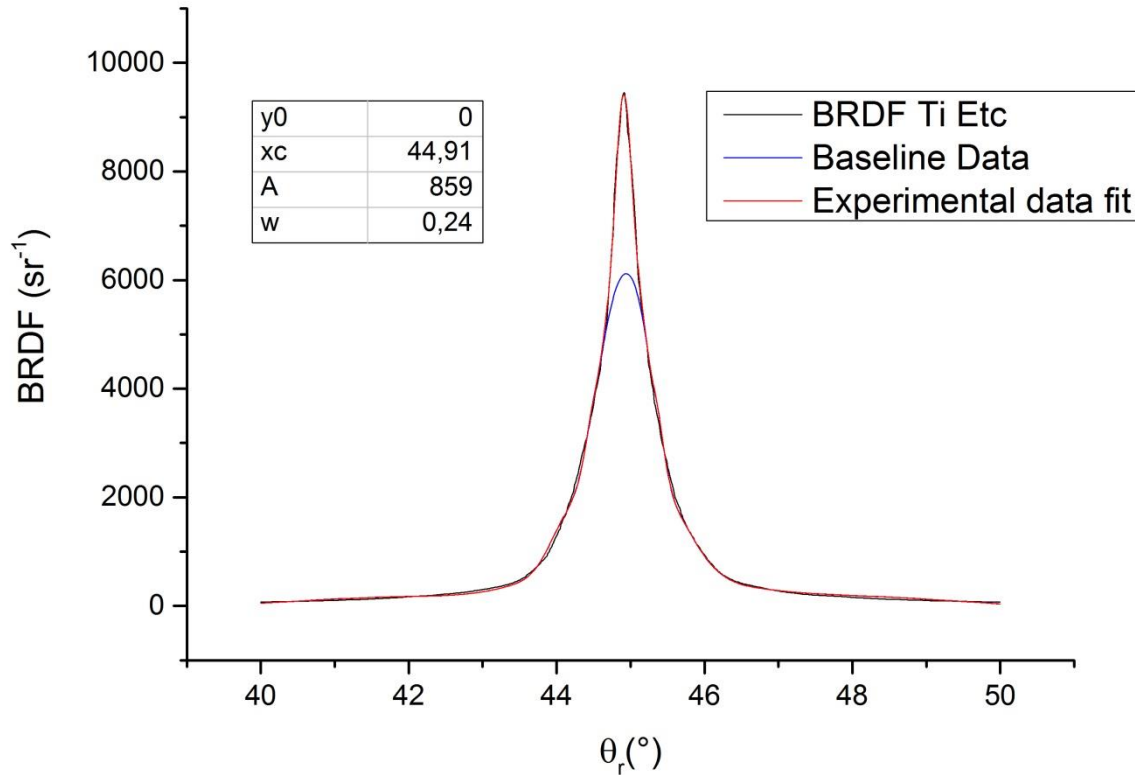
Figure 104 : Fit of the BRDF of the non-anodized titanium etched sample with the separation of the diffuse and the specular contributions: baseline (blue curve), Gaussian fit of the baseline-subtracted experimental data summed with the baseline, called here "experimental data fit", (red curve) and experimental BRDF (black curve). The values of the Gaussian function parameters are presented in the table on the top left corner of the figure.

To quantify the amount of diffuse and specular contributions to the BRDF, the baseline will also be fitted. We first tried to apply a Gaussian fit on the baseline (see Figure 105).
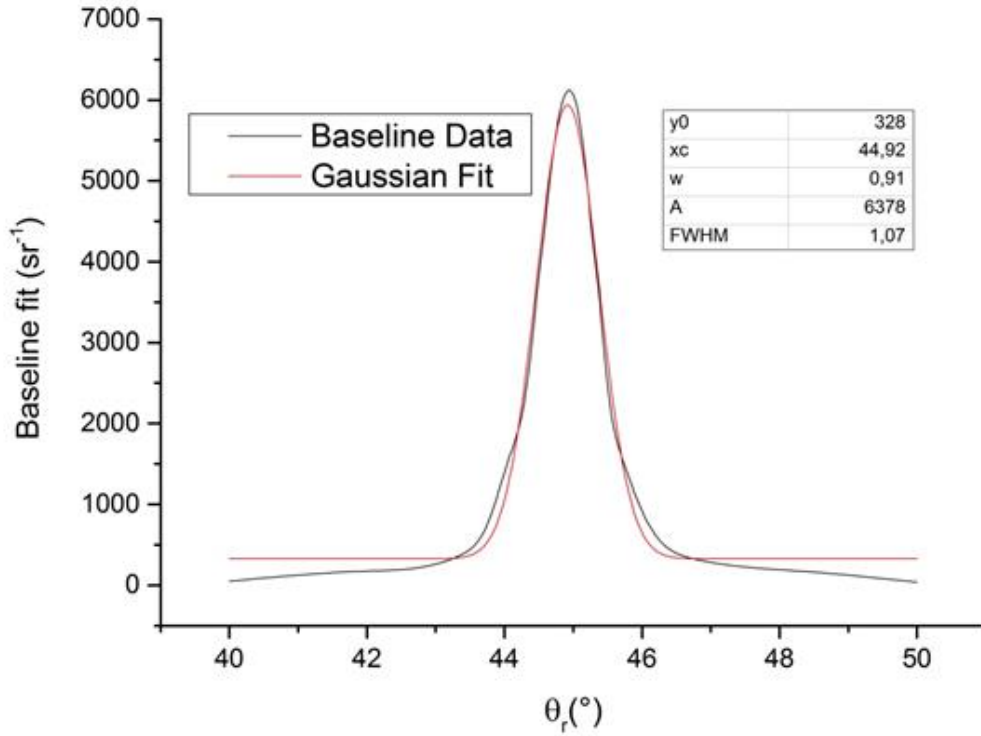
Figure 105: Gaussian fit of the baseline for the non-anodized titanium etched sample. The values of the Gaussian function parameters are presented in the table on the top right corner of the figure.

The Gaussian fit of the baseline in the out of angular range [40°-44°]U[46°-50°] is not optimal. In order to optimize the fit, we decided to use a Lorentzian function, defined as:

$$y = y_0 + \frac{2Aw}{w^2 + 4(x - x_c)^2} \times \frac{1}{\pi}$$

(71)

where x_c is the position of the center of the peak, w is the FWHM and A is the integral under the curve. This fit is obtained through a Levenberg-Marquardt algorithm. The fit is then applied to the baseline as on Figure 105 (see Figure 106). Even if it is not perfect the Lorentzian function offers a better fit in the out of specular angular range [40°-44°]U[46°-50°] than the Gauss function.

The same operation, i.e.: Gaussian fit of the baseline-subtracted experimental data summed with the baseline, has been performed on all the etched samples and the graphs can be found in the Appendices F and G. The Lorentzian function was found to offer a better fit of the baseline than the Gaussian one for all etched samples thus only the Lorentzian fits are presented in the Appendices. The values of the baseline and baseline-subtracted experimental data FWHM are reported in Table 33. They are respectively denoted diffuse and specular FWHM. This figure also shows Lorentzian A parameters for the baseline ($A_{diffuse}$) and the Gaussian A parameter for the baseline subtracted experimental data ($A_{specular}$). The relative contribution of the diffuse part to the BRDF is quantified by the ratio:

$$C_{diffuse} = \frac{A_{diffuse}}{A_{diffuse} + A_{specular}}$$

(72)

112

Note that the contribution of the specular part is then 1 - $C_{diffuse}$.
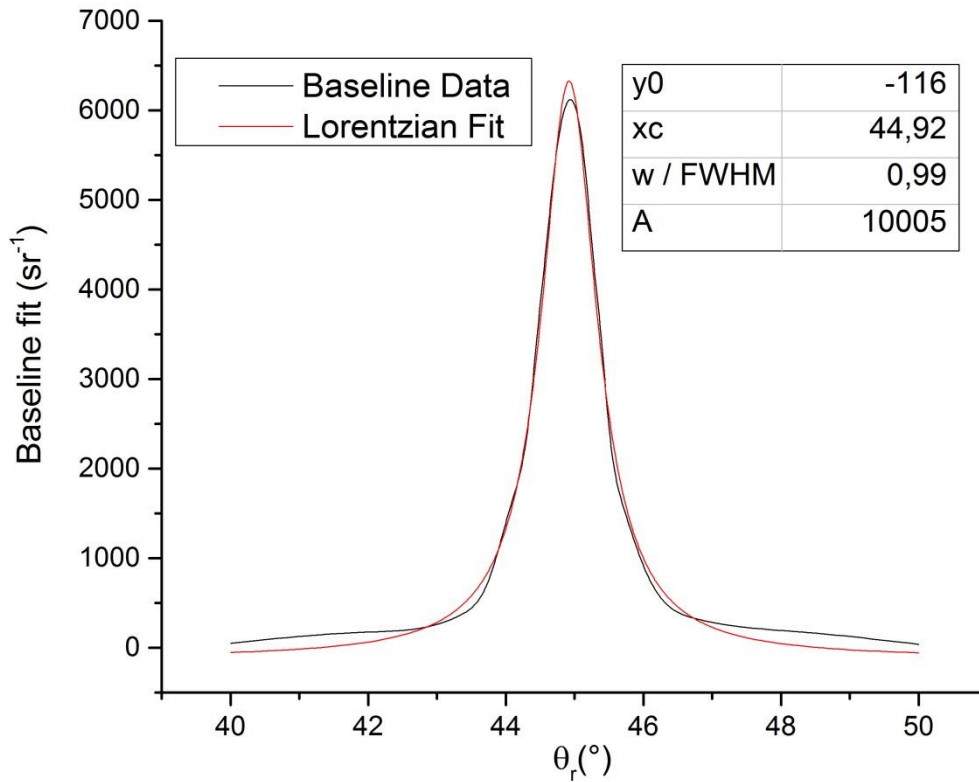
Figure 106: Baseline Lorentzian fit for the non-anodized titanium etched sample. The values of the Lorentzian function parameters are presented in the table on the top right corner of the figure.

	Diffuse FWHM	Specular FWHM	$A_{diffuse}$ (sr^{-1})	$A_{specular}$(sr^{-1})	$C_{diffuse}$
Ti Etc sample	0.99°	0.24°	10005	859	0.92
10 V Etc sample	0.84°	0.25°	286	136	0.68
90 V Etc sample	0.57°	0.23°	264	245	0.52

Table 33 : Full Width at Half Maximum (FWHM) values Lorentzian fit of the baseline and of the Gaussian fit of the baseline subtracted experimental data, called respectively diffuse and specular FWHM, for the etched samples. Are also presented the Lorentzian A parameters for the baseline ($A_{diffuse}$) and the Gaussian A parameter for the baseline subtracted experimental data ($A_{specular}$) as well as the diffuse contribution $C_{diffuse}$.

We observe that the diffuse FWHM and $C_{diffuse}$ are the largest for the non-anodized sample and the lowest for the 90 V anodized sample. In all cases, the specular FWHM is really close to the goniometer angular resolution, attesting for a good decoupling of the diffuse and specular contributions to the BRDF.

For all the etched samples the diffuse FWHM is between 2 and 4 times higher than the goniometer resolution, so the maximum value of the BRDF is no longer directly linked to the total reflectance of the sample and equation (70) does not give a correct value for the total reflectance. This explains the high intensity discrepancies we obtained between the non-rescaled Abeles modeled spectra and the experimental spectra in section III 2).

In this section, we have analyzed the spectral angular variations of the BRDF showing that the etched samples BRDF clearly present a diffuse part, at variance with the non-etched samples ones. We will now study the angular color evolution of the samples.

VI. Color evolution with the observation angle.

1) Conversion from BRDF to color coordinates

In order to characterize the gonio-apparent behavior of the samples, we will measure the color evolution of the samples with a variation of the observation angle under a fixed incidence angle. To obtain such results, conversions of the BRDF measurements data into colorimetric data are needed. The BRDF have been first converted into CIE1931 XYZ colorimetric coordinates by using the following equations, with the D65 illuminant spectral power density for $S(\lambda)$ (see equation (1)):

$$X = K \sum_{\lambda_i=380\,nm}^{780\,nm} S(\lambda_i) \times \bar{x}(\lambda_i) \times R(\theta_i, \theta_r, \lambda_i)$$

$$Y = K \sum_{\lambda_i=380\,nm}^{780\,nm} S(\lambda_i) \times \bar{y}(\lambda_i) \times R(\theta_i, \theta_r, \lambda_i)$$

$$Z = K \sum_{\lambda_i=380\,nm}^{780\,nm} S(\lambda_i) \times \bar{z}(\lambda_i) \times R(\theta_i, \theta_r, \lambda_i)$$

$$K = \frac{100}{\sum_{\lambda_i=380\,nm}^{780\,nm} S(\lambda_i) \times \bar{y}(\lambda_i)}$$

Charrière et al. [39] explained that the large variation of luminance values between rough and polished samples is a key problem for the definition of a color from BRDF measurements. Indeed, when comparing those two types of samples, smooth (i.e.: highly specular) samples may exhibit a luminance in specular condition higher than a perfect white light diffuser. This explains the reason for using the CIE chromaticity diagram rather than for example CIE L*a*b* to represent the sample colors. CIE L*a*b* data are obtained by rescaling with the CIE XYZ tristimulus values of the reference white point, which are ill-defined for highly specular samples.

2) Color evolution of samples around the specular direction

The XYZ coordinates are converted into xy chromaticity coordinates using equation 2. Figure 107 displays the CIE xy-chromaticity coordinates of the non-etched sample anodized at 10 V for observation angles from 44.8° to 45.2°. Increasing further the angular range yields unreliable data points because of too small values and noisy measurements of the BRDF. For this sample, the hue variation is small. We measure the hue by the angle between the x-axis and the line passing through the D65 point and the considered color point. The range of hue variation is 10°, thus characterising a mainly non-gonioapparent sample.
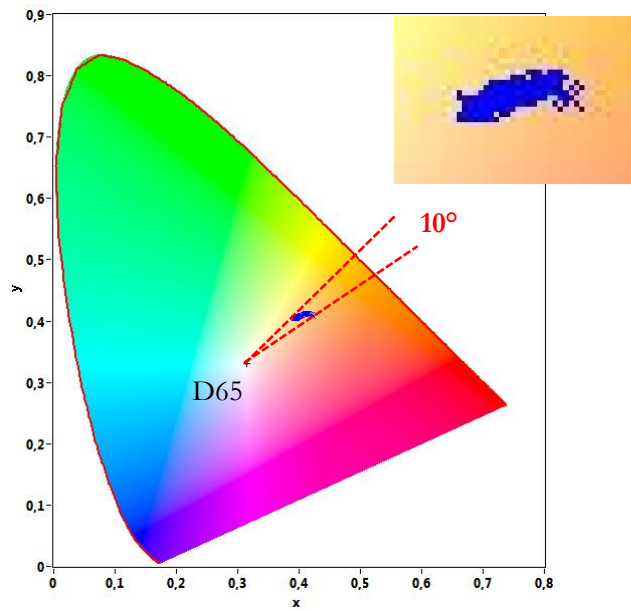
Figure 107: Chromaticity diagram obtained from BRDF measurements for the non-etched sample anodized at 10 V for an incidence angle of 45° and observation angles from 44.8° to 45.2°. The black cross corresponds to the white reference D65. Is also indicated the total hue variation of the sample color. On the right is presented a magnification of the chromatic path of the sample color.

In Figure 108 are presented the CIE xy-chromaticity coordinates of the etched sample anodized at 10 V for observation angles from 44.1° to 45.9°. The extension of the angular measurement range implies a contribution of scattered points to the BRDF because the values of the BRDF are small and affected by the noise at the outer boundaries of the range. For this sample, the hue variation is small: 8°. The sample is non-gonioapparent. When the angle of observation is the range [44.1°-44.6°]U[45.4°-45.9°] (outer boundaries of the observation range), a diffuse background appears.
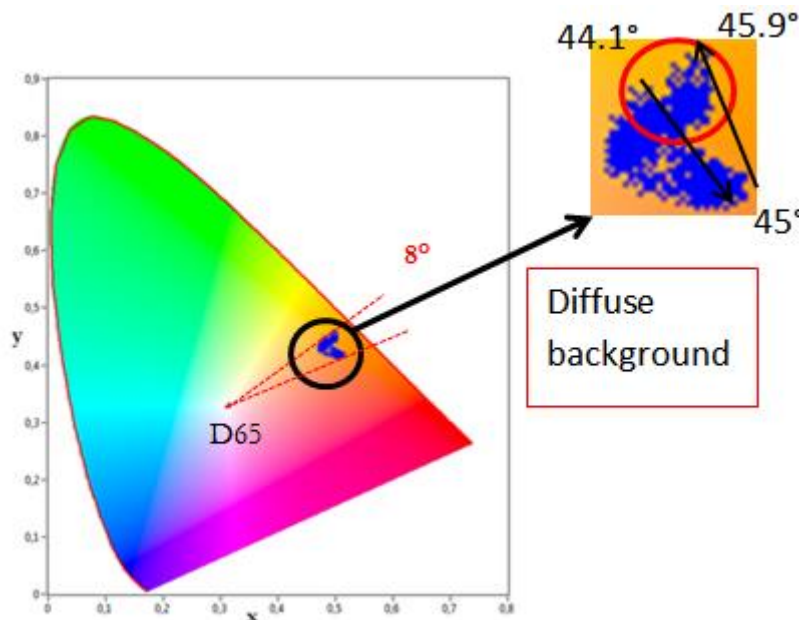
Figure 108: Chromaticity diagram obtained from BRDF measurements for the etched sample anodized at 10 V for an incidence angle of 45° and observation angles from 44.1° to 45.9°. The black cross corresponds to the white reference D65. Is also indicated the total hue variation of the sample color. On the right is presented a magnification of the chromatic path of the sample color with the observation angle.
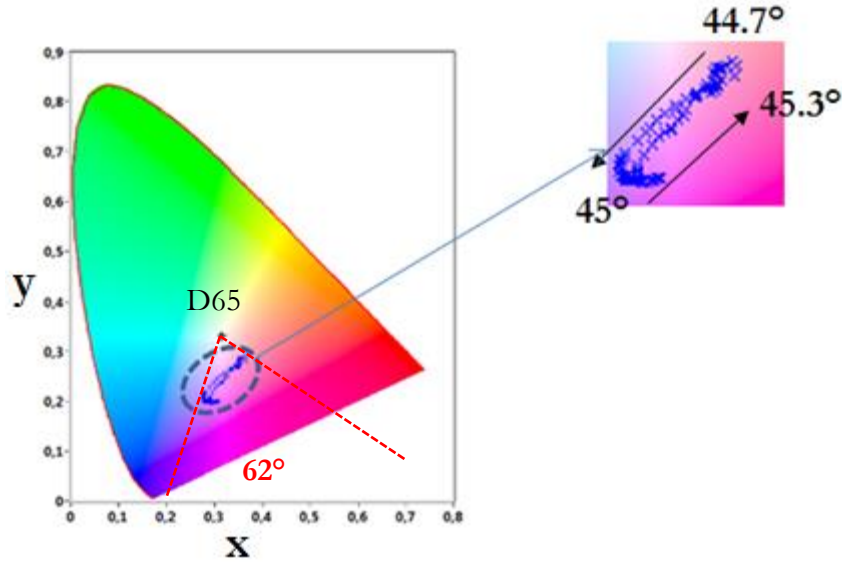
Figure 109: Chromaticity diagram obtained from BRDF measurements for the non-etched sample anodized at 90 V for an incidence angle of 45° and observation angles from 44.7° to 45.3°. The black cross corresponds to the white reference D65. Is also indicated the total hue variation of the sample color. On the right is presented a magnification of the chromatic path of the sample color with the observation angle.

Figure 109 shows the 90 V anodized non-etched sample colors in a CIE xy chromaticity diagram for observation angles from 44.7° to 45.3°. The angular range is narrower in this case because outside of these angle values, the BRDF values are highly impacted by the noise. We can clearly see that the hue is changing with the observation angle; this is a clear characteristic of a gonioapparent sample. This sample has a total hue variation of 62° over the angular range [44.7°-45.3°].
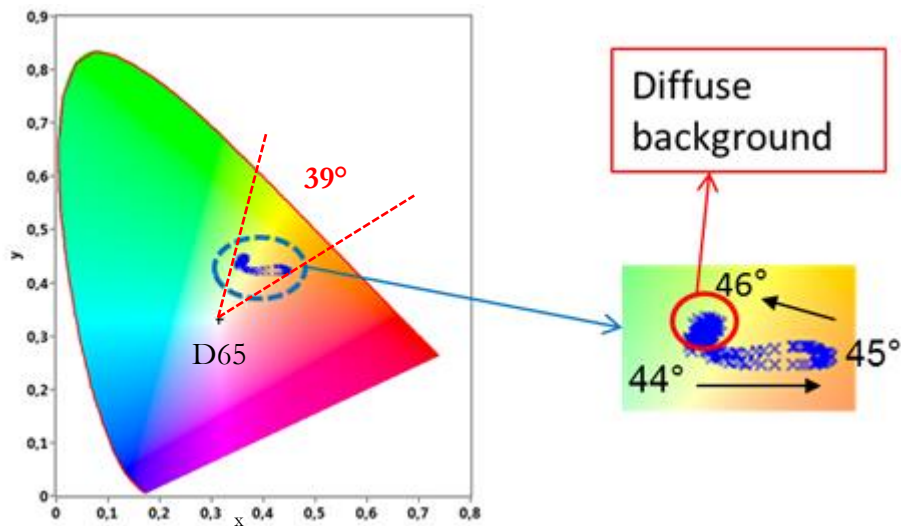
Figure 110: Chromaticity diagram obtained from BRDF measurements for the non-etched sample anodized at 90 V for an incidence angle of 45° and observation angles from 44° to 46°. The black cross corresponds to the white reference D65. Is also indicated the total hue variation of the sample color. On the right is presented a magnification of the chromatic path of the sample color with the observation angle.

Figure 110 shows the color CIE x-y coordinates of the 90 V etched sample for observation angles ranging from 44° to 46°. We observe that as for the 90 V non-etched sample, the hue is changing with the observation angle. However when the angles are reaching values more than 0.4° away from the specular angle, the color coordinates are all located in a small region (circled

116

in red in the magnified area Figure 108). It corresponds to the diffuse background, which is visible on the BRDF angular evolution as "wings" around the peak (see Figure 101). We can remark that this diffuse background has a mainly green hue whereas the specular hue is orange. This sample has a total hue variation of 39° over the angular range [44°-46°].

Important note: the chromaticity diagrams presented in this section are not corrected for a potential chromatic aberration. However, it can be noted that measured and visually observed colors are qualitatively in good agreement.

3) Spectral evolution of samples around the specular direction

The 90 V samples are the most gonioapparent ones. We focus on these samples for the study of the spectral evolution around the specular direction.
Figure 111 and Figure 112 present the reflectance spectra of the 90 V non-etched and etched samples for an incidence angle of 45° and for observation angles around the specular direction. All the spectra are rescaled by dividing each spectrum by its average over the wavelength range [380 nm–780 nm]. The observation angular range is [44.7°-45.3°] for the non-etched sample and [44.3°-45.7°] for the etched one. Increasing the observation angular range further leads to noisy spectra. Whereas the reflectance spectra for the non-etched sample have almost all the same shape, we observe a clear shift of the spectra shapes for the etched sample: the spectra extrema are shifted towards the "blue" wavelengths.
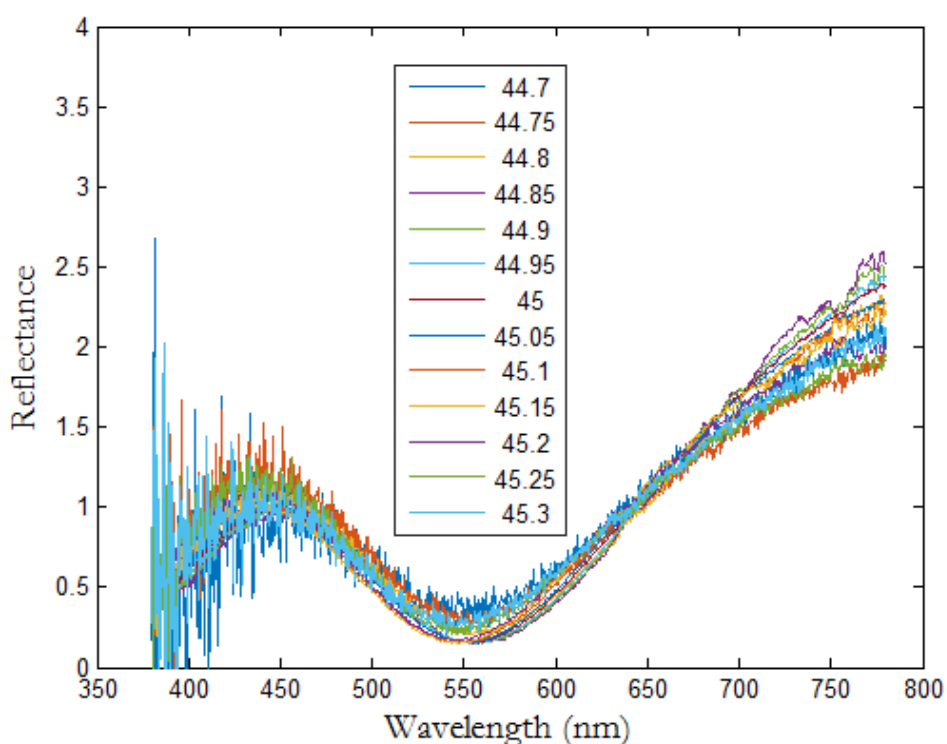
Figure 111: Normalized reflectance spectra for an incidence angle of 45° and observation angles ranging from 44.7° to 45.3° of the non-etched titanium sample anodized at cell potential of 90 V. To compare the shape of the spectra, each spectrum was rescaled by dividing each spectrum by its average over the visible wavelength range [380 nm -780 nm].

It is interesting to notice that this shift of the spectra extrema is much larger than the extrema shift observed when changing the incidence angle, that is when the value of the angle in the phase-shift formula (equations (59) and (56)) is changed. To illustrate this phenomenon, reflectance spectra were modeled with the Abeles matrices formalism for a TiO_2/Ti sample for

117

non-polarized light. The TiO$_2$ layer thickness is chosen equal to 180 nm (close to the value of the oxide layer thickness of the 90 V etched sample) and the Ti and TiO$_2$ refractive indexes are taken from [72]. The incidence angle is set from 44.3° to 45.7°. The resulting spectra are shown on Figure 113. We observe only a very slight shift of the spectra (a few nanometers).
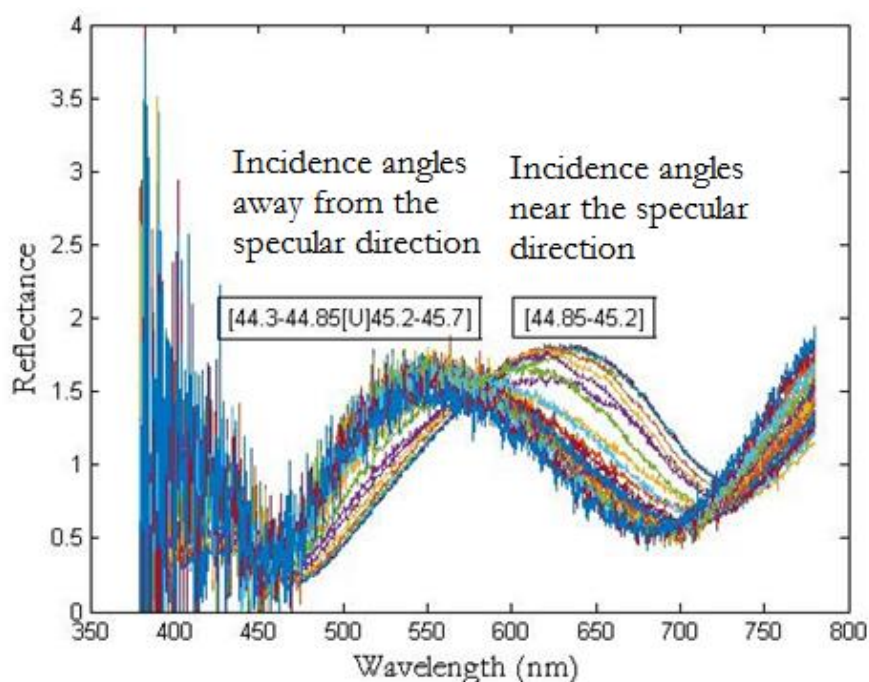
Figure 112: Normalized reflectance spectra for an incidence angle of 45° and for observation angles ranging from 44.3° to 45.7° of the etched titanium sample anodized at cell potential of 90 V. To compare the shape of the spectra, each spectrum was rescaled by dividing each spectrum by its average over the visible wavelength range [380 nm -780 nm].
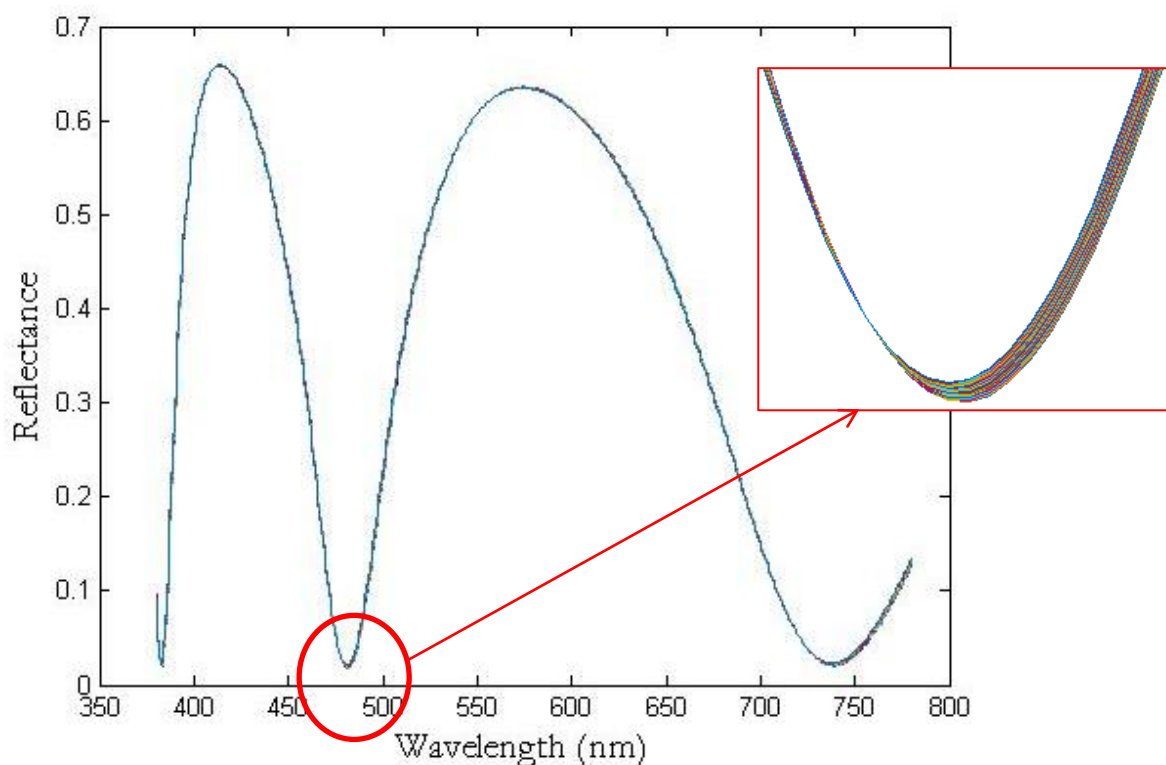
Figure 113: Reflectance spectra for observation angles ranging from 44.3° to 45.7° of a modeled anodized titanium sample with an oxide layer thickness of 180 nm and refractive indexes extracted from [72]. On the right is presented a magnification of the area around the second minimum.

The reflectance spectra of the samples anodized at 10 V are presented in the Appendix H and a similar behavior can be observed, a not as clear as for the 90 V anodized samples

Etching in an HF/HNO₃ solution changes the roughness of the sample. The colors of anodized samples are different if the sample is etched or not before anodizing. The perceived samples gloss is also modified going from bright colors for non-etched samples to matte colors for etched ones. Etching indeed adds a diffuse background to the BRDF. However, HF/HNO₃ etching may possibly have other impacts on the substrate than only modifying the roughness. These possible impacts are listed in the following concluding section.

VII. Conclusion

In this chapter, we presented titanium and anodized titanium samples (cell potentials at 10 V and 90 V) with different controlled surface substrate roughnesses. The roughness was controlled by HF/HNO₃ etching: some samples were etched and the other ones were not. These samples were characterized with the goniospectrophotometer Optimines.

By using the BRDF spectral variations we tried to estimate the oxide layer thickness of the anodized samples with two different approaches; with Abeles matrices-based fits of the sample reflectance, or by using the positions of the reflectance extrema. We showed that when using the reflectance extrema, it is necessary to take into account the phase shift induced by the reflection of the light on the titanium substrate. This phase shift is linked to the argument of the Fresnel coefficient of the Ti/TiO₂ interface. The errors on the oxide thickness made by considering an argument of π, i.e. by neglecting the imaginary part of the titanium substrate refractive index, can reach 500%, as for example for the non-etched sample anodized at a cell potential of 10 V.

We noticed that the samples etched before anodizing exhibit a larger oxide layer thickness than the non-etched samples and higher that cell potentials lead also to a larger oxide layer thickness. This is consistent with the results from [77]. However, it is important to note that all oxide thickness estimations were made by using refractive indexes given by a handbook of optical constants [72], instead of measured ones. This could lead to an error in the estimation of the oxide layer thickness.

The study of the BRDF angular variations revealed that the etched samples BRDF can be decomposed in two contributions, a specular and a diffuse contribution. These contributions have been evaluated by fitting separately the diffuse and specular parts of the BRDF. The specular part is obtained by substracting a baseline containing the diffuse part.
This diffuse aspect has been also observed when monitoring the sample color evolution around the specular direction. More precisely, the diffuse background observed for the etched sample anodized at a cell potential of 90 V has a hue significantly different from the hue exhibited by the sample close to the specular direction. This is not the case for the etched sample anodized at a cell potential of 10 V where the two hues are almost identical. It is also important to note that the hue variations around the specular direction are more important for the samples anodized at a cell potential of 90 V than at a potential of 10 V, whether etched prior anodizing or not. We can conclude that the samples anodized at a cell potential of 90 V are more gonioapparent than at a cell potential of 10 V.

Despite all the limitations and assumptions highlighted in this chapter, the measured and calculated colors of these samples are in good agreement with the visually perceived ones, including those of the most gonioapparent samples. To our knowledge, this is a first successful

attempt at an instrumental characterization of the gonio-appearance of structurally colored metallic samples with controlled roughness. As such, the sample preparation and measurement procedures developed in this work constitute a significant step towards the specification and fabrication of reference colored metallic samples.

We observed that HF/HNO_3 etching can be used to change the surface roughness of a sample but this step might also change the titanium substrate microstructure. Titanium is partially dissolved during the process. The chemical composition might also change by a deposition of hydride and fluoride, which also diffuse in the bulk of the material [84]. The presence of these elements might change the reactivity of the surface but also the mechanical properties of the material, in particular hydrides which might be responsible for hydrogen embrittlement [88][89]. In [84], fluor was mainly found in the form of fluorine, implying that the fluor is not binding with titanium, oxygen or carbon. HF/HNO3 etching seems thus unlikely to modify the substrate refractive index.

Samples anodized after an HF/HNO_3 etching reach a larger oxide layer thickness than non-etched ones, for the same anodizing parameters. We do not know if this should be attributed directly to the roughness variation of the titanium substrate or to a possible change of the surface reactivity of physico-chemical origin.

In order to separate a possible reactivity modification of physico-chemical origin of the titanium substrate by the etching step from the sole topographic effect, we prepared samples with different levels of roughness by using different steps of mechanical and chemical polishing. Furthermore, hydrofluoric acids are highly corrosive and toxic and its industrial use presents severe hazards. The sample preparation protocol of these new samples series and the investigation of their colored visual rendering are presented in the next chapter.

Chapter 4: Influence of the substrate roughness on the oxide thickness, diffuse aspect and colors of anodized titanium samples

In this chapter, the influence of the substrate roughness on the oxide thickness and optical properties of anodized titanium samples are investigated. First, a complete study of a small number of samples exhibiting three different substrate roughness levels anodized at three different cell potentials is presented. A second batch of samples is then presented featuring samples with four substrate roughness levels and 24 cell potentials ranging from 5 V to 120 V. This second batch was prepared to confirm the observations made on the first batch, and to measure the whole color gamut of anodized titanium samples.

I. Modifications of the Optimines optical system

In Chapter 3 section III 2) an intensity difference between the Abeles modeled spectra and the measured spectra for the non-etched anodized samples was observed. This difference could be due to a misalignment of the goniospectrophotometer or an injection problem into the detection fiber. In order to be less sensitive to misalignment or injection problems, the Optimines detection fiber has been changed to a larger diameter fiber.

The fiber used in the Chapter 3 was a circle to line fiber bundle from Ocean Optics™ where each fiber has core diameter of 100 μm, resulting into a total entrance diameter of about 300 μm. This fiber is described on Figure 114.
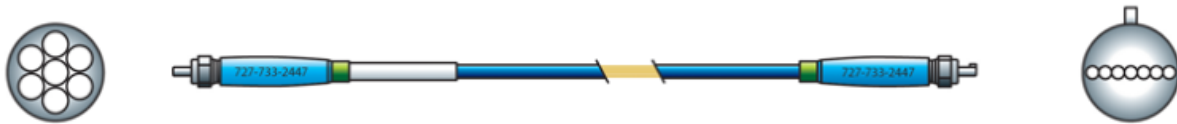
Figure 114: Circle to line fiber bundle. The fiber bundle is composed of 7 fibers positioned as a circle at the entrance and linearly at the exit.

The new detection fiber is a single-core quartz fiber from LOT-QuantumDesign™ with a core diameter of 1 mm. This fiber change will have an impact on the BRDF measurements. In the previous chapter, the BRDF peaks widths were shown to be linked to the goniospectrophotometer detector angular resolution, which is in turn linked to the size of the fiber core. The goniospectrophotometer resolution will be thus more than doubled and the BRDF FWHM will be modified accordingly.

In order check our new setup, we measured the Fresnel coefficient of a mirror polished grade 2 titanium sample, obtained by vibrometer finishing. The measurements are done in the specular direction for angles from 10° to 85°. The Fresnel coefficients are deduced from the sample reflectance, as given by equation (42).
This experimental Fresnel coefficient is compared to the theoretical Fresnel coefficient computed from a titanium refractive index taken from [90], at a wavelength of 680.2 nm. The results are

given on Figure 115. The experimental results are in very good agreement with the theoretical values for all the measured angles, implying a good alignment of the detection fiber.
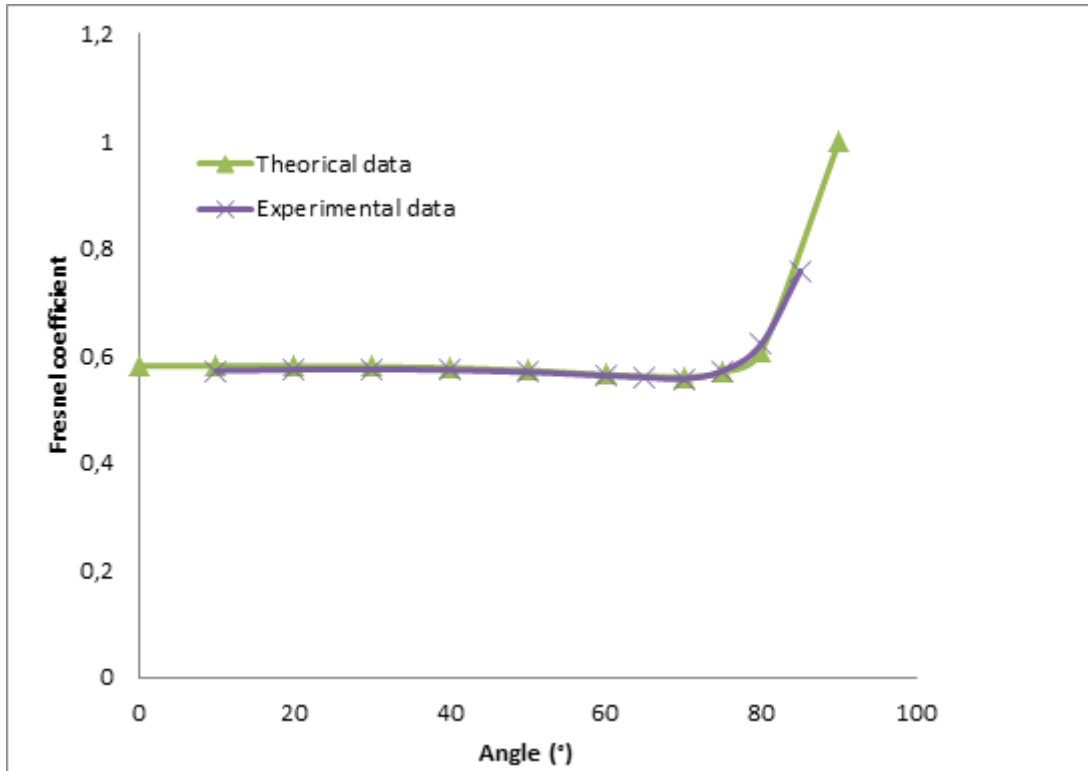
Figure 115: Fresnel coefficient of a mirror polished Grade 2 titanium sample obtained in the specular direction for different angles at a wavelength of 680.2 nm. The experimental values are compared to theoretical values computed from a titanium refractive index given by [90]**.**

II. Samples description

In order to obtain titanium surfaces with different levels of roughness, samples were prepared by using different steps of mechanical and chemical polishing. Some other treatments to change the roughness of the surface could have been used like sandblasting but the resulting substrate roughness would be higher than the roughness levels of the domain of interest in this study, which are from tens to hundreds of nanometers.

1) Sample preparation

Experiments were carried out on ASTM Grade 2 titanium. Samples were cut out of a 1 mm thick titanium sheet. Three different series of samples were prepared with three different roughness levels. A simple polishing with a SiC P300 grinding paper was used to obtain a rough surface on the first batch; these samples will be denoted "P300" in the following. This first step removes initial defects and improves the flatness of the sample. Note that a rotating sample holder was used to avoid a periodicity in the scratches formed during the grinding process and to randomize the direction of these residual scratches. Then, two series with mirror finishing have been prepared: the first mirror finishing series has been obtained by a complete mechanical polishing (including diamond paste solution from 6 μm to 1 μm) and a final step using a grinding cloth and an alumina solution with a particle size of 0.6 μm. Those samples will be referred to as

"Alumina" or "Alum". To further decrease the surface roughness, a vibratory polisher, Buehler Vibromet2, and a 60 nm colloidal solution, were used to obtain the last series designated either as "Vibrometer" or "Vibro" in the following. The samples were polished separately, one by one. Although this procedure is not well suited to preparing a large number of samples, it improves the surface quality of each individual samples.

Samples have been anodized by following the protocol presented in the first section of Chapter 3 at three different cell potentials: 10V, 20V and 90V. The samples have been anodized in a 0.5M H_2SO_4 electrolytic solution with a 20 mA/cm² current density.

2) <u>Roughness characterization of the samples</u>

Roughness measurements have been carried out by a non-contact white light interferometric optical system, Bruker Nanoscope Wyko ® NT9100, before anodizing to obtain the roughness of the titanium substrate, and after anodizing for the roughness of the oxide layer. The size of the measured area is 1.15 mm×0.86 mm (representing 480×640 data points) with a sampling interval of 1.8 μm in both in-plane directions. For each sample, five measurements have been made around the center of the sample to obtain a reliable assessment of the roughness of this area (represented in red in Figure 116). The center of the sample is the area where the goniospectrophotometric measurements are performed.

To monitor the homogeneity of the surface, at least four more measurements were performed on each sample, at some randomly chosen areas near each corner (represented in blue in Figure 116). It is important to note that the results were not corrected numerically, i.e. by removing a tilt or a polynomial fit of the surface for example. The value of the R_a parameter did not change when such filters were applied, attesting for a good flatness of the samples.
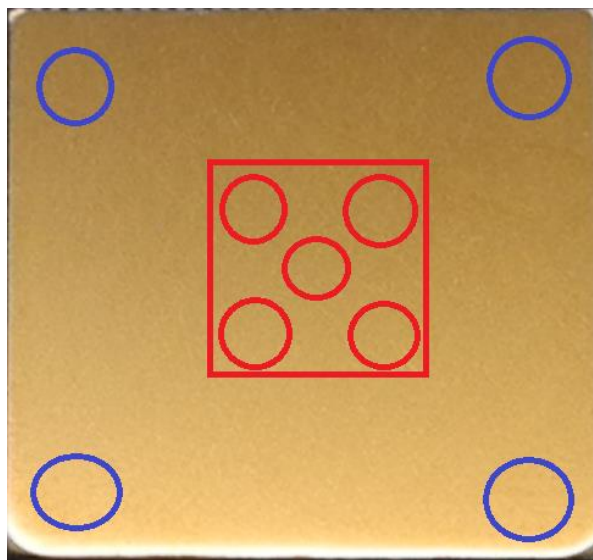
Figure 116: Areas selected during roughness R_a measurements. In red are represented the areas which are taken into account to obtain the average roughness R_a of the sample. In blue are represented the measurement area used to monitor the homogeneity of the surface. The areas are here represented on the Vibrometer series sample anodized at 10V. The sample is a square with a side length of 20 mm.

The averages of the five measurements of the R_a parameter performed on the "red" area have been calculated for each sample and are reported in Table 34. The uncertainty values presented in the Table 34 correspond to the measurement repeatability over the five measurements made in the "red" area, Figure 114.

The material is considered isotropic so the R_a (1-dimension parameter) and the S_a (2 dimension parameter) can be considered equal in this case. Other roughness parameters such as the RMS roughness R_q were also collected but not used in the present study.

	Ra P300	Ra Alumina	Ra Vibrometer
10V Substrate	C: 215 ± 5 nm S: 230 ± 10 nm	C: 57± 1 nm S: 58 ± 2 nm	C: 15 ± 0.5 nm S: 15 ± 0.5 nm
10V Anodized	C: 220 ± 5 nm S: 230 ± 10 nm	C: 58 ± 1 nm S: 63 ± 2 nm	C: 15 ± 0.5 nm S: 15 ± 0.5 nm
20V Substrate	C: 215 ± 5 nm S: 230 ± 10 nm	C: 55 ± 1 nm S: 58 ± 1 nm	C: 15 ± 0.5 nm S: 15 ± 0.5 nm
20V Anodized	C: 220 ± 5 nm S: 230 ± 10 nm	C: 133 ± 1 nm S: 136 ± 6 nm	C: 19 ± 0.5 nm S: 19 ± 1 nm
90V Substrate	C: 210 ± 5 nm S: 230 ± 10 nm	C: 58 ± 2 nm S: 59 ± 2 nm	C: 15 ± 0.5 nm S: 15 ± 0.5 nm
90V Anodized	C: 235 ± 5 nm S: 260 ± 10 nm	C: 131 ± 2 nm S: 130 ± 6 nm	C: 48 ± 1 nm S: 48 ± 1 nm

Table 34: Roughness parameters R_a of the three series P300, Alumina and Vibrometer before and after anodizing. "Substrate" corresponds to a measurement made before anodizing, "Anodized" to a measurement made after anodizing, "C" to measurements made in the center of the sample (red area) and "S" to the measurements made near the sample corners (blue area). The uncertainty values correspond to the measurement repeatability over the five measurements taken in the "red" area for C and the measurement repeatability for the measurements taken in the "blue" areas for S.

Three ranges of substrate roughness can be observed with values of about 15 nm, 60 nm and 215 nm respectively for the Vibrometer, Alumina and P300 series. Roughness measurements of the titanium substrate revealed that the preparation of the samples was homogeneous over the sample surface for all three series; i.e. the values measured in the center of the sample were close to the ones measured in the corners. The best homogeneity is obtained for the Vibrometer series, as shown by identical values of R_a for S and C.

Regardless of the initial surface roughness, anodizing at a cell potential of 10V does not change the roughness of the sample, i.e. the R_a before and after anodizing are equal considering the measurement repeatability.

When the cell potential is greater than 10 V, the roughness of the anodized samples seems to depend on two different contributions: the roughness of the substrate called "R_aSub" and the roughness induced by the oxidation reaction called "R_aOx". It is important to notice that the time needed to reach the desired cell potential is only a few seconds during anodizing at 10 V or 20 V against nearly thirty seconds during anodizing at 90V. This anodizing time corresponds to the time of exposure of the titanium sample to anodic current, and also the time of sample exposure to the acidic solution. The R_aOx contribution is expected to be greater for longer anodizing time.

The R_aOx contribution for a cell potential of 20 V is negligible compared to the R_aSub contribution for the P300 series (a 2% increase), moderate for the Vibrometer (25%) series and significant for the Alumina series (230%).

For the 90V Vibrometer sample, the influence of the oxidation reaction on the roughness of the sample is preponderant and corresponds to an increase higher than 200% of the initial value. The R_aOx contribution is also noticeable in the case of the P300 series even if its effect is less remarkable (around 10%). The value of the roughness of the samples of the Alumina series did not change after anodizing when the potential was changed from 20 to 90V.

Figure 117 shows the R_a before and after anodizing for all the samples, as well as the roughness gain in % corresponding to the ratio of the roughness after anodizing to the roughness of the substrate.
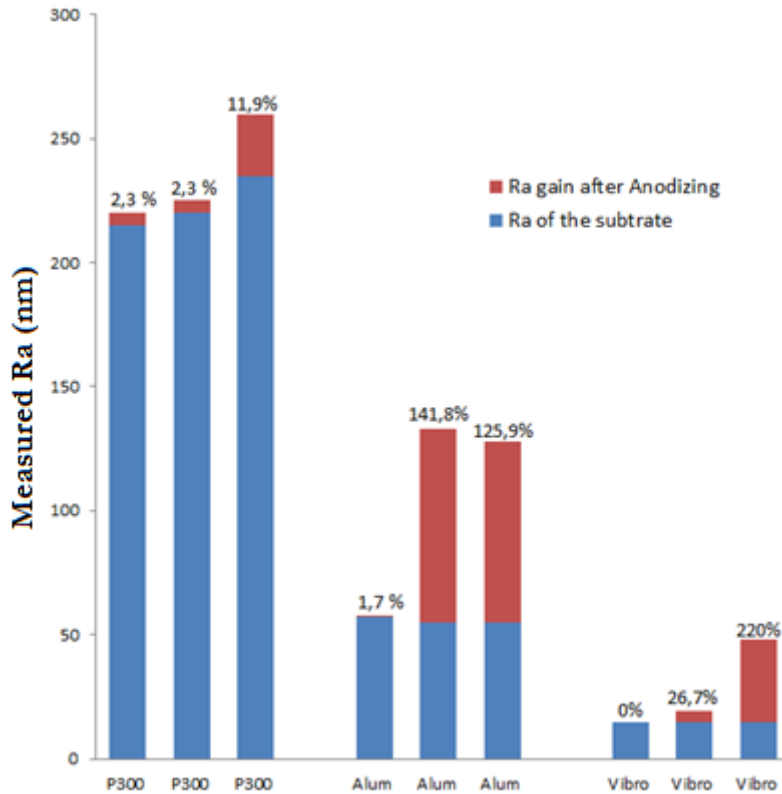
Figure 117: Evolution of the sample Ra after anodizing at 10V, 20V and 90V cell potentials for the three different surface finishing. P300 stands for the "P300 series", Alum for the "Alumina series" and Vibro for the "Vibrometer series".

When the potential is low, the surface topology remains the same and when a certain potential threshold is reached, the surface topology is changed during the oxidation reaction. This potential threshold seems to be influenced by the roughness of the substrate. The maximum relative value of R_aOx is obtained for the Vibrometer sample anodized at 90 V, and the maximum absolute values are obtained for the Alumina-finished samples anodized at 20 and 90V. The potential threshold value is higher when the sample is rough or smooth, i.e.: between 20V and 90V for the P300 and Vibrometer series, than for an intermediate roughness, i.e.: between 10V and 20V for the Alumina series. More experiments are needed such as adding intermediate and higher values of the cell potential or intermediate roughness values in order to confirm these observations and determine more accurately the threshold values.

3) <u>Visual characterizations of the samples</u>

Samples were observed visually under a bright sunlight and rotated slowly from 0° (horizontal position) to 90° (vertical position) in order to identify visually the gonioapparent character of each sample. The samples were sorted in three categories:
- non gonioapparent: the color remains visually the same during all the rotation process. The samples anodized at 10 V and the Vibrometer sample anodized at 20 V are in this category.
- gonioapparent at small angle: the color changes with a small rotation of the sample, smaller than 45°. The Alumina and P300 samples anodized at 20 V are in this category.
- gonioapparent at high angle, the color changes with a large rotation of the sample, higher than 45°. The samples anodized at 90 V are in this category.
Figure 118 shows the pictures of the samples taken at an observation angle of about 45° under a D65 diffuse light source (light booth).

125

At a cell potential of 10V, the color exhibited by the sample from the Vibrometer series is completely different from the color of the samples from the two other series and is totally desaturated (a gray color against a gold color). The sample of the P300 series exhibits a less vivid color than that of the Alumina series.

At a cell potential of 20V, the color exhibited by the sample from the Vibrometer series is completely different from the color of the other samples. It has a gold color against a purple color for the P300 series sample and a blue color for the Alumina series sample. The Vibrometer sample obtained at a cell potential of 20V has the same color as the sample anodized at a cell potential of 10V from the Alumina series.

At a cell potential of 90V, the samples have almost the same color; only a slight difference of hue is observed for the Alumina sample.
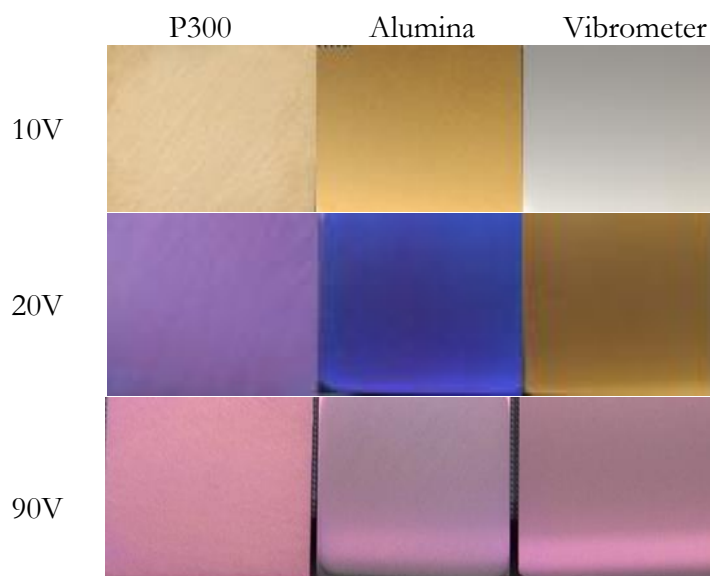
Figure 118: Digital pictures of anodized titanium samples taken at an observation angle of about 45° under a D65 diffuse illuminant. From the left to the right: P300, Alumina and Vibrometer series. From the top to the bottom, cell potentials: 10V, 20V and 90V.

In the present section the gonioapparent behavior of the samples was characterized visually and their roughness before and after anodizing measured. In the next section the sample BRDF will be measured and their angular variations studied in order to characterize the diffuse and specular aspects of each sample.

III.   Bidirectional Reflectance Distribution Function (BRDF) measurements of the different samples with the goniospectrophotometer Optimines: analysis of the angular variations

1) General observations

BRDF angular variations characterizations of the three series of samples were performed on the goniospectrophotometer Optimines around the specular direction with angles of incidence of 15°, 45° and 75° (See Figure 122). In order to collect enough signal in the detection arm for the P300 samples, the optical density filter used in the light source arm has been changed from OD4 (transmittance of about 10^{-4} see Figure 119) to OD1 (transmittance of about 10^{-1} see Figure 120).

The change of density filter is taken into account when calculating the BRDF by adding a correction term which is dependent on the wavelength. This term is the ratio of the spectral transmittance of the OD4 density filter over the OD1 density filter and is shown on Figure 121.

Note that the density filter transmittance values taken into account here are the values given by the supplier and might slightly differ from the exact transmittance of our density filters, as these values are not measured on exactly the same filter specimen. The provider of the optical densities is Thorlabs™ and the densities were NDUV10A (OD1) and NDUV40A (OD4).
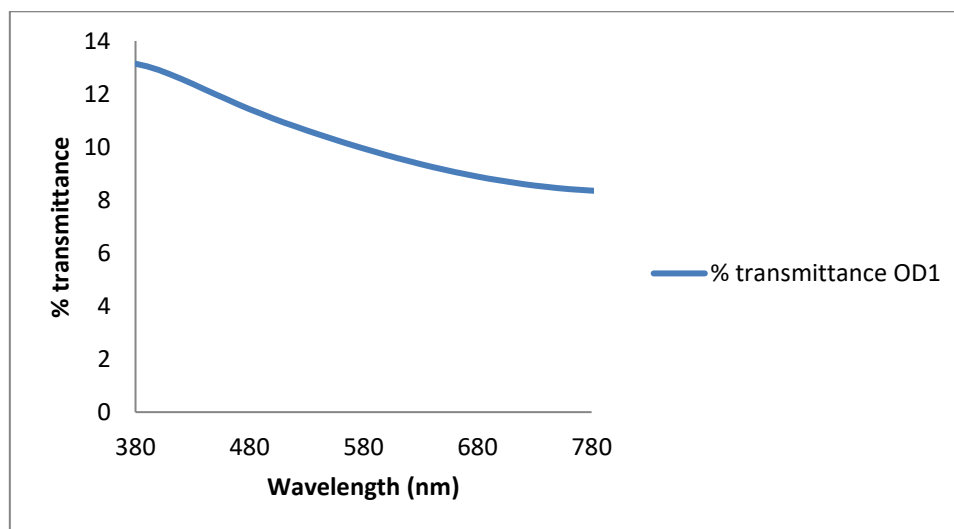
Figure 119: Transmittance values of the OD1 density filter used on the goniospectrophotometer Optimines on the visible wavelengths given online by the supplier.
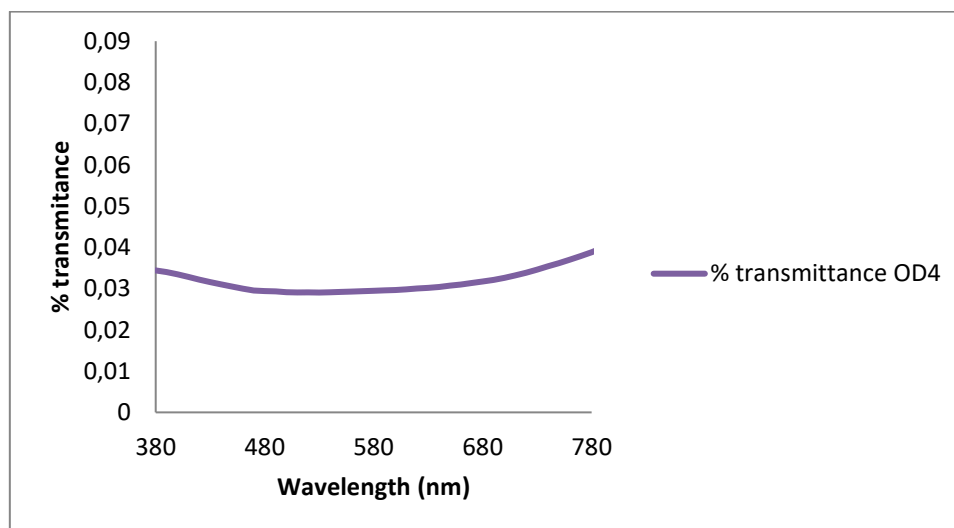
Figure 120: Transmittance values of the OD4 density filter used on the goniospectrophotometer Optimines on the visible wavelengths given online by the supplier.

The effect of the roughness on the BRDF measurement for an incident angle of 45° and for a 10V cell potential is presented in the graphs a), b) and c) of Figure 122. Note that the BRDF are averaged over the visible light wavelengths (380 nm-780 nm).

It is important to note that the BRDF intensity scale is different for the 3 samples varying from 5.10^4 sr^{-1} for the smoothest sample (Vibrometer series) to 140 sr^{-1} for the roughest sample (P300 series). The rougher the sample, the larger its BRDF, due to a higher contribution of the diffuse part.

Figure 123 represents the BRDF averaged over the visible light wavelengths (380 nm-780 nm) of the sample anodized at a 10 V cell potential from the Alumina series for the three different incidence angles: 15°, 45° and 75°. We can observe that the light source incidence angle seems to have an impact on the diffuse contribution to the BRDF. This diffuse contribution seems lower in the case of an incidence angle of 75° than for the two other incidence angles. However, it is difficult to compare the diffuse contribution to the BRDF for the two other incidence angles: 15° and 45°.

We can also notice that the BRDF are not perfectly centered on the specular direction. This could be explained by the fact that the light source arm and/or the detection arm were not perfectly aligned during the measurements.

10V Alu for a 15° incident angle	10V Alu for a 45° incident angle	10V Alu for a 75° incident angle
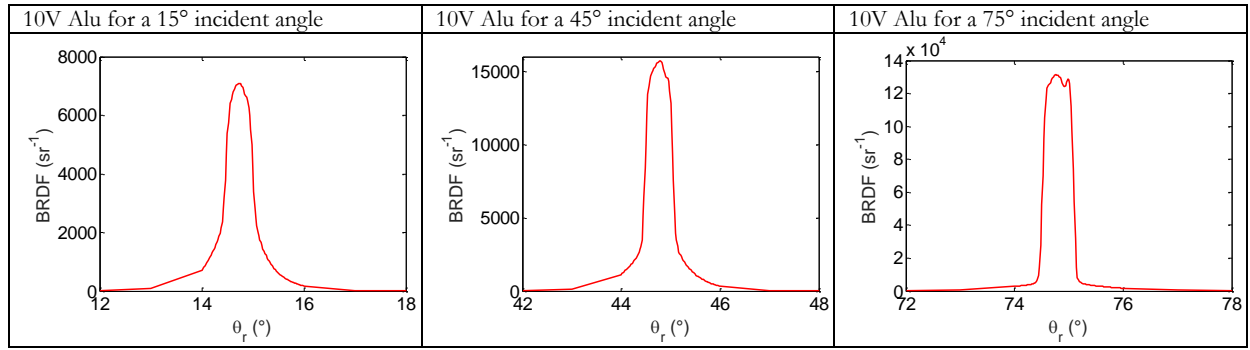
Figure 123 : Averaged BRDF over the visible wavelengths (380 nm to 780 nm) of the Alumina series samples anodized at a 10 V cell potentials for different incidence angles: (a) 15°, (b) 45° and (c) 75°. Note that the y axis scale can be different between the graphs.

In order to confirm these preliminary observations, the BRDF angular variations have been fitted, with a function different from the ones used in Chapter 3.

2) Detailed analysis of the BRDF angular variations with a fitting function

In order to quantify the amount of diffuse and specular contributions to the BRDF peaks, as well as to characterize the Full Width at Half Maximum (FWHM) of the peak, we fitted the BRDF of the different samples with a parametric function. Contrary to the fits previously made in Chapter 3, a Gaussian function does not fit well the experimental measurements. Indeed, the angular response of the goniospectrophotometer is different because of the change of detection fiber. With the new fiber a super Gaussian function (also called flat-top Gaussian) best fits the experimental data. This function is given by the following equation:

$$y = y_0 \ + \ A exp\left(-\left(\frac{x - x_c}{w}\right)^4\right)$$

(73)

where x_c is the position of the center of the peak and A its amplitude. The FWHM of this flat top Gaussian function is given by the following equation:

$$FWHM = 2w \times \left(ln(2)\right)^{\frac{1}{4}}$$

(74)

The fits are obtained with a Levenberg-Marquardt algorithm.All the BRDF have been fitted, but the fit procedure on some characteristic samples only will be detailed.
Figure 124 shows the BRDF of the 10V Vibrometer sample (black curve) as well as its Flat-top Gaussian fit (red curve). The parameters of the flat-top Gaussian function are represented in a table on the figure.
In the case of the 10V Alumina sample, the fit procedure is similar to the one used in Chapter 3 section IV 3) for the etched samples, i.e.: the total BRDF is split into two additive components, one for the specular peak and one for the diffuse contribution. The diffuse contribution to the BRDF is characterized by a baseline and the baseline-subtracted experimental data are fitted with a flat-top Gaussian function in order to get the specular FWHM. The diffuse FWHM is then obtained by a fit of the baseline.
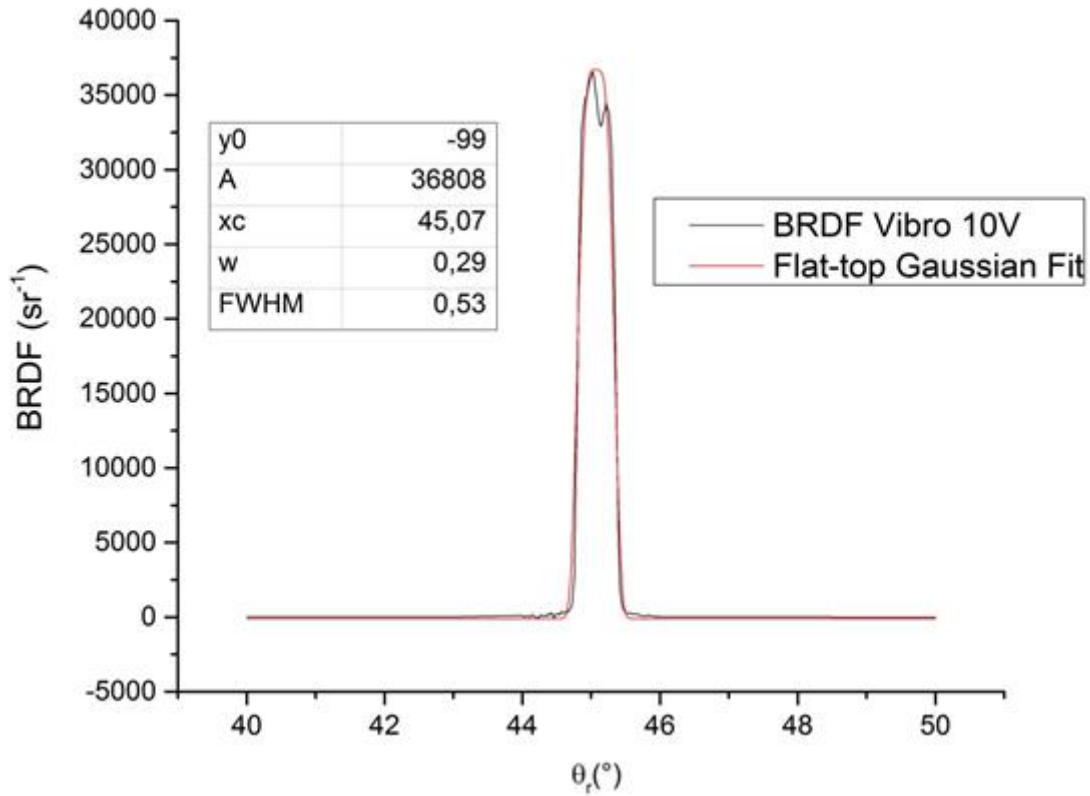
Figure 124 : Flat-top Gaussian fit (red curve) of the BRDF of the 10V Vibrometer sample (black curve) for an incidence angle of 45°. The parameters of the flat-top Gaussian function obtained through the fit algorithm are shown in a table in the corner of the figure.

Figure 125 shows the BRDF of the 10V Alumina sample: we can observe in black the BRDF measured with the goniospectrophotometer, in blue the baseline and in red the flat-top Gaussian fit of the baseline subtracted experimental data summed with the baseline. On the left of the figure, the values of the flat-top Gaussian function parameters are also presented.

To quantify the amount of diffuse contribution to the BRDF, the baseline is also fitted. A Lorentzian function is fitted to the baseline (see Figure 126).

The same fitting procedure, ie: a Flat-top Gaussian fit (or Gaussian), or when not directly applicable a Flat-top Gaussian fit of the baseline-subtracted experimental data followed by a baseline fit, have been performed on all the anodized samples for all 3 cell potentials: 10V, 20V and 90V, and for all the observation angles (see Appendix I). The fits of the baseline by either a Gaussian or a Lorentzian function can be found in Appendix J. The values of the baseline and baseline-subtracted experimental data FWHM are reported in Table 35. They are respectively denoted diffuse and specular FWHM. This table shows the area under the curves (A parameters) noted $A_{diffuse}$ for the baseline and $\tilde{A}_{specular}$ for the baseline-subtracted experimental data as well as the contribution of the diffuse part to the BRDF $C_{diffuse}$ obtained with equation (73). Note that contrary to equation (72) for a Lorentzian function, $\tilde{A}_{specular}$ does not correspond to the A parameter of equation (72) and is thus denoted with the symbol ~.

130
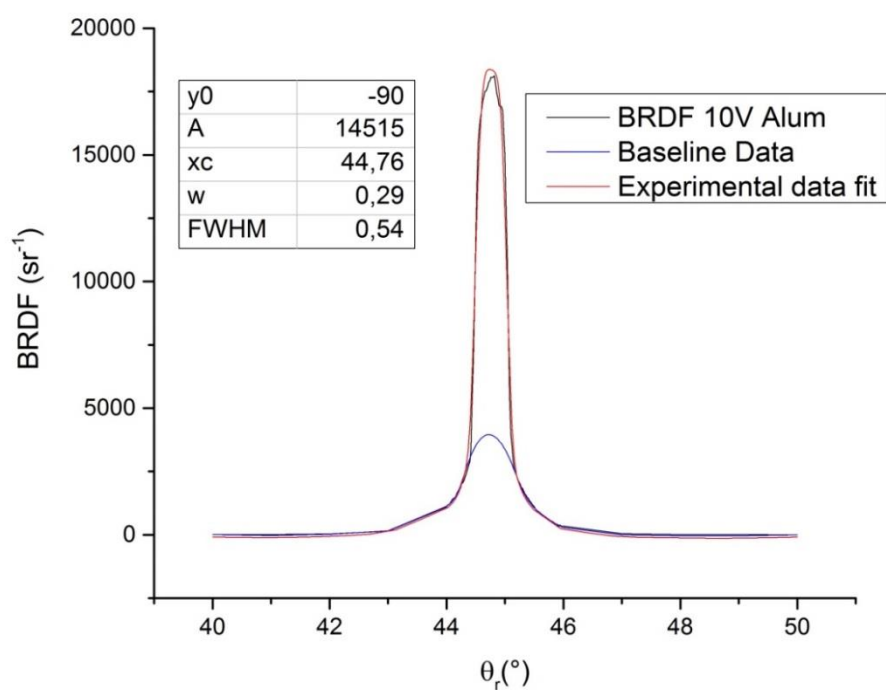
Figure 125: Fit of the BRDF for the 10V alumina sample for an incidence angle of 45° with the separation of the diffuse and the specular contributions: baseline (blue curve), Flat-top Gaussian fit of the baseline subtracted experimental data summed with the baseline, called here "experimental data fit", (red curve) and experimental BRDF (black curve). The values of the Flat-top Gaussian function parameters are presented in the table on the top left corner of the figure.
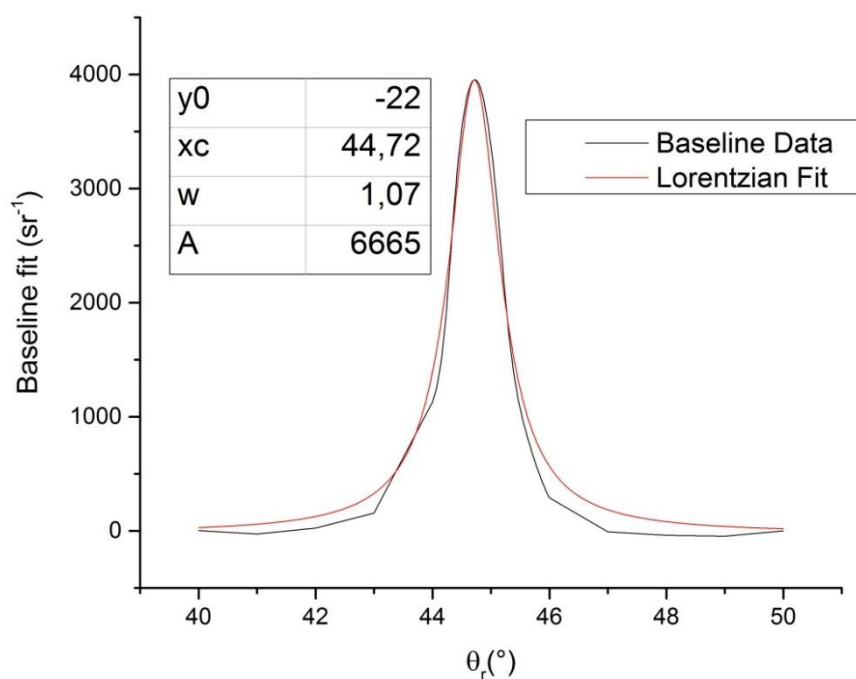
Figure 126: Baseline Lorentzian fit for the 10V Alumina sample for an incidence angle of 45°. The values of the Lorentzian function parameters are presented in the table on the top left corner of the figure.

	Diffuse FWHM	Specular FWHM	$A_{diffuse}$ (sr^{-1})	$\tilde{A}_{specular}(sr^{-1})$	$C_{diffuse}$
Vibrometer 10V 15°		0.51			
Vibrometer 10V 45°		0.53			
Vibrometer 10V 75°		0.55			
Vibrometer 20V 15°		0.55			
Vibrometer 20V 45°		0.55			
Vibrometer 20V 75°		0.52			
Vibrometer 90V 15°	1.08	0.34	668	3196	17.3%
Vibrometer 90V 45°		0.47			
Vibrometer 90V 75°		0.54			
Alumina 10V 15°	1.05	0.50	4485	2192	67.2%
Alumina 10V 45°	1.07	0.54	6665	7723	46.3%
Alumina 10V 75°	1.77	0.55	16487	72028	18.6%
Alumina 20V 15°	1.14	0.50	2828	804	77.8%
Alumina 20V 45°	1.44	0.54	4071	3492	53.8%
Alumina 20V 75°	1.03	0.55	12895	56780	18.5%
Alumina 90V 15°	1.42	0.54	1513	235	86.5%
Alumina 90V 45°	1.04	0.54	4638	3722	55.5%
Alumina 90V 75°	1.60	0.53	9358	46477	16.8%
P300 10V 45°	3.74	0.55	448	3	99.3%
P300 20V 45°	2.71	0.61	301	1	99.7%
P300 90V 45°	2.72	0.54	244	8	96.8%

Table 35: Full Width at Half Maximum (FWHM) values of the Gaussian/Lorentzian fits of the baselines and of the Flat-top Gaussian/Gaussian fits of the baseline subtracted experimental data, called respectively diffuse and specular FWHM.

On one hand, it is possible to notice, that the goniometer angular resolution after changing the detection fiber diameter has been increased to a value close to 0.5° as attested by the FWHM of the specular contribution to the BRDF, especially for the Vibrometer samples which exhibited mostly only a specular behavior.

A diffuse behavior is noticeable at an incidence angle of 15° for the Vibrometer sample anodized at 90V. All the Alumina samples exhibit a diffuse contribution to the BRDF at all cell potentials and observation angles. For all the Alumina and P300 samples, the diffuse FWHM is between 2 and 3 times larger for the former and between 4 to 6 times larger for the latter than the goniospectrophotometer angular resolution. Consequently, for these samples, the maximum value of the BRDF is not anymore directly linked to the total reflectance of the sample and equation (33) does no longer give a correct value for the total reflectance.

The diffuse FWHM and $C_{diffuse}$ values are the largest for P300 samples. Indeed, uncoupling the diffuse and the specular contributions to the BRDF is difficult for the P300 samples, i.e.: the fit algorithm convergence to a specular FWHM close to the goniometer angular resolution is laborious. Once the fit algorithm properly converged, which might require a fair amount of trials for the initial parameters of the fit function, it is also difficult to properly fit the baseline, even when trying to fit with either a Gaussian or a Lorentzian function. The $C_{diffuse}$ values might thus exhibit an error up to to 4%, depending on the function and the sample considered. Note that the lowest values of $C_{diffuse}$ were presented in Table 35. These values are already close to 100%, which shows an almost complete diffuse behavior of the samples.

It is also possible to remark that in all the cases where the samples exhibit a diffuse contribution, the $C_{diffuse}$ contribution decreases with the incidence angle. The diffuse contribution also increases with the anodizing cell potential, which is in accordance with the fact that the sample roughness increases with the cell potential (see Figure 117).

In the present section, an analysis of the BRDF angular variations of the samples has been presented and showed a wide range of visual rendering behavior of the samples, from totally specular for the Vibrometer ones, to almost totally diffuse for the P300 ones. The following sections are dedicated to the analysis of the spectral variations of the samples BRDF in correlation with oxide layer thickness estimations.

IV.   Material refractive indexes and oxide layer thickness in correlation with BRDF spectral variations.

As pointed out in the Chapter 3 section III 2) c), thickness estimations are highly dependent on a good assessment of the material refractive indexes. Ellipsometric measurements were performed in order to obtain a good assessment of the refractive indexes. Note that ellipsometric measurements also give an estimation of the oxide layer thickness. Refractive indexes and oxide layer thicknesses obtained through the ellipsometric measurements have been used as parameters for Abeles matrices-modelled spectra and compared to the measured reflectance spectra of the samples. To confirm the oxide layer thickness estimations obtained through ellipsometric measurements, X-ray reflectometry measurements have also been conducted.

1) <u>Ellipsometric measurements</u>

Ellipsometric measurements have been carried out by a phase modulation ellipsometer, Horiba Jobin Yvon UVISEL® on the Alumina and Vibrometer series in the Hubert Curien Laboratory (Saint-Etienne, France). The P300 series could not be characterized by ellipsometry, due to its too high roughness.

Ellipsometry techniques are described in details in [91]. To describe the spectral behavior of the refractive index, two dispersion laws were used:

- The classical dispersion model is based on the Lorentz classical theory (1878) and Drude dispersion model (1900) of interaction between light and matter. This law is used for the titanium substrate.

- The new amorphous dispersion model is an optimized model to obtain extinction coefficient and refractive index. It is derived from the Forouhi-Bloomer formulation applicable to amorphous, semi-conductors and dielectrics. It is used for the assumed amorphous TiO_2 layer.

The anodized titanium sample is represented as a four-layer material in the ellipsometric model, as described in Figure 127. The first layer is the titanium substrate, assumed to have an infinite thickness. The second layer is the interface between the titanium substrate and the titanium oxide layer and is noted L1. This layer represents the surface roughness of the substrate and is considered as a composite material, made of 50% Ti and 50% TiO_2. The third layer is the oxide layer noted L2. The fourth layer noted L3 corresponds to the interface between the oxide layer and air. It is modeled as a mixed material composed of air (50%) and TiO_2 (50%), again in order to simulate the oxide layer roughness.
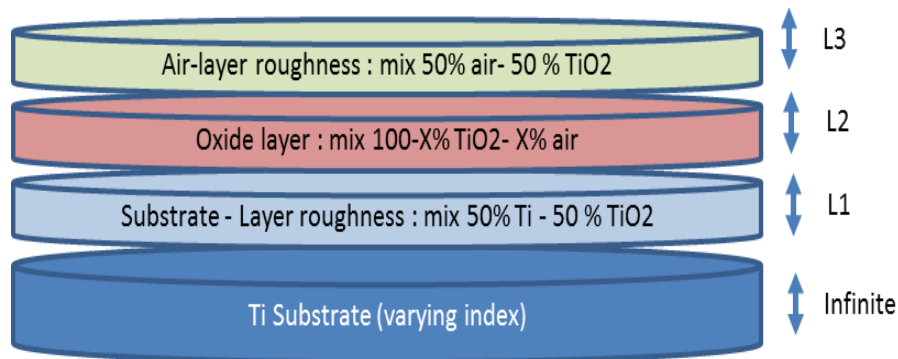
Figure 127: Representation of the four layer ellipsometric model material

Ellipsometric measurements were performed on all samples at three different angles: 65°, 70°and 75°. It is important to notice that all the parameters were adjusted at the same time. The optimization takes into account the 6 samples for the three angles (18 configurations).

The titanium substrate is considered the same for all samples (same refractive index) and its refractive index is adjusted during the measurement modelling and parameter identification, starting from a value coming from the database of the ellipsometer software. The TiO2 material is considered the same for all the samples. When the refractive index value drops in layer L2, the model assumes that pores are present in this layer. This porosity is noted as the factor X, considered as air in the model. It is important to note that this porosity is adjusted separately for all the samples during the parameter identification. The thickness and porosity of the different layers as well as the refractive index of the titanium and the titanium dioxide layer as estimated with the ellipsometric model are shown in Table 36 and Figure 128.

134

Only the oxide layer of the samples anodized at 90V is found to be porous. It is consistent with the fact that Anodic Spark Deposition (ASD) appears at this cell potential, and with the appearance of some small craters on the surface [70]. In the case of the sample of the Vibrometer series, the estimated porosity is about 2%, indicating that the pores might be small and rare.

This decrease in the oxide layer refractive index for the 90 V samples could also be explained by the presence of another phase which would change the overall refractive index of the oxide layer. The literature reports that an anatase crystalline phase starts to grow at cell potentials higher than about 70V [70], and therefore would be only found in the samples anodized at 90V in this study. Such crystalline phase wouldn't be found in the samples anodized at 10 V or 20 V, which is in accordance with the absence of apparent porosity in these samples. Nevertheless, the refractive index of anatase is expected to be higher than that of the amorphous phase [92], because of the higher density of the crystalline structure. Porosity is thus more likely to be the origin of the refractive change observed for the 90 V sample. Such observations could be confirmed by Scanning or Transmission Electron Microscopy images of surface cross-sections of the samples. However, the L3 values of the different samples estimated by ellipsometry are in complete disagreement with the roughness values measured by profilometry (see Table 34). Even the variations of the L3 and R_a values with the cell potential or the surface finishing are different.

	L1 (nm)	L2 (nm)	L3 (nm)	X (%)
Alumina 10V	3.4	26.9	2.2	0
Alumina 20V	10.8	41.1	3.2	0
Alumina 90V	38.8	171.5	8.6	12.7
Vibrometer 10V	2.7	11.2	6.2	0
Vibrometer 20V	3.5	27.4	2.1	0
Vibrometer 90V	31.3	148	7.1	2.2

Table 36: Thicknesses and oxide layer porosity factor X estimated by ellipsometric measurements.
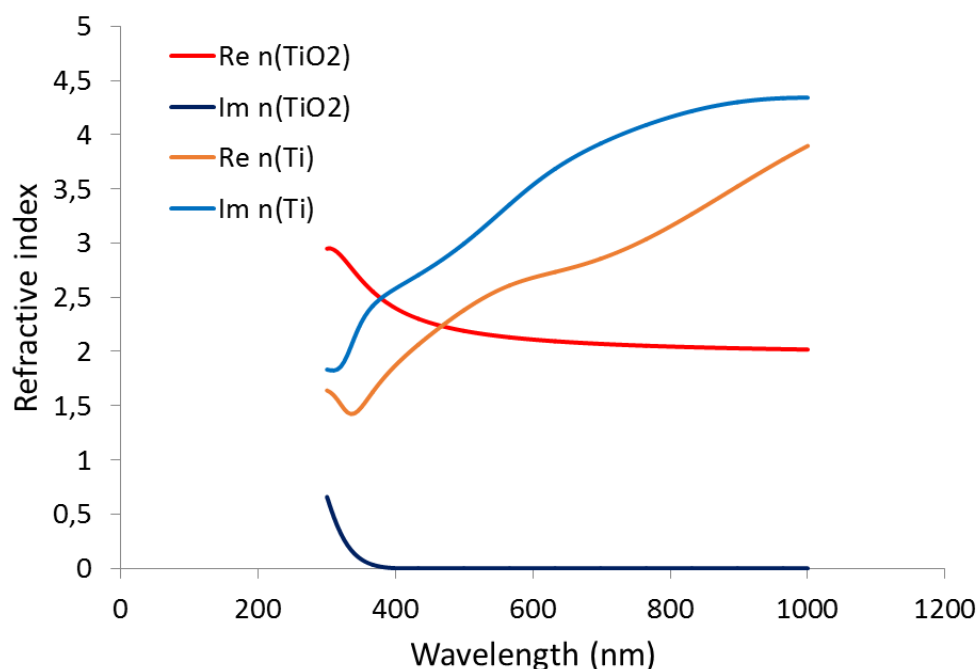
Figure 128: Real and imaginary parts of the refractive indexes of the titanium substrate and the oxide layer in the wavelengths range [300 nm – 1000 nm] estimated by ellipsometry.

2) <u>Comparison between experimental reflectance spectra and Abeles matrices modeled reflectance spectra</u>

The spectral BRDF measurements were converted into reflectance spectra with equation (42). Note that this reflectance corresponds to the total reflectance (as given by the Abeles matrices model) for the Vibrometer sample series, as for these samples the BRDF angular FWHM were equal to the goniometer angular resolution. This is not the case for the Alumina sample series as these samples have a diffuse contribution to their BRDF. The experimental reflectance spectra were compared to Abeles matrices modeled reflectance spectra (see Chapter 1 section II 3) and [34]). The material is supposed to be composed of a homogeneous TiO_2 layer and an infinite Ti substrate. Both interfaces are plane and parallel. The Ti and TiO_2 refractive indexes and the TiO_2 layer thickness obtained through ellipsometric measurements were used as parameters for the model.

Two different types of models are compared to the experimental spectra (see Figure 129) for the Vibrometer and Alumina series and for the three cell potentials 10V, 20V and 90V for an incidence angle of 45°:

- The first one (noted model 1) considers an oxide layer thickness equal to the L2 value of the ellipsometric measurements.
- The second one (noted model 2) considers the oxide layer thickness and the interfaces between the oxide layer and the titanium substrate and between the oxide layer and the air. The oxide layer thickness is then equal to $L2 + \frac{L1+L3}{2}$.
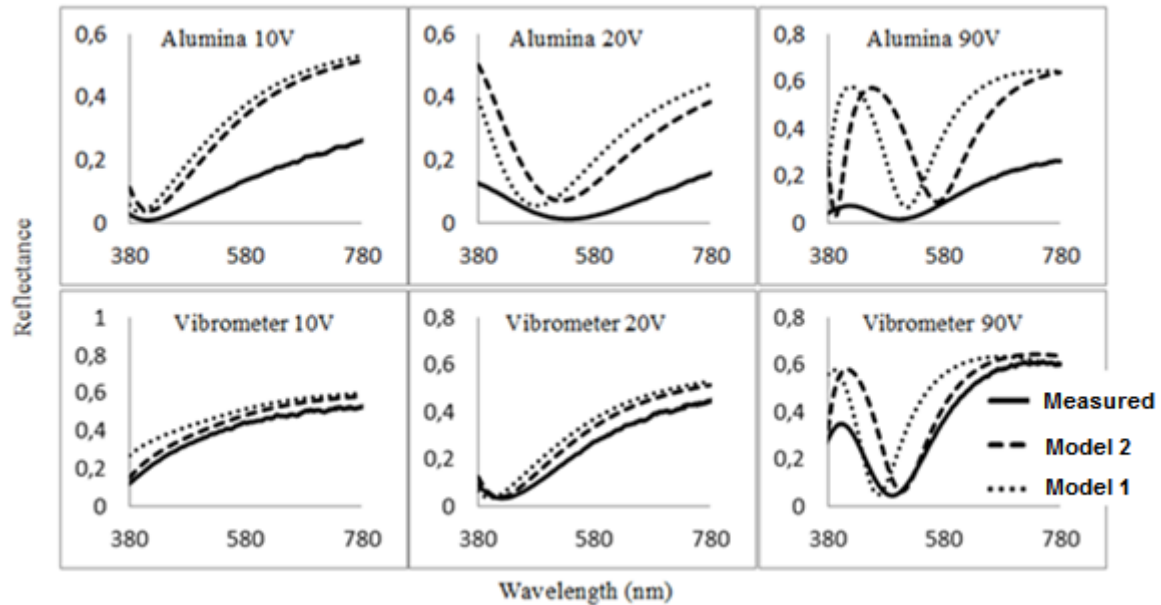
Figure 129: Comparison between Abeles matrices modeled spectra using the material parameters obtained through the ellipsometric measurements (models 1 and 2) and reflectance measurements for the Alumina and Vibrometer series for the three cell potentials 10, 20 and 90V. Both are obtained for an incidence angle of 45°.

Both models are overestimating the value of the reflectance for all the potentials and for all the surface finishing. The results are in a better agreement for the Vibrometer series than for the Alumina series, which is in accordance with the fact that equation (42) does not give properly the total reflectance for the Alumina series. Note also that, contrary to the Abeles matrices modeled spectra presented in Chapter 3, no scaling factor was needed to match the experimental spectra, which confirms the fact that the detection fiber change improved the measurements accuracy.

136

The number of extrema and their positions are in quite good agreement between the model and the measurements, as well as the global shape of the spectra. Except for the 90V samples, the second model seems to retrieve more accurately the positions of the extrema of the spectra. For the 90V Vibrometer sample the second model overestimates the positions of the extrema whereas the first model underestimates them. For the 90 V Alumina sample both models overestimate the positions of the extrema, but the first model gives extrema positions closer to the measured spectrum extrema. These shifts observed for both 90 V samples might be explained by the fact that the optical model doesn't take into account the oxide layer porosity. The refractive indexes used in the optical model are the same for all the samples, which is different from the ellipsometric model. A more complete Abeles matrices model matching exactly the ellipsometric model material of Figure 127 could be tested.

Goniospectrophotometric measurements were also performed for incidence angles equal to 15° and 75°. The same models as previously described are applied to the Vibrometer and Alumina samples anodized at a cell potential of 20V for the three incidence angles of 15°, 45° and 75° and compared to the experimental spectra (see Figure 130). For all incidence angles the same observations as previously observed at an incidence angle of 45° can be made. In particular, for the Vibrometer samples, the shape of the modeled spectra is in good agreement with the experimental one for all incidence angles. For both samples the extrema positions given by the model 2 are in good agreement with the experimental extrema positions at all angles. The same behavior is also visible for the samples anodized at 10V and 90V, as shown in Appendix K.
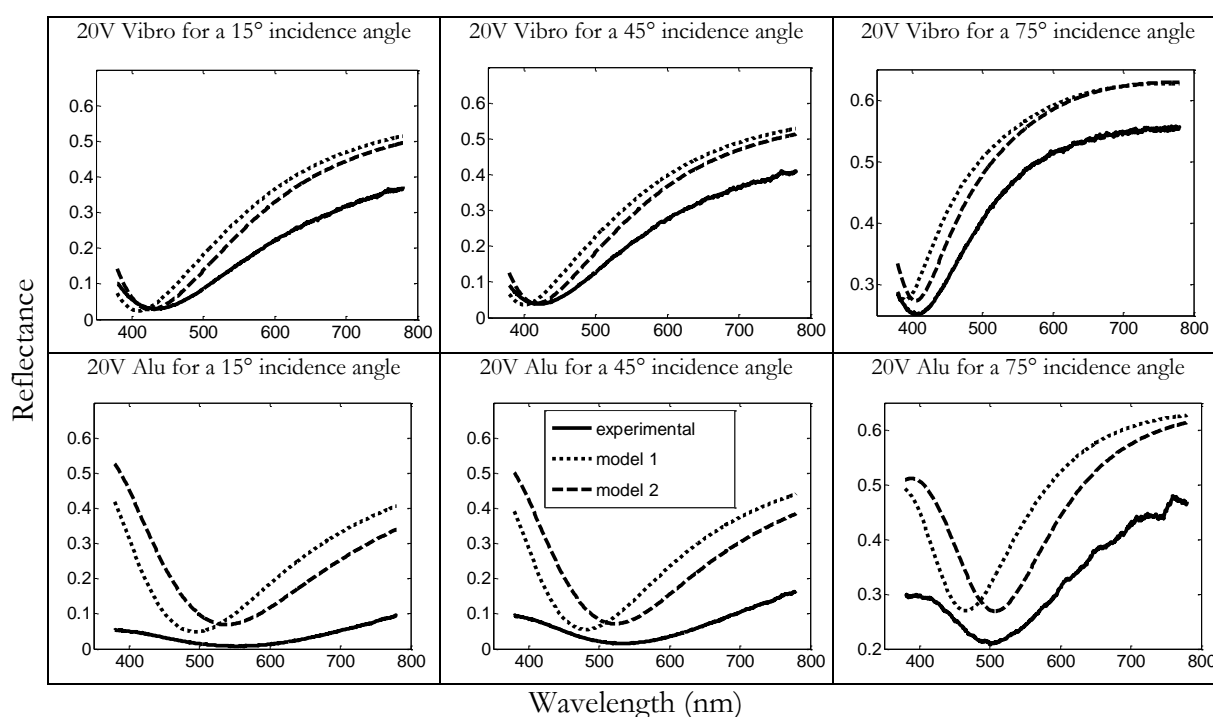
Figure 130: Comparison between Abeles matrices modeled spectra using the material parameters obtained through ellipsometric measurements (models 1 and 2) and reflectance measurements for Alumina and Vibrometer samples anodized at a cell potential of 20V for incidence angles of 15°, 45° and 75°.

3) Oxide layer thickness estimation from the extrema of the spectral BRDF of the titanium anodized samples

Oxide thicknesses were estimated from the extrema of the reflectance spectra with equation (69) for the different incidence angles. The refractive indexes are taken from the ellipsometric measurements (see Figure 128). The thickness values are given in Table 37.

The thickness values obtained from the extrema positions are really close to each other for all angles (variations lower than 7 nm when excluding the Alumina 90 V sample). These values are also very close to the values obtained by ellipsometric measurements; the agreement is even better when considering an oxide layer thickness equal to $L2 + \frac{L1+L3}{2}$ (variations lower than 12 nm in this latter case when excluding the Alumina 90 V sample).

Higher discrepancies of the thickness values are observed for the Alumina 90 V sample, both between oxide thickness values estimated from different extrema, as well as between oxide thickness values estimated from the extrema and oxide thickness values obtained from ellipsometric measurements. The oxide layer refractive index used to estimate the oxide thickness from the extrema is the "bulk" refractive index, i.e.: the porosity is not taken into account. This explains the discrepancies between oxide thickness estimated from ellipsometry and from the extrema positions. Note also that the discrepancies observed in between the oxide thickness estimations from different extrema might also be an indication that the refractive indexes used for these estimations do not match perfectly the "real" material refractive indexes.

For wavelengths smaller than 410 nm, the ellipsometric measurements give a small imaginary part for the TiO_2 refractive index. As equation (69) is not valid for an absorbent oxide layer, this imaginary part has been neglected for the oxide layer thickness estimations from the reflectance spectra extrema positions.

In order to confirm the previous oxide thickness estimations, the Vibrometer series was also investigated through X-Ray reflectometry (XRR) to obtain a non-optical estimation of the oxide thickness. It is indeed interesting to have non-optical thickness/refractive index estimations. A non-optical thickness estimation will allow to uncouple refractive index and thickness estimations.

	Extremum wavelength in nm (type)	Interference order k	$n_{TiO_2}(\lambda)$ $(n_{Ti}(\lambda))$	arg($r_{2-3}^{TE}(\lambda)$) [arg($r_{2-3}^{TM}(\lambda)$) − π] (°)	$\delta\varphi_{corr}(\lambda)$ (°)	Thickness corrected with $\delta\varphi_{corr}(\lambda)$ (nm)
Vibrometer 10V 15°	355.6 (min)	0	2.63+0.06i (1.53+2.33i)	-94.42 [-93.54]	-93.98	17.7
Vibrometer 10V 45°	349.6 (min)	0	2.66+0.08i (1.48+2.27i)	-94.67 [-87.73]	-91.20	17.3
Vibrometer 10V 75°	361.2 (min)	0	2.59+0.05i (1.57+2.37i)	-102.70 [-89.55]	-96.12	20
Vibrometer 20V 15°	436.1 (min)	0	2.30 (2.08+2.72i)	-116.26 [-115.50]	-115.88	30.7
Vibrometer 20V 45°	421.4 (min)	0	2.33 (2.00+2.66i)	-117.53 [-111.27]	-114.40	30.2
Vibrometer 20V 75°	408.5 (min)	0	2.37+0.002i (1.93+2.61i)	-117.58 [-105.14]	-111.36	29.2
Vibrometer 90V 15°	412.2 (max)	2	2.36 (1.95+2.63i)	-112.93 [-112.13]	-112.53	159.3
	508.1 (min)	1	2.18 (2.42+3.04i)	-128.33 [-127.61]	-127.97	159.1
Vibrometer 90V 45°	404.8 (max)	2	2.38+0.01i (1.91+2.60i)	-114.06 [-107.71]	-110.88	162.3
	497.6 (min)	1	2.19 (2.38+2.99i)	-129.60 [-123.88]	-126.74	161.0
Vibrometer 90V 75°	466.9 (min)	1	2.24 (2.23+2.84i)	-127.74 [-116.01]	-121.87	155.6
Alumina 10V 15°	420.0 (min)	0	2.34 (1.99+2.66i)	-114.46 [-113.66]	-114.06	28.6
Alumina 10V 45°	414.5 (min)	0	2.35 (1.96+2.64i)	-116.15 [-109.85]	-113	29.0
Alumina 10V 75°	400.2 (min)	0	2.40+0.02i (1.88+2.58i)	-115.62 [-103.11]	-109.37	27.7
Alumina 20V 15°	559.4 (min)	0	2.14 (2.59+3.32i)	-133.12 [-132.44]	-132.78	48.6
Alumina 20V 45°	538.6 (min)	0	2.15 (2.53+3.20i)	-133.78 [-128.31]	-131.04	48.3
Alumina 20V 75°	505.8 (min)	0	2.18 (2.41+3.03i)	-133.04 [-121.79]	-127.41	45.8
Alumina 90V 15°	425.1 (max)	2	2.38 (1.91+2.60i)	-114.06 -107.71	-110.88	162.4
	521.3 (min)	1	2.17 (2.47+3.11i)	-129.69 -128.99	-129.34	164.4
Alumina 90V 45°	416.8 (max)	2	2.35 (1.98+2.65i)	-117.53 [-111.27]	-114.40	169.0
	504.0 (min)	1	2.19 (2.40+3.02i)	-130.71 [-125.05]	-127.88	164.8
Alumina 90V 75°	420.9 (max)	2	2.33 (2.00+2.66i)	-120.31 [-107.99]	-114.15	180.3
	472.4 (min)	1	2.23 (2.26+2.87i)	-128.66 [-117.01]	-122.83	157.6

Table 37: Calculated TiO₂ layer thickness from the reflectance spectra extrema positions **for incidence angles equal to 15°, 45° and 75° for the samples with Alumina or Vibrometer finishing and anodized at 10 V,20 V and 90 V cell potentials. The Ti and TiO₂ refractive indexes are taken from the ellipsometric measurements.**

4) <u>X-ray reflectometry measurements</u>

XRR is a non-destructive surface-sensitive analytical technique used to characterize surfaces in particular thin films and multilayers. It can be used to characterize crystalline (single or polycrystalline) or amorphous materials. It is used to estimate layer thicknesses (up to 1000 nm), interlayer roughnesses and material mass densities for multi-layered materials. XRR uses the material densities instead of the optical refractive indexes and will be used here as a non-optical method to obtain the oxide layer thickness.

It is important to note that an X-ray beam that strikes a surface at a small angle (<2°) is totally reflected. Indeed, materials refractive indexes for X-rays are smaller than that of air. It explains that above the critical angle of total reflectance θc, the beam penetrates the sample, in which the angle of refraction θ₂ is smaller than the angle of incidence θ₁ (see Figure 131). Note also that for X-rays, the incidence and refracted angles are defined from the tangent to the surface, whereas they are defined from the normal to the surface for an optical beam.

The refractive index of a material under X-ray radiation is written as $n = 1 - \delta$ with δ the dispersion term for the X-ray beam, which is linked to the material density.

By using the Snell-Descartes law:

- We can write $cos\theta_2 = \frac{n_1}{n_2} cos\theta_1$ and if we consider n_1 the refractive index of air equal to 1 and n_2 the X-ray refractive index of the material lower than 1 we have: $\theta_2 < \theta_1$.

- At the critical angle, total reflection occurs and we have then $\theta_2 = 0°$. Considering $n_1 = 1$ and $n_2 = 1 - \delta_2$, can be deduced $\theta_c = arcos(1 - \delta_2)$ which can be approximated for $\delta \ll 1$ by:

$$\theta_c = \sqrt{2\delta_2}$$

(75)
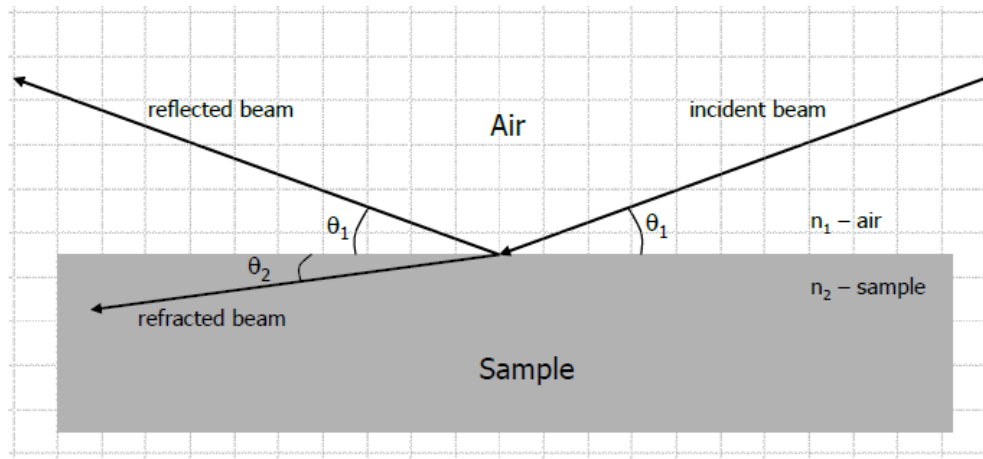
Figure 131: XRR principle with n_1 the refractive index of air, n_2 the refractive index of the studied material, θ_1 the X-rays angle of incidence and θ_2 the angle of the refracted X-ray beam.

δ_2 and the material density are linked by the following equation:

$$\delta_2 = \frac{N_A r_0 \lambda^2}{2\pi} \sum_j \frac{\varrho_j}{A_j}(Z_j + f_j')$$

(76)

with N_A the Avogadro number, r_0 the classical electron radius, λ the wavelength, ϱ_j the density of the jth atom in the compound, A_j the atomic mass of the jth atom, Z_j the atomic number of the jth atom and f'_j the correction factor for the X-ray dispersion for the jth atom.

The reflectivity R is defined as the ratio of the intensity of the reflected beam over the intensity of the incident beam:

$$R = \frac{Intensity\ of\ the\ reflected\ beam}{Intensity\ of\ the\ incident\ beam} \qquad (77)$$

If the sample is multilayered, the X-rays are reflected at all the interfaces as shown in Figure 132.
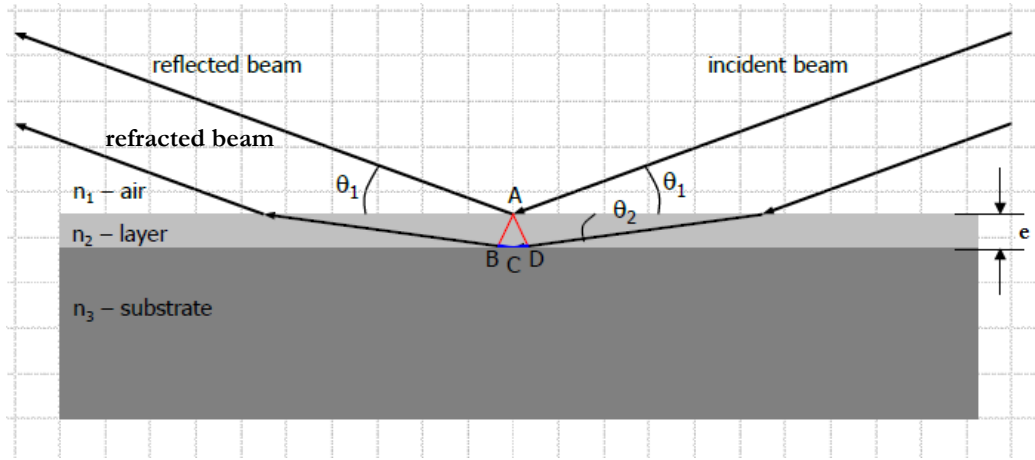
Figure 132: Reflection of X-rays on a multilayered sample with n_1 the refractive index of air, n_2 the refractive index of the layer, n_3 the refractive index of the substrate, θ_1 the X-rays angle of incidence (and reflection) and θ_2 the angle of the refracted beam.

As shown in Chapter 1 in the case of an optical beam, interferences between the reflected and the refracted beams are present also in the case of X-rays. The optical path difference between the reflected and the refracted beams is given by the distance $L = $ BC+CD. The oscillations on the graph of the reflectivity versus the incidence angle are due to these interferences (see Figure 133). In a similar fashion as for the optical wavelengths, Bragg's law can be used to obtain the thickness of the layer.

Important note: the following XRR graphs have "Incident angle" as abscissa axis with values taken from the interval 0.1° to 2° with a graduation of 0.1 degree and "Intensity" in counts (logarithmic axis) as the ordinates axis.
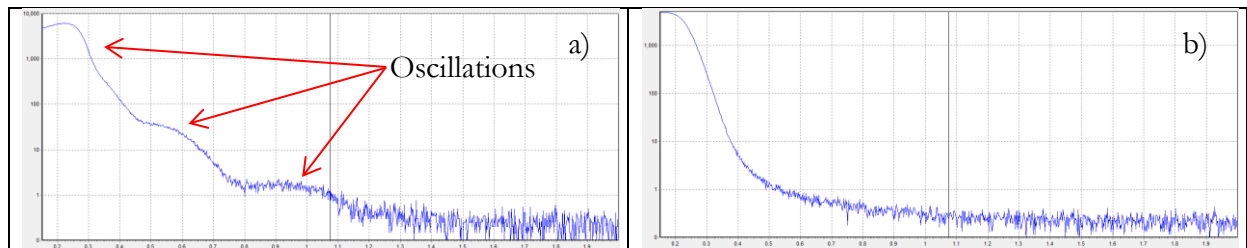
Figure 133 : X-ray reflectivity versus the incidence angle for the Vibrometer samples anodized at cell potentials of 10V (a) and 90V (b). Oscillations are not present on graph b) and no thickness estimation can be made.

At a maximum, we can write $L = n\lambda = \text{BC+CD} = 2esin\theta_2$ with n an integer.

It is then possible to express θ_2 as a function of θ_1 and the layer refractive index $n_2 = 1 - \delta_2$ by using the Snell-Descartes law and some approximations:

- with $n_1 \approx 1$ we can write $cos\theta_1 = (1 - \delta_2)cos\theta_2$ and then $\theta_2 = \arccos\left(\frac{cos\theta_1}{1-\delta_2}\right)$, which can be approximate by $\theta_2 = \sqrt{\theta_1^2 - 2\delta_2}$ for $\delta_2 \ll 1$.

- then $L = 2esin(\sqrt{\theta_1^2 - 2\delta_2})$ which can be approximate for $\theta_2 \ll 1$ by:

$$\text{L} = n\lambda = 2e\sqrt{\theta_1^2 - 2\delta_2} \text{ with } n \text{ an integer}$$

(78)

X-ray reflectivity curves were performed with the X'Pert Reflectivity software from PANanalytical. The Vibrometer sample anodized at 90V does not exhibit any oscillations, making any thickness estimation impossible. It could be due to a too high sample roughness or to a too high oxide thickness. In the latter case the X-ray beam cannot reach the susbtrate and no refracted beam can interfere with the reflected beam.

Analyzes are obtained by fitting the measured data. The fitting parameters are the oxide layer thicknesses, the oxide layer densities and the interfacial roughnesses. The substrate density is fixed to a value of 4.5g/cm³. The process to obtain the oxide layer thickness is presented in the reference [93].

Figure 134 shows the graphs of the reflectivity versus the incidence angle for the Vibrometer samples anodized at 10 V and 20 V, as well as the fitted functions given by the software.

At low angles, between 0.2° and 0.4°, the fit are not perfect and this could be attributed to measurement imperfections (use of a non-adapted slit on the X-ray beam). This leads to an uncertainty on the critical angle position which might have an influence on the oxide layer thickness estimations. Nevertheless, in both cases, the general shape of the experimental reflectivity curve is respected. The fitted parameters give a value of the oxide thickness equal to 9 nm with an interface roughnesses of 0.9 nm for Ti/TiO₂ and 0.7 nm for TiO₂/Air for the sample anodized at 10 V and an oxide thickness of 20.3 nm (interface roughnesses of 2 nm for Ti/TiO₂ and 1 nm for TiO₂/Air) for the sample anodized at 20 V.

The fits give also an oxide layer density of 3.6 g/cm³ for the 10V sample and an oxide layer density of 3.5 g/cm³ for the 20 V sample, which is acceptable for amorphous TiO₂.
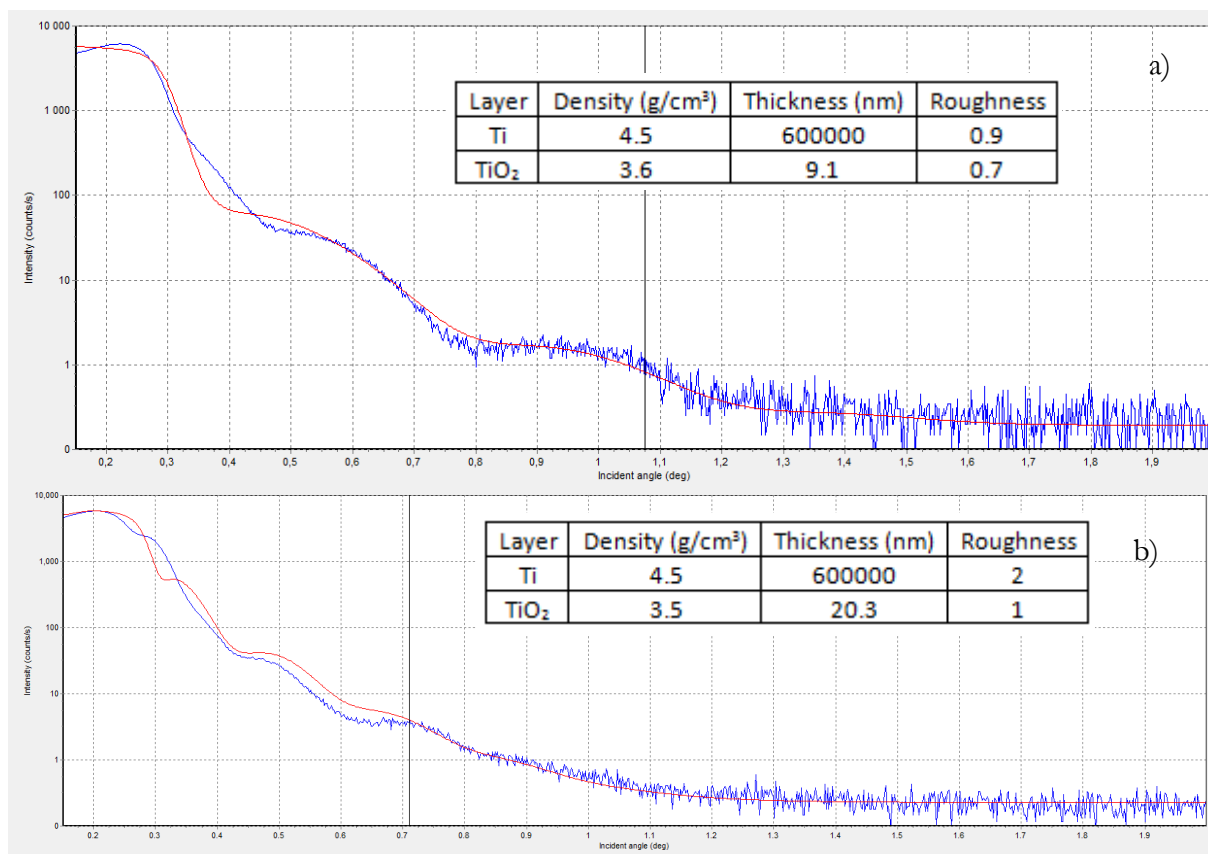
Figure 134: X-ray reflectivity versus the incidence angle for the Vibrometer samples anodized at cell potentials of 10V (a) and 20V (b). The red line represents the fit given by the software. The table on the graphs indicates the parameters given by the fit.

5) <u>Comparison between all the oxide layer thickness estimation techniques</u>

The oxide layer thickness has been estimated by different techniques as presented in the previous sections and the results are summarized in Table 38. Note that the measurement area is different for each technique: some are local and others are made on the whole sample.

	XRR value (nm) / Roughness at the Ti/TiO$_2$ and TiO$_2$/Air interfaces (nm)		Ellipsometry value (nm)		Average thickness over all incidence angles and extrema (nm) /Std deviation (nm)
			$L2$	$L2 + \frac{L1+L3}{2}$	
Vibrometer 10V	9	0.9 and 0.7	11.2	15.6	18.3 ± 1.5
Vibrometer 20V	20.3	2 and 1	27.4	30.2	30 ± 0.8
Vibrometer 90V			148	167.4	159.5 ± 2.5
Alumina 10V			26.9	29.7	28.4 ± 0.7
Alumina 20V			41.1	48.1	47.6 ± 1.5
Alumina 90V			171.5	195.2	166.4 ± 7.8

Table 38: Oxide layer thickness estimation, comparison between X-rays reflectometry, ellipsometry and spectra extrema positions.

The values estimated from the extrema positions and obtained by ellipsometry are in good agreement, particularly if we consider $L2 + \frac{L1+L3}{2}$. However, it is important to note that these

techniques are both based on the same refractive indexes. For all the 10 V and 20 V samples the refractive indexes are exactly the same and a very good agreement between ellipsometry and extrema thickness estimations can be observed. For the 90 V samples and particularly for the Alumina 90V sample, we observe a higher discrepancy between the oxide thickness estimations. Indeed, in these cases, the TiO_2 refractive index considered for the extrema position thickness estimations does not take into account the oxide layer porosity and is thus different from the TiO_2 refractive index considered for the ellipsometry thickness estimation.

The values of oxide layer thickness obtained by XRR are lower than the ones obtained by the two other techniques, but it is possible to explain to some extent the difference. First, as noticed in the section 5) d), the fits of the XRR signal are not perfect, particularly close to the critical angle. This could lead to a biased estimation of the material density (see equations (75)-(76)) and thus to a biased estimation of the oxide layer thickness (see equation (78)). Secondly, the values of the TiO_2/Air interface roughness given by XRR do not correspond to the R_a values found by profilometric roughness measurements. Nevertheless, inserting a roughness value for the TiO_2/Air interface of about 15 nm (Ra value for the 10 V and 20 V Vibrometer samples) as an input parameter for the XRR fit predicts a disappearance of the oscillations, which is not in agreement with the experimental XRR signal. Note also that the XRR interface roughnesses are agreeing well with the L_1 and L_3 values given by ellipsometry. The R_a parameter may thus not be the right parameter to compare with the other interface roughness estimation techniques.

In order to have a relative estimation of the oxide thickness discrepancies between the three estimation techniques, the following ratios have been computed:

$$\frac{oxide\ thickness\ tech_1 - oxide\ thickness\ tech_2}{\max(oxide\ thickness\ tech_1, oxide\ thickness\ tech_2)} \times 100$$

where oxide thickness tech i denotes the oxide estimation by the technique numbered i. The results are summarized in Table 39.

	XRR / $L2$	XRR / $L2 + \frac{L1+L3}{2}$	XRR/extrema	$L2$/extrema	$L2 + \frac{L1+L3}{2}$ / extrema
Vibrometer 10V	19.6%	42.3%	50.8%	38.8%	14.8%
Vibrometer 20V	25.9%	32.8%	32.3%	8.7%	0.7%
Vibrometer 90V				7.2%	4.7%
Alumina 10V				5.3%	4.4%
Alumina 20V				13.7%	1%
Alumina 90V				3%	14.8%

Table 39: Relative discrepancy in % between each couple of thickness estimation techniques.

The highest discrepancies are observed between XRR and the two other techniques, as well between the L2 ellipsometry value and the extrema position estimated value for the Vibrometer 10 V samples.

a) Oxide layer thickness estimation from the extrema of the spectral BRDF with refractive indexes extracted from ellipsometric measurements.

Rough samples are difficult, if possible at all, to characterize by ellipsometry and XRR. However, it is possible to use equation (69) in order to estimate the oxide thicknesses from the extrema of the reflectance spectra. The results are presented in Table 40 considering for the Ti/TiO₂ refractive indexes, the ones obtained previously by ellipsometry on the Alumina and Vibrometer samples. The thickness values for the P300 series were expected to be higher than the ones found for the Alumina and Vibrometer series as the P300 samples are the roughest ones. Indeed the thickness values for the Alumina series were higher than for the Vibrometer series and the observations of the Chapter 3 samples tended to show that the oxide thickness increases with the substrate roughness. However, the thickness values of the P300 series are not higher, which invalidates the fact that the oxide layer thickness increases monotonously with the surface roughness. It seems that there is an "optimal" value of the surface roughness with respect to the oxide layer growth kinetics, as also suggested by the absolute values of the R_a gain reported in Table 34 and Figure 115. Further tests with substrates with different surface roughness levels need to be performed, as well as reproducibility tests in order to confirm this finding.

	Extremum wavelength in nm (type)	Interference order k	$n_{TiO_2}(\lambda)$ $(n_{TiO}(\lambda))$	arg($r_{2-3}^{TE}(\lambda)$) [arg($r_{2-3}^{TM}(\lambda)$) − π] (°)	$\delta\varphi_{corr}(\lambda)$ (°)	Thickness corrected with $\delta\varphi_{corr}(\lambda)$ (nm)
10V P300	363.1 (min)	0	2.58+0.04i (1.60+2.40i)	-103.11 [-96.43]	-97,57	19.8
20V P300	471.5 (min)	0	2.26 (2.23+2.86)	-124.74 [-118.88]	-121.81	37.2
90V P300	402.0 (max)	2	2.39+0.001i (1.89+2.59i)	-113.36 [-106.98]	-110.17	159.0
	490.3 (min)	1	2.20 (2.34+2.95i)	-123.02 [-116.39]	-119.71	156.8

Table 40 : Oxide thickness estimation from the reflectance spectra extrema on the P300 samples series for an incidence angle of 45°.

b) Comparison between experimental reflectance spectra and Abeles matrices modeled reflectance spectra

The BRDF measurements were converted into reflectance spectra with equation (42). Note that this reflectance does not correspond to the total reflectance (as given by the Abeles matrices model) for the P300 sample series as these samples are highly diffuse. The experimental reflectance spectra were compared to Abeles matrices-based modeled reflectance spectra by using the ellipsometric measurements of the Ti/TiO₂ refractive indexes and the estimations of the oxide layer thickness obtained from the spectra extrema positions as parameters.

The comparison between the experimental spectra and the Abeles based model reflectance spectra for the P300 series samples for an incidence angle of 45° are presented in Figure 135. The blue curves correspond to the experimental data and the red curves to the modeled reflectance spectra. The modeled spectra were normalized as follows:

$$\Omega_{norm}^{simulated}(\lambda) = \Omega^{simulated}(\lambda) \times \frac{mean_{\lambda_i}\left(\Omega^{measured}(\lambda_i)\right)}{mean_{\lambda_i}\left(\Omega^{simulated}(\lambda_i)\right)} \quad (79)$$

where $\Omega^{simulated}(\lambda_i)$ and $\Omega^{measured}(\lambda_i)$ are respectively the Abeles matrices modeled spectrum and the experimental spectrum at the wavelength λ_i. Note that the spectra mean values are taken for the wavelength λ_i in the interval [380 nm – 780 nm].

In the case of the sample anodized at 90V, the doted curve corresponds to the model using the oxide layer thickness obtained from the first extrema and the dashed curve corresponds to the model using the oxide layer thickness obtained from the second extrema.
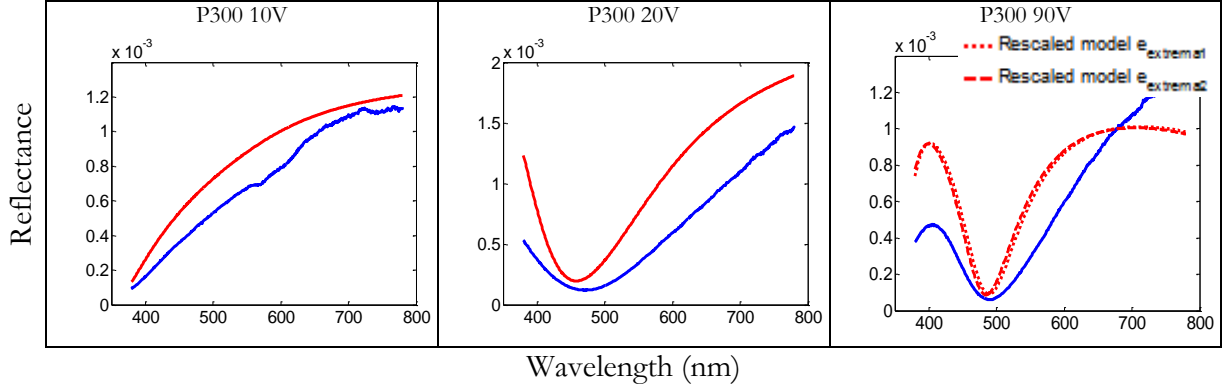
Figure 135: Comparison between experimental spectra (blue curves) and normalized Abeles matrices modeled reflectance spectra (red curves) for the P300 series for the three cell potentials 10V, 20V and 90V for an incidence angle of 45°. The Ti/TiO$_2$ refractive indexes are obtained through the previous ellipsometric measurements and the oxide layer thickness are estimated from the spectra extrema. In the case of the 90V sample, the doted curve corresponds to the model using the oxide layer thickness obtained from the first extrema and the dashed curve corresponds to the model using the oxide layer thickness obtained from the second extrema.

The shapes of the normalized modeled reflectance spectra using the ellipsometric refractive indexes are in quite good agreement with the experimental reflectance spectra.

V. Diffuse reflectance characterization of the samples

1) Comparison between spectral measurements made with the goniospectrophotometer Optimines and a commercial spectrophotometer

The goal of this section is to offer a comparison between the measurements made with the laboratory goniospectrophotometer Optimines and a commercial spectrophotometer. As the instruments have different measurement geometries, they give different information about the optical properties of a material. The goniospectrophotometer can perform specular and out of specular BRDF measurements at various incidence angles and the spectrophotometer offers a standard out of specular geometry adapted to color measurements.

The reflectance of the samples presented in the previous section was also measured at CMIC with a Konica Minolta CM-2500C spectrophotometer. It is a portable spectrophotometer that offers a standard 45°a:0° geometry. An integrating hemisphere, an illumination slit and a Xenon light source with a ring-shaped aperture give a perfect annular illumination. The measurement wavelength range of is [360 nm - 740 nm] with a resolution of 10 nm. The sample is illuminated with a light source with an incidence angle of 45° in respect to the surface normal and the detection is made alongside the normal surface (0° angle).

The goniospectrophotometer Optimines is not well adapted for BRDF measurements in a 45°:0° geometry particularly for specular samples, because of a low signal to noise ratio. A direct comparison of the spectrophotometer and Optimines measurements in the exact same geometry

146

is then difficult to obtain. The comparison will be then between the BRDF measurement in a specular 45°:45° geometry and the spectrophotometer out of specular measurement. The aim of this study is to compare the samples specular reflectance for an incidence angle of 45° with the diffuse reflectance at the same incidence angle.

The comparison of the reflectance measurements obtained with Optimines and with the spectrophotometer for the samples anodized at 90V for the Vibrometer, Alumina and P300 series are presented in Figure 136. In all cases the purple curve corresponds to the reflectance spectrum measured with the spectrophotometer and the red curve corresponds to the one measured with the goniospectrophotometer.

<u>Important note:</u> the reflectance spectrum obtained for the P300 series with the spectrophotometer was normalized as per equation (81) in order to compare it to the one obtained with Optimines:

$$\Omega_{norm}^{Konica}(\lambda) = \Omega^{Konica}(\lambda) \times \frac{mean_{\lambda_i}\left(\Omega^{Optimines}(\lambda_i)\right)}{mean_{\lambda_i}\left(\Omega^{Konica}(\lambda_i)\right)} \qquad (80)$$

where $\Omega^{Konica}(\lambda_i)$ and $\Omega^{Optimines}(\lambda_i)$ are respectively the spectrophotometer and Optimines reflectance spectra at the wavelength λ. Note also that respectively the Optimines and spectrophotometer spectra mean values are taken for $\boldsymbol{\lambda_i}$ in the wavelength ranges [380 nm – 780 nm] and [360 nm – 740 nm] respectively. Indeed, the reflectance values given by the spectrophotometer are much higher than the values given by Optmines for the P300 series, due to the improper use of the equation (42) for the total reflectance of diffuse samples.

In all cases, the reflectance values given by the spectrophotometer are higher than the one given by Optimines. The case where these values are the closest is for the Vibrometer samples, in accordance with the fact that the equation (42) is adapted for total reflectance calculation from BRDF measurement for Vibrometer (ie: highly specular) samples. The positions of the maxima of the reflectance are slightly shifted towards the "blue wavelengths" when the measurement is made in the specular direction when compared to the out of specular condition. However the positions of the minima are shifted towards the "red wavelengths" under the same conditions. The difference in the reflectance values between the spectrophotometer and Optimines are smaller for smoother, more specular samples. The same comparison has been made for the samples anodized at 10V and 20V and their reflectance spectra are presented in appendix L. The same shift of the minima is observed for these samples. However, the samples anodized at 10V do not exhibit maxima, so no conclusion could be drawn concerning the shift of the maxima in these samples. It is also interesting to notice that the difference in the reflectance values between the two devices is smaller for the samples anodized at 10V than for the samples anodized at 90V. Indeed, all things equal, the samples anodized at a lower potential exhibit a lower roughness.

90V "Vibrometer"

90V "Alumina"

90V "P300"

Sample Name	Extrema position « Konica » (nm)	Extrema position « Optimines » (nm)
90V Vibro	410.0 (max) 510.0 (min)	404.8 (max) 497.6 (min)
90V Alumina	410.0 (max) 510.0 (min)	416.8 (max) 504.0 (min)
90V P300	400.0 (max) 500.0 (min)	402.0 (max) 490.3 (min)
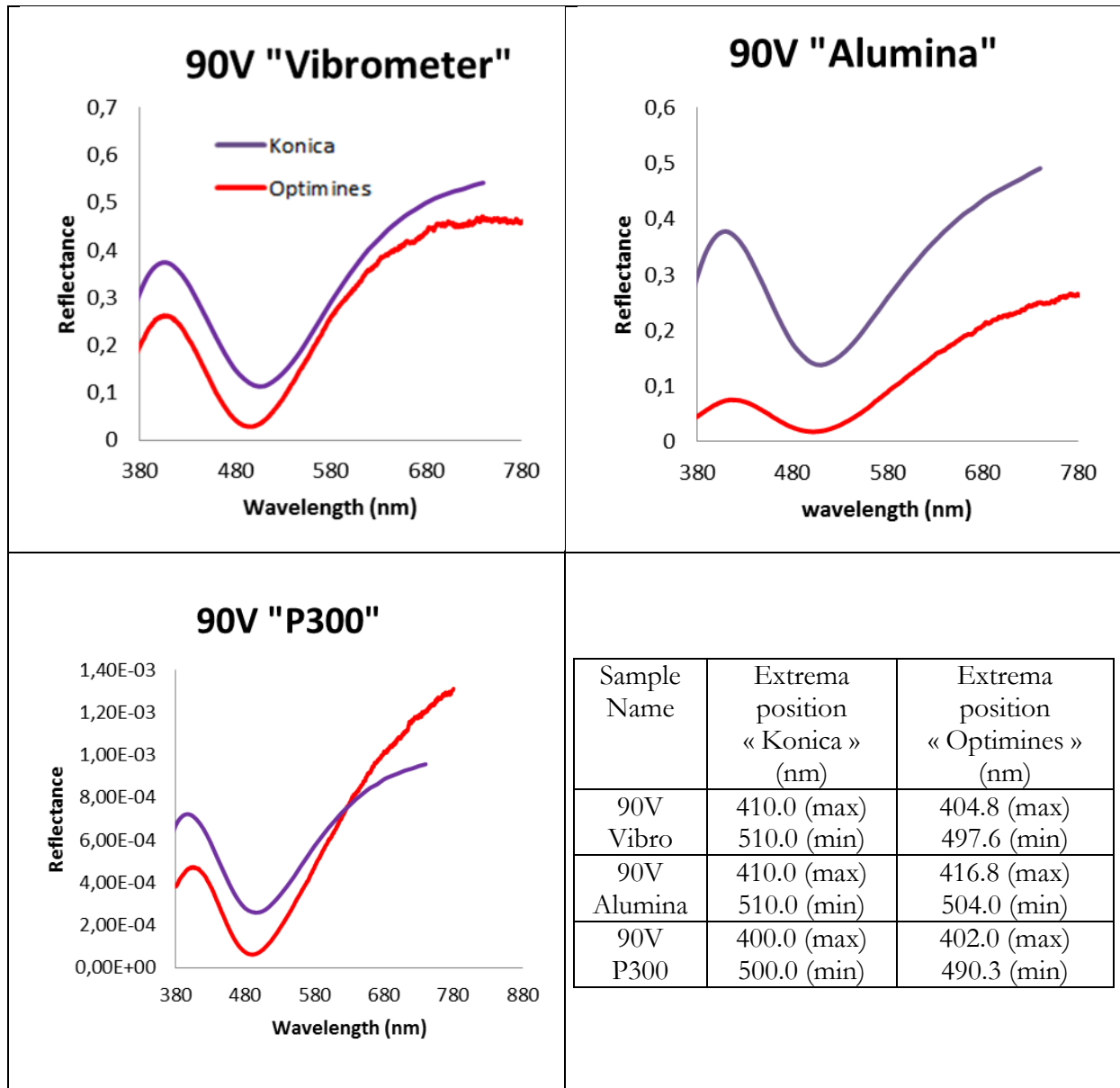
Figure 136: Comparison between reflectance measurements obtained with the goniospectrophotometer Optimines and the commercial spectrophotometer Konica Minolta CM-2500C for the 3 samples series. The Optimines measurement geometry is 45°:45° and the Konica measurement geometry is 45°a:0°. In the table are represented the extrema positions of the reflectance spectra for both devices.

2) Diffuse reflectance modeling of oxidized metals and thin films

In this section a literature review will focus on the information which can be deduced from the comparison between specular and diffuse reflectance spectra.

a) Modeling of multilayer materials with correlated or uncorrelated interface roughnesses.

Carniglia [94] presented different models of the diffuse reflectance of multilayer optical coatings depending on the correlation of roughnesses at the interfaces. The results presented here will be focused on monolayer (i.e.: layer/substrate) samples. All the results presented in the article are obtained for real refractive indexes but in section 4 of the article a generalization to complex

indexes is proposed. Carniglia presented as a starting point, the Abeles model where the two interfaces layer/air and layer/substrate are perfectly flat. It is the model proposed in the Chapter I of this manuscript and Carniglia's result is presented in Figure 137. Note that the optical thickness corresponds to the layer thickness times its refractive index, i.e. $e_{layer} \times n_{layer}$.
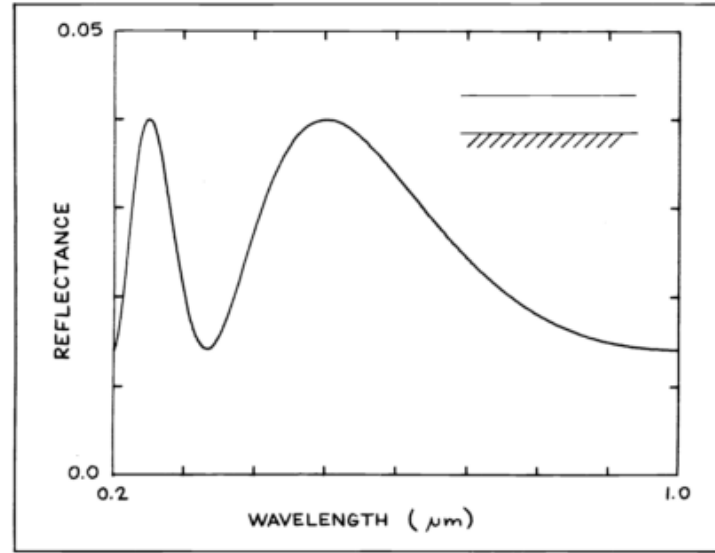
Figure 137: Abeles matrices based modeled reflectance spectrum for a single layer with n_{layer} =1.38 with an optical thickness of 250 nm. The substrate has an index of $n_{substrate}$ = 1.5. Note that the optical thickness corresponds to the layer thickness times its refractive index, i.e. $e_{layer} \times n_{layer}$ (from [94]).

Carniglia presented a model for uncorrelated interface roughnesses for the same single layer film used in the previous Abeles model (see Figure 138). This model has been presented first by Eastman in [95] and is based on the scalar scattering theory [96]. Eastman extended this theory to multilayer films by introducing matrices. Eastman's model is applicable to either totally correlated or totally uncorrelated rough interfaces.
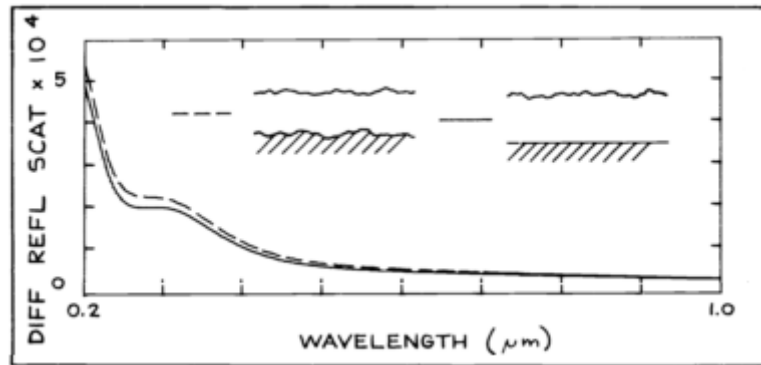
Figure 138: Eastman modeled reflectance spectra for uncorrelated interface roughnesses for a single layer with n_{layer} =1.38 with an optical thickness of 250 nm. The substrate has an index of $n_{substrate}$ = 1.5. The solid curves correspond to a rough layer on a smooth substrate whereas the dashed curve corresponds to a layer with two uncorrelated rough surfaces. All rough surfaces have an RMS roughness equal to 20 Å. From [94].

The solid curve of Figure 138 applies to the case of a rough layer on a smooth substrate. The dashed curve corresponds to the case of two uncorrelated rough interfaces. In both cases all rough surfaces have a Root Mean Square (RMS) roughness equal to 20 Å. The addition of the rough substrate has a small effect on the diffuse reflectance indicating that the outer surface is the

major contributor. In both cases, the diffuse reflectance has an interference pattern opposite in phase to the specular interference seen in Figure 137.

Carniglia also presented Eastman's model in the case of correlated interface roughnesses. Figure 139 presents this model (solid curve) for a single layer film with the same parameters as in the previous models.
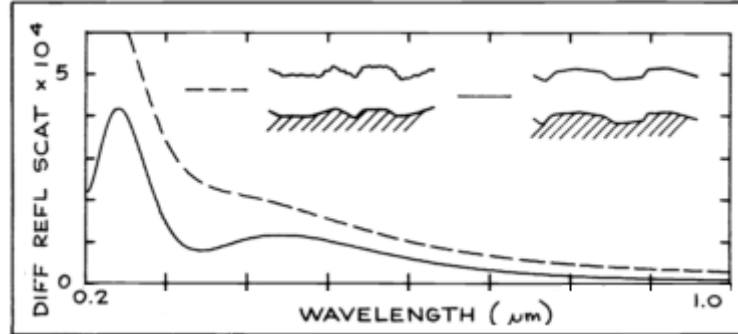
Figure 139: Eastman modeled diffuse reflectance spectrum of totally correlated interface roughnesses (solid curve). "Additive roughness" reflectance spectrum (dashed curve). Both models are for a single layer with n_{layer} =1.38 with an optical thickness of 250 nm. The substrate has an index of $n_{substrate}$ = 1.5. In the case of Eastman's model both interfaces have a RMS roughness of 20 Å. In the case of the "Additive roughness" model the layer/substrate interface has a RMS roughness of 20 Å whereas the air/layer interface has a RMS roughness of 28 Å (from [94]).

Carniglia also developed a new model, derived from Eastman's model, called "additive roughness". This model considers that each layer adds roughness to the next interfaces because of layer thickness inhomogeneities. This model corresponds to the case where the roughnesses of the two interfaces are partially correlated. The global roughness pattern is the same between the two interfaces but the thickness inhomogeneities add a "small" surface to the next interface.

Figure 139 also presents the "additive roughness" model (dashed curve) for a single layer film with the same parameters as the previous models. In this case the air/layer interface has an initial RMS roughness of 20 Å with RMS layer thickness variations of 20 Å. The final air/layer RMS roughness is thus $20\sqrt{2} = 28$ Å.

In the case of totally correlated interface roughnesses, the diffuse reflectance spectrum is in phase with the specular reflectance spectrum of Figure 137. In the case of "Additive roughness", the diffuse reflectance is highly increased, due to the higher roughness of the air/layer interface, but is also globally in phase with the specular reflectance spectrum.

Carniglia developed a new model, adapted when the scattering is caused by inhomogeneities in the refractive index of the layers themselves (see Figure 140). This case is identical to the case of uncorrelated surface roughnesses with a rough substrate and a smooth outer surface (previous Eastman model for totally uncorrelated interfaces). It is reasonable that these two cases should agree. Indeed, the outer surface is smooth in both cases. In addition, the reflected scattering from the rough substrate surface is equivalent to scattering from a wave having passed through an inhomogeneous layer.
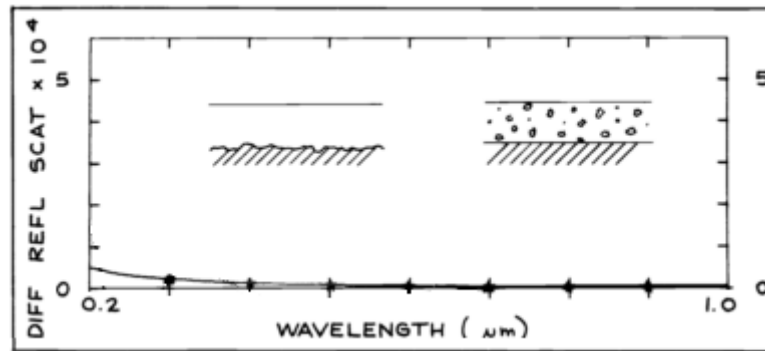
Figure 140 : Carniglia modeled diffuse reflectance spectrum for plane interfaces but with an inner layer containing inhomogeneities and Eastman modeled reflectance spectrum in case of a smooth outer interface and a rough inner interface (uncorrelated roughness). Both models give the same curve. Both models are for a single layer with n_{layer} =1.38 with an optical thickness of 250 nm. The substrate has index $n_{substrate}$ = 1.5. The rough substrate has a RMS roughness of 20 Å and the inner layer has RMS roughness variations of 20 Å (from [94]).

In both of these cases the diffuse reflectance spectra is quite small compared to all the other cases and does not exhibit any interference pattern. Surprisingly the model of a smooth outer interface and a rough inner interface is not equivalent to the case of uncorrelated interface roughnesses presented on Figure 138 despite having a similar layout. It shows the high influence of the air/layer interface on the diffuse reflectance of the material.

b)   <u>Observation of the diffuse reflectance of oxidized metals.</u>

Roos *et al*. [97] compared for different kinds of oxide coated metals the diffuse and specular components of the reflectance. Figure 141 presents a comparison of the reflectance spectra of two equally thick oxide layers obtained by a thermal oxidation (a) and chemical oxidation (b) of copper samples prepared by sputtered and evaporated films on glass substrates. Thermal oxidation is performed in a laboratory oven at 150-180°C and the chemical oxidation was performed in a 70°C sodium chlorite bath. In order to measure the total hemispherical reflectance, a Beckman 5240 double-beam spectrophotometer equipped with an integrating sphere was used in the 350nm - 2500nm wavelength range (incidence angle not indicated in the paper). This device allows to measure separately the diffuse and the total reflectance of a given sample. The specular reflectance spectrum is then obtained by simply subtracting the diffuse reflectance from the total reflectance. This quantity has been also measured directly with a Perkin Elmer 157 specular spectrophotometer (geometry not indicated) [98] and the two values are in agreement. Roughness effects are here caused by the process of oxidation because samples prepared by films sputtering and evaporation exhibit very smooth surfaces. The chemical oxidation method produces a rough oxide-metal interface which considerably increases the optical absorption in comparison with the thermally oxidized surface [99]. The sample roughnesses are not given in [97].

A diffuse reflectance which is opposite in phase to the specular interference pattern can be observed in both cases in Figure 141 a) and b). By comparing Figure 141 a) and b) the chemical oxidation produces a surface with a higher absorption. The total reflectance is lower in the case of chemical oxidation. This result is coherent with a previous study performed by Roos and Karlsson [99].
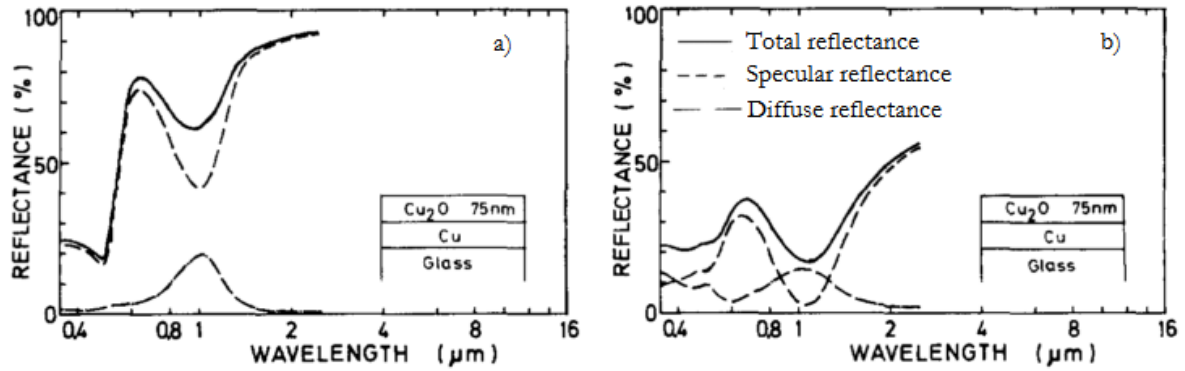
Figure 141: Comparison of the reflectance spectra of two Cu₂O equally thick oxide layers obtained by a thermal oxidation (a) and chemical oxidation (b) of copper samples prepared by sputtering and evaporated films on glass substrates. The total reflectance (solid curve) is divided into a specular reflectance (dashed curve) and a diffuse reflectance (chain curve). The total reflectance and the diffuse reflectance are directly measured and the specular reflectance is obtained by subtracting the specular reflectance to the total reflectance (from [97]).

Roos *et al.* [97] observed the effect of changing the substrate on which the copper was oxidized. In Figure 142 a) the substrate is rolled copper and in Figure 142 b) the copper was evaporated on a rolled stainless-steel substrate and then totally anodized. In both cases, the substrate was macroscopically rough, especially compared to the previous smooth glass substrate. The oxide layer was then obtained by thermal oxidation and in both cases the oxide layer composition was verified to be chemically the same by X-ray diffraction. In Figure 142 a), it is interesting to observe that the phase of the oscillation of the diffuse reflectance is not exactly opposite to that of the specular signal. However, the diffuse reflectance is perfectly in phase with the specular signal, contrarily to the previously presented cases when the substrate is rolled stainless steel as shown in Figure 142 b). The authors propose that the out-of-phase diffuse interference depends on the substrate metal and is more than just an effect of the oxide/metal interface roughness.
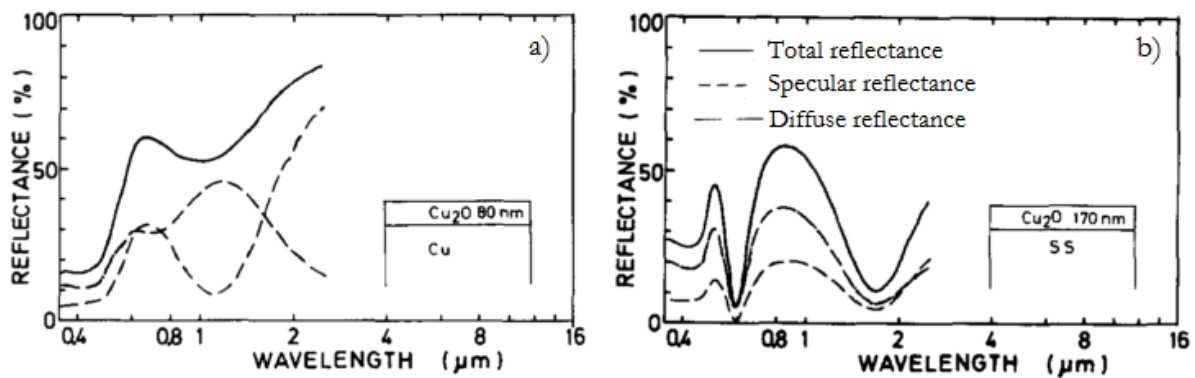
Figure 142: Comparison of the reflectance spectra of two Cu₂O oxide layers obtained by a thermal oxidation of a rolled copper substrate (a) and by evaporation on a rolled stainless-steel substrate (b). The total reflectance (solid curve) is divided into a specular reflectance (dashed curve) and a diffuse reflectance (chain curve). The total reflectance and the diffuse reflectance are directly measured and the specular reflectance is obtained by subtracting the specular reflectance to the total reflectance (from [97]).

The authors also reproduced the same experiment on titanium samples thermally oxidized at 600°C with different oxide layer thicknesses: 135 nm in Figure 143 a) and 40 nm in Figure 143 b).
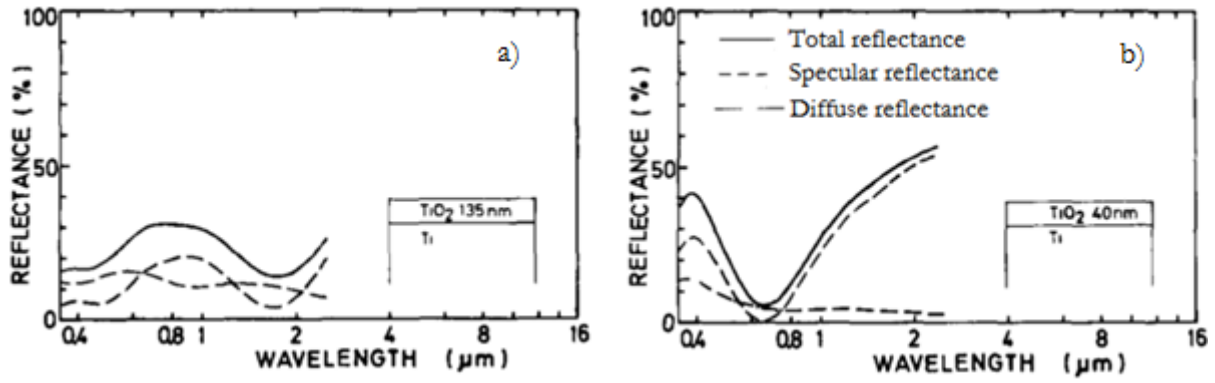
Figure 143: Comparison of the reflectance spectra for thermally oxidized polished titanium samples with oxide layer thicknesses equal to 135 nm (a) and 40 nm (b). The total reflectance (solid curve) is separated additively into a specular reflectance (dashed curve) and a diffuse reflectance (chain curve). The total reflectance and the diffuse reflectance are directly measured and the specular reflectance is obtained by subtracting the specular reflectance to the total reflectance (from [97]).

In Figure 143 a) the diffuse reflectance is not exactly out of phase with that of the specular reflectance even if it is not as clear as the for previous cases because of the low diffuse reflectance of the titanium-based samples compared to the copper-based ones. If the oxide layer thickness is reduced as described in Figure 143 b) the diffuse reflectance does not show any specific behavior anymore. The authors suggested that the appearance of the out-of-phase diffuse interference is connected with the growth mechanism of the oxide.

In a latter study, Ross and Ribbing [100] proved by observation of diffuse reflectance from cuprous oxide on copper and gold obtained by thermal oxidation of evaporated copper films that the origin of the diffuse interference is localized at the oxide/metal interface. Indeed, the oxidation process generates a roughness which remains as long as the oxidation proceeds in the parent metal. If the oxidation is continued until the oxidation front reaches the nobler metal (gold), the roughness nearly vanishes and the diffuse interference disappears.

Bergkvist et al. [101] showed a relationship between the electric field at the interfaces and the diffuse reflectance of oxidized copper samples. The samples were prepared by sputtering and evaporating copper films on glass substrates and a thermal oxidation in air at a temperature between 180°-200°. The variation of the electric field E along the direction z perpendicular to the interfaces is characterized by the ratio $\varepsilon = \frac{\langle E^2(z) \rangle}{\langle E^{+2}(z) \rangle}$ where $\langle E^2(z) \rangle$ is the time average of the square of the total electric field and $\langle E^{+2}(z) \rangle$ is the time average of the square of the incident electric field at the position z. The methods to calculate the incident total electric field and the electric field at the interfaces are described in details [101]. Figure 144 represents the calculated variations of ε with the wavelength at the oxide/metal interface (z=0, dashed curve) for two different cuprous oxide thicknesses (40 nm and 185 nm). The experimental measurements of the variations with the wavelength of the diffuse reflectance R_d (doted curve) of thermally oxidized copper samples with the same oxide thickness are also represented on the same figure. In Figure 144 a) the variations of the electric field E at the oxide/metal interface more closely follows the variations of the diffuse reflectance than the variations of the electric field at the air/oxide interface. The difference is more noticeable if the oxide layer thickness is thicker, as shown in Figure 144 b). This article showed solid evidence that the local electric field intensity at the oxide/metal interface and the diffuse reflectance vary in the same way versus the wavelength. This article also showed that these quantities vary the same way versus the oxide thickness.

153

c) Modeling of the diffuse reflectance of oxidized metals.

Roos *et al.* [102] proposed a method to model the diffuse reflectance and transmittance spectra of an interference layer over a substrate for a normal incident light. The model is based on electric field calculations inside the interference layer as presented in Chapter 7 of [72] called "Thin-film absorbance measurements using laser calorimetry". The interfaces are assumed to be totally uncorrelated.

The modeled total scattered intensity from the two interfaces is written as:

$$R_D(\lambda) = \frac{\varepsilon(\lambda, -d)}{\varepsilon_{film}(\lambda)} R_{D_{AL}} + \frac{\varepsilon(\lambda, 0)}{\varepsilon_{substrate}(\lambda)} R_{D_{LS}} \times \exp(-\alpha d)\, T_{AL} + \frac{\varepsilon(\lambda, -d)}{\varepsilon_{film}(\lambda)} T_{D_{AL}} R_{LS} \times \exp(-2\alpha d)\, T_{LA} \qquad (81)$$

where:

- $\alpha = \frac{4\pi k}{\lambda}$ $with$ $k = Im(n_{layer})$ where n_{layer} is the refractive index of the layer.
- $\varepsilon(\lambda, z) = \frac{\langle E^2(z) \rangle}{\langle E_{inc}^2(z) \rangle}$ is the normalized time average of the square of the electric field.
- $\varepsilon_{film}(\lambda)$ is the normalized time average of the square of the electric field when the layer/substrate interface is moved to infinity along the positive z axis.
- $\varepsilon_{substrate}(\lambda)$ is the normalized time average of the square of the electric field when the air/layer interface is moved to infinity along the negative z axis.
- 0 is the position of the layer/substrate interface along the z axis.
- (-d) is the position of the air/layer interface along the z axis.
- λ is the light wavelength

The subscripts AL or LA correspond to the air/layer interface and the subscript LS corresponds to the layer/substrate interface. AL is used when the light is coming from the air medium and LA when the light is coming from the layer and going into the air medium.

The diffuse reflectance R_D is defined as the difference between the specular reflectance for a perfectly plane interface (Fresnel coefficient) and the specular reflectance in case of a rough surface. Its expression is:

$$R_{Di} = \left(1 - \exp\left(-\left(\frac{4\pi n_j \delta_i}{\lambda}\right)^2\right)\right) R_i$$

$$T_{Di} = \left(1 - \exp\left(-\left(\frac{4\pi (n_{j-1} - n_k)\delta_i}{\lambda}\right)^2\right)\right) T_i$$

(82)

where $i = $ AL or LS, j is equal to "air" if $i = $ AL and to "layer" if $i = $ LS, k is equal to "layer" if $i = $ AL and to "subs" if $i = $ LS. $n_{air} = 1$, n_{layer} is the layer refractive index and n_{subs} is the substrate refractive index. T_i and R_i correspond to the Fresnel coefficients for either transmission or reflection (see equations (21)(23)). δ_i corresponds to the RMS roughness of the interface i.

The incident electric field is defined as:

$$E_{inc} = E_0 \exp(i \times \gamma_{air} \times (z + d)) \qquad \text{where } \gamma_{air} = \frac{2\pi}{\lambda} n_{air} \qquad (83)$$

The total electric field in the air medium is then:

$$E_{tot}^{air} = E_0 \exp(i\gamma_{air}(z + d)) + r_{AL} \times \exp(-i\gamma_{air}(z + d))$$
$$+ t_{AL}r_{LS}t_{LA} \times \exp(-i\gamma_{air}(z + d) + 2i\gamma_{layer}d) \times \frac{1}{1 - r_{LS}r_{LA}\exp(2i\gamma_{layer}d)} \qquad (84)$$

The total electric field in the layer is then:

$$E_{tot}^{layer} = E_0 t_{AL} \times \left[\exp\left(i\gamma_{layer}(z + d)\right) \times \frac{1}{1 - r_{LS}r_{LA}\exp(2i\gamma_{layer}d)}\right.$$
$$\left. + r_{LS}\exp\left(i\gamma_{layer}(-z + d)\right) \times \frac{1}{1 - r_{LS}r_{LA}\exp(2i\gamma_{layer}d)}\right] \qquad (85)$$

The total electric field in the substrate is then:

$$E_{tot}^{substrate} = E_0 t_{AL}t_{LS}\exp(i\gamma_{subs}z) \times \exp(i\gamma_{layer}d) \times \frac{1}{1 - r_{LS}r_{LA}\exp(2i\gamma_{layer}d)} \qquad (86)$$

where r_i and t_i ($i = AL, LS, LA$) correspond to the amplitude Fresnel coefficients (see equations (26)(27)).

This model has been used [103] and compared to experimental spectra. The experimental reflectance spectra were measured for a dielectric material made of a tin oxide layer (SnO_2) on a corning glass substrate prepared by pyrolytic deposition at a temperature of 425°C. The comparison between modeled spectra with a perfectly plane oxide/substrate interface and a rough air/oxide interface and the experimental data for a 500 nm thick oxide layer are presented in Figure 145. The roughness of the air/oxide interface is either 20 nm or 25 nm for the modelled spectra.

The experimental data and the modeled spectra are in good agreement in terms of intensity and positions of the extrema. For the longest wavelengths however, the calculated spectra are higher than the experimental ones for both roughness parameters. The authors explain this phenomenon by an effective RMS roughness dependent on the wavelength. The good agreement between the modeled and experimental data seems to indicate that the roughnesses of the interfaces are not correlated for this tin oxide/glass sample.
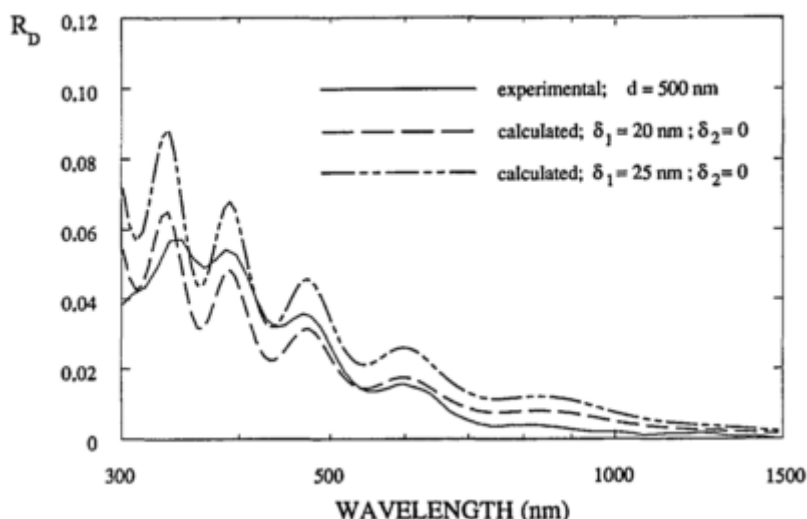
Figure 145: Experimental and calculated diffuse reflectance spectra for a SnO_2/glass sample with a 500 nm thick oxide. The roughness of the air/oxide interface is either 20 nm or 25 nm and the oxide/glass interface is perfectly smooth for the modeled spectra.

d) Application of Roos diffuse reflectance model in the case of Ti/TiO$_2$ samples.

A MATLAB® code developed in GFL by Renee Charrière based on the previously presented model developed by Roos *et al.* [102] has been used to investigate the Ti/TiO$_2$ samples presented in the previous sections of this chapter. The diffuse reflectance spectrum of a 185 nm thick TiO$_2$ oxide layer on a titanium substrate for a normal incident light is compared to an Abeles based model (assuming flat interfaces) of the specular reflectance for the same sample for normal incident light. The diffuse reflectance model assumes RMS roughnesses of the Ti/TiO$_2$ and air/TiO$_2$ interfaces both equal to 15 nm (see Figure 146). The Ti and TiO$_2$ refractive indexes are given by the ellipsometric measurements presented previously in section IV) of this chapter.

The two modeled reflectance spectra are opposite in phase as expected for uncorrelated rough interfaces. Carniglia [94] showed that for dielectric materials, the specular reflectance and the diffuse reflectance are opposite in phase for uncorrelated rough interfaces. It is also the case for anodized titanium, in particular for the Ti and TiO$_2$ refractive indexes measured by ellipsometry on the samples presented previously.
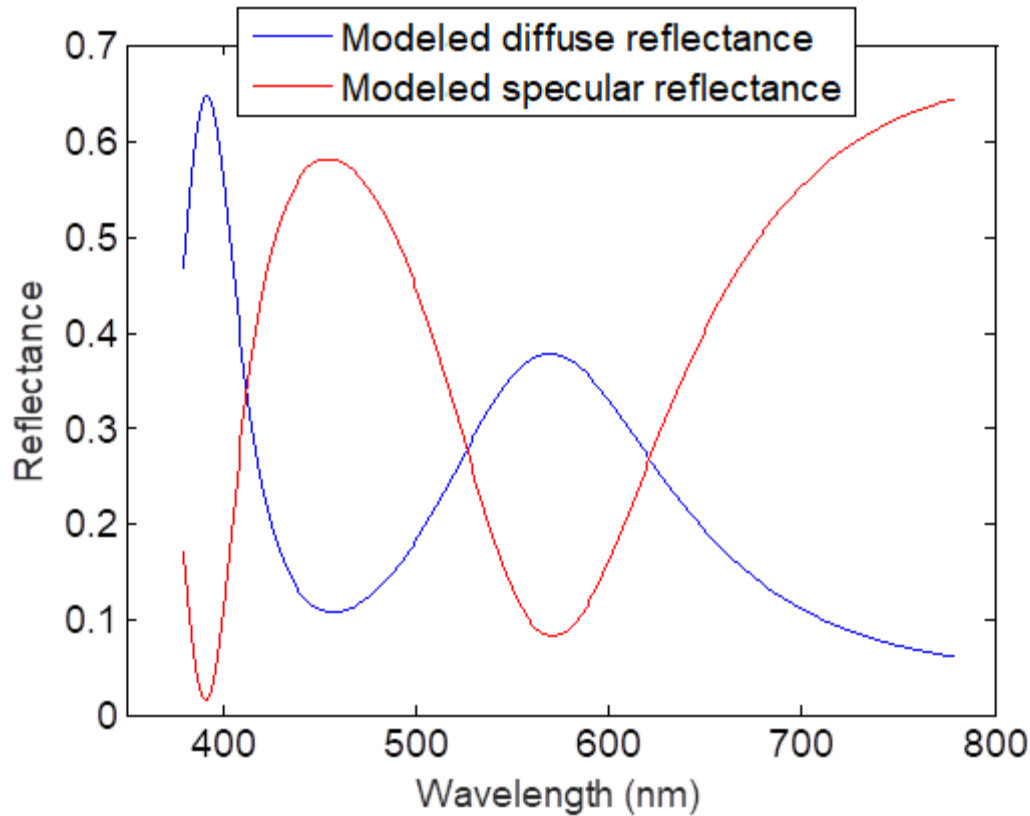
Figure 146: Comparison of the diffuse reflectance spectrum obtained with Roos *et al.* [102] model with the specular reflectance spectrum obtained with an Abeles matrices based model for normal incident light. The sample is a 185 nm thick TiO_2 oxide layer on a titanium substrate. The diffuse reflectance model assumes RMS roughnesses of the Ti/TiO_2 and air/TiO_2 interfaces both equal to 15 nm, whereas the Abeles matrices based one assumes perfectly flat interfaces. The refractive indexes are given by the ellipsometric measurements of section IV.

At the beginning of the present section (page 136), measurements of the specular reflectance for an incidence angle of 45° were compared to measurements of the diffuse reflectance in the geometry 45°a:0° for the samples anodized at a cell potential of 90 V from the three different series. The specular and diffuse reflectance were in phase. This seems to be a first indication that the interface roughnesses are correlated. Nevertheless, it is important to be cautious with this interpretation because, first, the experimental spectra were observed at an incidence angle of 45° whereas the modeled ones were computed at normal incidence. The modeled spectra give also the total diffuse reflectance in an hemisphere, whereas the diffuse reflectance was measured in this section in the particular 45°a:0° geometry. Note also that the modeled diffuse spectra presented in Figure 146 assumes an RMS roughness of 15 nm for the TiO_2/Ti interfaces which might not correspond to the sample presented in this section. The 90V Vibrometer sample has indeed a roughness R_a parameter of about 50 nm after anodizing (15 nm before) which is certainly different from an RMS roughness of 15 nm. Additional experiments are thus needed to confirm the interface roughness correlation of the sample presented before.

VI.   Color evolution with the observation angle

1) General observations about the samples: reflectance spectra, sample colors in the specular direction for an incidence angle of 45° and gonioappearance.

Due to a large difference in the reflectance values, reflectance spectra of the samples of the Alumina and Vibrometer series are represented together for each cell potential in the top row of

157

Figure 147 and all the P300 samples are represented in the bottom row of Figure 147. For a cell potential of 10V, the shape of the reflectance spectra of the P300 and Vibrometer series are different in the visible range and it explains their different colors. No local minimum is observed in the visible wavelength range for the Vibrometer sample, explaining its very low color saturation, i.e.: grey color. For a cell potential of 20V, the shapes of the reflectance spectra are almost the same for the Alumina and P300 series, with lower values on the "blue" wavelengths and higher values in the "red" wavelengths for the P300 series explaining its purple color. However, the shape of the reflectance spectrum of the Vibrometer series is similar to the shape of the Alumina sample anodized at 10 V and both have a yellow color. The local minima of the Vibrometer and P300 reflectance spectra anodized at 90V are reached for the same wavelengths, whereas it is slightly shifted towards the "red" wavelengths for the Alumina sample. All the 90 V samples exhibit almost the same color.
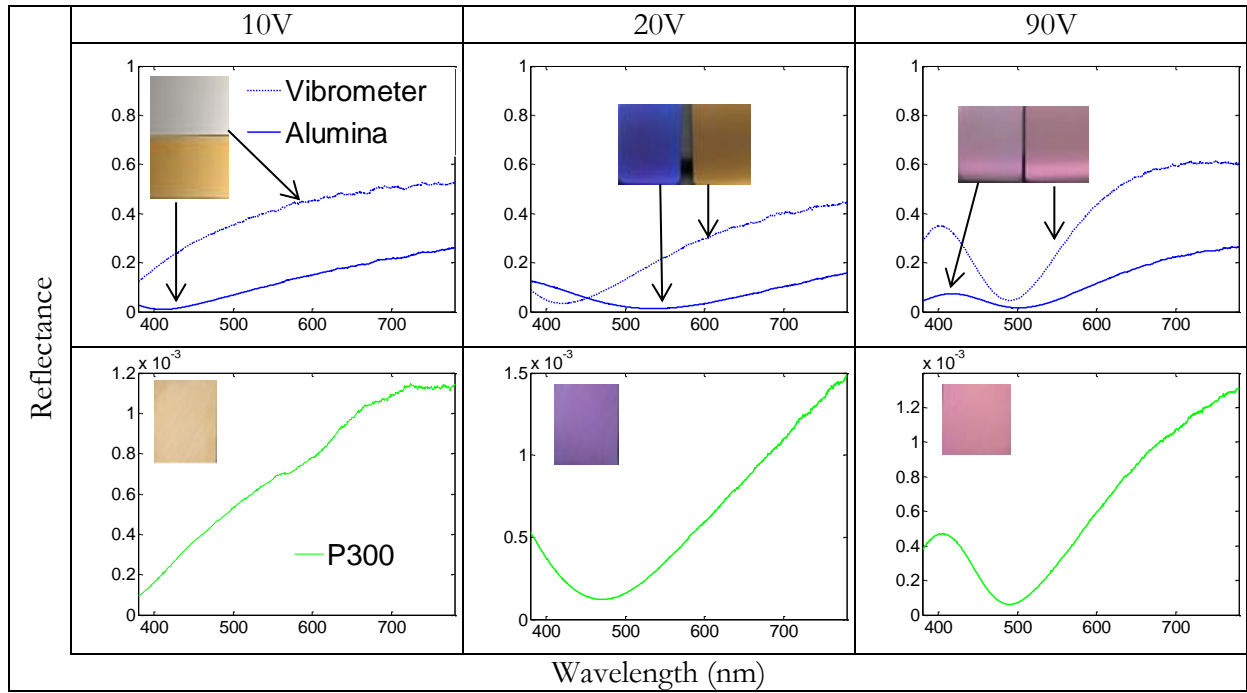
Figure 147: Reflectance spectra of anodized titanium samples obtained in a specular condition for an incidence angle of 45° for the P300, Alumina and Vibrometer series and for the 10V, 20V and 90V cell potentials. A color picture of each sample is also presented.

2) Estimation of the error induced by the chromatic aberration

As mentioned in the Chapter 3 section 4), chromatic aberration has been observed while performing goniospectrophotometric measurements around the specular condition but its impact was not estimated. Tests were performed in order to determine which error on the color measurements might be attributed to the chromatic aberration. These tests were performed without any sample.

First the detection and the illuminating arms face each other, i.e. incidence and detection angles are equal to 90°. Then the detection arm is moved $\pm$ 1° away from this "specular" condition with a 0.02° step. The measurement process is exactly the same as a BRDF measurement of the sample. When the source and detection arm face each other the direct source flux is measured and then a "BRDF" (according to equation (33)) is computed for each position of the detection arm $\pm$ 1° around the "specular" condition. Such measurements have been made for five different axial positions of the detection lens focusing the beam inside the detection fiber in order to

slightly change the lens/fiber distance around the focal length. As the "BRDF" intensity varies a lot around the "specular" direction, all the BRDF are normalized by dividing each "BRDF" by its average over the visible wavelengths range [380 nm – 780 nm].

Figure 148 presents the comparison between the normalized "BRDF" for the five different detection lens positons, in the case where the source and detection arm are exactly facing each other. Note that the chromatic aberration is not characterized here. Indeed, for each measurement, i.e. each position of the detection lens, the computation of the "BRDF" according to equation (33) implies that the signal is divided by the direct flux source. This corresponds to the position when the two arms are facing each other. In this position, the "BRDF" should be thus equal to 1 which is almost the case (see Figure 148). Slight shifts from this value could be due to a small 90° position difference of the detection arm when the "BRDF" is measured and when the detection arm scans the position from 91° to 89°).
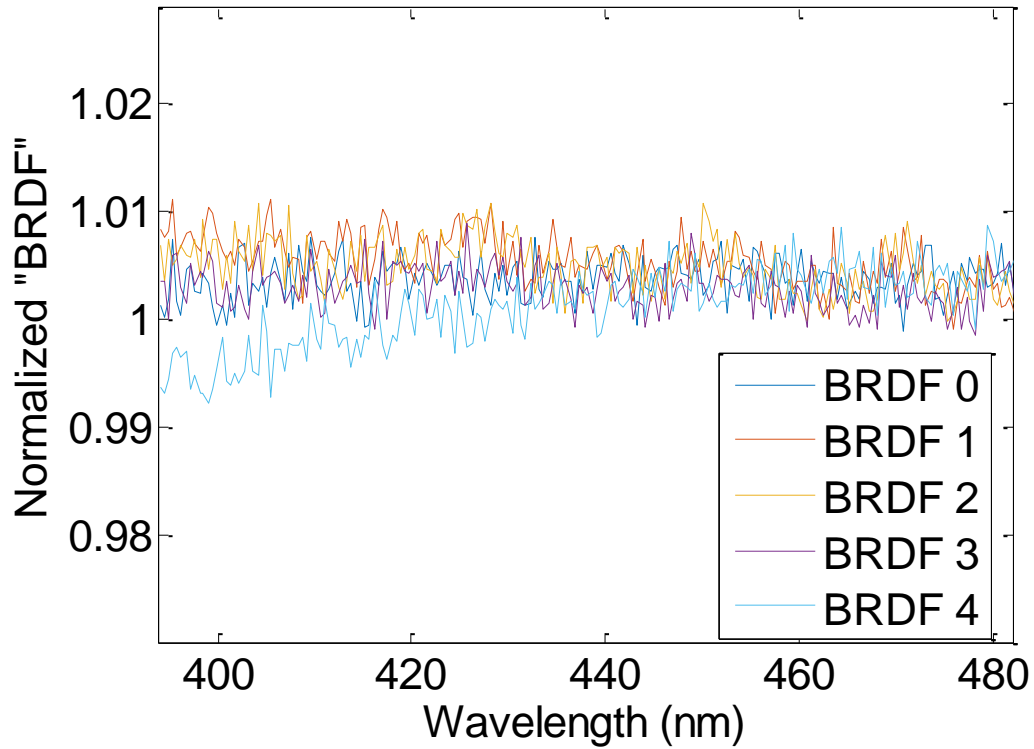
Figure 148: Normalized "BRDF" for five different detection lens positions in the case where the source and the detection arm are facing each other (incidence and detection angle equal to 90°). To compare the shape of the spectra, each spectrum was rescaled by dividing each spectrum by its average over the visible wavelength range [380 nm -780 nm].

In Figure 149 a) and Figure 149 b), the normalized "BRDF" are plotted for five different detection lens when the observation angle is respectively equal to 89.7° and 90.3°. In both cases presented in Figure 149, the normalized "BRDF" is not equal to 1, as observed in Figure 148. The normalized "BRDF" becomes dependent on the wavelengths. In all cases except BRDF 3 for an observation angle of 90.3°, the normalized "BRDF" is lower than 1 in the "blue" wavelengths and higher than 1 in the "red" wavelengths. The variations of the normalized "BRDF" with the wavelength are dependent on the detection lens position, which is on the position of the detection fiber around the focus point. This is characteristic of chromatic aberration.

The normalized "BRDF" for one position of the detection lens (position "0") was measured when varying the observation angle ± 0.3° around the specular direction (see Figure 150).
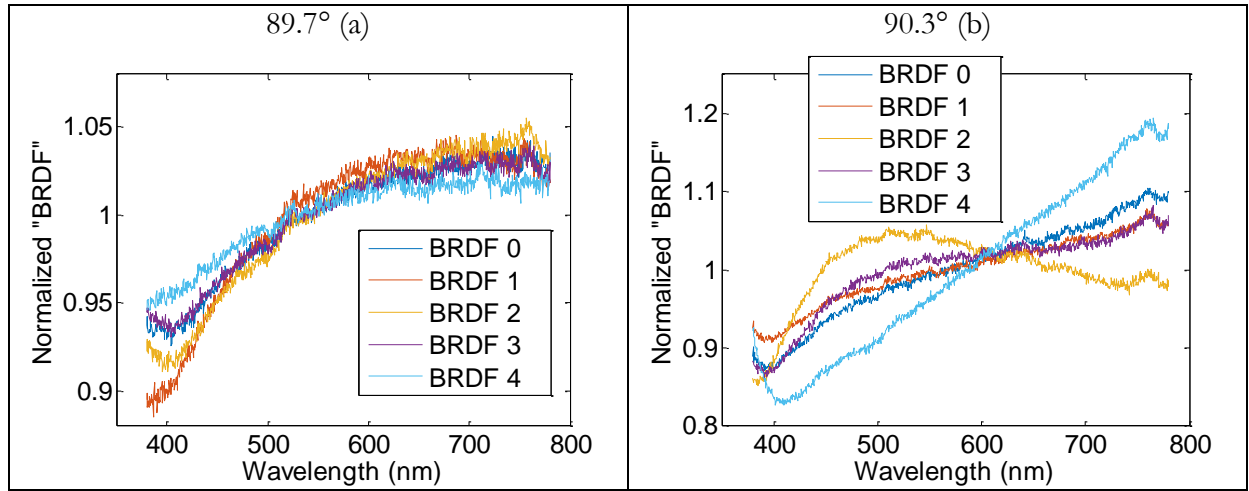
Figure 149: Normalized "BRDF" for five detection lens positions with observation angles of 89.7° a) and 90.3° b) and an incidence angle of 90°. To compare the shape of the spectra, each spectrum was rescaled by dividing each spectrum by its average over the visible wavelength range [380 nm -780 nm]

In Figure 150 for observations angles far from the "specular" direction 90°, the normalized "BRDF" have lower values on the "blue" wavelengths (around 450 nm) and higher values on the "red" wavelengths (around 700 nm) than the normalized "BRDF" close to the specular direction. This is coherent with the observations made in the chapter 3 section III 4) for the titanium non-anodized etched sample. The fact that the normalized "BRDF" variations with the wavelength are also dependent on the detection arm position around the "specular" direction, which corresponds to the distance of the detection fiber relatively to the lens optical axis is also an indication of an observation of chromatic aberration.
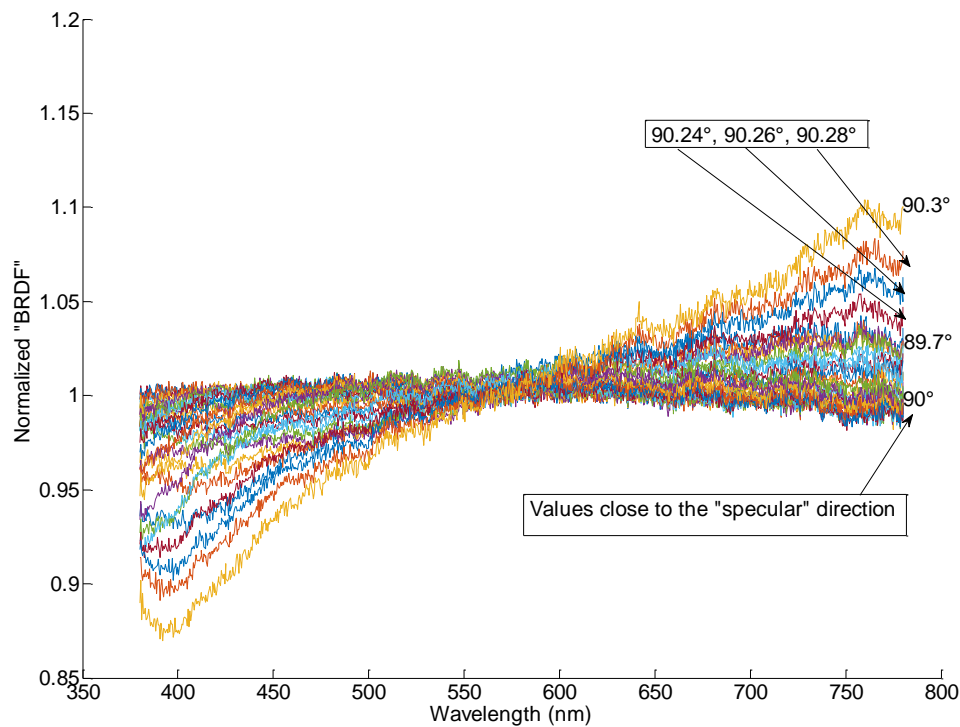
Figure 150: Normalized "BRDF" for one given detection lens position (called "0") with observation angles ranging from 89.7° to 90.3°. To compare the shape of the spectra, each spectrum was rescaled by dividing each spectrum by its average over the visible wavelength range [380 nm -780 nm].

In order to quantify the error on the color measurements due to the chromatic aberration, the normalized "BRDF" data were converted into CIE 1931 xy chromaticity coordinates in the same manner as presented in chapter 3 section V 2). The xy coordinates for each normalized "BRDF" measurement taken for an observation angle varying from $\pm1°$ around the "specular" direction have been calculated. This has been done for the five previous positions of the detection lens. In the total absence of chromatic aberration, all the normalized "BRDF" should be equal to 1 for all wavelengths. In the case of a constant BRDF equal to 1, the xy coordinates are equal to the reference white point (D65 in this study). Thus to quantify the error due to the chromatic aberration on the color measurements, the distance D from the xy coordinates computed from the normalized "BRDF" measurements to the D65 xy coordinates have been computed as the following:

$$D = \sqrt{(x - x_{ref})^2 + (y - y_{ref})^2}$$ (87)

where x_{ref} and y_{ref} are the D65 xy coordinates and are equal to $x_{ref} = 0{,}31271$ and $y_{ref} = 0{,}32902$. The results are presented in Figure 151. The maximum acceptable value for the distance D is fixed to 0.02 which corresponds to a variation relatively to the D65 position of 4.4%. It is represented by the red line in Figure 151.

For all the detection lens position, there is an acceptable angular range for the detection arm of $\pm0.3°$ around the "specular" direction where D is lower or equal to 0.02.
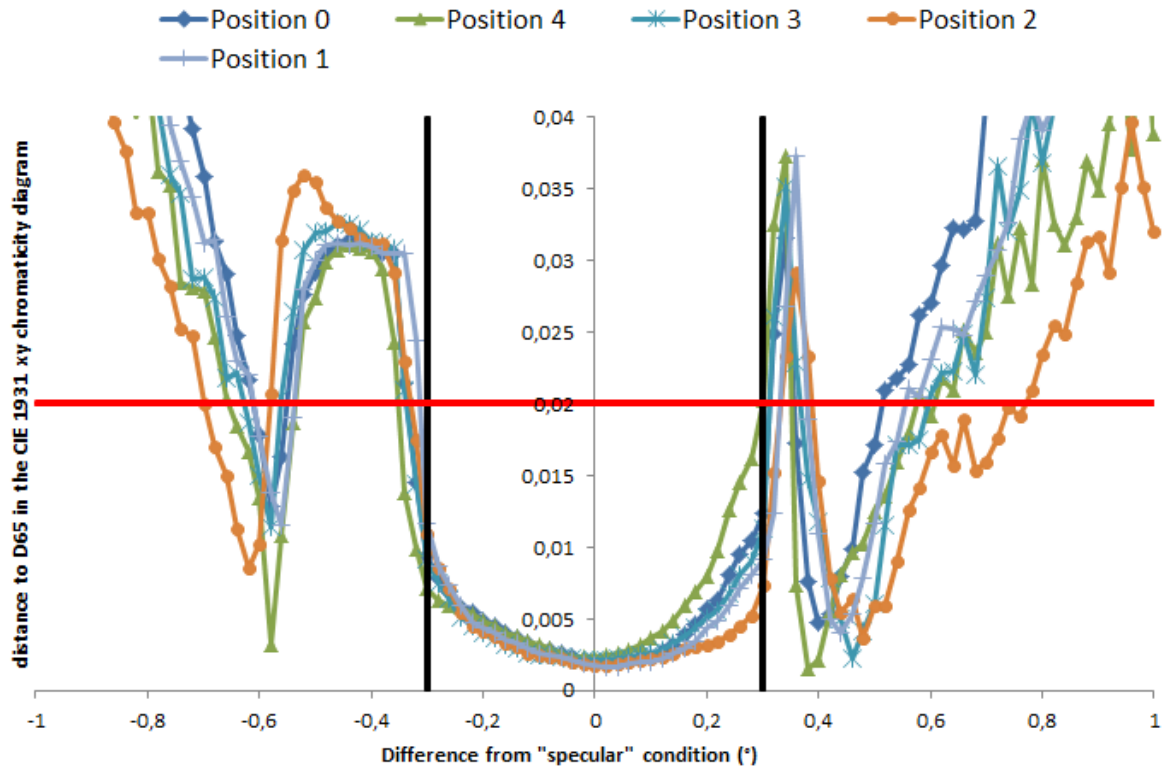
Figure 151: Distance D in the CIE 1931 xy chromaticity diagram between the D65 reference white point and the xy coordinates computed from the normalized "BRDF" measurements for an incidence angle of 90° and detection angles varying from $\pm1°$ around the "specular" condition for the five different positions of the detection lens. The red horizontal line corresponds to a maximum value of 0.02 for D (4.4% variation relatively to the D65 position). The black vertical lines indicates the observation angular range where D is lower than 0.02.

3) Influence of the sample roughness on its color evolution around the specular direction

   a) Comparisons between Optimines and a commercial spectrophotometer for an incidence angle of 45°.

The samples BRDF are converted into CIE 1931 xy-chromaticity coordinates according to equation 2 from Chapter 1. In Figure 152 are presented the CIE xy-chromaticity coordinates of the samples anodized at 10 V for observation angles respectively from 44.5° to 45.5° for the Vibrometer series, 44°-46° for the Alumina series and 30° to 60° for the P300 series. A further increase of the angular range results into scattered points because of too small and noisy values of the BRDF. The red points correspond to the points where the error due to the chromatic aberration is lower than 4.4%, i.e. to observation angles closer than ±0.3° to the specular condition, and the green points correspond to the angular values further than 0.3° from the specular condition. The points further than 0.3° from the specular direction were kept because the light reflected by the sample has a diffuse component, in particular for the Alumina and the P300 series. The direct beam of the source, which is similar to the case of a perfectly specular sample, was used when evaluating the chromatic aberration impact on the color. Nevertheless the impact of the chromatic aberration for diffuse light could be different. Making the measurements presented in the previous section with a diffuser added on the source beam could allow to quantify the influence of chromatic aberration in the case of diffuse light.

The same samples were also measured at the CMIC laboratory with a Konica Minolta CM-2500C spectrophotometer. It is a portable spectrophotometer that offers a 45°a:0° geometry as described previously in section 6a). The spectrophotometer gives CIE $L^*a^*b^*$ coordinates which are converted into CIE 1931 xy-chromaticity coordinates with a D65 reference white point. The spectrophotometer measurements are represented as blue dots in Figure 152.

The Optimines and Konica measurements are made with different geometries. However it is important to note that the Optimines goniospectrophotometer is not performing well when measuring the BRDF of a sample in a 45°:0° geometry because of a too low and noisy signal. A direct comparison of the measurements is then difficult to obtain.

For these 10 V samples, the color hue and saturation are not changing much when only the red points are considered. When the green points are considered, the color stays in the "gold" region with different saturations and small hue variations (*Δhue* equal to 0°, 14° and 6° respectively for the Vibrometer, Alumina and P300 series) It reaches a faded gold (grey color) in case of the Vibrometer sample. In all the cases the color given by the spectrophotometer is close to the specular color (observation angle of 45°) given by the Optimines goniospectrophotometer (red points). The best correspondence is achieved for the Vibrometer sample and a slight shift is observed when the roughness is increased. Note that this result is coherent with the non-gonioapparent behavior observed visually for all the samples anodized at 10V.

The same measurements have been made for the samples anodized at 90 V for observation angles respectively from 44.5° to 45.5° for the Vibrometer series, 44°-46° for the Alumina series and 30° to 60° for the P300 series (see Figure 153, same color code as in Figure 152). For the samples anodized at 90V, the hue changes significantly (*Δhue* equal to 28°, 39° and 48° respectively for the Vibrometer, Alumina and P300 series), resulting in different sample colors depending on the observation angle. In all cases, the color given by the spectrophotometer is far from the specular color given by the goniospectrophotometer and is closer to the out of specular colors. This is coherent with the fact that the spectrophotometer geometry (45°a:0°) is corresponding to a color measurement in the out of specular direction. It is important to notice that the further the observation angle is from the specular direction the closer the Optimines

color is to the one given by spectrophotometer. It is particularly true for the smoothest samples. This might be explained by the gonioapparent behavior of the samples at a cell potential of 90V, as observed visually.
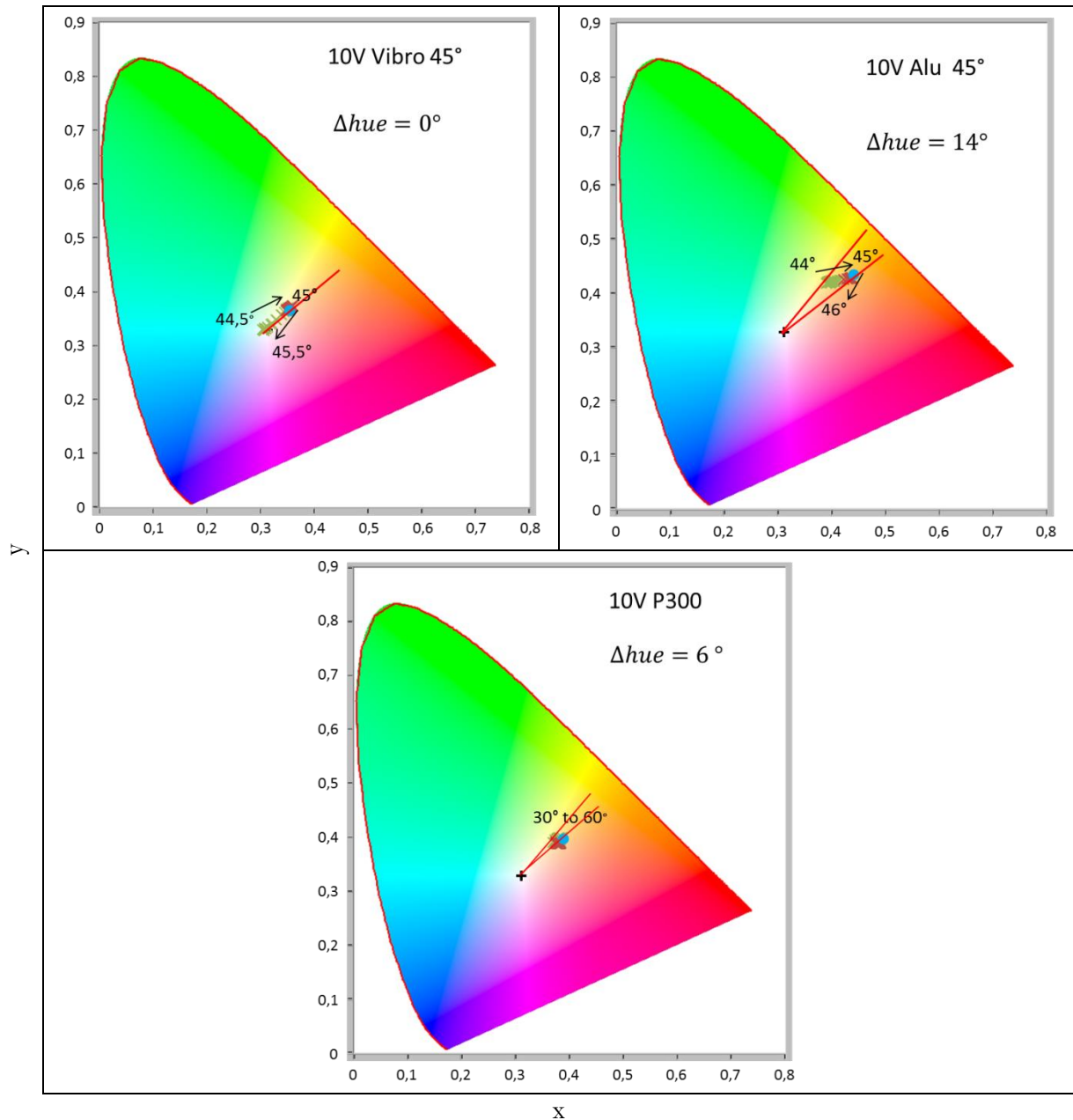
Figure 152: CIE 1931 xy-chromaticity diagrams obtained from BRDF measurements for the three Vibrometer, Alumina and P300 series, for samples anodized at 10V for an incidence angle of 45° and observation angles from 44.5° to 45.5° for the Vibrometer series, 44° to 46° for the Alumina series and 30° to 60° for the P300 series. The blue circle corresponds to the measurement of the same sample with the Konica Minolta CM-2500C spectrophotometer (45°a:0° geometry). The black cross corresponds to the white reference D65. The red points correspond to the points where the error due to the chromatic aberration is lower than 4.4%, i.e. for observation angles closer than ±0.3° to the specular condition, and the green points correspond to the angular values further than ±0.3° from the specular condition. The maximum hue variations of the samples are also indicated.

In the case of the P300 samples, it is important to remind that the points obtained for observation angles over 5° away from the specular direction are difficult to interpret. Indeed, these points could be highly impaired by the chromatic aberration. The behavior of these points might also be explained by a multiple gonioappearance of the sample, i.e. the sample color

presents two highly different color hues. A better assessment of the gonioappearance of the sample is required. Visually, the sample does not seem to exhibit multiple gonioappearance.
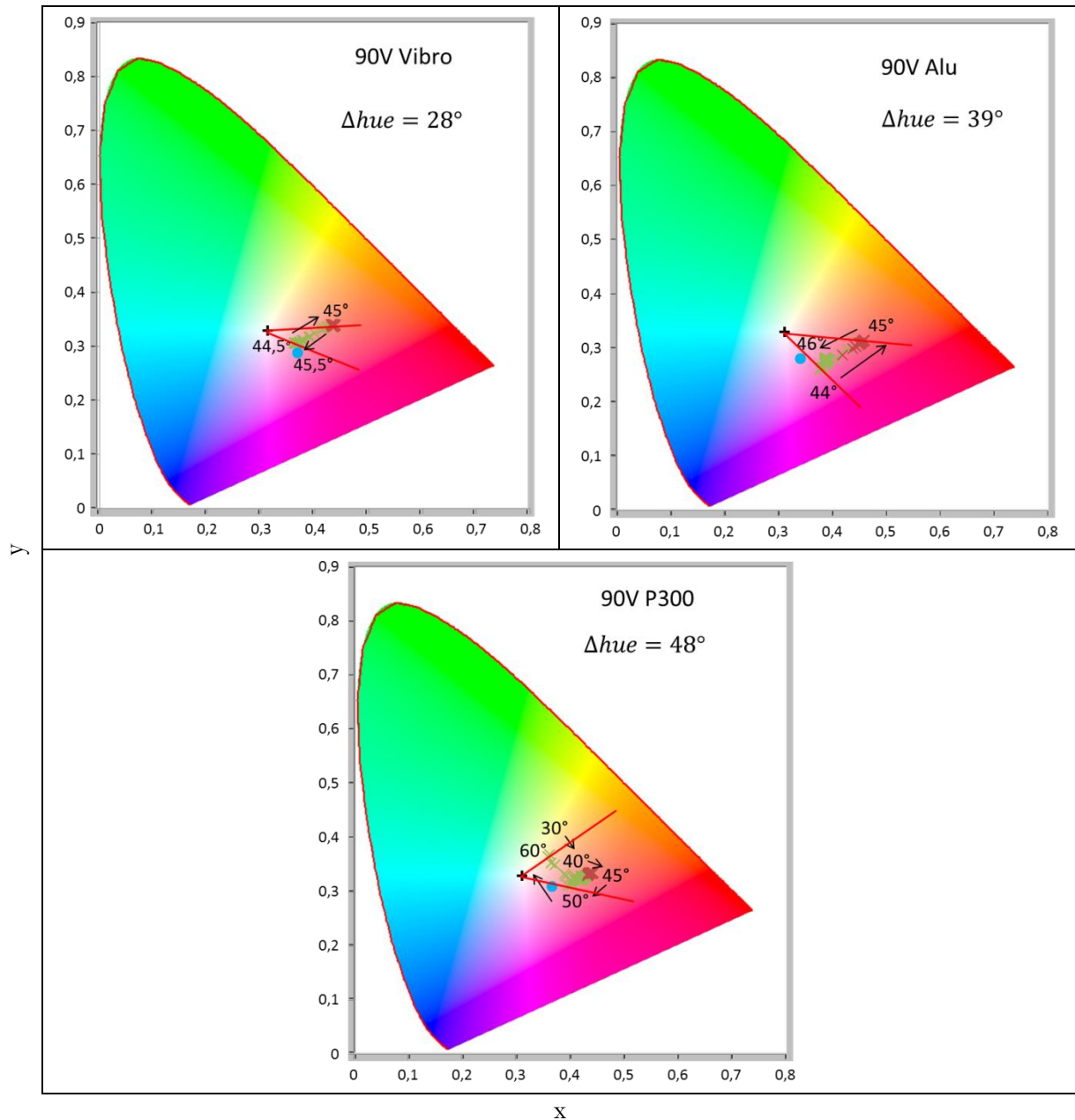
Figure 153: CIE 1931 xy-chromaticity diagrams obtained from BRDF measurements for the three Vibrometer, Alumina and P300 series, for samples anodized at 90V for an incidence angle of 45° and observation angles from 44.5° to 45.5° for the Vibrometer series, 44° to 46° for the Alumina series and 30° to 60° for the P300 series. The blue circle corresponds to the measurement of the same sample with the Konica Minolta CM-2500C spectrophotometer (45°a:0° geometry). The black cross corresponds to the white reference D65. The red points correspond to the points where the error due to the chromatic aberration is lower than 4.4%, i.e. for observation angles closer than ±0.3° to the specular condition, and the green points correspond to the angular values further than ±0.3° from the specular condition. The maximum hue variations of the samples are also indicated.

Figure 154 presents once again the same measurements but for the samples anodized at 20V. For the samples from the P300 and Alumina series anodized at 20V, the hue is changing a lot (*Δhue* equal to 27° and 67° respectively for the Alumina and P300 series) resulting in different sample colors depending on the observation angle. In both cases the color given by the spectrophotometer is far from the specular color given by the goniospectrophotometer and is closer to the out of specular color. The same behavior as for the samples anodized a cell potential

of 90V is thus observed. However in the case of the Vibrometer sample, the sample color hue is almost not changing ($\Delta hue = 9°$), only its saturation is changing when the observation angle is moved away from the specular direction. This sample behaves exactly like the samples anodized at 10V and exhibits a similar color. This observation is coherent with the visual observations of the samples.
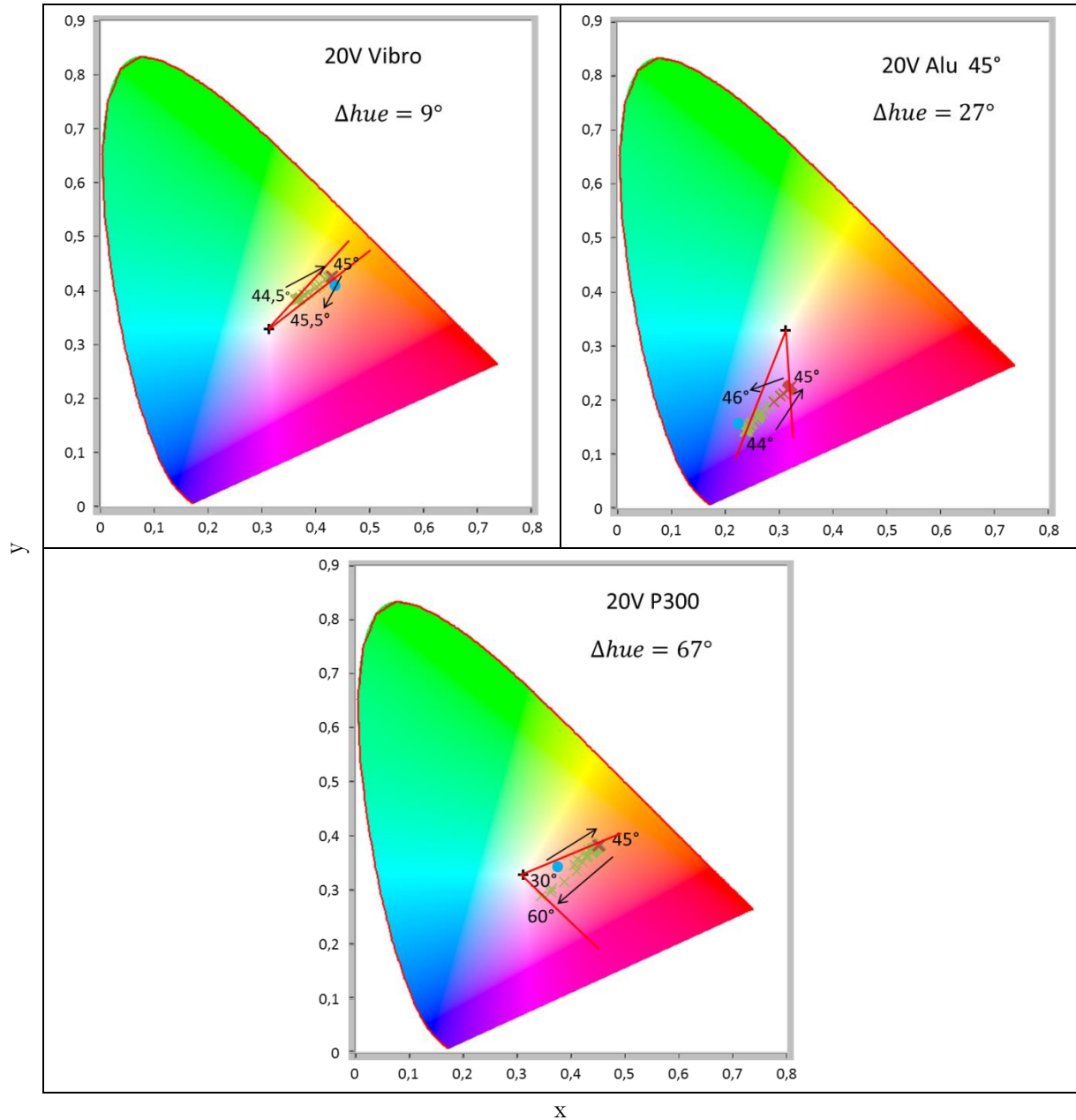
Figure 154: CIE 1931 xy-chromaticity diagrams obtained from BRDF measurements for the three Vibrometer, Alumina and P300 series, for samples anodized at 20V for an incidence angle of 45° and observation angles from 44.5° to 45.5° for the Vibrometer series, 44° to 46° for the Alumina series and 30° to 60° for the P300 series. The blue circle corresponds to the measurement of the same sample with the Konica Minolta CM-2500C spectrophotometer (45°a:0° geometry). The black cross corresponds to the white reference D65. The red points correspond to the points where the error due to the chromatic aberration is lower than 4.4%, i.e. for observation angles closer than ±0.3° to the specular condition, and the green points correspond to the angular values further than ±0.3° from the specular condition. The maximum hue variations of the samples are also indicated.

b) Sample color evolution for different incidence angles

BRDF measurements were also taken for two additional incidence angles, 15° and 75° for the Vibrometer and Alumina series.
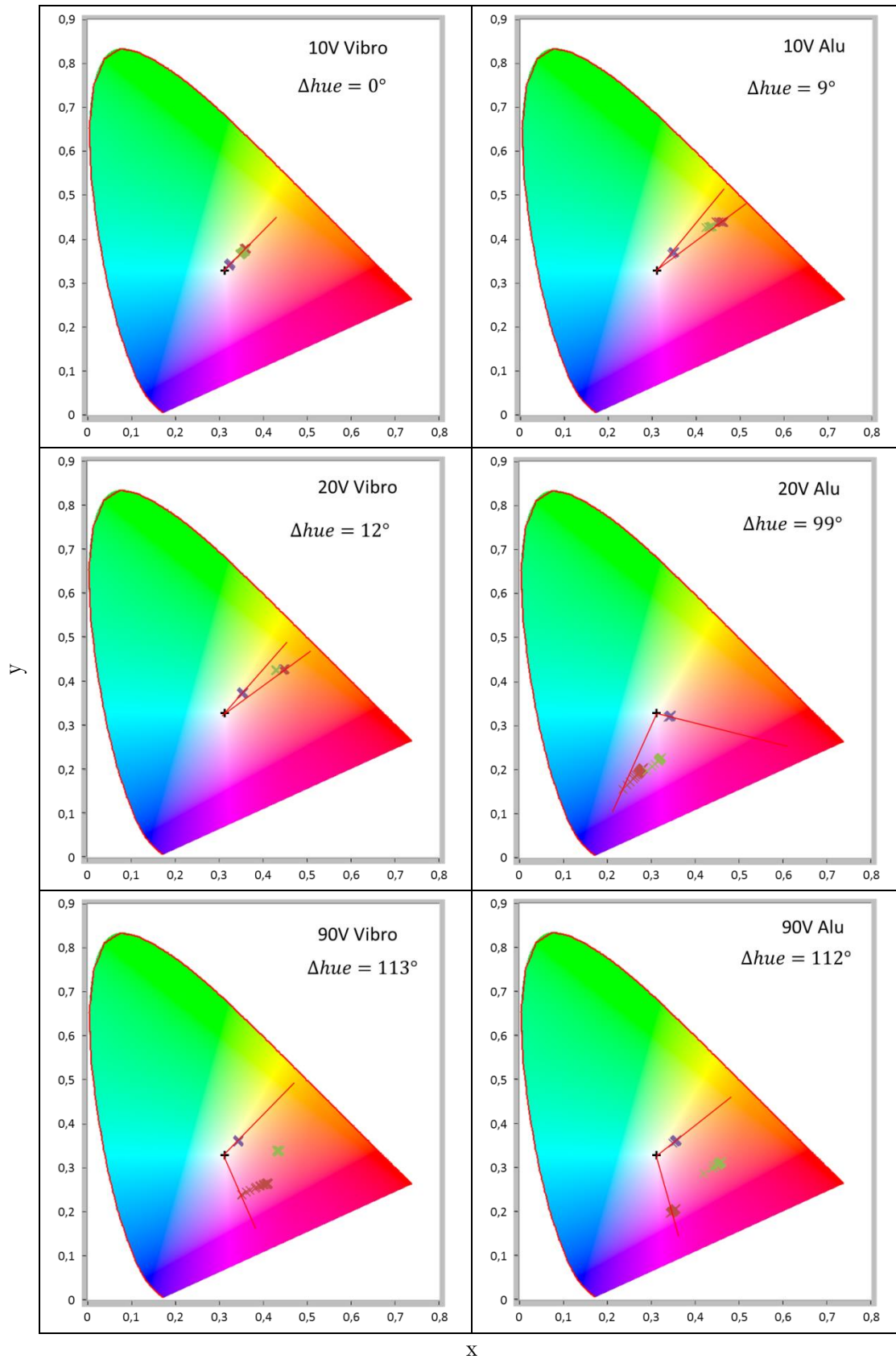
Figure 155: CIE 1931 xy-chromaticity diagrams obtained from BRDF measurements for the samples from the Vibrometer and Alumina series for the three cell potentials (10 V, 20 V and 90 V) for incidence angles of 15° (red), 45° (green) and 75° (purple). The observation angle values are ranging from the specular direction to values up to ± 0.3° around the specular direction. The black cross corresponds to the white reference D65. The maximum hue variations of the samples are also indicated.

In Figure 155 are presented the CIE xy chromaticity diagrams obtained from BRDF measurements for the samples from the Vibrometer and Alumina series for the three cell potentials (10 V,20 V and 90 V) for incidence angles of 15° (red), 45° (green) and 75° (purple). We made the assumption that the chromatic aberration was similar for all the incidence angles. This is why we chose observation angles values ranging from the specular conditions to values up to ± 0.3° around the specular conditions in order to have an influence of the chromatic aberration on the color lower than 4,4%, as explained in the previous section.

The colors exhibited by the samples at all potentials are close to the white reference D65 when the incidence angle is 75°, implying that the colors exhibit a very low saturation at grazing angles. It is also important to note that the non gonioapparent behavior of the samples anodized at 10V and of the Vibrometer sample anodized at 20V is confirmed as showed by a very low hue color change (*Δhue* equal to 0° for the 10 V Vibrometer sample, 9° for the 10 V Alumina sample and 12° for the 20 V Vibrometer sample) when the incidence angle is changed. Also the gonioapparent behavior of the samples anodized at 90V (*Δhue* equal to 113° and 112° respectively for the Vibrometer and Alumina series) and of the Alumina sample anodized at 20V (*Δhue* = 99°) is confirmed as shown by a high change of hue when the incidence angle is changed.

VII.   Additional samples series: study of the influence of the substrate roughness on oxide growth and on anodized titanium color gamut.

As pointed out in section IV of the present chapter, the highest oxide thicknesses were observed for the Alumina series, ie: samples with an intermediate substrate roughness. In order to confirm this influence of substrate roughness on oxide thickness, additional samples with an intermediate roughness level (R_a about 100 nm – 150 nm before anodizing) are needed. This observation also needs to be confirmed for a higher number of oxide thicknesses. For these reasons four new sample series have been prepared, with four different roughness levels. The samples were anodized at cell potentials from 5 V to 120 V with a 5 V step. Note that these series also allowed to have a better assessment of the influence of the anodizing process on the roughness after anodizing. They also allowed to measure the influence of the substrate roughness on the color gamut of anodized titanium.

1) Sample preparation

Experiments were carried out on the same material with the same protocol as described in section III 1) of the present chapter. They were cut from a different base plate from the same provider. Four different series of samples were prepared in order to obtain 4 different levels of surface roughness:

- a simple polishing with a SiC P300 grinding paper was used to obtain a rough surface on the first batch; this series will be called "P300";
- a series with an intermediate surface roughness has been added. It was obtained through a complete mechanical polishing with SiC P300, SiC P600, SiC P1200 and SiC P2400 grinding papers and a final step using a grinding cloth with a 6μm diamond paste solution. This series will be called "6 μm";
- two series with mirror finishing have been made thereafter; the first mirror finishing series has been obtained by a complete mechanical polishing (including diamond paste solution from 6μm to 1 μm) and a final step using a grinding cloth and an alumina

solution with particle size of 0.6 μm; these samples will be referred as "Alumina or Alum";

- to further decrease the surface roughness, a vibratory polisher, Buehler Vibromet2, and a 60 nm colloidal solution were used to obtain the last series designated further as "Vibrometer or Vibro";

For each series, 32 samples were prepared and 24 samples were then selected on the basis of their roughness level as described later in this section.

The samples were bound to sample holder with cyanoacrylate glue and each batch was composed of at least 14 samples. This process is well fitted to prepare a large batch of samples, but at the expense of a lower overall finishing quality. For this reason, the roughness level of the "new" Vibrometer series is not comparable to the roughness level of the Vibrometer series presented in section II.

2) Roughness measurements and samples selection

a) Roughness measurements protocol

The roughness measurements have been again carried out with Bruker Nanoscope Wyko® NT9100 optical profilometer, before anodizing, to obtain the roughness of the titanium substrate. The measurements have been made after anodizing on the selected sample in order to obtain the roughness of the oxide layer. As explained in section II, five measurements have been made around the center of the sample to obtain a robust assessment of the roughness of this area for each sample. To monitor the homogeneity of the surface, at least four more measurements were performed on each sample near the corners.

b) Samples selection

For each sample, all the five R_a roughness parameter measurements around the center were used to calculate an average roughness value. The standard global deviation of these average R_a values over all the 32 samples of each series was then calculated. Once the measurements were performed, 24 samples were chosen among each series, in order to perform anodizing at cell potentials from 5 V to 120 V with a potential step of 5V. This selection was done by accepting all the samples that had an average roughness R_a value at a maximum distance from the global average R_a over the 32 samples lower or equal to 1.25 times the global standard deviation. When it was possible to select more than 24 samples, the overall aspect of the sample was taken into account, i.e. the presence of defects/scratches due to manipulations. But generally the samples with the closest R_a value to the global average value over the series were selected. The standard deviation calculated on the five measurements around the center, called "intra-sample" standard deviation, is calculated for each selected sample. The maximum "intra-sample" standard deviation over the selected samples of each series which corresponds to the maximum roughness variations that can be found inside a sample among the selected samples of a series is also computed.

For each series the global average of the R_a values and the global standard deviation of the average R_a values over the 32 samples of each series, as well as the maximum "intra-sample" standard deviation over the selected samples are reported in Table 41. It can be noticed that the maximum "intra-sample" standard deviation over the selected samples is generally higher than the global standard deviation.

	Global average R_a value over the 32 samples of each series (nm)	Standard deviation over the 32 samples of the average R_a values (nm)	Maximum "intra-sample" standard deviation over the selected samples (nm)
P300 series	253	13.4	19
6μm series	160.5	4.5	14
Alumina series	62.8	6.3	5
Vibrometer series	29	3.9	6

Table 41: Global average of the R_a value over the 32 samples of each series, Standard deviation over the 32 samples of the average R_a values (over the 5 R_a measurements taken around the center of each sample) and Ω values for the Vibrometer, Alumina, 6 μm and P300 series.

c) <u>Roughness measurements after anodizing on the selected samples</u>

The selected samples have been anodized by following the protocol presented in chapter 3 section I at 24 different cell potentials ranging from 5 V to 120 V with a 5 V step. The 6μm series does not contain samples anodized at 95 V and 115 V because of an unexpected power supply failure when anodizing these samples.

The roughness of the samples was measured after anodizing by following the protocol described previously. The gain in nm corresponding to the difference of the average R_a roughness after anodizing with the average R_a roughness before anodizing (substrate roughness) is presented in Figure 156. R_a measurements were not made at the exact same position before and after anodizing and it may introduce a measurement uncertainty σ_g on the gain value. In order to estimate this uncertainty for each sample, the following equation has been used:

$$\sigma_g = \sqrt{\sigma_{Layer}{}^2 + \sigma_{Substrate}{}^2}$$

(88)

where σ_{Layer} is the standard deviation over the 5 R_a measurements taken in the center of each sample after anodizing and $\sigma_{substrate}$ is the standard deviation over the 5 R_a measurements taken in the center of each sample before anodizing. In Figure 156 are represented error bars corresponding to $\pm\sigma_g$.

For all the series, the roughness R_a parameter almost remains the same until the potential reaches 85-90V. At cell potentials higher than 90 V the roughness is highly increased after anodizing. It is coherent with the fact that at cell potentials higher than about 70 V an anatase phase starts to grow inside the amorphous oxide layer. The anatase phase crystallites could then act as local defects on the roughness profile of the surface, locally increasing the roughness. When the potential is further increased, the anatase phase proportion increases and the roughness increases accordingly because of a larger size of the anatase crystallites inside the amorphous oxide layer. However the roughness R_a parameter drops when the potential reaches 110V. It might be explained by the fact that the anatase crystallites tend to populate the surface and are no longer isolated surface singularities that increase the surface roughness.

It can be also noticed that at a cell potential of 20V, the roughness is modified, a decrease is observed for the P300 series and an increase is observed for all other series. We have no explanation for this phenomenon.
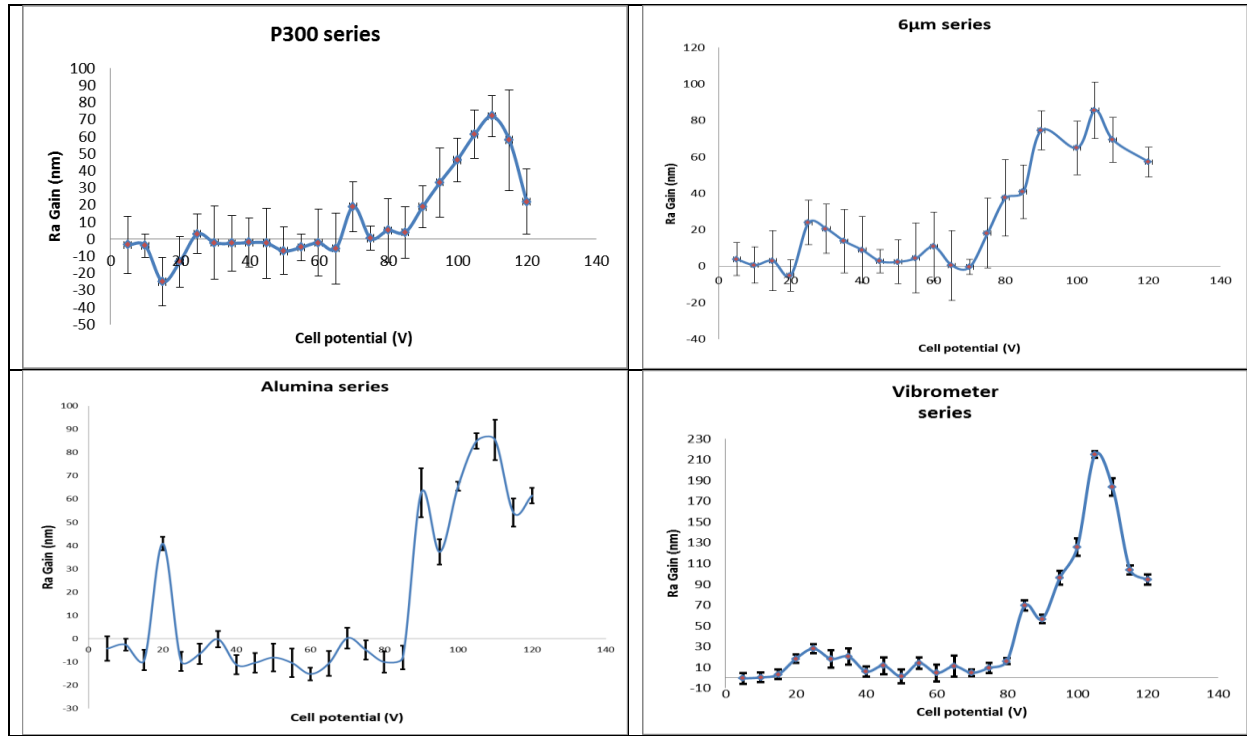
Figure 156: R_a gain as a function of the anodizing cell potential for the four series. The error bars correspond to $\pm\sigma_g$.

3) <u>Oxide layer thickness estimations from reflectance spectrum extrema</u>

All the samples reflectance spectra were measured with the Konica Minolta CM-2500C spectrophotometer (45°a:0° geometry). The oxide layer thickness of the samples anodized at 10 V, 20 V, 50 V, 90 V and 120 V was estimated by using the same method as presented in Chapter III. Note that this method is adapted to reflectance measurements performed in specular conditions. Nevertheless, as presented in section V only a slight shift between the extrema in the 45°:45°specular condition and the extrema in the 45°a:0° geometry is observed. Thus estimating oxide thickness values from a 45°a:0° geometry reflectance spectra gives a good assessment.

The refractive indexes used for the titanium substrate and the oxide layer come from the ellipsometric measurements presented in the Chapter 3. The spectrophotometer gives reflectance spectra with a 10 nm wavelength step. In order to obtain a better assessment of the extrema position, the reflectance spectra were interpolated with a 0.1 nm step. However, in some cases the extrema position is difficult to evaluate as shown on Figure 157. On this example, the reflectance spectrum exhibits around 500 nm a doublet instead of a single peak. The estimation at this specific position was not taken into account in order to lower the error. Besides these particular cases, the oxide thickness is obtained as an average of the thicknesses estimated from the different extrema of the samples reflectance spectra (see Appendix M). Figure 158 presents these oxide layer thickness estimations versus the cell potential.

120V 6µm
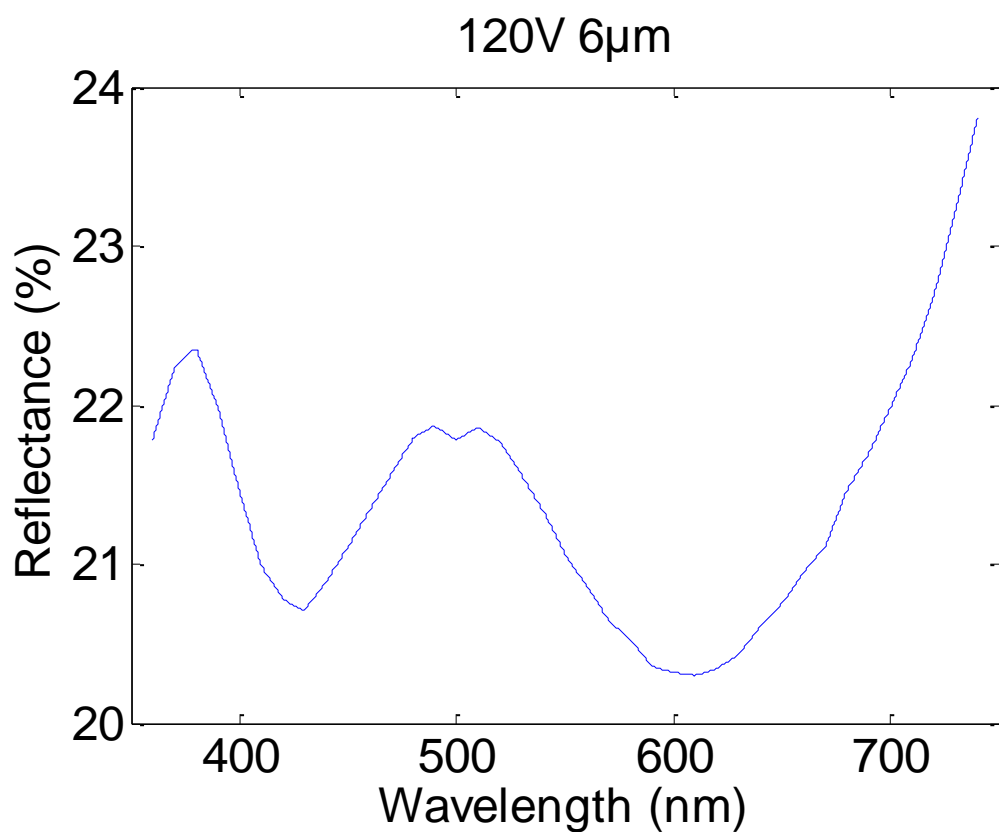
Figure 157: Reflectance spectrum obtained with the commercial Konica Minolta CM-2500C spectrophotometer (45°a:0° geometry) of the titanium sample from the 6µm series anodized at a cell potential of 120V.

	P300	6µm	Alu	Vibro
10V	24,8	24,8	29,8	26,4
20V	41	39,4	51,1	61,3
50V	86,8	111,2	86,8	91,3
90V	162,6	165,9	171,6	169,4
120V	210,7	220,1	211,8	217,3
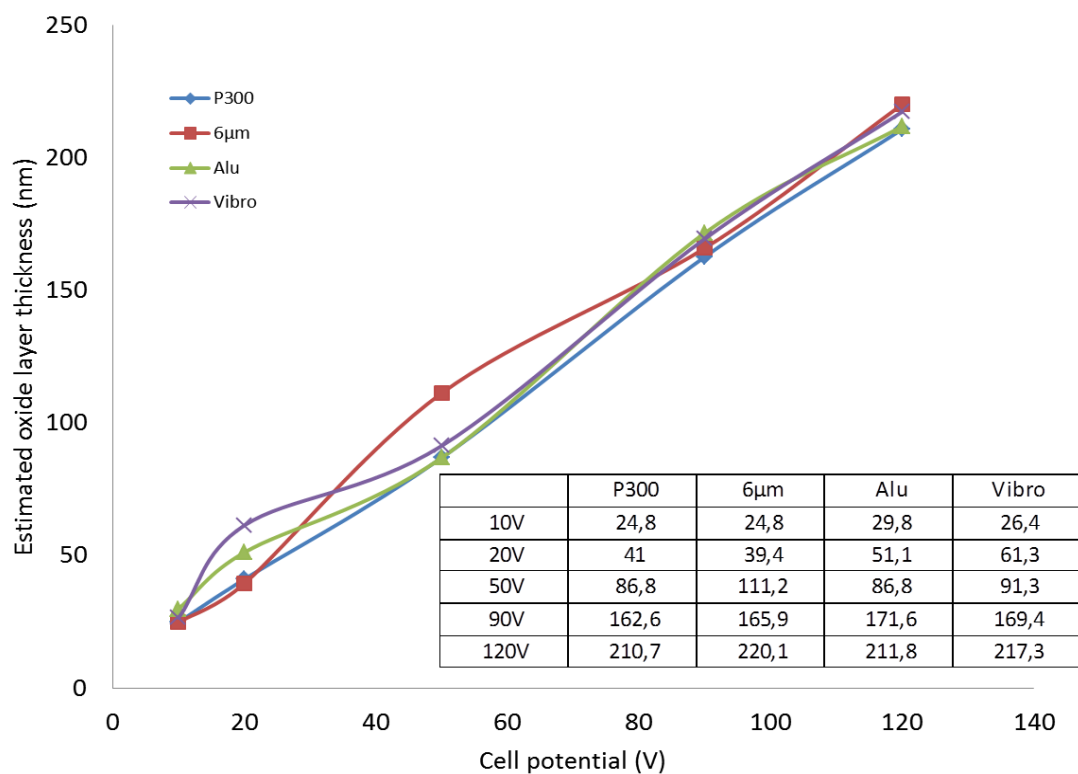
Figure 158: Oxide layer thickness versus the cell potential for the P300, 6 µm, Alumina and Vibrometer series for 5 different cell potentials: 10V, 20V, 50V, 90V and 120V. The oxide thickness is here estimated from the reflectance spectra extrema positions measured with the Konica Minolta CM 2500C spectrophotometer (45°a:0° geometry). In the table are reported the oxide layer values in nm.

It is important to remind that the sample preparation is not exactly the same between these samples and the ones presented in the section II of this chapter. The samples from both Vibrometer series do not have the same substrate R_a and it is thus difficult to compare both results. However it is possible to conclude that a rough substrate, as shown by the P300 series, leads to the formation of a thinner oxide layer for all the potentials. At potentials up to 20V, the anodizing of a smooth substrate results into a sample with a thicker oxide layer than for a rougher substrate, as shown by the Alumina and Vibrometer series which have the thickest oxide layers. At cell potentials above 50V all the thickness values are close to each other, except for the sample obtained of the 6μm series at cell potential of 50V.

This study shows that, despite a few isolated samples for which either the surface preparation or the anodization yield anomalous values of the oxide thickness, the general trend is that the initial substrate roughness has no influence on the oxide thickness.

4) <u>Influence of substrate roughness on the color gamut of anodized titanium</u>

The reflectance spectra measured with the Konica Minolta CM-2500C spectrophotometer (45°a:0° geometry) were converted into CIE 1931 xyY colorimetric coordinates and are presented in Figure 159 for the Vibrometer, Alumina, 6μm and P300 series for cell potential ranging from 5 V to 120 V with a 5V step. We remind that the 6μm series doesn't contain samples anodized at 95 V and 115 V. The x, y, Y and corresponding cell potential values are reported in the Appendix N.

As a general observation, it is possible to notice that no saturated green color was obtained for any mechanically prepared sample series. Also, the color gamuts obtained for all the series are quite similar. On one hand, the P300, Alumina and Vibrometer series generally offer samples with a relatively high color saturation, represented by a repartition of the samples chromaticity coordinates far from the D65 points. On the other hand, the 6μm series offer samples with a narrower range of color saturations, represented by a cluster of samples exhibiting chromaticity coordinates close to the D65 point. Also, for the Vibrometer series, some pinks hues are missing, represented as a "hole" between the chromaticity coordinates in the purple region and the chromaticity coordinates in the orange region. Additional cell potentials with a smaller step (1 V for example) could allow the filling of these "holes".
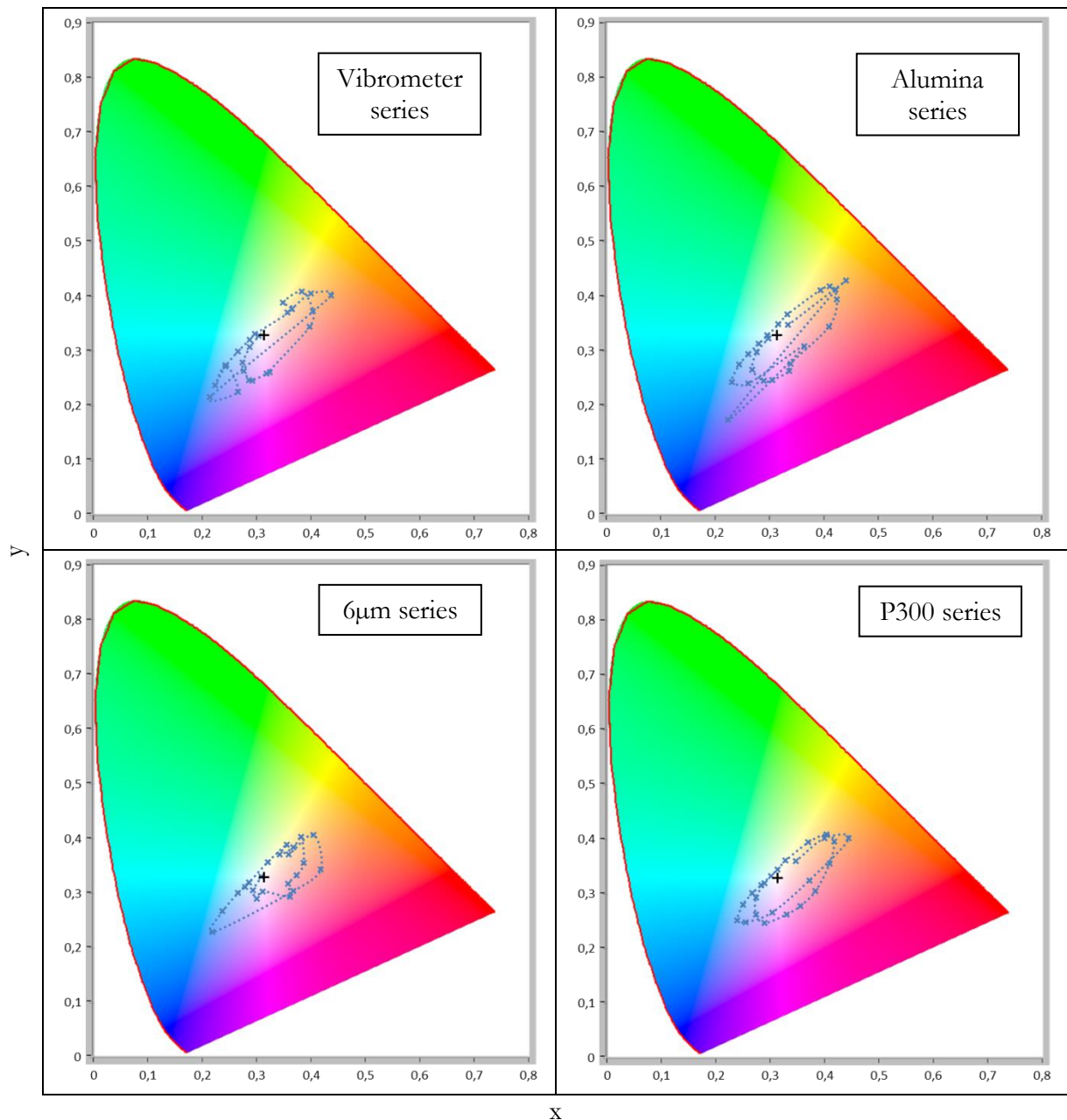
Figure 159: CIE 1931 xy-chromaticity diagrams obtained from Konica Minolta CM-2500C spectrophotometer reflectance spectra (45°a:0° geometry) for the samples from the Vibrometer, Alumina, 6μm and P300 series for cell potential ranging from 5 V to 120 V with a 5V step. The black cross corresponds to the white reference D65.

The sample reflectance spectra were also converted into CIELAB color coordinates as the CIELAB color space is a color space were the lightness, color hue and saturation are well defined. The L^*, a^* and b^* and corresponding cell potential values are also reported in the Appendix N. From the a*b* coordinates it is possible to represent the color gamut exhibited by the samples of the different series as presented in Figure 160. The same observations as on the xy-chromaticity diagrams can be made: lack of saturation in the green region, smaller color saturation for the 6μm samples and lack of certain pink hues for the Vibrometer series.
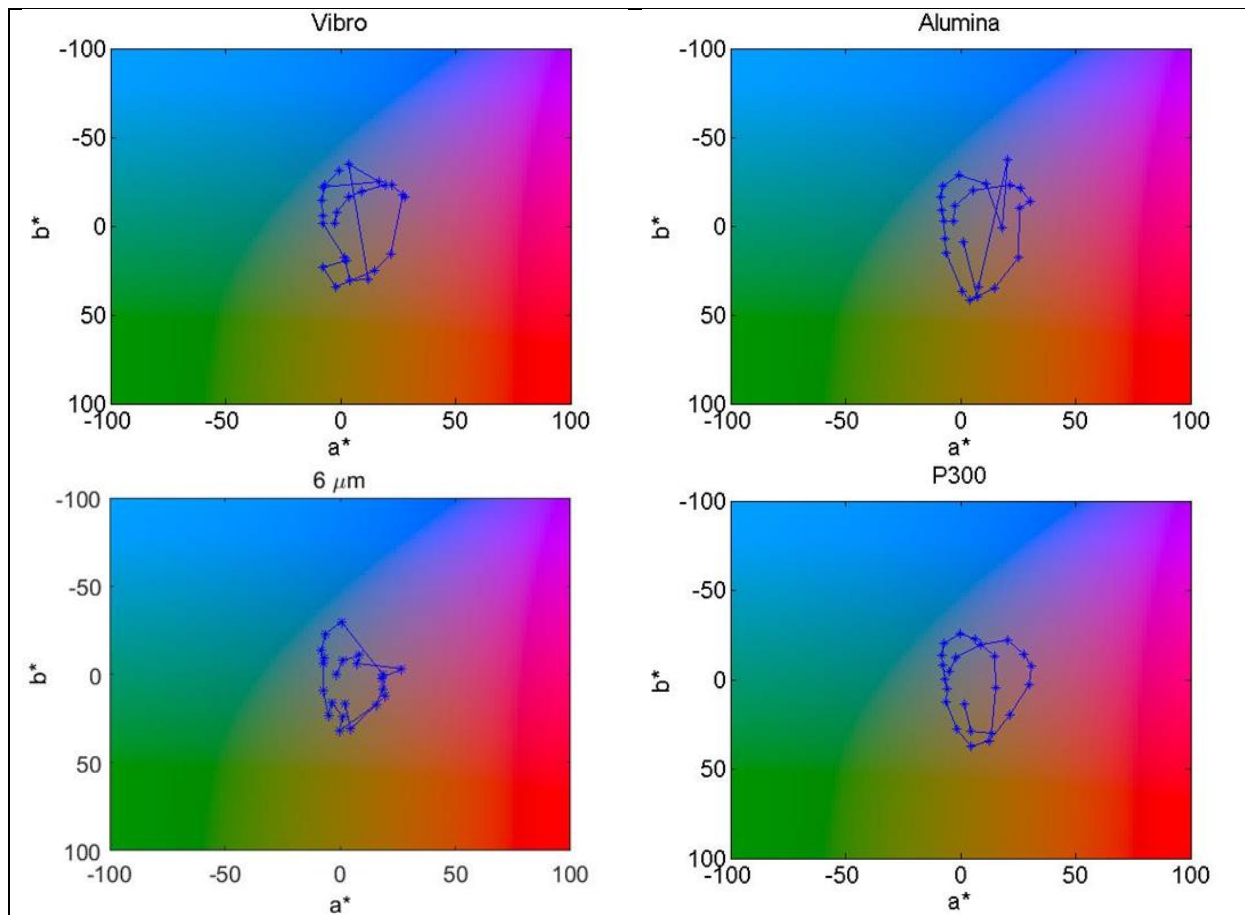
Figure 160: Color gamut obtained through titanium anodizing for the four series with different substrate surface roughness respectively Vibrometer, Alumina, 6µm and P300 series.

The lightness range of all the series (L^* is in the 30 to 80 range) is presented on Figure 161. The brightness range is similar for all the series even if the one of the Alumina series is slightly larger. Colored titanium samples obtained through anodizing cannot be totally white ($L^* = 100$) or black ($L^* = 0$). The brightness all the series are in the 30 to 80 range. For the development of a reference color chart using anodized titanium samples, the lack of white and black samples will require the addition of samples colored with another process to have a complete color chart.
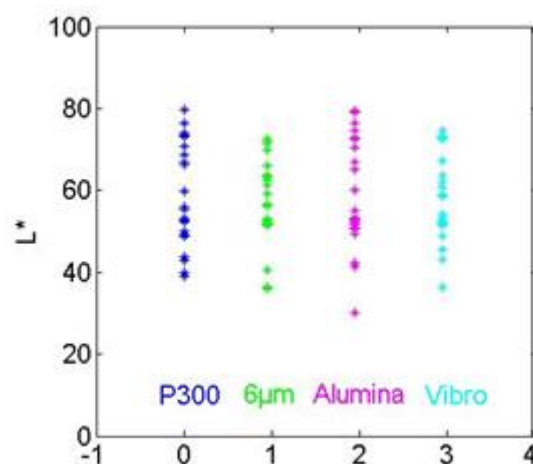
Figure 161: Samples color lightness range for the four different samples series.

174

VIII.   Conclusion

In this chapter, the influence of the substrate roughness on the diffuse/specular aspect, oxide thickness and colors of anodized titanium samples were studied. The substrate roughness was controlled by different steps of mechanical/chemical polishing.

A fitting method of the angular variations of the samples BRDF, allowing to extract the diffuse and specular contributions to the BRDF has been developed. A parameter called $C_{diffuse}$ was computed in order to estimate the diffuse aspect of the samples. This diffuse aspect has been estimated for three different incidence angles (15°, 45° and 78°) and an influence of the incidence angle on $C_{diffuse}$ has been shown. After having shown in chapter 3 that the gonioappearence of structurally colored metallic samples could be successfully characterized around the specular direction using conventional models for error correction, these results shows that the diffuse color on the one hand, as measured by standard spectrometers, and the specular one on the other, as characterized by dedicated instruments such as the modified Optimines goniospectrophotometer, can be successfully separated, measured and modelled in order to design and specify dedicated standard reference samples with specific diffuse/specular color rendering properties.

Ellipsometric measurements were conducted in order to measure both refractive indexes of titanium and titanium dioxide as well as to estimate the oxide layer thickness. These parameters measured by ellipsometry have been put into an Abeles matrices-based model in order to simulate the specular spectral reflectance of the samples. The modeled spectra were compared to experimental reflectance spectra obtained from spectral BRDF measurements. The global shape of the spectra as well as the positions of the extrema are in quite good agreement between the modeled and the experimental spectra. This has been observed for three different incidence angles, including one close to grazing (75°). From the results of Chapter 3, this accurate estimation of the extrema positions of the reflectance spectra allows for a reliable prediction of color, even at angles that are not usually accessible to standard spectrophotometric instruments.

The extrema of the experimental reflectance spectra were also used to estimate the oxide layer thickness with the method developed in the chapter III section 3) by using the Ti and TiO_2 refractive indexes measured by ellipsometry. Good agreement was found between the thickness estimated by ellipsometry and the one estimated from the extrema. In order to have a non-optical measurement of the oxide thickness, X-Ray reflectometry (XRR) has been performed on two samples from the smoothest Vibrometer series. Despite the fact that the orders of magnitude are the same, the XRR measured thicknesses are lower than the thicknesses obtained with the two other techniques. This discrepancy has to be investigated further. For example, a non-optical measurement of the Ti and TiO_2 refractive indexes could also be performed through Reflection Electron Energy Loss Spectroscopy (REELS). Note that ellipsometry and XRR can only be performed on the smoothest samples.

Using the extrema of the reflectance spectra of the roughest P300 samples, their oxide layer thickness has been estimated. The samples anodized at the same cell potential but with different substrate surface finishing exhibit different oxide layer thicknesses. For this reason, additional samples have been prepared, with four different levels of roughness and additional anodizing potentials. For the mechanically prepared samples investigated in this study, no global influence of the substrate roughness on the oxide thickness was observed with the implemented galvanostatic anodization method. However, these additional samples allowed to show a sharp increase of the roughness after anodizing for cell potentials higher than 85-90 V, which corresponds to the cell potentials where the ellipsometric measurements indicated a decrease of

the oxide refractive index, attributed to porosity. It also corresponds to the cell potentials at which an anatase crystalline phase appears in the oxide layer.

By comparing the reflectance of anodized titanium samples in the specular 45°:45° geometry and their diffuse reflectance in the 45°a:0° geometry, the specular and the diffuse reflectance were proved to exhibit interferences which are in phase. Optical models have been developed in the literature and showed that multilayer materials with roughness correlated interfaces should exhibit diffuse reflectance spectra with an interface pattern in phase with the specular interference pattern, whereas materials with roughness uncorrelated across interfaces should exhibit diffuse and specular reflectance spectra which are out of phase. This observation has to be confirmed, but it is a first indication that titanium anodization in the range of conditions of this study leads to correlated Ti/TiO_2 and TiO_2/Air interfaces, regardless of the initial roughness.

The colors of the anodized titanium samples have been measured, both with the Optimines goniospectrophotometer and with a commercial Konica Minolta CM-2500C spectrophotometer (45°a:0° geometry). Both devices could not be compared in the exact same geometry because of a too low signal to noise ratio of the Optimines goniometer in the 45°:0° geometry. Nevertheless, the xy-chromaticity coordinates obtained with both devices have been proved to be in a good agreement considering the different measurement geometries. In particular, depending on the gonioapparent aspect of the samples, the xy-chromaticity coordinates given by the commercial spectrophotometer are close to the xy-chromaticity coordinates given by Optimines either in the specular 45°:45° geometry or in an "out of specular" geometry $45°:45° \pm x$, where x corresponds to the maximum distance from the specular direction where the signal to noise ratio of the Optimines goniospectrophotometer is acceptable. x is about 0.5° for the smoothest samples and 15° for the roughest samples.

The gonioapparent character of the samples has been characterized with the Optimines goniospectrophotometer by measuring the xy-chromaticity coordinates of the samples around the specular direction, for three incidence angles (15°, 45° and 75°). For one given cell potential, a sample can exhibit different colors and be gonioapparent or not, depending on the substrate roughness. This may be either due to differences in the oxide thickness as a function of the initial roughness or to different partitions of the total reflectance between the specular and the diffuse components with roughness.

The additional samples with four different level of roughness were measured with Konica Minolta CM-2500C spectrophotometer (45°a:0° geometry) in order to characterize the color gamut of anodizing titanium. The color gamut was shown pretty similar for all the samples series. However no sample with a green saturated color was observed. Saturated green color effects are usually obtained at cell potentials around 100V for chemically-etched specimens and above 120V [5], i.e.: outside the range of the present study. The lightness range was found to be in the 30-80 range for all the four series, possibly too far from perfect white and perfect black to compose a reference color chart using only anodized samples.

A clear influence of the Optimines optical system chromatic aberration on color measurements has been highlighted. This influence has been characterized with a collimated beam incident on the detection system, which mimics the case of a perfectly specular sample, but still remains to be done for a diffuse incident light. The present study lays the basis of an experimental procedure to efficiently correct these chromatic aberration effects in future studies.

Conclusions and Perspectives

This work is an analysis of the structural color effects and optical properties of oxidized titanium obtained by anodizing. It focuses mainly on the influence of the surface preparation of the titanium substrate and different material parameters such as the sample color, the oxide layer thickness and the oxide and substrate refractive indexes are characterized. This document is a first step towards the development of a standard calibration color chart for gonioapparent colored metals and more generally for gonioapparent materials.

A literature review showed that the anodizing process is the most promising oxidation technique in order to obtain a series of samples exhibiting a wide range of colors, with a good color reproducibility. The anodizing parameters, such as current density, electrolytic solution type and concentration, cell potential, influence the characteristics of the oxide layer of anodized titanium samples such as its crystallinity and its thickness. Preliminary investigations revealed that the substrate roughness influences the color of the samples after anodizing and could also affect their gonioappearence.
In order to confirm these observations, anodized titanium samples were prepared with different controlled levels of roughness, either by an HF/HNO_3 etching of the substrate or by using different stages of mechanical or chemical polishing. These samples series which exhibit different roughness levels could be used to obtain a calibration color chart able to calibrate samples with different levels of gloss.

A first sample batch was realized where the sample roughness was modified by HF/HNO3 etching of the substrate. A comparison between etched samples and non-etched samples was made. The optical properties of these samples were then characterized with the Optimines goniospectrophotometer.
By using the BRDF spectral variations, the oxide layer thickness of the anodized samples is estimated with two different approaches: Abeles matrices-based fits of the sample reflectance or by using the positions of the reflectance extrema. It has been demonstrated that when using the reflectance extrema, it is necessary to take into account the electric field phase shift induced by the reflection of the light on the absorbent titanium substrate. This phase shift is linked to the argument of the Fresnel reflection coefficient of the Ti/TiO_2 interface. The error on the oxide thickness estimation made when neglecting this phase shift can reach 500%.
Higher cell potentials lead to a larger oxide layer thickness, which is expected and coherent with literature data. Samples etched before anodizing were also found to have a larger oxide layer thickness than the non-etched samples for the same cell potential.
The study of the BRDF angular variations revealed that the BRDF of etched samples can be decomposed into two contributions, a specular one and a diffuse one. These contributions have been evaluated by fitting specific functions to the diffuse and specular parts of the BRDF. The specular part is obtained by substracting a baseline representing the diffuse part.
This diffuse aspect of the etched samples has been also reported when monitoring the sample color evolution around the specular direction. Hue variations can be observed between the hue exhibited by the sample close to the specular direction or and the one out of the specular direction, especially for samples obtained with a high cell potential. The predicted gonioapparent color effects are in agreement with visual observations. Such an instrumental characterization is difficult to carry out with conventional spectrophotometers.

To separate possible physico-chemical effects of chemical etching from the sole effect of the initial roughness, samples with different levels of roughness obtained by successive stages mechanical and chemical polishing were then prepared.

A fitting method of the angular variations of the samples BRDF, allowing to extract the diffuse and specular contributions to the BRDF has been developed. An influence of the incidence angle on the diffuse aspect of the samples has been shown by repeating the measurements for three different incidence angles (15°, 45° and 75°).

The refractive indexes of the substrate and the oxide layer as well as the oxide layer thickness were measured by ellipsometry on the two smoothest series. An Abeles matrices-based model using these parameters measured by ellipsometry was used to simulate the specular spectral reflectance of the samples. The modeled spectra were compared to experimental reflectance spectra obtained from spectral BRDF measurements. The global shape of the spectra as well as the positions of the extrema were in quite good agreement between the modeled and the experimental spectra for the three different incidence angles.

The extrema of the experimental reflectance spectra were also used to estimate the oxide layer thickness by using the Ti and TiO_2 refractive indexes measured by ellipsometry. Good agreement was found between the thickness estimated by ellipsometry and the one estimated from the extrema. In order to have a non-optical measurement of the oxide thickness, X-Ray reflectometry (XRR) has been performed on samples from the smoothest series. Despite the fact that the orders of magnitude are the same, the thicknesses measured by XRR were lower than the thickness obtained with the two other techniques. The origin of this discrepancy remains to be investigated.

The oxide layer thickness of the roughest samples has been estimated by using the extrema of the reflectance spectra. The samples anodized at the same cell potential but with different substrate surface finishing was shown to exhibit different oxide layer thicknesses. For this reason, additional samples have been prepared, with four different levels of roughness and additional anodizing potentials. Nevertheless it wasn't possible to demonstrate a global influence of the substrate roughness on the oxide thickness. However these additional samples allowed to show a clear increase of the roughness after anodizing for cell potential higher than about 90 V, which corresponds to the cell potentials where the ellipsometric measurements indicated a decrease of the oxide refractive index, attributed to porosity. It also corresponds to the cell potentials where an anatase crystalline phase starts to appear in the oxide layer.

By comparing the reflectance of anodized titanium samples in the specular 45°:45° geometry and their diffuse reflectance in the 45°a:0° geometry, the specular and the diffuse reflectance were proved to exhibit interferences which are in phase. Optical models developed in the literature showed that multilayer materials with correlated rough interfaces should exhibit in-phase diffuse and specular reflectance spectra. This is a first indication that titanium anodizing leads to correlated Ti/TiO_2 and TiO_2/Air rough interfaces.

The colors of the anodized titanium samples were measured, both with the Optimines goniospectrophotometer and with a commercial Konica Minolta CM-2500C spectrophotometer in different geometries (respectively 45°:45° and 45°a:0°). The xy-chromaticity coordinates obtained with both devices were in good agreement, considering the different geometries.

Using the additional samples with the four different levels of roughness, the color gamut of anodized titanium was measured. This color gamut range was shown pretty similar for all the samples series. The lightness range was found to be in the 30-80 range for all the four series excluding perfectly white and black samples and no sample with a green saturated color was found, which could be a problem for the development of a complete color chart.

The gonioapparent character of the samples has been characterized with the Optimines goniospectrophotometer by measuring the xy-chromaticity coordinates of the samples around

the specular direction, for three incidence angles (15°, 45° and 75°). For one given cell potential, a sample can exhibit different colors and be gonioapparent or not, depending on the substrate roughness. This is due to the fact that, for a given cell potential, the oxide thickness is different depending on the substrate roughness.

A detrimental influence of the Optimines optical system chromatic aberration on color measurements has been highlighted. This influence has been characterized with a collimated beam incident on the detection system, which mimics the case of a perfectly specular sample, but not for a diffuse incident light. The relevant correction procedure was described.

Perspectives

In order to obtain a complete calibration color chart, some complementary studies are needed. First, a study of the aging of the anodized titanium samples is needed in order to confirm their stability with time. Secondly, a study of the gamut and the chromatic paths of commercial gonioapparent materials is needed to obtain a database. These gamut and chromatic paths need to be compared to the ones obtained with the anodized titanium samples. Optical measurements with the goniospectrophotometer Optimines are necessary to characterize these chromatic paths.

Improvements of the Optimines goniospectrophotometer

A clear influence of the Optimines optical system chromatic aberration on color measurements has been reported. In order to characterize the system chromatic aberration under a diffuse beam, different types of diffusers could be added on the light source beam. The chromatic aberration could also be removed by changing the source and detection goniospectrophotometer optical systems into reflective systems using mirrors, which do not exhibit chromatic aberration.

The detection optical fiber of the goniospectrophotometer was shown to influence the shape of the BRDF spectra. By using a mono-core optical fiber with a large core diameter (1 mm) the injection problems are reduced, at the cost of a lower angular sensitivity and a larger spectral bandwidth of the spectrophotometer. The latter is due to the fact that the detection spectrometer does not have an optical slit. A new optical system has been built where the detection arm angular acceptance is decoupled from the detection optical fiber width (as shown in Figure 162) where a filter wheel including different pinholes with different diameters is determining the angular resolution. The new detection fiber core diameter is optimized in order to lower the injection problems while keeping an acceptable spectral bandwidth on the spectrometer. An optical slit is planned to be added later.

Having a selectable pinhole diameter will also allow to improve the goniospectrophotometer signal to noise ratio. It will allow for example to perform measurements in the diffuse 45°:0° angular condition and obtain a direct comparison with commercial spectrophotometers with a 45°a:0° geometry.
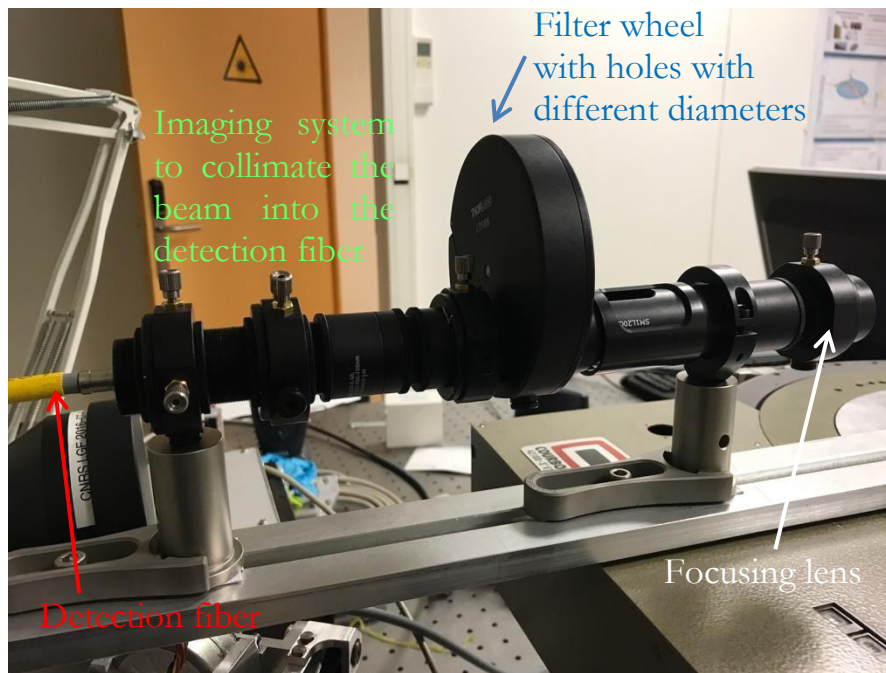
Figure 162: New Optimines detection arm setup.

Anodized titanium parameters characterizations

The oxide thickness estimations based on the reflectance spectra extrema positions as well as ellipsometric estimations are very dependent on the material refractive indexes and other non-optical measurements, such as Reflection Electron Energy Loss Spectroscopy (REELS) would be useful to obtain a second assessment of these crucial parameters.

Direct oxide layer thickness measurements obtained with Scanning Electron Microscopy (SEM) imaging or Focused Ion Beam (FIB) imaging cross-sections can also be used as a comparison with the other estimations techniques. These imaging techniques could also be used to confirm the presence of porosity found when characterizing the samples anodized at 90 V by ellipsometry.

The oxide thickness of titanium after anodizing has been shown to be dependent on the crystalline orientation of the grains of the substrate [77]. This could be used to obtained samples exhibiting multiple colors after a unique anodizing. Ti-6Al-4V alloy samples were sampled in foundry ingots provided by the Timet (Savoie, France) company. The samples exhibit grains with a size up to a centimeter. After a careful sample preparation revealing the grain structure, Electron Backscattered diffraction (EBSD) mapping will be performed to obtain the grain orientation. The samples will be then anodized and the color of each individual grain will be monitored. It will be then possible to link the substrate grain orientation to a color for each cell potential and finally obtained a color mapping correlated with the substrate grain orientation and the cell potential.

Samples with smaller (milimetric) grains might also be used to create a visual texture on the sample, for example to mimic the spangled effect of the commercial gonioapparent materials (car paints for example).

Roughness measurements were carried out in this PhD by a non-contact white light interferometric profilometer before anodizing to obtain the roughness of the titanium substrate and after anodizing for the roughness of the oxide layer. For each sample, five measurements

were made around the center of the sample to obtain a reliable assessment of the roughness of this area. The center of the sample corresponds to the area where the spectrophotometric measurements were performed. However the roughness measurements made before and after anodizing weren't taken on the exact same position on the sample. It could induce an error coming from the difference of positions between the measurement before and after anodizing. This error could be removed by laser engraving a mark on the titanium sample before anodizing. The shape and the size of the mark have to be in accordance with the size and shape of the profilometer measurement area. The surface thermally affected by the laser has also to be taken into account. The mark has to remain visible after anodizing. In Figure 163, a square mark of 1 mm × 1 mm has been engraved with a Nd:YAG laser with a wavelength of 1064 nm and a nominal power of 56W on the titanium substrate. The sample has been later anodized at a cell potential of 140 V. This anodizing potential corresponds to severe conditions with the presence of a lot of anodic spark deposition. The mark is still present after anodizing and no color modification can be observed around the mark.
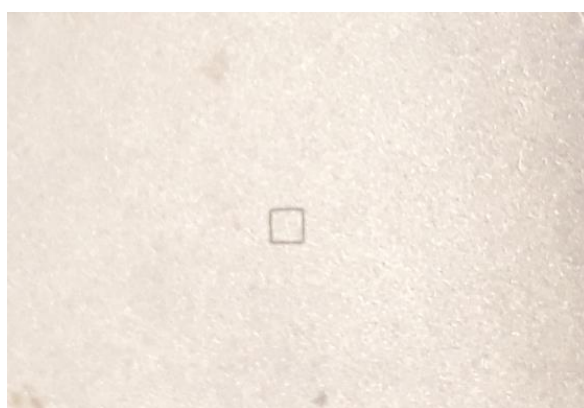
Figure 163 : A 1 mm × 1 mm square mark has been engraved by a Nd:YAG laser with a wavelength of 1064 nm and a nominal power of 56W on a titanium substrate. The sample is then anodized at a cell potential of 140V in a 0.5M H$_2$SO$_4$ solution with a 20mA/cm² current density.

The optical profilometer measurement area is roughly equal to a 1 mm × 1 mm. Based on previous studies made on titanium alloys in the laboratory, the thermally affected surface is estimated to have a width smaller than 200 microns under the specific laser parameters used to engrave the mark. When taking account this information, the optimized engraved mark should be a circle with a diameter equal to 1.2 mm.

Visual characterization of gonioappearrance

The gonioappearance of the samples was observed visually under natural ligning conditions. The incidence and observation angles where color changes are observed, are thus not well defined. In order to obtain a finer assessment of the angles where these perceived color changes occur, an experimental setup to perform perception tests of the gonioapparence of the samples was designed and built. To be able to compare the visual assessments to standard color measurements, the device has been designed to offer the same geometries of illumination and observation as the most common multi-angle spectrophotometers. In particular these geometries include the geometries specified by ASTM E2539 [104] for multi-angle color measurements of interference pigments.

This device, called Goniobox, consists of two illumination and six observation holes, a rotating sample holder and an observation tube as shown in Figure 164.
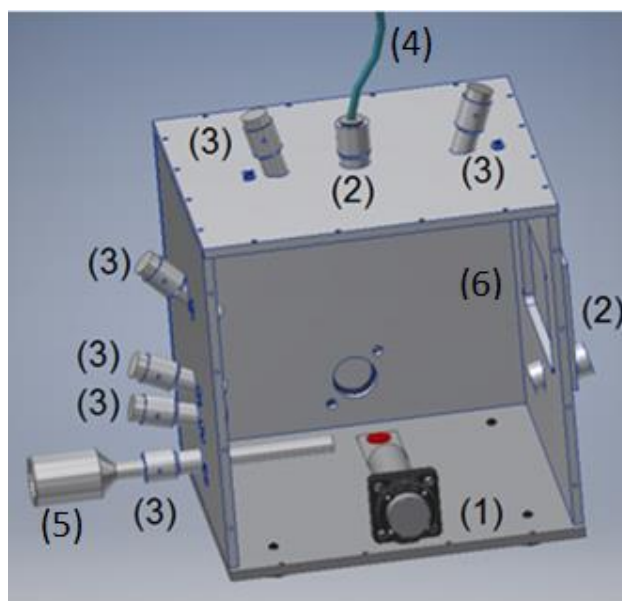
Figure 164: Descriptive diagram of the Goniobox. (1) a rotating sample holder, (2) light source holes, (3) observation holes, (4) illumination fiber, (5) observation tube and (6) trapdoor to introduce the sample.

The light source is a D65 illuminant bulb projected into the box through a collimated optical fiber. The observation tube is graduated and used to observe the sample at the same distance regardless of the observation angle. The sample is introduced by a trapdoor which is sealed by 4 screws in order to limit any possible contamination with stray light. For the same reason stoppers were also designed for the holes unused during a measurement. A referenced color map will also be used in conjunction with the box to help the observer describe the different colors of the samples.

The angular positions of the different holes are shown in Figure 165.
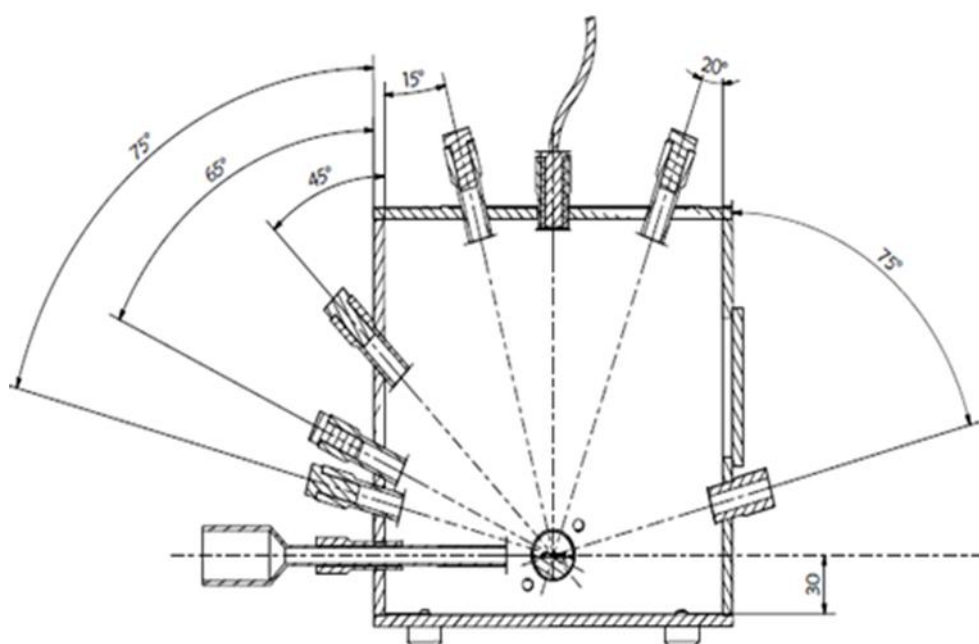
Figure 165 : Angular configuration of the Goniobox. Using the tilt of the sample holder offers the possibility to study numerous angular configurations.

Possible measurement geometries are the following:

- Specular conditions for 15°, 20°, 45°, 65°, 75° by using the rotation of the sample holder with the 0° and 75° illumination holes.
- Various non-specular conditions for an illumination angle of 45° (45°/65° (as110°), 45°/30° (as 75°), 45°/0° (as 45°) , 45°/20° (as 25°), 45°/30° (as 15°)) as specified in ASTM E2539.

During the preliminary tests some improvements were found to be needed. Indeed the illumination system needs to be optimized to obtain a good lighting of the sample surface, both in terms of homogeneity and irradiance, while avoiding the potential inconvenience for the user of a too high irradiance. It is particularly true in the case of the mirror polished samples. Tests were performed with a lower irradiance light intensity to overcome the problem but the resulting irradiance was not enough to observe the roughest samples series.

The samples were first fixed with double face tape but this system was changed after the preliminary tests. The sample holder and the samples have been then covered by a directional magnetic tape. It reduced drastically the time needed to change the sample.

Preliminary tests made with few coworkers revealed that it is easier to determine the gonioappearance of a sample with the Goniobox by doing observations in different specular conditions than fixing the incidence angle and changing the observation angle. This might be due to the current lightning conditions and needs to be confirmed after the optimization of the incident light irradiance.

To perform the perception tests a rigorous measurement protocol has to be followed and still needs to be written. It is also necessary to define a minimum number of observers to constitute a reliable panel. These observers have also to be trained to become familiar with the concepts of color (as lightness, saturation, hue…) to be able to recognize and describe color changes of gonioapparent samples.

Bibliography:

[1]   X. Chen *et al.*, "Large-scale synthesis of water-soluble luminescent hydroxyapatite nanorods for security printing," *J. Colloid Interface Sci.*, vol. 468, pp. 300–306, 2016.

[2]   Q. Xu, W. J. Ye, S. Z. Feng, and H. Y. Sun, "Synthesis and properties of iridescent Co-containing anodic aluminum oxide films," *Dye. Pigment.*, vol. 111, pp. 185–189, 2014.

[3]   N. Akafuah, S. Poozesh, A. Salaimeh, G. Patrick, K. Lawler, and K. Saito, "Evolution of the Automotive Body Coating Process—A Review," *Coatings*, vol. 6, no. 2, p. 24, 2016.

[4]   C. Park, K. Koh, and U. Jeong, "Structural Color Painting by Rubbing Particle Powder," *Sci. Rep.*, vol. 5, pp. 1–5, 2015.

[5]   M. V. Diamanti, B. Del Curto, and V. Masconale, "Production and Anodic Colouring of Newly-Designed Titanium Jewels," *Colour Des. Creat.*, vol. 5, no. 16, pp. 1–9, 2010.

[6]   M. Aziz-Kerrzo, K. G. Conroy, A. M. Fenelon, S. T. Farrell, and C. B. Breslin, "Electrochemical studies on the stability and corrosion resistance of titanium-based implant materials," *Biomaterials*, vol. 22, pp. 1531–1539, 2001.

[7]   X. H. Xie *et al.*, "Enhanced osteointegration of orthopaedic implant gradient coating composed of bioactive glass and nanohydroxyapatite," *J. Mater. Sci. Mater. Med.*, vol. 21, no. 7, pp. 2165–2173, 2010.

[8]   N. Poondla, T. S. Srivatsan, A. Patnaik, and M. Petraroli, "A study of the microstructure and hardness of two titanium alloys: Commercially pure and Ti-6Al-4V," *J. Alloys Compd.*, vol. 486, no. 1–2, pp. 162–167, 2009.

[9]   W. Kroll, "The Production of Ductile Titanium," *Trans. Electrochem. Soc.*, vol. 78, no. 1, p. 35, 1940.

[10]   M. Niinomi, "Mechanical properties of biomedical titanium alloys," *Mater. Sci. Eng. A243*, vol. 243, pp. 231–236, 1998.

[11]   D. Banerjee and J. C. Williams, "Perspectives on titanium science and technology," *Acta Mater.*, vol. 61, no. 3, pp. 844–879, 2013.

[12]   H. Fujii, K. Takahashi, and Y. Yamashita, "Application of titanium and its alloys for automobile parts," *Nippon Steel Tech. Rep.*, no. 88, pp. 70–75, 2003.

[13]   R. R. Boyer, "An overview on the use of titanium in the aerospace industry," *Mater. Sci. Eng. A*, vol. 213, no. 1–2, pp. 103–114, 1996.

[14]   M. Bellardita *et al.*, "Photocatalytic activity of TiO2/SiO2systems," *J. Hazard. Mater.*, vol. 174, no. 1–3, pp. 707–713, 2010.

[15]   Y. Lu, K. Matsuzaka, L. Hao, Y. Hirakawa, H. Yoshida, and F. S. Pan, "Photocatalytic activity of TiO2/Ti composite coatings fabricated by mechanical coating technique and subsequent heat oxidation," *Mater. Sci. Semicond. Process.*, vol. 16, no. 6, pp. 1949–1956, 2013.

[16]   M. Smits *et al.*, "Photocatalytic degradation of soot deposition: Self-cleaning effect on titanium dioxide coated cementitious materials," *Chem. Eng. J.*, vol. 222, pp. 411–418, 2013.

[17]   S. Pazokifard, M. Esfandeh, S. M. Mirabedini, M. Mohseni, and Z. Ranjbar, "Investigating the role of surface treated titanium dioxide nanoparticles on self-cleaning behavior of an

acrylic facade coating," *J. Coatings Technol. Res.*, vol. 10, no. 2, pp. 175–187, 2013.

[18] V. A. Ganesh, H. K. Raut, A. S. Nair, and S. Ramakrishna, "A review on self-cleaning coatings," *J. Mater. Chem.*, vol. 21, no. 41, p. 16304, 2011.

[19] M. Hunger, G. Hüsken, and H. J. H. Brouwers, "Photocatalytic degradation of air pollutants - From modeling to large scale application," *Cem. Concr. Res.*, vol. 40, no. 2, pp. 313–320, 2010.

[20] J. Kolarik and J. Toftum, "The impact of a photocatalytic paint on indoor air pollutants: Sensory assessments," *Build. Environ.*, vol. 57, pp. 396–402, 2012.

[21] K. Demeestere, J. Dewulf, B. De Witte, A. Beeldens, and H. Van Langenhove, "Heterogeneous photocatalytic removal of toluene from air on building materials enriched with TiO2," *Build. Environ.*, vol. 43, no. 4, pp. 406–414, 2008.

[22] M. V. Diamanti *et al.*, "Photoactive and colored anodic oxides on titanium for architectural and design applications," *ResearchGate*, vol. 1, no. grade 2, pp. 170–173, 2008.

[23] "Features of Titanium Material." [Online]. Available: https://www.nssmc.com/product/catalog_download/pdf/T003en.pdf.

[24] *ASTM E2194-14(2017) Standard Test Method for Multiangle Color Measurement of Metal Flake Pigmented*. ASTM International, West Conshohocken, PA, 2017.

[25] C. S. McCamy, "Observation and measurement of the appearance of metallic materials. Part I. Macro appearance," *Color Res. Appl.*, vol. 21, pp. 292–304, 1996.

[26] M. Bertin, J.-P. Faroux, and J. Renault, *Optique et physique ondulatoire*. Dunod, 1994.

[27] S. Kinoshita, S. Yoshioka, and J. Miyazaki, "Physics of structural colors," *Reports Prog. Phys.*, vol. 71, no. 7, p. 076401, 2008.

[28] *Colorimetry: understanding the CIE system*, CIE Reprin. 2006.

[29] R. S. Berns, *Billmeyer and Saltzman's Principles of Color Technology*, 3rd ed. 2000.

[30] N.Matsapey, "Rendu visuel de surfaces nano-structurees: effet de l'ordre à courte distance," PhD thesis, Ecole des mines de Saint-Etienne, 2013.

[31] E. F. Schubert, *Light-Emitting Diodes*. Cambridge Universtiy Press, 2006.

[32] H. A. MacLeod, *Thin-Film Optical Filters,* 3rd ed. Bristol and Philadelphia: Institue of Physics, 2001.

[33] F. Abelès, "Recherches sur la propagation des ondes électromagnétiques sinusoidales dans les milieux stratifiés," *Ann. Phys. (Paris).*, vol. 12, no. 5, pp. 706–782, 1950.

[34] F. Abelès, "La théorie générale des couches minces," *J. Phys. Radium*, vol. 11, no. 7, pp. 307–309, 1950.

[35] M. Born and E. Wolf, *Principles of optics: electromagnetic theory of propagation, interference and diffraction of light*. Pergamon Press, 1964.

[36] K. Wenzel, "The fourth colour filter of tristimulus colorimeters," Budapest, 1988.

[37] D. Randall, "INSTRUMENTS FOR THE MEASUREMENT OF COLOR," *Datacolor Int.*, pp. 1–11, 1954.

[38] E. Perales, E. Chorro, V. Viqueira, and F. M. Martínez-Verdú, "Reproducibility comparison among multiangle spectrophotometers," *Color Res. Appl.*, vol. 38, no. 3, pp. 160–167, 2013.

[39] R. Charrière, G. Lacaille, M. P. Pedeferri, J. Faucheu, and D. Delafosse, "Characterization

of the gonioapparent character of colored anodized titanium surfaces," *Color Res. Appl.*, vol. 40, no. 5, pp. 483–490, 2015.

[40]   F. Leloup, P. Hanselaer, M. Pointer, and J. Versluys, "Characterization of gonio-apparent colours," *10th AIC Congr. Granada*, pp. 515–518, 2005.

[41]   J. L. Meyzonnette and T. Lépine, *Bases de radiométrie optiques*. Toulouse, 2001.

[42]   N. Matsapey, J. Faucheu, M. Flury, and D. Delafosse, "Design of a gonio-spectro-photometer for optical characterization of gonio-apparent materials," *Meas. Sci. Technol.*, vol. 24, p. 065901, 2013.

[43]   J. M. Yanoff and J. S. Duker, *Ophthalmology*, 3rd editio. 2009.

[44]   G. Obein, S. Ouarets, and G. Ged, "Evaluation of the shape of the specular peak for high glossy surfaces," in *Proc. SPIE 9018*, 2014, pp. 05–11.

[45]   H. J. Patrick, C. J. Zarobila, and T. A. Germer, "The NIST Robotic Optical Scatter Instrument (ROSI) and its application to BRDF measurements of diffuse reflectance standards for remote sensing," vol. 8866, p. 886615, 2013.

[46]   J. E. Proctor and P. Y. Barnes, "NIST high accuracy reference reflectometer-spectrophotometer," *J. Res. Natl. Inst. Stand. Technol.*, vol. 101, no. 5, p. 619, 1996.

[47]   G. Obein, R. Bousquet, and M. E. Nadal, "New NIST reference goniospectrometer," in *Proc. SPIE 5880*, 2005.

[48]   J. G. Ward, "Measuring and modeling anisotropic reflection," *Comput. Graph*, vol. 26, no. Jully, pp. 265–272, 1992.

[49]   J. Ren and J. Zhao, "Measurement of a bidirectional reflectance distribution and system achievement based on a hemi-parabolic mirror," *Opt. Lett.*, vol. 35, no. 9, p. 1458, 2010.

[50]   S. Burachas *et al.*, "Defect clusters of variable composition as an origin of coloration of oxide crystals under thermal treatment and irradiation," *Radiat. Meas.*, vol. 42, no. 4–5, pp. 561–564, Apr. 2007.

[51]   I. Komatsu, H. Aoki, M. Ebisawa, A. Kuroda, K. Kuroda, and S. Maeda, "Color change mechanism of niobium oxide thin film with incidental light angle and applied voltage," *Thin Solid Films*, vol. 603, pp. 180–186, Mar. 2016.

[52]   M. C. Eastman, S. Jeknic, and J. Jiao, "Investigation of coloration defects in porous zirconium by X-ray photoelectron spectroscopy," *J. Alloys Compd.*, vol. 728, pp. 1260–1268, Dec. 2017.

[53]   K. Ogura, W. Lou, and M. Nakayama, "Coloration of stainless steel at room temperature by triangular current scan method," *Electrochim. Acta*, vol. 41, no. 18, pp. 2849–2853, Jan. 1996.

[54]   Z. L. Li *et al.*, "Analysis of oxide formation induced by UV laser coloration of stainless steel," *Appl. Surf. Sci.*, vol. 256, no. 5, pp. 1582–1588, Dec. 2009.

[55]   F. P. Netzer, *Oxide Materials at the Two-Dimensional Limit*, Springer. 2016.

[56]   a. Pérez Del Pino, P. Serra, and J. L. Morenza, "Coloring of titanium by pulsed laser processing in air," *Thin Solid Films*, vol. 415, no. 1–2, pp. 201–205, 2002.

[57]   A. Pérez del Pino, J. M. Fernández-Pradas, P. Serra, and J. L. Morenza, "Coloring of titanium through laser oxidation: Comparative study with anodizing," *Surf. Coatings Technol.*, vol. 187, no. 1, pp. 106–112, 2004.

[58]   S. O'Hana, a. J. Pinkerton, K. Shoba, a. W. Gale, and L. Li, "Laser surface colouring of

titanium for contemporary jewellery," vol. 24, no. 2, pp. 147–153, 2008.

[59] S. Izman *et al.*, "Surface Modification Techniques for Biomedical Grade of Titanium Alloys: Oxidation , Carburization and Ion Implantation Processes," *Www.Intechopen.Com*, 2006.

[60] C. Langlade, a. B. Vannes, J. M. Krafft, and J. R. Martin, "Surface modification and tribological behaviour of titanium and titanium alloys after YAG-laser treatments," *Surf. Coatings Technol.*, vol. 100–101, pp. 383–387, 1998.

[61] L. Bartlett, "An unusual phenomenon observed when anodising CP titanium to produce coloured surfaces for jewellery and other decorative uses," *Opt. Laser Technol.*, vol. 38, no. 4–6, pp. 440–444, 2006.

[62] O. a. Galvis *et al.*, "Formation of grooved and porous coatings on titanium by plasma electrolytic oxidation in H2SO4/H3PO4 electrolytes and effects of coating morphology on adhesive bonding," *Surf. Coatings Technol.*, vol. 269, pp. 238–249, 2015.

[63] D. M. Brunette, P. Tengvall, M. Textor, and P. Thomsen, *Titanium in Medicine*. Springer, 2001.

[64] M. Fazel, H. R. Salimijazi, M. a Golozar, and M. R. Garsivaz, "Applied Surface Science A comparison of corrosion , tribocorrosion and electrochemical impedance properties of pure Ti and Ti6Al4V alloy treated by micro-arc oxidation process," *Appl. Surf. Sci.*, vol. 324, pp. 751–756, 2015.

[65] S.-D. Wu, H. Zhang, X.-D. Dong, C.-Y. Ning, A. S. L. Fok, and Y. Wang, "Physicochemical properties and in vitro cytocompatibility of modified titanium surfaces prepared via micro-arc oxidation with different calcium concentrations," *Appl. Surf. Sci.*, vol. 329, pp. 347–355, 2015.

[66] Y.-T. Sul, C. B. Johansson, Y. Jeong, and T. Albrektsson, "The electrochemical oxide growth behaviour on titanium in acid and alkaline electrolytes," *Med. Eng. Phys.*, vol. 23, no. 5, pp. 329–346, Jun. 2001.

[67] J. Kapusta-Kołodziej, O. Tynkevych, A. Pawlik, M. Jarosz, J. Mech, and G. D. Sulka, "Electrochemical growth of porous titanium dioxide in a glycerol-based electrolyte at different temperatures," *Electrochim. Acta*, vol. 144, pp. 127–135, 2014.

[68] M. V. Diamanti, P. Pozzi, F. Randone, B. Del Curto, and M. P. Pedeferri, "Robust anodic colouring of titanium: Effect of electrolyte and colour durability," *Mater. Des.*, vol. 90, pp. 1085–1091, 2016.

[69] S. Van Gils, P. Mast, E. Stijns, and H. Terryn, "Colour properties of barrier anodic oxide films on aluminium and titanium studied with total reflectance and spectroscopic ellipsometry," *Surf. Coatings Technol.*, vol. 185, no. 2–3, pp. 303–310, Jul. 2004.

[70] M. V. Diamanti and M. P. Pedeferri, "Effect of anodic oxidation parameters on the titanium oxides formation," *Corros. Sci.*, vol. 49, no. 2, pp. 939–948, Feb. 2007.

[71] M. V. Diamanti, B. Del Curto, V. Masconale, C. Passaro, and M. P. Pedeferri, "Anodic coloring of titanium and its alloy for jewels production," *Color Res. Appl.*, vol. 37, pp. 384–390, 2012.

[72] E. D. Palik, *Handbook of optical constants of solids*. Academic Press, 1998.

[73] M. V. Diamanti, B. Del Curto, and M. Pedeferri, "Interference colors of thin oxide layers on titanium," *Color Res. Appl.*, vol. 33, no. 3, pp. 221–228, Jun. 2008.

[74] A. F. Yetim, "Investigation of wear behavior of titanium oxide films, produced by anodic

oxidation, on commercially pure titanium in vacuum conditions," *Surf. Coatings Technol.*, vol. 205, no. 6, pp. 1757–1763, 2010.

[75]   A. C. Alves, F. Oliveira, F. Wenger, P. Ponthiaux, J.-P. Celis, and L. A. Rocha, "Tribocorrosion behaviour of anodic treated titanium surfaces intended for dental implants," *J. Phys. D. Appl. Phys.*, vol. 46, no. 40, p. 404001, 2013.

[76]   J. Moon *et al.*, "The correlation between the interference colour and growth procedure of anodic titanium dioxide nanotube arrays," *Color. Technol.*, vol. 130, no. 1, pp. 1–7, 2014.

[77]   M. V. Diamanti, F. C. Spreafico, and M. P. Pedeferri, "Production of Anodic TiO2 Nanofilms and their Characterization," *Phys. Procedia*, vol. 40, pp. 30–37, 2013.

[78]   H. Habazaki, M. Uozumi, H. Konno, K. Shimizu, P. Skeldon, and G. E. Thompson, "Crystallization of anodic titania on titanium and its alloys," *Corros. Sci.*, vol. 45, no. 9, pp. 2063–2073, Sep. 2003.

[79]   M. V. Diamanti, M. Pedeferri, and C. A. Schuh, "Thickness of anodic titanium oxides as a function of crystallographic orientation of the substrate," *Metall. Mater. Trans. A*, vol. 39A, pp. 2143–2147, 2008.

[80]   P. Pedeferri, "Method of coloring titanium and its alloys through anodic oxidation," 2002.

[81]   H. C. Genuino, N. N. Opembe, E. C. Njagi, S. McClain, and S. L. Suib, "A review of hydrofluoric acid and its use in the car wash industry," *J. Ind. Eng. Chem.*, vol. 18, no. 5, pp. 1529–1539, 2012.

[82]   R. Markle, "Etching Titanium with HF and Nitric Acid Solutions Part 1." [Online]. Available: http://www.chemcut.net/wp-content/uploads/2015/02/Etching-Titanium-with-HF-and-Nitric-Acid-Solutions-Part1.pdf.

[83]   J. Guo, R. J. Padilla, W. Ambrose, I. J. De Kok, and L. F. Cooper, "The effect of hydrofluoric acid treatment of TiO2 grit blasted titanium implants on adherent osteoblast gene expression in vitro and in vivo," *Biomaterials*, vol. 28, pp. 5418–5425, 2007.

[84]   S. F. Lamolle, M. Monjo, M. Rubert, H. J. Haugen, S. P. Lyngstadaas, and J. E. Ellingsen, "The effect of hydrofluoric acid treatment of titanium surface on nanostructural and chemical changes and the growth of MC3T3-E1 cells," *Biomaterials*, vol. 30, pp. 736–742, 2009.

[85]   T. Kazuhiro, T. Yamazaki, T. Nishijima, and H. Shimizu, "Effect of Grain Size and Initial Surface Condition on Glossiness and Whiteness of the Pickled Titanium Surface," 2002.

[86]   I. T. Kazuhiro Takashi, Ryo Matsuhashi, "Change of Morphology of Titanium Surface by Pickling in Nitric Hydrofluoric Acid Solutions.pdf," 2002.

[87]   U. Balaji and S. K. Pradhan, "Titanium anodisation designed for surface colouration - Systemisation of parametric interaction using response surface methodology," *Mater. Des.*, vol. 139, pp. 409–418, 2018.

[88]   C. L. Briant, Z. F. Wang, and N. Chollocoop, "Hydrogen embrittlement of commercial purity titanium," *Corros. Sci.*, vol. 44, no. 8, pp. 1875–1888, 2002.

[89]   E. Tal-Gutelmacher and D. Eliezer, "The hydrogen embrittlement of titanium-based alloys," *J. Miner. Met. Mater. Soc.*, vol. 57, no. 9, pp. 46–49, 2005.

[90]   J. R. DeVore, "Refractive Indices of Rutile and Sphalerite," *J. Opt. Soc. Am.*, vol. 41, no. 6, p. 416, Jun. 1951.

[91]   R. M. . Azzam and B. N.M, *Ellipsometry and polarized light*. Amsterdam, North-Holland, 1988.

[92] A. Bendavid and P. J. Martin, "Review of thin films materials deposition by the filtered cathodic vacuum arc process at CSIRO," *J. Aust. Ceram. Soc.*, vol. 501, no. April, pp. 86–101, 2014.

[93] M. Yasaka, "X-ray thin-film measurement techniques," *V. X-ray reflectivity Meas. Rigaku J.*, vol. 26, no. 2, pp. 1–9, 2010.

[94] C. K. Carniglia, "Scalar Scattering Theory for Multilayer Optical Coatings," *Opt. Eng.*, vol. 18, no. 2, pp. 104–115, 1979.

[95] J. M. Eastman, "Surface scattering in optical interference coatings," Rochester, New York, 1974.

[96] P. Beckmann and A. Spizzichino, *The scattering of electromagnetic waves from rough surfaces / Petr Beckmann, Andre Spizzichino. - Version details - Trove.* New York: Oxford, 1963.

[97] A. Roos, M. Bergkvist, and C. G. Ribbing, "Observation of diffuse interference in reflectance from oxide-coated metals," *Thin Solid Films*, vol. 125, no. 3–4, pp. 221–227, 1985.

[98] A. Roos and B. Karlsson, "Properties of oxidized copper sufaces for solar applications II," *Sol. Energy Mater.*, vol. 7, pp. 467–480, 1983.

[99] A. Roos and B. Karlsson, "Properties of oxidized copper surfaces for solar applications I," *Sol. Energy Mater.*, vol. 7, no. 4, pp. 453–465, 1983.

[100] A. Roos and C. G. Ribbing, "Oxidation induced roughness as observed by diffuse optical reflectance," *Phys. Lett. A*, vol. 108, no. 4, pp. 225–227, 1985.

[101] M. Bergkvist, A. Roos, and C. G. Ribbing, "Interference structure in optical scattering from oxide/metal interfaces," *J. Vac. Sci. Technol. A Vacuum, Surfaces, Film.*, vol. 5, no. 4, pp. 1661–1665, 1987.

[102] A. Roos and D. Rönnow, "Diffuse reflectance and transmittance spectra of an interference layer: 1. Model formulation and properties," *Appl. Opt.*, vol. 33, no. 34, pp. 7908–7917, 1994.

[103] D. Rönnow and A. Roos, "Diffuse reflectance and transmittance spectra of an interference layer: 2. Evaluation of tin oxide-coated glass," *Appl. Opt.*, vol. 33, no. 34, pp. 7918–7927, 1994.

[104] ASTM International, *ASTM E2539-14(2017), Standard Test Method for Multiangle Color Measurement of Interference Pigments.* ASTM International, West Conshohocken, PA, 2017.

Appendices

Appendix A: Relatives spectral power distribution of CIE illuminants (from [28])

λ, nm	Standard Illuminant A	Standard Illuminant D65	Illuminant C	Illuminant D50	Illuminant D55	Illuminant D75
300	0,930 483	0,034 100 0	0,00	0,019	0,024	0,043
305	1,128 21	1,664 30	0,00	1,035	1,048	2,588
310	1,357 69	3,294 50	0,00	2,051	2,072	5,133
315	1,622 19	11,765 2	0,00	4,914	6,648	17,470
320	1,925 08	20,236 0	0,01	7,778	11,224	29,808
325	2,269 80	28,644 7	0,20	11,263	15,936	42,369
330	2,659 81	37,053 5	0,40	14,748	20,647	54,930
335	3,096 61	38,501 1	1,55	16,348	22,266	56,095
340	3,589 68	39,948 8	2,70	17,948	23,885	57,259
345	4,136 48	42,430 2	4,85	19,479	25,851	60,000
350	4,742 38	44,911 7	7,00	21,010	27,817	62,740
355	5,410 70	45,775 0	9,95	22,476	29,219	62,861
360	6,144 62	46,638 3	12,90	23,942	30,621	62,982
365	6,947 20	49,363 7	17,20	25,451	32,464	66,647
370	7,821 35	52,089 1	21,40	26,961	34,308	70,312
375	8,769 80	51,032 3	27,50	25,724	33,446	68,507
380	9,795 10	49,975 5	33,00	24,488	32,584	66,703
385	10,899 6	52,311 8	39,92	27,179	35,335	68,333
390	12,085 3	54,648 2	47,40	29,871	38,087	69,963
395	13,354 3	68,701 5	55,17	39,589	49,518	85,946
400	14,708 0	82,754 9	63,30	49,308	60,949	101,929
405	16,148 0	87,120 4	71,81	52,910	64,751	106,911
410	17,675 3	91,466 0	80,60	56,513	68,554	111,894
415	19,290 7	92,458 9	89,53	58,273	70,065	112,346
420	20,995 0	93,431 8	98,10	60,034	71,577	112,798
425	22,788 3	90,057 0	105,80	58,926	69,746	107,945
430	24,670 9	86,682 3	112,40	57,818	67,914	103,092
435	26,642 5	95,773 6	117,75	66,321	76,760	112,145
440	28,702 7	104,865	121,50	74,825	85,605	121,198
445	30,850 8	110,936	123,45	81,036	91,799	127,104
450	33,085 9	117,008	124,00	87,247	97,993	133,010
455	35,406 8	117,410	123,60	88,930	99,228	132,682
460	37,812 1	117,812	123,10	90,612	100,463	132,355
465	40,300 2	116,336	123,30	90,990	100,188	129,838
470	42,869 3	114,861	123,80	91,368	99,913	127,322
475	45,517 4	115,392	124,09	93,238	101,326	127,061
480	48,242 3	115,923	123,90	95,109	102,739	126,800
485	51,041 8	112,367	122,92	93,536	100,409	122,291
490	53,913 2	108,811	120,70	91,963	98,078	117,783
495	56,853 9	109,082	116,90	93,843	99,379	117,186
500	59,861 1	109,354	112,10	95,724	100,680	116,589
505	62,932 0	108,578	106,98	96,169	100,688	115,146
510	66,063 5	107,802	102,30	96,613	100,695	113,702
515	69,252 5	106,296	98,81	96,871	100,341	111,181
520	72,495 9	104,790	96,90	97,129	99,987	108,659
525	75,790 3	106,239	96,78	99,614	102,098	109,552
530	79,132 6	107,689	98,00	102,099	104,210	110,445
535	82,519 3	106,047	99,94	101,427	103,156	108,367
540	85,947 0	104,405	102,10	100,755	102,102	106,289
545	89,412 4	104,225	103,95	101,536	102,535	105,596
550	92,912 0	104,046	105,20	102,317	102,968	104,904
555	96,442 3	102,023	105,67	101,159	101,484	102,452
560	100,000	100,000	105,30	100,000	100,000	100,000
565	103,582	98,167 1	104,11	98,868	98,608	97,808
570	107,184	96,334 2	102,30	97,735	97,216	95,616
575	110,803	96,061 1	100,15	98,327	97,482	94,914
580	114,436	95,788 0	97,80	98,918	97,749	94,213
585	118,080	92,236 8	95,43	96,208	94,590	90,605
590	121,731	88,685 6	93,20	93,499	91,432	86,997
595	125,386	89,345 9	91,22	95,593	92,926	87,112
600	129,043	90,006 2	89,70	97,688	94,419	87,227
605	132,697	89,802 6	88,83	98,478	94,780	86,684
610	136,346	89,599 1	88,40	99,269	95,140	86,140
615	139,988	88,648 9	88,19	99,155	94,680	84,861
620	143,618	87,698 7	88,10	99,042	94,220	83,581
625	147,235	85,493 6	88,06	97,382	92,334	81,164
630	150,836	83,288 6	88,00	95,722	90,448	78,747

Reference plane

Plane in which the surface of a sample or standard is placed during measurements.
For reflection measurements, the measurement geometry is defined with respect to the reference plane. For transmission measurements, there is a reference plane for the incident light and a second reference plane, moved according to the sample thickness, for the transmitted light.

Sampling aperture

Area of the reference plane on which measurements are made.
The sampling aperture is delimited by the area illuminated or by the area over which the receiver collects the flux. If the illuminated area is the largest, the area measured is said to be "over filled"; if it is the smallest, the area measured is said to be "under filled".

Irradiation or influx (illumination or incidence) geometry

Angular distribution of the incident radiation on the sample being measured with respect to the center of the sampling aperture.

Reflection/transmission or efflux (collection, measuring) geometry

Angular distribution of the receiver responsivity with respect to the centre of the sampling aperture

Radiance:

In radiometry, radiance is the radiant flux emitted, reflected, transmitted or received by a surface, per unit solid angle per unit projected area. It is expressed in watt per steradian per square meter ($W \cdot sr^{-1} \cdot m^{-2}$)

Spectral radiance:
The radiance of a surface per unit frequency or wavelength, depending on whether the spectrum is taken as a function of frequency or of wavelength. Expressed in watt per steradian per square meter, per meter if expressed in wavelengths ($W \cdot sr^{-1} \cdot m^{-3}$) or per Hertz if expressed in frequencies ($W \cdot sr^{-1} \cdot m^{-2} Hz^{-1}$).

Electrostatic discharge (ESD)
A the sudden flow of electricity between two electrically charged objects caused by contact, an electrical short-circuit, or dielectric breakdown.

Sandblasting

It is the operation of forcibly propelling a stream of abrasive material, sand in the case of sandblasting, against a surface under high pressure to smooth a rough surface, roughen a smooth surface, shape a surface, or remove surface contaminants. Other blasting methods also exist such as water (hydro-blasting), glass beads (bead blasting) or frozen carbon dioxide particles (dry-ice blasting).

Pickling

It is a metal surface treatment used to remove impurities, such as stains, inorganic contaminants, rust or scales from ferrous metals, copper, precious metals or aluminum alloys. Strong acids are usually used to remove the surface impurities. The primary acids used are hydrochloric acid or sulfuric acid.

Galvanostatic regime:

The reaction, for example anodizing, is done while maintaining a constant current.

Potentiostatic regime:

The reaction, for example anodizing, is done while maintaining a constant potential.

The electric field $\vec{E}$ and the magnetic field $\vec{H}$ can be written for a TM polarization with the following formula:

$$\begin{cases} H_x(y,z) = U(z)\exp(-i\omega t + i\gamma y) \\ E_y(y,z) = V(z)\exp(-i\omega t + i\gamma y) \\ E_z(y,z) = W(z)\exp(-i\omega t + i\gamma y) \end{cases}$$

(89)

$$\gamma^2 = \frac{\omega^2}{c^2}n(z)^2\sin^2(\theta(z)) \quad \text{which is a constant according to the Snell-Descartes law.}$$

(90)

i.   Computation of the Abeles matrices

The differential equations of $U(z)$ and $V(z)$ can be written as:

$$\begin{cases} \dfrac{dU}{dz} = -i\omega\varepsilon_0\varepsilon_r(z)V(z) \\ \dfrac{dV}{dz} = i\omega\mu_0\left[-\mu_r(z) + \dfrac{S^2}{\varepsilon_r(z)}\right]U(z) \end{cases} \qquad \text{And we also have } W(z) = \frac{\gamma}{\omega\varepsilon_0\varepsilon_r(z)}U(z)$$

(91)

where $S = \gamma * \dfrac{c}{\omega}$

From the differential equations system, can be deducted two uncoupled second order differential equations for U and V. In each homogeneous layer I we have:

$$\begin{cases} \dfrac{d^2U}{dz^2} = \dfrac{-\omega^2}{c^2}(n_i^2 - S^2)U(z) \\ \dfrac{d^2V}{dz^2} = \dfrac{-\omega^2}{c^2}(n_i^2 - S^2)V(z) \end{cases} \qquad \text{where } n_i^2 = \varepsilon_r^i n_r^i$$

(92)

The Abeles matrices are defined as:

$$\begin{bmatrix} U(z_i) \\ V(z_i) \end{bmatrix} = M_i(z_i - z_{i-1})\begin{bmatrix} U(z_{i-1}) \\ V(z_{i-1}) \end{bmatrix}$$

(93)

We then obtain:

$$M_i(z) = \begin{bmatrix} U_2^i(z) & U_1^i(z) \\ V_2^i(z) & V_1^i(z) \end{bmatrix} \text{ with } \begin{cases} U_1^i(z) = -\dfrac{i}{P_i'}\sin(k_z^i z) \\ U_2^i(z) = \cos(k_z^i z) = V_1^i(z) \\ V_2^i(z) = -iP_i'\sin(k_z^i z) \end{cases}$$

(94)

where:

$$P'_i = \frac{\sqrt{n_i^2 - S^2}}{c\varepsilon_0 \varepsilon_r^i} \quad \text{and} \quad k_z^i = \frac{\omega}{c}\sqrt{n_i^2 - S^2}$$

Let's first compute the magnetic field reflection coefficient:
The electric field H_x^0 in the incident medium can be written as:

$$H_x^0(y,z) = H_x^{inc}(y,z) + H_x^{ref}(y,z) \tag{95}$$

Where H_x^{inc} is the incident magnetic field propagating towards the negative values of z and with an expression proportional to $\exp(-i\omega t - ik_z^0 z)$ and H_x^{ref} is the reflected magnetic field propagating along the positive value of z and with an expression proportional to:

$$\exp(-i\omega t + ik_z^0 z)$$

U_1^0 and U_2^0 form a basis of the solutions for the magnetic field in the incident medium, so we can write:

$$H_x^0(y,z) = U^0(z)\exp(-i\omega t + i\gamma y) = [AU_1^0(z) + BU_2^0(z)]\exp(-i\omega t + i\gamma y)$$

$$= \left[-A\frac{i}{P'_0}\sin(k_z^0 z) + B\cos(k_z^0 z) \right]\exp(-i\omega t + i\gamma y) \tag{96}$$

It can also be written as:

$$H_x^0(y,z) = \frac{1}{2}\left[\exp(ik_z^0 z)\left(\frac{-A}{P'_0} + B \right) + \exp(-ik_z^0 z)\left(B + \frac{A}{P'_0} \right) \right]\exp(-i\omega t + i\gamma y) \tag{97}$$

We thus have: $\begin{cases} H_x^{inc}(y,z) = \frac{1}{2}\left(B + \frac{A}{P'_o} \right)\exp(-ik_z^0 z)\exp(-i\omega t + i\gamma y) \\ H_x^{ref}(y,z) = \frac{1}{2}\left(B - \frac{A}{P'_o} \right)\exp(+ik_z^0 z)\exp(-i\omega t + i\gamma y) \end{cases}$

The magnetic field reflection coefficient in amplitude can be written as:

$$r_H^{TM} = \frac{H_x^{ref}(y,0)}{H_x^{inc}(y,0)} = \frac{B - \frac{A}{P'_o}}{B + \frac{A}{P'_o}} \tag{98}$$

Let's express A and B as a function of $U^0(0)$ and $V^0(0)$.

$$V^0(z) = -\frac{1}{i\omega\varepsilon_0\varepsilon_r^0}\frac{dU^0}{dz} = -\frac{1}{i\omega\varepsilon_0\varepsilon_r^0}\left[A\frac{dU_1^0}{dz} + B\frac{dU_2^0}{dz} \right] = AV_1^0(z) + BV_2^0(z) \tag{99}$$

Thus we have: $\begin{cases} U^0(0) = B \\ V^0(0) = A \end{cases}$

And finally:

$$r_H^{TM} = \frac{H_x^{ref}(y,0)}{H_x^{inc}(y,0)} = \frac{U^0(0) - \frac{V^0(0)}{P_0'}}{U^0(0) + \frac{V^0(0)}{P_0'}}$$

(100)

With the Abeles formalism, we can write:

$$\begin{bmatrix} U^{N+1}(0) \\ V^{N+1}(0) \end{bmatrix} = M_{nN}(0) \ldots M_i(z_i - z_{i-1}) \ldots M_1(z_1) \begin{bmatrix} U^0(0) \\ V^0(0) \end{bmatrix} = M \begin{bmatrix} U^0(0) \\ V^0(0) \end{bmatrix} \text{, we thus have:}$$

$$U^{N+1}(0) \begin{bmatrix} 1 \\ P'_{N+1} \end{bmatrix} = M \begin{bmatrix} U^0(0) \\ V^0(0) \end{bmatrix} \text{ which can also be written as } \begin{bmatrix} U^0(0) \\ V^0(0) \end{bmatrix} = U^{N+1}(0) M^{-1} \begin{bmatrix} 1 \\ P'_{N+1} \end{bmatrix}.$$

By noting $M^{-1} = \begin{bmatrix} M_{11}' & M_{12}' \\ M_{21}' & M_{22}' \end{bmatrix}$ it is possible to write:

$$r_H^{TM} = \frac{M_{11}' P_0' + M_{12}' P_0' P_{n+1}' - M_{21}' - P_{n+1}' M_{22}'}{M_{11}' P_0' + M_{12}' P_0' P_{n+1}' + M_{21}' + P_{n+1}' M_{22}'}$$

(101)

Let's now compute the magnetic field transmission coefficient:
The magnetic field bellow the multilayers can be written as:

$$H_x^{N+1}(y,z) = \frac{1}{2}\left[\exp(ik_z^{N+1}z)\left(\frac{-A'}{P'_{N+1}} + B' \right) + \exp(-ik_z^{N+1}z)\left(B' + \frac{A'}{P'_{N+1}} \right) \right] \exp(-i\omega t + i\gamma y)$$

(102)

As there is no incident magnetic field coming from under the multilayer, the magnetic field from under the multilayer gets only a propagation direction towards the negative values of the z axis.

We thus have: $B' = \frac{A'}{P'_{N+1}}$ and $U^{N+1}(0) = \frac{V^{N+1}(0)}{P'_{N+1}}$.

The magnetic field bellow the multilayer is then written as:

$$H_x^{N+1}(y, z - z_n) = U^{N+1}(0) \exp(-i\omega t + i\gamma y) \exp\left(-ik_z^{N+1}(z - z_N) \right)$$

(103)

The magnetic field transmission coefficient in amplitude is then written as:

$$t_H^{TM} = \frac{H_x^{N+1}(y,0)}{H_x^{inc}(y,0)} = \frac{2U^{N+1}(0)}{U^0(0) + \frac{V^0(0)}{P_o}}$$

(104)

By introducing the Abeles matrices, we obtain:

$$t_H^{TM} = \frac{2P_0'}{M_{11}' P_0' + M_{12}' P_0' P_{N+1}' + M_{21}' + P_{N+1}' M_{22}'}$$

(105)

iii.   <u>Computation of the electric field reflection and transmission coefficients</u>

The expression of the electric field is:

$$\begin{cases} E_y(y,z) = V(z)\exp(-i\omega t + i\gamma y) \\ E_z(y,z) = W(z)\exp(-i\omega t + i\gamma y) \end{cases}$$ (106)

With $W(z) = \dfrac{\gamma}{\omega\varepsilon_0\varepsilon_{r(z)}}U(z)$ and $V(z) = \dfrac{1}{-i\omega\varepsilon_0\varepsilon_r^0}\dfrac{dU}{dz}$.

The total electric field is written:

$$\vec{E} = (V(z)\vec{e}_y + W(z)\vec{e}_z)\exp(-i\omega t + i\gamma y)$$

in the incident medium, it can be written by derivation of $U^0(z)$:

$$V^0(z) = V^0(0)V_1(z) + U^0(0)V_2^0(z) = V^0(0)\cos(k_z^0 z) + U^0(0)(-iP_0')\sin(k_z^0 z)$$
$$= \frac{1}{2}[\exp(ik_z^0 z)(V^0(0) - P_0'U^0(0)) + \exp(-ik_z^0 z)(V^0(0) + P_0'U^0(0))]$$ (107)

And for $W^0(z)$ we have:

$$W^0(z) = \frac{1}{2}\frac{\gamma}{\omega\varepsilon_0\varepsilon_r^0}\left[\exp(ik_z^0 z)\left(\frac{-V^0(0)}{P_0'} + U^0(0)\right) + \exp(-ik_z^0 z)\left(\frac{V^0(0)}{P_0'} + U^0(0)\right)\right]$$ (108)

This allows to decompose the electric field components into an incident field (propagation towards the negative values of the z axis) and a reflected field (propagation towards the positive values of the z axis).

In the medium bellow the multilayer, it can be written:

$$U^{N+1}(0) = \frac{V^{N+1}(0)}{P_{N+1}'}$$ because there is no incident field coming from under the medium and then:

$$V^{N+1}(z - z_N) = \frac{1}{2}[\exp(ik_z^{N+1}(z - z_N))(V^{N+1}(0) - P_{N+1}'U^{N+1}(0)) + \exp(-ik_z^{N+1}(z - z_N))(V^{N+1}(0) + P_{N+1}'U^{N+1}(0))]$$
$$= P'_{N+1}U^{N+1}(0)\exp(-ik_z^{N+1}(z - z_N))$$ (109)

and $$W^{N+1}(z - z_n) = \frac{\gamma}{\omega\varepsilon_0\varepsilon_r^{N+1}}U^{N+1}(0)\exp(-ik_z^{N+1}(z - z_N))$$ (110)

Let's calculate the electric field reflection coefficient in TM polarization.
We have:

$$\begin{cases} \vec{E}^{inc} = \frac{1}{2}\left[(V^0(0) + P_0'U^0(0))\vec{e}_y + \frac{\gamma}{\omega\varepsilon_0\varepsilon_r^0}\left(U^0(0) + \frac{V^0(0)}{P_0'}\right)\vec{e}_z\right]\exp(-ik_z^0 z)\exp(-i\omega t + i\gamma y) \\ \vec{E}^{ref} = \frac{1}{2}\left[(V^0(0) - P_0'U^0(0))\vec{e}_y + \frac{\gamma}{\omega\varepsilon_0\varepsilon_r^0}\left(U^0(0) - \frac{V^0(0)}{P_0'}\right)\vec{e}_z\right]\exp(+ik_z^0 z)\exp(-i\omega t + i\gamma y) \end{cases}$$

By using (90) we can write:

$$\frac{\frac{\gamma}{\omega\varepsilon_0\varepsilon_r^0}\left(U^0(0) + \frac{V^0(0)}{P_0'}\right)}{V^0(0) + P_0'U^0(0)} = \frac{\gamma}{\omega\varepsilon_0\varepsilon_r^0 P_0'} = \frac{n_0\sin(\theta_o)}{\sqrt{n_0^2 - n_0^2\sin^2(\theta_o)}} = \tan(\theta_0)$$ (111)

196

and
$$\frac{\frac{\gamma}{\omega\varepsilon_0\varepsilon_r^0}\left(U^0(0) - \frac{V^0(0)}{P_0'}\right)}{V^0(0) - P_0'U^0(0)} = \frac{-\gamma}{\omega\varepsilon_0\varepsilon_r^0 P_o'} = \frac{-n_0\sin(\theta_o)}{\sqrt{n_0^2 - n_0^2\sin^2(\theta_o)}} = -\tan(\theta_0) \qquad (112)$$

So we can write:

$$\begin{cases} \vec{E}^{inc} = \frac{1}{2}\left[\frac{(+V^0(0) + P_0'U^0(0))}{\cos(\theta_0)} \ \vec{e}^{inc}\right]\exp(-ik_z^0 z)\exp(-i\omega t + i\gamma y) \\ \vec{E}^{ref} = \frac{1}{2}\left[\frac{(-V^0(0) + P_0'U^0(0))}{\cos(\theta_0)} \ \vec{e}^{ref}\right]\exp(+ik_z^0 z)\exp(-i\omega t + i\gamma y) \end{cases} \qquad (113)$$

with $\vec{e}^{inc}$ and $\vec{e}^{ref}$ are unit vectors with the following expressions:

$$\begin{cases} \vec{e}^{inc} = +\cos(\theta_0)\vec{e}_y + \sin(\theta_0)\vec{e}_Z \\ \vec{e}^{ref} = -\cos(\theta_0)\vec{e}_y + \sin(\theta_0)\vec{e}_Z \end{cases}$$

Finally the electric field reflection coefficient is given by:

$$r_E^{TM} = \frac{-V^0(0) + P_0'U^0(0)}{V^0(0) + P_0'U^0(0)} = r_H^{TM} \qquad (114)$$

Let's calculate the electric field transmission coefficient in TM polarization.
The electric field bellow the multilayer is then written as:

$$\vec{E}^{N+1} = U^{N+1}(0)\left[P_{N+1}'\vec{e}_y + \frac{\gamma}{\omega\varepsilon_0\varepsilon_r^{N+1}}\vec{e}_Z\right]\exp(-ik_z^{N+1}(z - z_n))\exp(-i\omega t + i\gamma y) \qquad (115)$$

By using (90), we obtain $\frac{\gamma}{\omega\varepsilon_0\varepsilon_r^{N+1}P_{N+1}'} = \tan(\theta_{N+1})$.

then $\qquad \vec{E}^{N+1} = U^{N+1}(0)\frac{P_{N+1}'}{\cos(\theta_{N+1})}\vec{e}^{trans}\exp(-ik_z^{N+1}(z - z_n))\exp(-i\omega t + i\gamma y) \qquad (116)$

$\vec{e}^{trans}$ is an unit vector with the following expression: $\vec{e}^{trans} = \cos(\theta_{N+1})\vec{e}_y + \sin(\theta_{N+1})\vec{e}_Z$

Finally the electric field transmission coefficient in TM polarization is given by:

$$t_E^{TM} = \frac{\cos(\theta_0)}{\cos(\theta_{N+1})}\frac{2P_{N+1}'U^{N+1}(0)}{V^0(0) + P_0'U^0(0)} = \frac{\cos(\theta_0)}{\cos(\theta_{N+1})}\frac{P_{N+1}'}{P_0'}t_H^{TM} = \sqrt{\frac{\mu_r^{N+1}}{\varepsilon_r^{N+1}}}\sqrt{\frac{\varepsilon_r^0}{\mu_r^0}}t_H^{TM} \qquad (117)$$

Appendix D: SEM Images of Grade 2 Titanium mirror polished and etched for 30 sec in an HF/HNO₃ solution: (top) at low and (bottom) at high magnification.
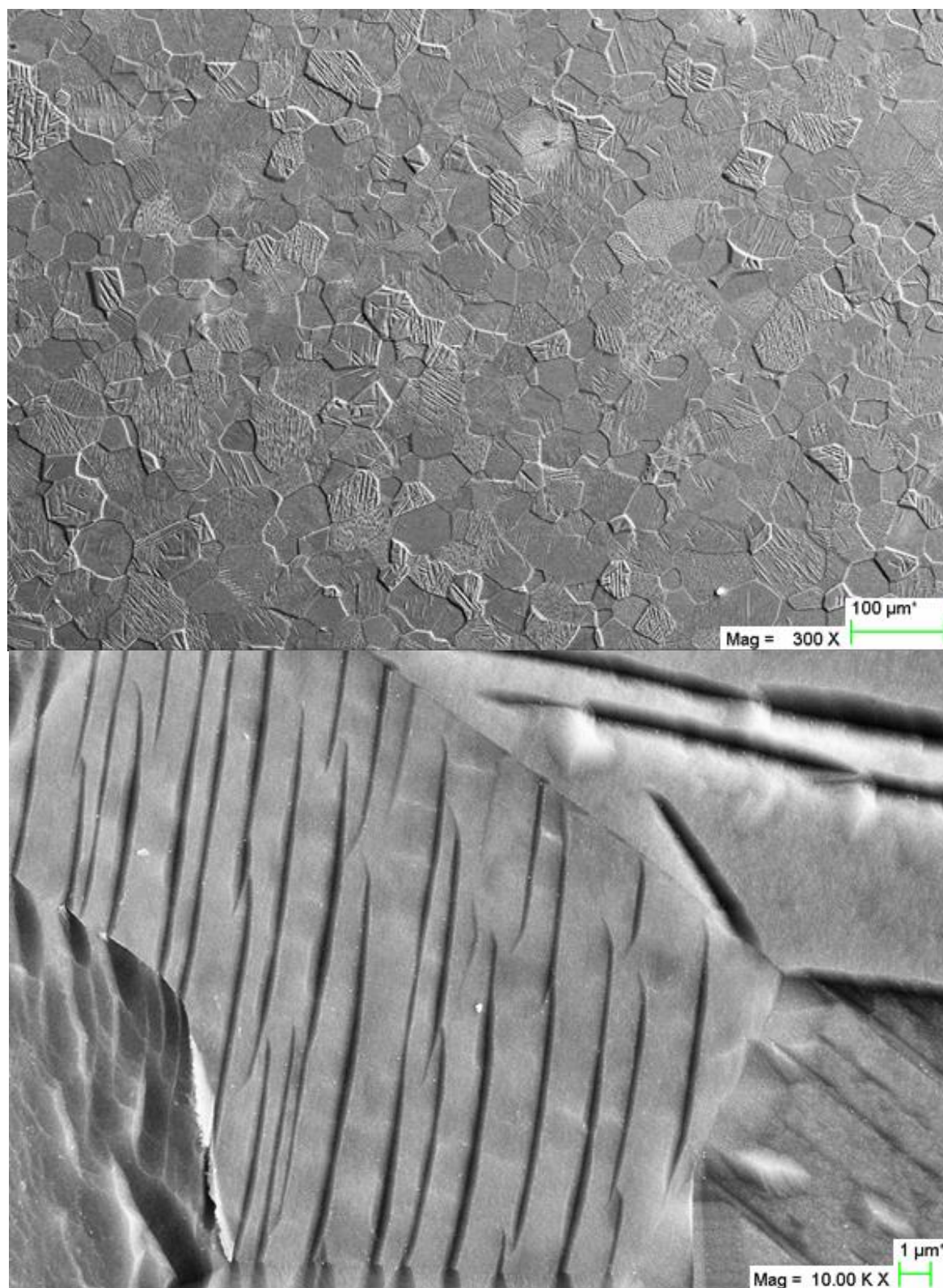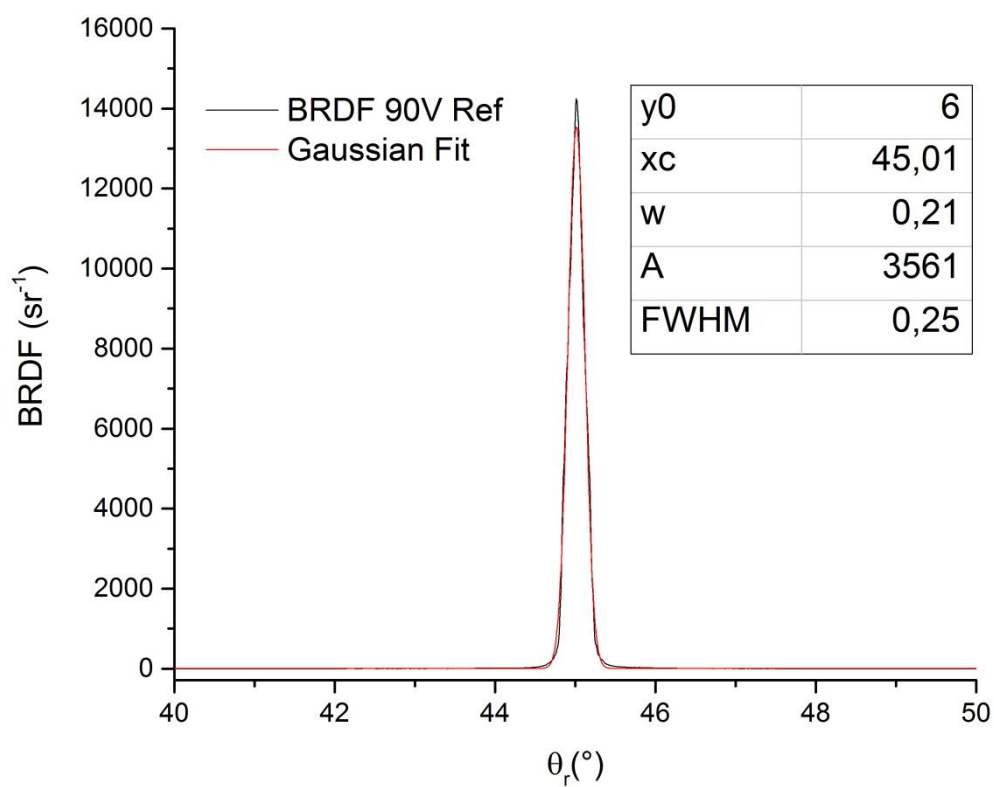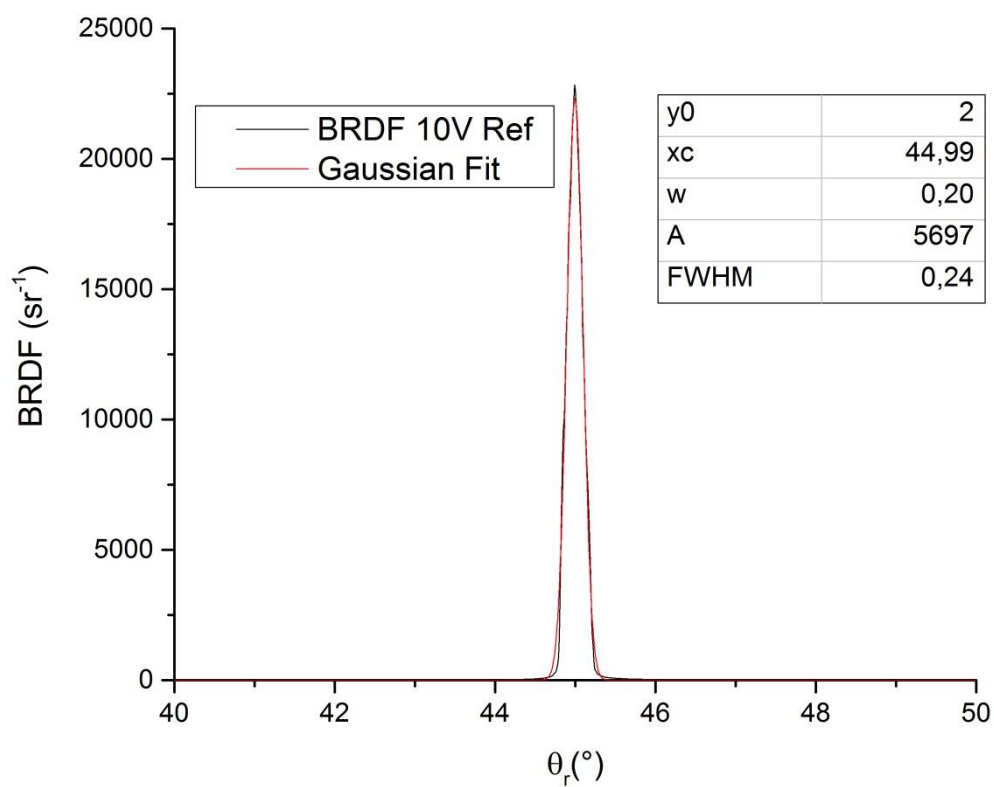
y0	2
xc	44,99
w	0,20
A	5697
FWHM	0,24

y0	6
xc	45,01
w	0,21
A	3561
FWHM	0,25

Rescaled reflectance spectra forobservation angles ranging from 44.7° to 45.3° of the non-etched titanium sample anodized at a cell potential of 10V

Rescaled reflectance spectra forobservation angles ranging from 44.3° to 45.7° of the etched titanium sample anodized at a cell potential of 10V

[44.3-44.85[U]44.85-45.7]

Away from the specular direction

Near the specular direction

[44.85-45.15]
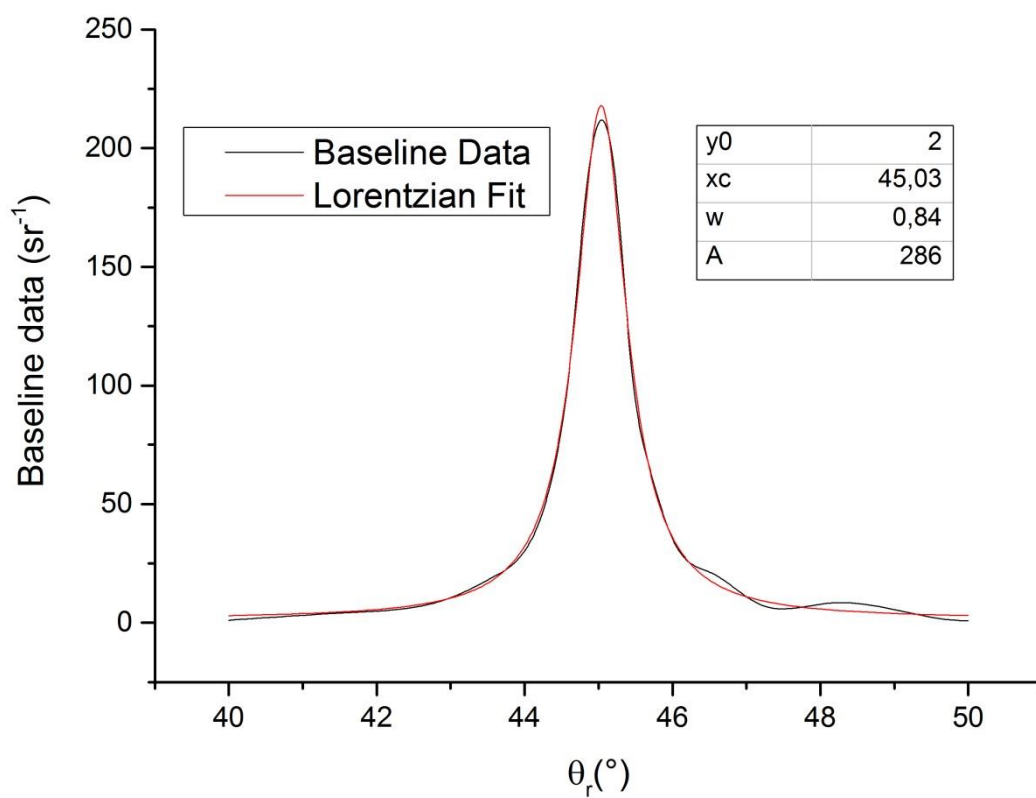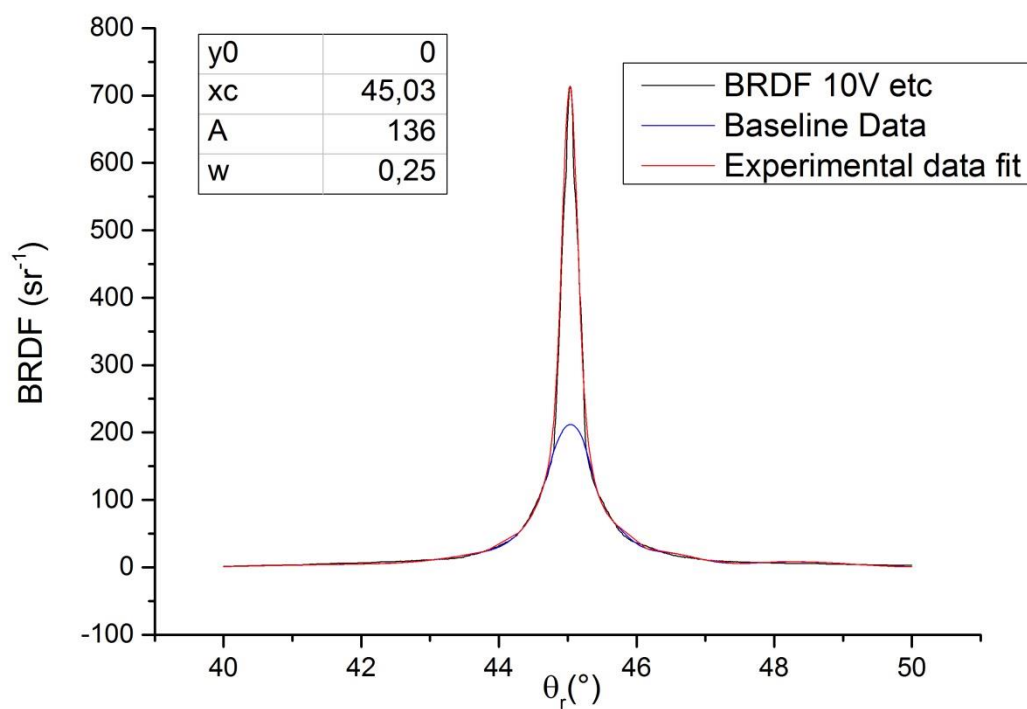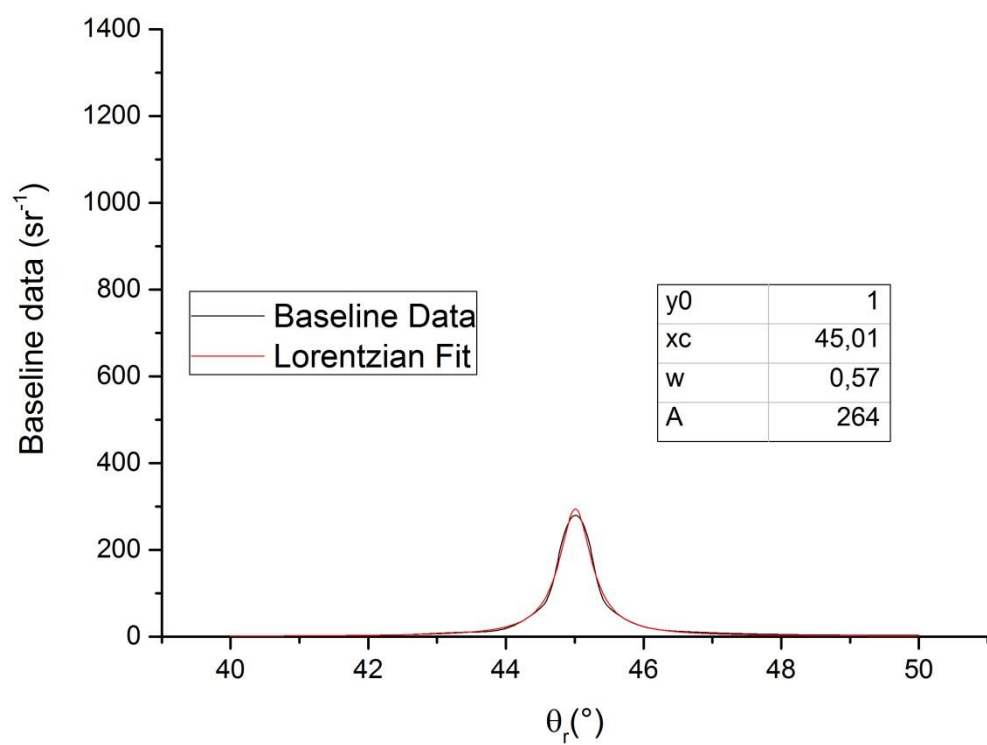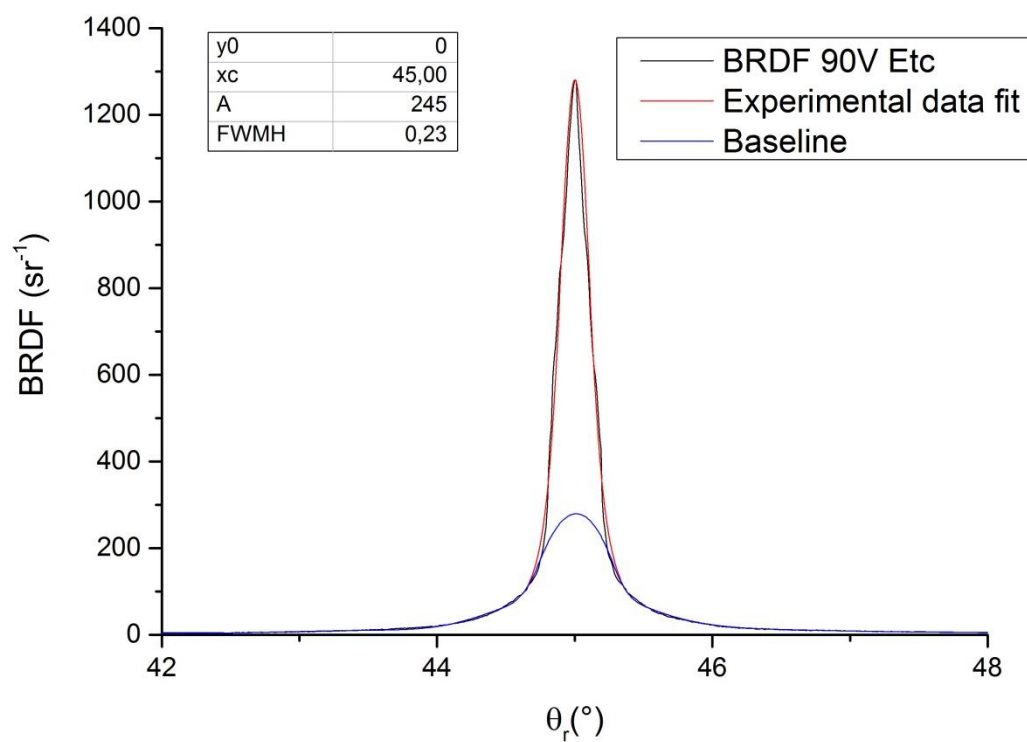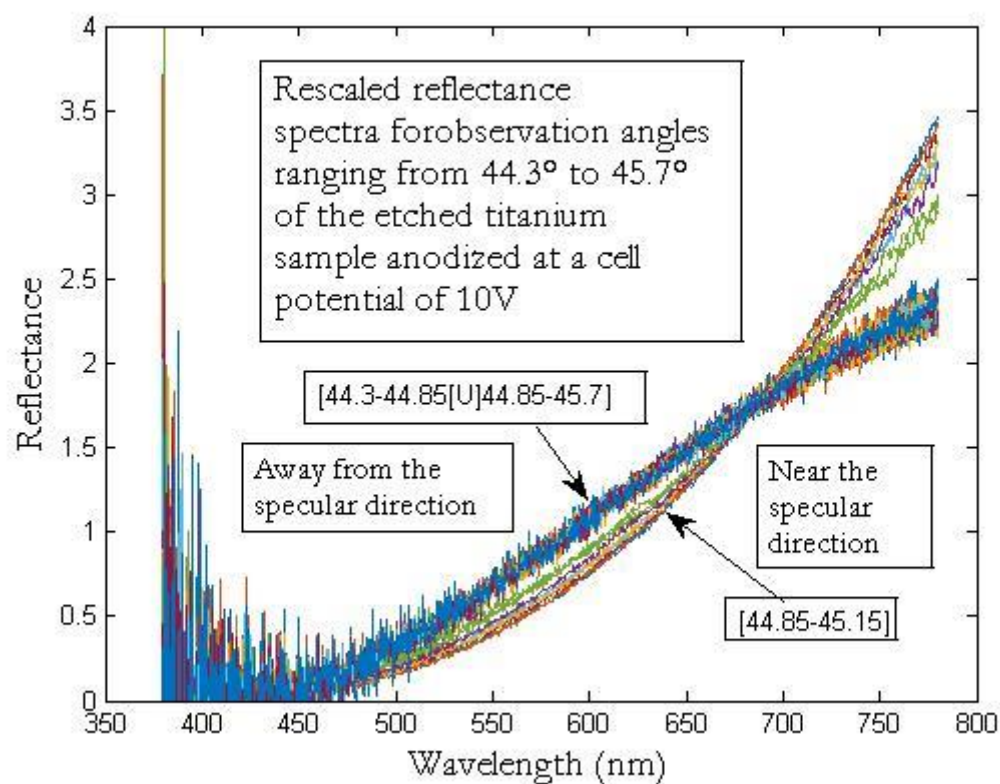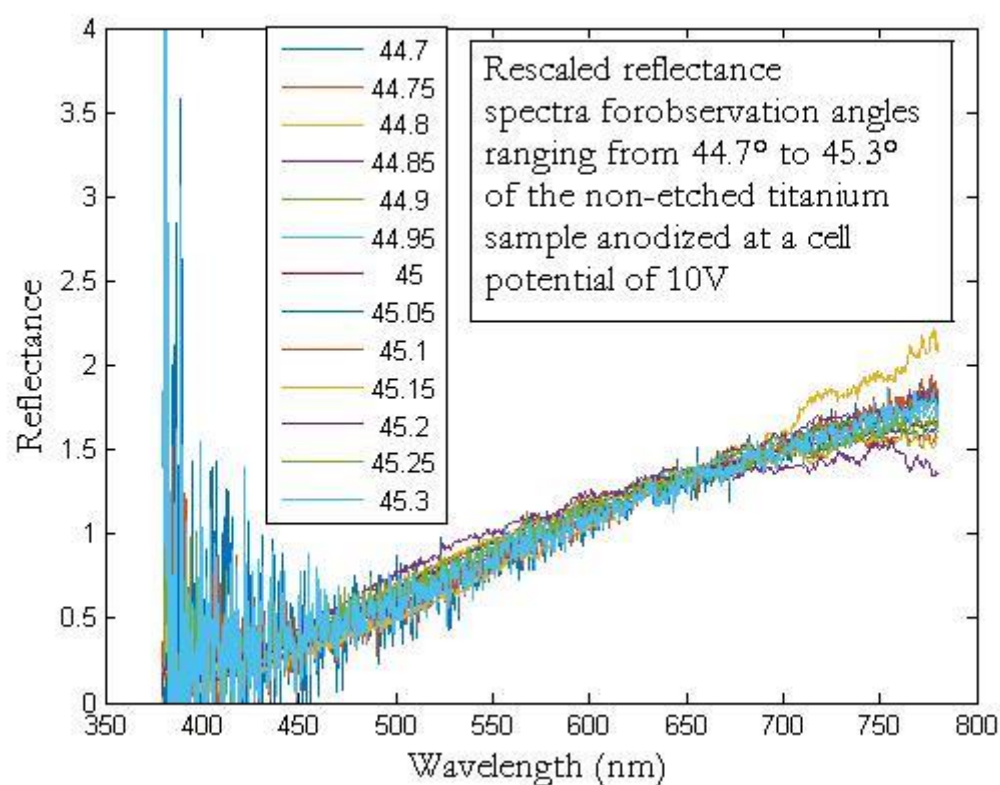
Appendix I: BRDF fits of Vibrometer, Alumina and P300 samples for different incidence angles and different cell potential as indicated on the table.

Color code: direct Flat-top Gaussian fit of the experimental data (green curve), when a baseline (blue curve) is necessary, Flat-top Gaussian fit of the baseline subtracted experimental data summed with the baseline (red curve) and experimental BRDF (black curve). The magenta curve corresponds to a Gaussian (instead of a Flat-top Gaussian) fit of the baseline subtracted experimental data summed with the baseline.

The table on the graphs indicates the parameters of the flat-top Gaussian (or Gaussian) fitting function of the (if applicable, baseline subtracted) experimental data.
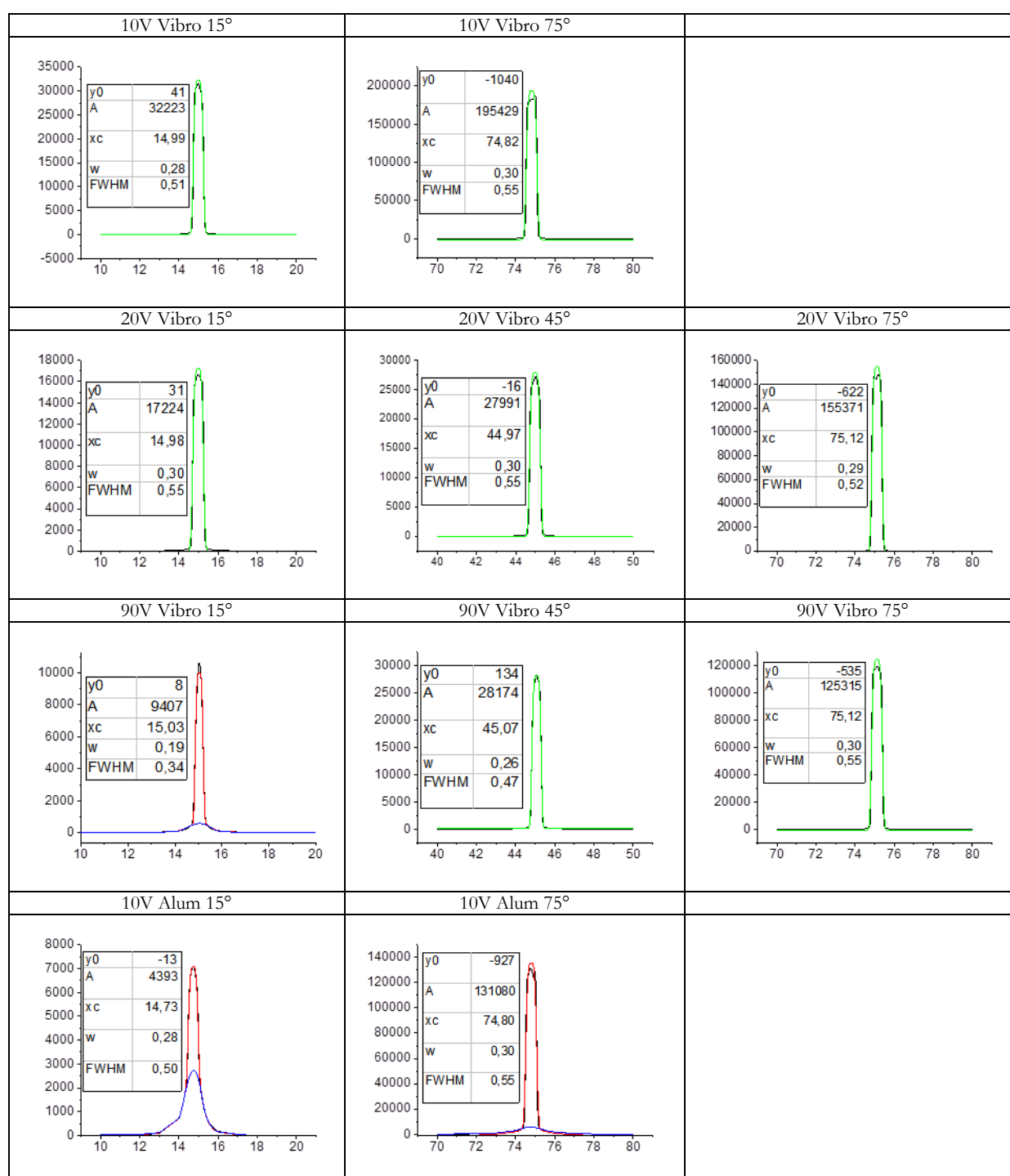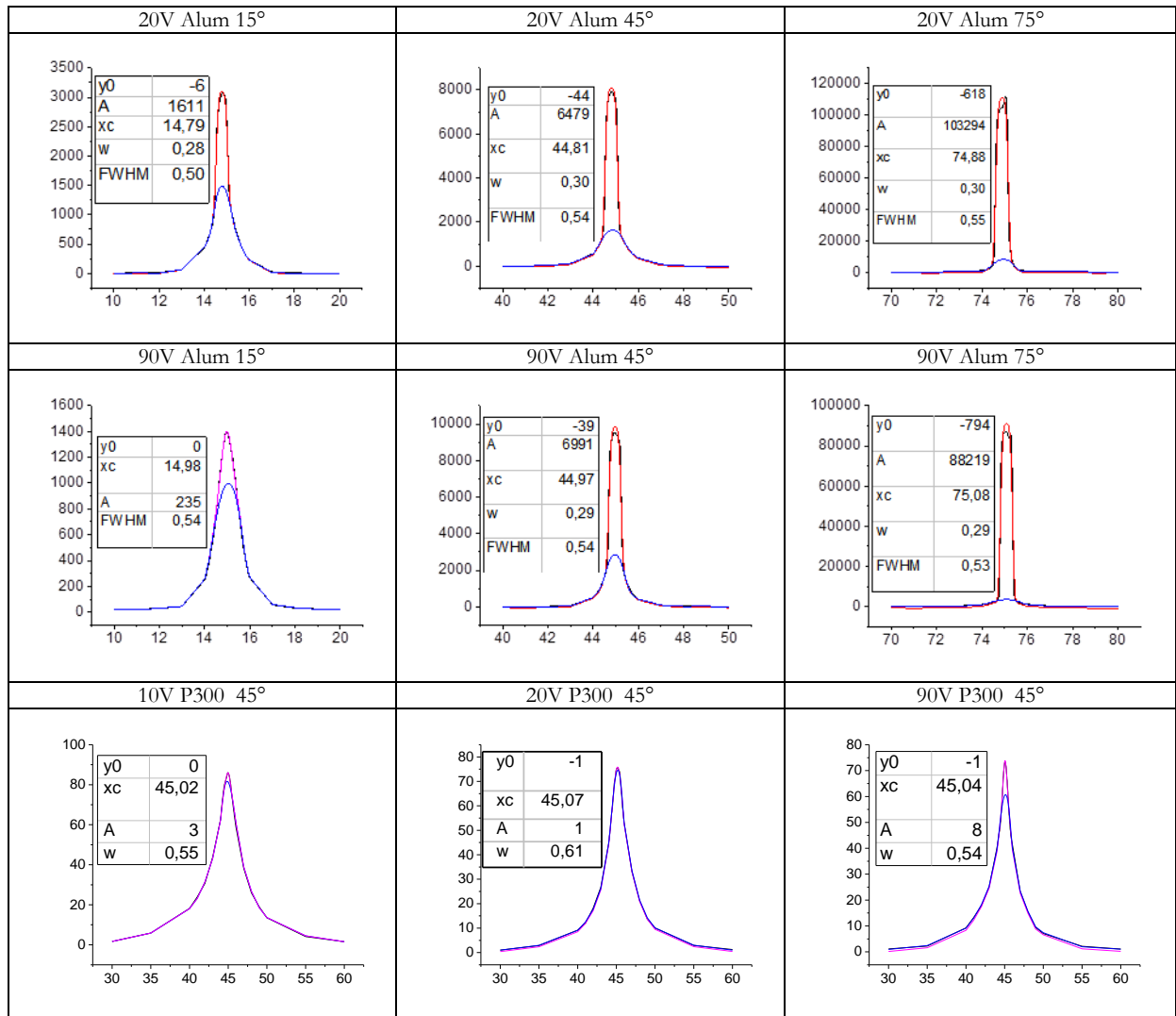
The abscissa axis corresponds to the BRDF value in sr^{-1} and the ordinate axis corresponds to the observation angle θ_r in degrees.

Color code: Gaussian fits (green curve), Lorentzian fits (red curve). The table on the graphs indicates the parameters of the Lorentzian (or Gaussian) function fitting the baseline.

10V Vibro 15°	10V Vibro 75°	
20V Vibro 15°	20V Vibro 45°	20V Vibro 75°
90V Vibro 15°	90V Vibro 45°	90V Vibro 75°

10V Alum 15°	10V Alum 75°	

20V Alum 15°	20V Alum 45°	20V Alum 75°

90V Alum 15°	90V Alum 45°	90V Alum 75°

10V P300 45°	20V P300 45°	90V P300 45°
y0 4 / xc 44,94 / w 3,74 / A 448	y0 4 / xc 45,16 / w 2,71 / A 300	y0 4 / xc 45,0 / w 2,72 / A 244

P300	Min (nm)	Refractive Indexes TiO$_2$/Ti	Thickness (nm) / average (nm)	
10V	390 (min)	2.44 / 1.81 + 2.54i	24.8	
20V	490 (min)	2.20 / 2.34 + 2.95i	41.0	
50V	450.1 (max)	2.27 / 2.15 + 2.77i	86.8	
90V	407.1 (max)	2.38 / 1.92 + 2.61i	162.0	162.6
	500.1 (min)	2.19 / 2.39 + 3.00i	163.2	
120V	408.1 (min)	2.37 / 1.92 + 2.61i	208.3	210.7
	484 (max)	2.21 / 2.31 + 2.92i	213.4	
	607.8 (min)	2.11 / 2.69 + 3.58i	210.5	

6μm	Min (nm)	Refractive Indexes TiO$_2$/Ti	Thickness (nm) / average (nm)	
10V	390 (min)	2.44 / 1.81 + 2.54i	24.8	
20V	500 (min)	2.19 / 2.38 + 3.00i	39.4	
50V	393.5 (min)	2.42 / 1.83 + 2.56i	110.5	111.2
	530 (max)	2.16 / 2.50 + 3.16i	111.9	
90V	410 (max)	2.37 / 1.94 + 2.62i	164.1	165.9
	509.9 (min)	2.18 / 2.43 + 3.05i	167.6	
120V	380 (max)	2.48 / 1.74 + 2.50i	222.9	220.1
	429.7 (min)	2.31 / 2.05 + 2.69i	226.9	
	607.7 (min)	2.11 / 2.69 + 3.58i	210.5	

Alum	Min (nm)	Refractive Indexes TiO$_2$/Ti	Thickness (nm) / average (nm)	
10V	420 (min)	2.34 / 1.99 + 2.66i	29.8	
20V	560 (min)	2.14 / 2.59 + 3.32i	51.1	
50V	450.2 (max)	2.27 / 2.15 + 2.77i	86.8	
90V	420 (max)	2.34 / 1.99 + 2.66i	171.0	171.6
	520 (min)	2.17 / 2.47 + 3.10i	172.2	
120V	372.3 (max)	2.52 / 1.68 + 2.46i	214.1	211.8
	400 (min)	2.40 / 1.87 + 2.58i	200.9	
	483.4 (max)	2.21 / 2.31 + 2.92i	213.1	
	606.9 (min)	2.11 / 2.69 + 3.57i	210.2	

Vibro	Min (nm)	Refractive Indexes TiO$_2$/Ti	Thickness (nm) / average (nm)	
10V	398.8 (min)	2.40 / 1.87 + 2.58i	26.4	
20V	380 (max)	2.48 / 1.74 + 2.50i	63.1	61.3
	620 (min)	2.10 / 2.71 + 3.63i	59.4	
50V	462.8 (max)	2.24 / 2.22 + 2.83i	91.3	
90V	413.5 (max)	2.36 / 1.96 + 2.63i	166.5	169.4
	520.1 (min)	2.17 / 2.47 + 3.10i	172.2	
120V	380 (max)	2.48 / 1.74 + 2.50i	222.9	217.3
	414.8 (min)	2.35 / 1.96 + 2.64i	214.1	
	616.6 (min)	2.10 / 2.71 + 3.62i	215.0	

Appendix N: CIE $L^* a^* b^*$ colorimetric coordinates and CIE xyY colorimetric coordinates of titanium samples from Vibrometer, Alumina, 6µm and P300 series anodized at cell potentials ranging from 5 V to 120 V. Measured with a commercial spectrophotometer Konica Minolta CM-2500C under a D65 illuminant (45°a:0° geometry).

Vibrometer series						
Cell potential (V)	L^*	a^*	b^*	x	y	Y
5	67,25	1,45	17,43	0,35627682	0,37035384	36,9639827
10	58,64	3,9	30,82	0,39989346	0,405815732	26,6404112
15	45,57	12,15	29,92	0,43652813	0,40158004	14,9531777
20	43,05	3,58	-34,92	0,21416994	0,21609468	13,1912435
25	36,39	16,71	-24,98	0,26508321	0,22514174	9,21236693
30	58,57	-7,68	-22,14	0,24302865	0,27494743	26,5655286
35	48,82	-0,89	-30,98	0,22365083	0,23758051	17,4482997
40	59,04	-7,02	-23,19	0,24215633	0,27212467	27,0710131
45	67,08	-8,32	-14,32	0,2656325	0,29991098	36,7379988
50	72,62	-7,89	-5,92	0,28680699	0,3212673	44,5883364
55	72,95	-7,54	-1,63	0,29660565	0,33123825	45,088303
60	62,15	2,38	19,22	0,36538702	0,37641206	30,5782748
65	74,55	-7,52	22,85	0,34835863	0,38855976	47,5654266
70	73,18	-2,09	34,48	0,38270588	0,40930946	45,4389656
75	63,6	14,89	25,02	0,40363781	0,373874	32,3121038
80	60,74	22,05	15,47	0,39732747	0,34447064	28,9528564
85	53,58	26,81	-17,32	0,31833374	0,25906761	21,5813847
90	54,08	27,76	-16,05	0,32392303	0,26180455	22,0499857
95	52,05	22,34	-23,32	0,29179042	0,24633181	20,1887961
100	51,35	19,7	-23,32	0,28632295	0,24739795	19,5721634
105	51,43	9,34	-19,62	0,2762585	0,26435604	19,6419912
110	51,89	3,3	-16,1	0,27417053	0,27892903	20,0467262
115	52,73	-1,76	-7,69	0,28743418	0,30788267	20,8000828
120	53,42	-2,42	-1,3	0,30392931	0,3276695	21,4328468

Alumina series						
Cell potential (V)	L^*	a^*	b^*	x	y	Y
5	74,7	1,29	8,94	0,33420108	0,34817634	47,802201
10	50,76	7,46	39,73	0,44010044	0,4288338	19,0622875
15	54,94	7,6	34,51	0,42176132	0,41225234	22,87176
20	30,01	20,63	-37,05	0,22376123	0,1749574	6,23997331
25	41,4	18,19	1	0,36385308	0,30944137	12,1160682
30	42,14	11,04	-24,04	0,26025997	0,24061479	12,5907359
35	49,51	-0,6	-29	0,23006004	0,2436105	18,0114564
40	60,18	-7,52	-22,4	0,24408855	0,27530611	28,3236316
45	66,96	-8,57	-16,28	0,26085667	0,29518267	36,5790365
50	72,76	-8,03	-9,12	0,27985815	0,31380388	44,7999896
55	76,28	-7,18	-2,55	0,29586529	0,32878412	50,3441242
60	79,01	-6,61	6,8	0,31608535	0,34921162	54,9457349
65	79,48	-6,56	15,14	0,33290137	0,36756473	55,7651999
70	72,45	0,55	36,96	0,39315386	0,4118772	44,3322266
75	70,52	3,99	41,78	0,41101674	0,41886819	41,4930696
80	65,1	14,67	34,83	0,42395786	0,39431701	34,1734319
85	60,04	25,08	17,31	0,40922805	0,34513009	28,1677629
90	52,63	25,57	-9,92	0,33812324	0,27742372	20,7094244
95	52,05	30,1	-13,89	0,33557529	0,26338884	20,1887961
100	50,72	25,97	-21,29	0,30465823	0,24731718	19,0280439
105	50,73	21,21	-23,32	0,28907489	0,24569452	19,036601
110	51,89	5,57	-19,99	0,26801689	0,26648892	20,0467262
115	53,36	-2,73	-11,28	0,27592041	0,29841398	21,3773213
120	53,06	-3,1	-2,97	0,29778213	0,32331183	21,101132

						6µm series

Cell potential (V)	L^*	a^*	b^*	x	y	Y
5	61,2	2,13	16,56	0,35888644	0,37044798	29,476637
10	56,47	4,63	31,01	0,40446815	0,40719079	24,3837679
15	36,41	19,44	12,47	0,41771714	0,34309286	9,22292148
20	35,95	18,63	0,13	0,36696717	0,30379913	8,98219932
25	40,59	0,52	-29,67	0,21885663	0,2288066	11,6103447
30	51,74	-6,51	-22,78	0,23712753	0,26695804	19,9141424
35	62,56	-8,11	-13,48	0,26534465	0,30024632	31,0620745
40	66,17	-7,46	-5,91	0,28558837	0,32030172	35,5439667
45	63,76	-6,96	-9,15	0,2780834	0,31110405	32,5073426
50	71,96	-7,28	9,04	0,32003939	0,35690071	43,5995186
55	72,57	-5,13	23,45	0,35473285	0,38869686	44,5129079
60	69,78	-3,62	15,8	0,3419815	0,37059959	40,437487
65	71,46	0,98	24,07	0,36785989	0,38404604	42,8602255
70	71,48	-0,35	32,03	0,38222563	0,40328599	42,8896355
75	63,29	15,64	17,19	0,3862309	0,35532985	31,9360563
80	59,09	18,42	8,82	0,37367118	0,33301047	27,1251623
85	56,12	18,15	2,41	0,35735405	0,31713913	24,032181
90	52,78	26,61	-3,13	0,36102878	0,29351862	20,845511
95	51,57	7,31	-6,18	0,3107291	0,3035067	19,7645891
100	51,99	8,44	-10,79	0,29976479	0,28964882	20,1354415
105	52,89	1	-7,71	0,29318925	0,30538741	20,9456859
110	53,02	-1,65	-0,25	0,30847804	0,33003033	21,0644875
115	61,2	2,13	16,56	0,35888644	0,37044798	29,476637
120	56,47	4,63	31,01	0,40446815	0,40719079	24,3837679

P300 series						
Cell potential (V)	L^*	a^*	b^*	x	y	Y
5	68,57	1,61	13,39	0,34663348	0,35992511	38,750296
10	56	4,61	28,7	0,39927756	0,40192687	23,9124195
15	43,64	13,44	30,14	0,4444099	0,40130179	13,5906096
20	39,8	15,3	4,82	0,37171534	0,32504472	11,1308577
25	39,15	14,79	-13,33	0,30355564	0,26649048	10,7463896
30	42,88	6,49	-22,68	0,25513634	0,24886124	13,0776418
35	48,78	-0,26	-25,5	0,23903961	0,25221275	17,4160179
40	59,73	-7,18	-20,27	0,24923434	0,28032992	27,8246623
45	67,04	-8,41	-13,77	0,26666991	0,30132526	36,6849603
50	73,45	-7,73	-7,91	0,28312066	0,31654944	45,8529273
55	73,99	-6,68	-0,43	0,30075119	0,3333679	46,6883781
60	76,44	-5,97	4,86	0,31319566	0,3448007	50,6064465
65	79,77	-6,15	12,38	0,32799267	0,36099751	56,2748692
70	73,13	-1,76	27,73	0,36956143	0,39423257	45,3625805
75	70,8	4,48	37,34	0,40284058	0,40898589	41,8972201
80	66,4	12,59	34,43	0,41728837	0,39548986	35,8432736
85	59,76	21,43	19,91	0,40887194	0,35551453	27,8577432
90	55,48	29,81	2,78	0,38340453	0,3057834	23,39805
95	53,3	30,94	-7,69	0,35583889	0,2785644	21,3218918
100	50,04	27,61	-14,31	0,32954809	0,2626569	18,4521606
105	48,99	20,3	-22,26	0,28969611	0,24710118	17,5859423
110	49,98	8,57	-19,78	0,27343669	0,26318374	18,4019127
115	52,5	-2,1	-12,5	0,2734357	0,29392626	20,5919629
120	52,75	-4,71	-4,72	0,28944143	0,31953514	20,8182462

École Nationale Supérieure des Mines
de Saint-Étienne

Quentin CRIDLING

INFLUENCE OF THE SUBSTRATE SURFACE PREPARATION ON OPTICAL PROPERTIES AND COLOR OF ANODIZED TITANIUM

Abstract :

The study and the development of goniochromic materials remains a challenge both for industry and for scientific research. In the industry, the color quality control is rendered difficult by the complex color effects of these materials. The development of standard goniochromic materials with referenced color effects could simplify this color quality control. By comparing the manufactured materials to the reference ones by for example acquiring pictures of both materials in given geometries could be an easy process for color quality control. The challenge for scientific research consists to be able to control the color evolution with the illumination and observation conditions and define color characterization geometries in agreement with perceived color effects.

A bibliographic review showed that anodized titanium is a promising candidate for reference goniochromic samples. In order to obtain samples with different levels of gloss, samples with substrate roughnesses ranging from a few to two hundred nanometers obtained through hydrofluoric etching or different mechanical and chemical polishing were prepared. Anodized titanium color is linked to the oxide layer thickness and the material refractive index. These parameters were estimated through different techniques in particular a technique based on the extrema of the material reflectance spectrum as well as ellipsometry and X-ray reflectometry. These parameters were put into an optical model in order to simulate the material specular reflectance. The diffuse and specular reflectances of the samples are also compared and a first simple model of the diffuse reflectance is presented. The Bidirectional Reflectance Distribution Function (BRDF) spectral and angular variations are used to characterize the diffuse appearance and goniochromism of the samples versus the substrate preparation and the anodizing cell potential.

École Nationale Supérieure des Mines
de Saint-Étienne

NNT : 2018 LYSEM015

Quentin CRIDLING

INFLUENCE DE LA PREPARATION DE SURFACE DU SUBSTRAT SUR LA COULEUR ET LES PROPRIETES OPTIQUES DU TITANE ANODISE

Spécialité: Sciences des matériaux et de l'ingénieur

Mots clefs : Mesures de couleur, titane anodisé, gonioapparence, rugosité, BRDF

Résumé :

L'étude et le développement des matériaux goniochromes reste un challenge aussi bien pour la recherche scientifique que pour l'industrie. Dans le domaine industriel, le contrôle qualité de la couleur est rendu difficile par les effets colorés de ces matériaux. Le développement d'un étalon de matériaux goniochromes avec des effets colorés référencés pourrait permettre de simplifier ce control qualité de la couleur. Le challenge pour la recherche scientifique consiste à être capable de contrôler l'évolution de la couleur avec les conditions d'illumination et d'observation et de définir les géométries de caractérisation en accord avec les effets colorés perçus.
Une revue bibliographique a montré que l'anodisation du titane est un candidat prometteur pour produire des échantillons goniochromes de référence. Afin d'obtenir des échantillons avec différents niveaux de brillant, des échantillons avec des substrats ayant une rugosité comprise entre quelques et deux cents nanomètres ont été préparés soit par un décapage à l'acide fluorhydrique soit par succession de polissages mécaniques et chimiques. La couleur du titane anodisé est liée à l'épaisseur de la couche d'oxyde et à l'indice de réfraction du matériau. Ces paramètres ont été estimés à l'aide de différentes techniques, en particulier une technique basée sur la lecture des extrema du spectre de réflectance du matériau mais aussi par ellipsométrie et réflectométrie par rayons X. Ces paramètres ont été utilisés dans un modèle optique afin de simuler la réflectance spéculaire du matériau. Les réflectances diffuse et spéculaire ont été comparées et un premier modèle de réflectance diffuse a été proposé. Les fonctions de distribution bidirectionnelle de la réflectance (BRDF) spectrales et angulaires ont été utilisées pour caractériser le goniochromisme et l'aspect diffus de ces échantillons en fonction de la rugosité du substrat et du potentiel d'anodisation.